

**NIST Technical Note 2054**

**Compartment Fire Experiments on  
Long-Span Composite-Beams with  
Simple Shear Connections  
Part 1: Experimental Design and Beam  
Behavior at Ambient Temperature**

Selvarajah Ramesh  
Lisa Choe  
Mina Seif  
Matthew Hoehler  
William Grosshandler  
Ana Sauca  
Matthew Bundy  
William Luecke  
Yi Bao  
Matthew Klegseth  
Genda Chen  
John Reilly  
Branko Glisic

This publication is available free of charge from:  
<https://doi.org/10.6028/NIST.TN.2054>

**NIST**  
**National Institute of  
Standards and Technology**  
U.S. Department of Commerce

NIST Technical Note 2054

# Compartment Fire Experiments on Long-Span Composite-Beams with Simple Shear Connections Part 1: Experimental Design and Beam Behavior at Ambient Temperature

Selvarajah Ramesh, Lisa Choe, Mina Seif,  
Matthew Hoehler, William Grosshandler,  
Ana Sauca, and Matthew Bundy  
*Fire Research Division  
Engineering Laboratory, NIST*

William Luecke  
*Materials Science and Engineering Division  
Material Measurement Laboratory, NIST*

Yi Bao  
*Stevens Institute of Technology*

Matthew Klegseth and Genda Chen  
*Missouri University of Science and  
Technology*

John Reilly and Branko Glisic  
*Princeton University*

This publication is available free of charge from:  
<https://doi.org/10.6028/NIST.TN.2054>

October 2019



U.S. Department of Commerce  
*Wilbur L. Ross, Jr., Secretary*

National Institute of Standards and Technology  
*Walter Copan, NIST Director and Undersecretary of Commerce for Standards and Technology*

This page intentionally left blank.

The policy of the National Institute of Standards and Technology is to use metric units in all its published materials. Because this report is intended for the U.S. building construction industry, in some cases U.S. customary units are used.

Certain commercial entities, equipment, products, or materials are identified in this document in order to describe a procedure or concept adequately. Such identification is not intended to imply recommendation or endorsement by the National Institute of Standards and Technology, nor is it intended to imply that the entities, products, materials, or equipment are necessarily the best available for the purpose.

The policy of the National Institute of Standards and Technology is to include statements of uncertainty with all NIST measurements. In this document, some measurements made by authors outside of NIST are presented, for which uncertainties are not reported and are unknown.

**National Institute of Standards and Technology Technical Note 2054  
Natl. Inst. Stand. Technol. Tech. Note 2054, 159 pages (October 2019)  
CODEN: NTNOEF**

**This publication is available free of charge from:  
<https://doi.org/10.6028/NIST.TN.2054>**



## ABSTRACT

---

A series of compartment fire experiments was conducted on long-span steel-concrete composite floor beams designed and constructed following U.S. building codes and standards. The test program consisted of five 12.8 m long composite floor beam specimens with various end support conditions. Each specimen was constructed as a partially-composite beam consisting of a W18×35 steel beam and an 83 mm thick lightweight concrete slab cast on top of 76 mm deep ribbed steel decking units. Test variables included two types of simple shear connections (shear-tab and welded/bolted double-angle connections) and the slab continuity over girders. One specimen with the double-angle connections at the ends was tested at ambient temperature and the remaining four specimens were tested under simultaneous mechanical and fire loading.

This report, Part 1, presents details of the test setup, specimens, design basis of fire loading, instrumentation, and the behavior of the composite beam with double-angle connections at ambient temperature. The ambient temperature test indicated that the composite beam specimen failed by a shear stud near the west end, followed by concrete breakout failure and yielding of the steel beam. The measured moment capacity was approximately 80% of the calculated flexural strength. The double-angle connection at the west end failed by weld fracture, which caused collapse of the composite beam. The ambient behavior of the composite beam specimen presented herein will serve as a baseline to compare with the composite beam assemblies tested under combined mechanical loads and fire exposure, which are presented in a subsequent report; Part 2 (Choe et al. 2019). The datasets obtained from these tests provide technical information to advance performance-based design of composite floor assemblies in steel-framed buildings subject to fire.

**Keywords:** Compartment fire, Composite beam; Connection; Experimental testing

This page intentionally left blank.

## PREFACE

---

This work was conducted as part of the project “Measurement of Structural Performance in Fire” under the National Institute of Standards and Technology (NIST) Engineering Laboratory’s Fire Risk Reduction in Buildings Program. We thank William Baker (Skidmore, Owings & Merrill), Craig Beyler (Jensen Hughes), Luke Bisby (University of Edinburgh), Ian Burgess (University of Sheffield), Charles Carter (AISC), Charles Clifton (University of Auckland), Michael Engelhardt (University of Texas), Graeme Flint (Arup), Nestor Iwankiw (Jensen Hughes), Kevin LaMalva (Simpson Gumpertz & Heger), Roberto Leon (Virginia Tech.), and Amit Varma (Purdue University) for their expert consultation. We also thank the NIST colleagues including Brian Story, Laurean DeLauter, Anthony Chakalis, Philip Deardorff, Marco Fernandez, Artur Chernovsky, Chao Zhang, Kevin McGrattan, Joseph Main, Fahim Sadek, Scott Jones and Dale Bentz for their significant contributions to design, material characterization, construction and execution of this test program.

This page intentionally left blank.

# TABLE OF CONTENTS

---

---

Abstract.....	i
Preface .....	iii
Table of Contents.....	v
List of Figures.....	ix
List of Tables .....	xiii
<b>Chapter 1 Introduction .....</b>	<b>1</b>
1.1 Background.....	1
1.2 Previous Work .....	3
1.3 Motivation and Objectives.....	5
1.4 Report Outline.....	6
<b>Chapter 2 Test Program.....</b>	<b>9</b>
2.1 Test Matrix.....	9
2.2 Design and Construction of Prototype Composite Beam .....	10
2.2.1 Design Basis.....	10
2.2.2 Loads .....	10
2.2.3 Shear Connections.....	12
2.2.4 Passive Fire Protection .....	13
2.2.5 Construction of Specimen .....	15
2.3 Construction Materials.....	18
2.3.1 Structural Steel, Bolts, Shear Studs, Reinforcing bar, and Welded wire fabric .....	18
2.3.2 Concrete.....	24
<b>Chapter 3 Experimental Setup .....</b>	<b>35</b>
3.1 Structural Setup.....	35
3.1.1 Mechanical Loading.....	38
3.1.2 Lateral Support Stiffness .....	41
3.2 Fire Conditions .....	44
3.2.1 Fire Load Development.....	44
3.2.2 Fire Simulation.....	48
<b>Chapter 4 Measurement System .....</b>	<b>55</b>

4.1	Structural Measurements .....	56
4.1.1	Forces .....	56
4.1.2	Strains.....	57
4.1.3	Displacements .....	57
4.1.4	Rotations.....	58
4.2	Fire Measurements.....	59
4.2.1	Natural Gas.....	59
4.2.2	Calorimeter.....	61
4.2.3	Thermocouples .....	61
4.2.4	Heat Flux Gauges .....	63
4.2.5	Plate Thermometers.....	63
4.3	Data Acquisition System.....	64
4.4	Fiber Optic Measurements.....	65
4.4.1	Distributed Fiber Optic Sensors .....	65
4.4.2	Fiber Bragg Grating Sensors .....	73
4.5	Measurement Uncertainty.....	77
<b>Chapter 5 Test 1- Structural Behavior at Ambient Temperature .....</b>		<b>83</b>
5.1	Instrumentation .....	83
5.2	Mechanical Loading.....	85
5.3	Results and Discussion .....	86
5.3.1	Global Behavior .....	86
5.3.2	End Slip and Gap Closure .....	89
5.3.3	Cross-Sectional Behavior .....	90
5.3.4	Connection Behavior.....	93
5.3.5	Fiber Optic Strain Measurements.....	93
5.3.6	Post Test Investigation of Failure Modes .....	97
<b>Chapter 6 Summary and Conclusions.....</b>		<b>101</b>
<b>References .....</b>		<b>103</b>
<b>APPENDIX A Drawings For Test Setup .....</b>		<b>109</b>
<b>APPENDIX B Survey Results for Design Parameters and Specimen Design Calculations .....</b>		<b>115</b>
<b>APPENDIX C Fire Dynamics Simulator Input Files.....</b>		<b>130</b>

<b>APPENDIX D Steel Mill Certificates .....</b>	<b>135</b>
<b>APPENDIX E Concrete Batch Tickets.....</b>	<b>138</b>
<b>APPENDIX F Concrete Results.....</b>	<b>141</b>

This publication is available free of charge from: <https://doi.org/10.6028/NIST.TN.2054>

This page intentionally left blank.



## LIST OF FIGURES

Figure 2-1 Cross-section of (a) composite beam specimen and (b) concrete slab on steel deck. All dimensions are nominal values specified in construction drawings. ....	12
Figure 2-2 Shear connections at the end of specimens (a) double angle and (b) single plate.....	13
Figure 2-3 Application of the Sprayed Fire Resistive Materials on the prototype floor beam assemblies. ....	14
Figure 2-4 Placement of (a) steel deck, shear stud, welded wire fabric, (b) embedded steel bearing plates, (c) a shear stud weld, (d) No. 4 reinforcing bar and welded wire fabric for slab continuity. ....	16
Figure 2-5 Front view of damaged concrete slab of CB-SP-SC. ....	17
Figure 2-6 Top view of damaged concrete slab of Specimen CB-SP-SC.....	17
Figure 2-7 (a) Formwork for repaired concrete slab (b) wire fabric joint by welding.....	18
Figure 2-8 Flat tensile specimen (A=57 mm, W=12.5 mm, B=75 mm C=20 mm, R=12.5 mm).....	19
Figure 2-9 Tensile specimen machined from A325 bolt. Units = cm.....	19
Figure 2-10 Tensile specimen machined from shear stud. Units = cm.....	20
Figure 2-11 Engineering stress versus strain for (a) W18x35 steel beam, (b) shear tab and double angle, (c) bolts and shear studs, and (d) reinforcing bar and welded wire fabric. ....	23
Figure 2-12 Average engineering strain rate during each test. Dashed colored lines denote the acceptable strain rate range in ISO 6892. ....	24
Figure 2-13 Casting of the specimens: (a) National Fire Research Laboratory test hall; (b) concrete placement in formwork; (c) initial curing with wet burlap covered in plastic; (d) subsequent curing in underground curing pit.....	26
Figure 2-14 Air temperature and relative humidity: (a) in curing pit; (b) approximate conditions in test hall.....	27
Figure 2-15 Monitoring of relative humidity in the slab during curing: (a) embedded wireless sensors (black ovals); (b) downhole relative humidity probe.....	28
Figure 2-16 Temperature in the test specimens. ....	28
Figure 2-17 Relative humidity in the test specimens.....	29
Figure 2-18 Compressive strength development (error bars are standard deviation) .....	33
Figure 3-1 (a) A 3D schematic and (b) photograph of the structural test setup (fire compartment walls are not shown).....	36
Figure 3-2 (a) Connection and slab end support conditions for specimen without slab continuity-side view, (b) beam-to-column connection, (c) connection of sacrificial and bearing plates to column. ..	37
Figure 3-3 (a) Connection and slab end support conditions for specimen with slab continuity (elevation view), (b) photograph of anchored slab (top view).....	38
Figure 3-4 (a) Mechanical loading system (lateral brace system not shown).....	39
Figure 3-5 (a) Rollers at the end of loading beams, (b) guide frame, (c) lateral-torsional brace to specimen, (d) loading truss. ....	40

Figure 3-6 Cross-section view of the specimen with loading system. ....	41
Figure 3-7 Setup for lateral stiffness test of braced columns (units in cm). ....	42
Figure 3-8 Photographs of (a) the lateral stiffness test setup, (b) displacement sensor, (c) slip sensor, and (d) targets for laser tracker system. ....	43
Figure 3-9 Average HRR and nominal temperature of NIST full-scale office fire experiments (Hamins et al. 2008) with time-temperature curve from ASTM E119. ....	45
Figure 3-10 Average compartment time-temperature response in Cardington Test 7 (BRE 2004). ....	46
Figure 3-11 Representative fire behavior showing simulated local heat release and soot. ....	49
Figure 3-12 Interior wall surface temperatures (in degree Celsius) viewed from below 120 min after ignition. ....	49
Figure 3-13 Interior wall heat fluxes (kW/m <sup>2</sup> ) viewed from below 120 min after ignition. ....	50
Figure 3-14 Exterior wall temperatures (in degree Celsius) 120 min after ignition. ....	51
Figure 3-15 Average temperatures of hot gas layer (blue), spatial average along lower flange of steel beam (orange), and average temperature of columns near beam connection (gray) for case 5Be. ....	51
Figure 3-16 Temperatures along lower flange of steel beam (case 5Be). ....	52
Figure 3-17 Laboratory-side wall temperature of at x=9.0, y=2.5 comparing 25 mm of ceramic fiber blanket (blue curve) to 50 mm of ceramic fiber blanket (red-dotted curve). ....	54
Figure 3-18 Temperature of front wall (outside) with temperatures of 300 °C and higher shown in black; 25 mm insulation on left compared to 50 mm on right. ....	54
Figure 4-1 (a) Hydraulic actuator mounted on yoke located underneath strong floor; (b) load cells mounted around the reinforcing bars (top view). ....	56
Figure 4-2 (a) Measurement of vertical displacement using string potentiometers; (b) attachment to the concrete slab; (c) gap measurement at beam end. ....	58
Figure 4-3 Inclinometers: (a) along centerline of the slab at east and west ends; (b) on top of the loading beam; (c) on the loading truss; (d) on the web of the beam at east and west ends. ....	59
Figure 4-4 (a) Burner; (b) drawing of gas burner assembly, units in cm. All dimensions have a standard uncertainty of ±0.5 cm. ....	60
Figure 4-5 Photograph of the testing area showing the strong floor, strong wall, and exhaust hood. ....	61
Figure 4-6 Thermocouples: (a) peened into drilled holes and covered with ceramic adhesive (prior to application of SFRM); (b) bare bead thermocouples attached to ceramic rod in slab prior to concrete casting; (c) Inconel sheathed thermocouples used to measure the temperature of the steel beam; (d) super OMEGACLAD sheathed thermocouples used to measure the temperature of the compartment. ....	62
Figure 4-7 Gardon gauge mounted on the east wall. ....	63
Figure 4-8 Location of plate thermometers: (a) east connection; (b) mid-span of the beam. ....	64
Figure 4-9 Data Acquisition hardware: (a) cDAQ-9188; (b) NI PXIe-1082; (c) NI-9213; (d) NI PXIe-4330. ....	65
Figure 4-10 Schematic view of an optical fiber cable. ....	66

Figure 4-11 Top view of the locations of distributed fiber optic sensors (DFOS) and Fiber Bragg Grating (FBG) sensors in the concrete slab. The length and locations of the FBG sensors in (a) CB-DA-AMB are different from those in (b) CB-DA and CB-DA-SC (units in mm)..... 69

Figure 4-12 Photographs of installed distributed fiber optic sensors: (a) transverse (T-DFOS) temperature sensors (blue), (b) longitudinal (L-DFOS) temperature (blue and pink) and strain (yellow, thin), and (c) temperature sensor on web of steel beam (blue tape over thick yellow optical fiber)..... 70

Figure 4-13 Side view of the locations of distributed fiber optic sensors (DFOS) and Fiber Bragg Grating (FBG) sensors in the concrete slab. The length and locations of the FBG sensors in CB-DA-AMB (left) are different from those in CB-DA and CB-DA-SC (right) (units in mm). ..... 71

Figure 4-14 Distributed fiber optic sensor (DFOS) measurements in L-DFOS-1 and L-DFOS-2 along the centerline of specimen CB-DA during the first 50 h after casting: (a) absolute Brillouin frequency distributions, (b) relative Brillouin frequency shifts. .... 72

Figure 4-15 Distributed fiber optic sensor (DFOS) measurements of temperature distribution in L DFOS 1 of specimen CB-DA during the first 50 h after casting. .... 73

Figure 4-16 Distributed fiber optic sensor (DFOS) measurements of strain distribution along the centerline of specimen CB-DA during the first 50 h after casting: (a) L DFOS 3 (Top), (b) L-DFOS-3 (Middle), and (c) L-DFOS-4 (Bottom). .... 73

Figure 4-17 Fiber Bragg Grating sensors in CB-DA-AMB indicated by red arrows. .... 74

Figure 4-18 Fiber Bragg Grating sensors in CB-DA. .... 75

Figure 4-19 Fiber Bragg Grating sensors in CB-DA-SC with thermocouple indicated by red arrow. .... 75

Figure 4-20 Fiber Bragg Grating strain during first week of concrete curing. .... 76

Figure 4-21 Fiber Bragg Grating thermocouple temperature during first week of concrete curing. .... 76

Figure 4-22 Fiber Bragg Grating strain development over first six months after casting (CB-DA-AMB = Slab 1; CB-DA = Slab 3; CB-DA-SC = Slab 5). .... 77

Figure 5-1 Instrumentation layout for Specimen CB-DA-AMB. .... 84

Figure 5-2 (a) Point-load versus time relationship; (b) loading truss; (c) rotation of loading trusses; and (d) distribution of six point loads during Cycle 1 at various load levels defined as the applied point load normalized by a peak value..... 86

Figure 5-3 (a) Point load versus vertical displacement at midspan, (b) point load versus lateral displacement during Cycle 1, (c) vertical displacement profile of the concrete slab during Cycle 1, (d) the maximum vertical displacement measured at the peak load of each cycle, and (e) beam rotation during Cycle 1. .... 88

Figure 5-4 (a) Slip between concrete slab and steel beam and (b) gap distance between sacrificial plate and beam web. .... 89

Figure 5-5 (a) Strain at midspan during first cycle, (b) strain at beam web near west connection, (c) strain at section 2 (2.13 m west of midspan), (d) strain at section 4 (2.13 m east of midspan), (e) strain distribution in the mid-section at different load levels during first loading cycle, and (f) strain distribution in the mid-section at each peak load of loading cycles..... 92

Figure 5-6 (a) strains in the top of the angle legs welded to the sacrificial plate and (b) strains in the top of the angle legs bolted to the beam web. .... 93

Figure 5-7 Strain measurements under ambient temperature with overlaid theoretical solution..... 94

Figure 5-8 Fiber Bragg Grating strain from CB-DA-AMB specimen. .... 95

Figure 5-9 Fiber Bragg Grating strain with applied load and SG3-3 shown for comparison. .... 95

Figure 5-10 First cracking measured by Fiber Bragg Grating sensor. .... 96

Figure 5-11 Final cracking measured by Fiber Bragg Grating sensor. .... 97

Figure 5-12 (a) fracture of first shear stud at west end, (b) west side of specimen after concrete removal, (c) cut-section of concrete slab at midspan, (d) cut-section of concrete slab at east end, (e) exposed concrete at 1 m left of beam centerline, (f) deflected specimen after the test. .... 99

Figure 5-13(a) west connection after the test and (b) east connection after the test. Paint pattern on right side of image (b) was used for Digital Image Correlation measurements (not reported here). .... 100

## LIST OF TABLES

---

---

Table 2-1 Test Matrix .....	10
Table 2-2 Measured thickness of the Sprayed Fire Resistive Material on steel surfaces. ....	15
Table 2-3 Tensile specimen geometries.....	20
Table 2-4 Summary data for tension tests, Units of E (Young's modulus), $S_{y0.02}$ (0.2% offset yield strength), $S_u$ (tensile strength) are MPa. Units of $\epsilon_{Su}$ (engineering strain at tensile strength) are mm/mm. ....	22
Table 2-5 Concrete mixture proportions for main pour.....	25
Table 2-6 Curing event timeline. ....	27
Table 2-7 Concrete mixture proportions for repair pour.....	30
Table 2-8 Matrix of concrete properties measured. ....	31
Table 2-9 Fresh concrete properties.....	31
Table 2-10 Measured hardened concrete properties. ....	32
Table 2-11 Compressive strength development.....	33
Table 3-1 Results from the lateral stiffness test.....	43
Table 3-2 Key geometric and proposed thermal parameters for composite beam study .....	48
Table 4-1 Sensors used in the experiments.....	55
Table 4-2 Summary of strain coefficients used for flexural testing.....	68
Table 4-3 Uncertainty in the experimental data.....	80

This page intentionally left blank.

# Chapter 1

## INTRODUCTION

---

### 1.1 BACKGROUND

Steel-concrete composite floor assemblies are a common type of construction for steel-framed buildings because they provide a cost-effective way to span large open spaces. About 35 % of steel-framed buildings incorporate floor beam spans longer than 12 m (Tsavdaridis 2015). Composite floor beams in commercial buildings typically range from 12 m to 15 m in length (SCI 2008). The end connections of composite beams to steel gravity frames (structural framing used to support gravity loads and that is not considered part of the lateral-force-resisting system) are typically designed to withstand vertical shear from gravity loads only. When a building is subjected to fire; however, the structural response of composite floor assemblies is complex. Fire not only degrades material strength and stiffness, but also introduces forces into the structural members as thermally induced deformations are restrained by adjoining parts of the structure and other subassemblies. Thermal elongation and contraction effects on a floor assembly can vary greatly depending on support conditions, including axial and rotational stiffness provided by support frames and connections. The World Trade Center (WTC) investigation conducted by the National Institute of Standards and Technology (NIST) (Sunder et al. 2008) identified potential vulnerabilities of long-span composite floor assemblies in uncontrolled fires. Furthermore, a recent study of composite steel structures by Ove Arup and partners (Flint et al. 2013) described “lessons learned about the detailed response of composite structures under fire loading” that included issues related to structural layout, sources of thermal restraint, and connections.

Currently, the American construction practice for steel-framed buildings follows prescriptive design provisions specified in the International Building Code (IBC) (ICC 2018). Details of passive fire protection systems (as opposed to active fire protection systems such as fire sprinklers), such as the type and thickness of insulating materials applied to the exposed structural steel surfaces, should be designed based on prescribed fire-resistance ratings. In addition, adequacy of applied insulation systems must be certified through standard fire testing methods specified in the American Society for Testing and Materials (ASTM) E119 standard (2018) or by using the American Society of Civil Engineers (ASCE) 29 standard (2007).

In the ASTM E119 fire testing, a gas-fueled (or oil-fueled) furnace is used to heat a small floor assembly (less than 6 m in length), either simply supported or fixed at the test frames, using the

prescribed gas temperature-time curve until one of the following temperature criteria is reached (Ruddy et al. 2003): (a) the maximum temperature of a protected steel beam at any given location reaches 704 °C, (b) the average temperature at any section reaches 593 °C, or (c) the average temperature on the unexposed surface (the top of concrete slab) reaches 139 °C. The termination time is typically reported as a fire-resistance rating in hours or minutes. Reported ratings of various insulation schemes have been published in the Underwriters Laboratories (UL) fire-resistance directories (<http://productspec.ul.com/index.php>). However, these values provide little insight into thermal response to real building fires that can vastly differ from the standard fire. Furthermore, the limiting criteria achieved during standard fire tests and structural responses of specimens (forces and displacements) need not be reported and generally remain as proprietary information (ASCE 2018).

Accurate assessment of structural responses of composite floor assemblies to fire is challenging. Steel and concrete have dissimilar material characteristics at elevated temperatures. There are unavoidable thermal gradients within the composite cross section. Composite interaction, often characterized by the slip capacity of shear connections at the interface between a concrete slab and steel floor beams, has dependencies on temperatures and level of applied loads. Thermally-induced restraints to the floor assemblies depend on the combined effects of stiffness of surrounding frames and ductility of member connection types. However, prescriptive design and testing methods cannot be used to evaluate all these factors contributing to the overall fire performance of composite floor assemblies.

With recognized limitations in the prescriptive approach to design for fire, there has been renewed interest in the United States to develop performance-based design methods following the 9/11 WTC disaster (Yang et al. 2015; Almand 2012; Almand et al. 2004). Alternative engineering approaches have been established along with guidance and design references, e.g., Appendix 4 of the American National Standards Institute/American Institute of Steel Construction (ANSI/AISC) Specification for Structural Steel Buildings (AISC 2016) and the ASCE Structural Fire Engineering manual of practice (ASCE 2018). However, most of the suggested methods are based on experimental studies on small-scale assemblies and focus on strength of isolated members and components at elevated temperatures. With lack of well-established performance-based design methodologies, fire-resistance design for composite floor assemblies has been mainly achieved using prescriptive construction details specified in the national building codes.



## 1.2 PREVIOUS WORK

Over the last few decades, there have been several experimental studies conducted to investigate structural responses of composite floor beam assemblies to elevated temperatures (e.g., Zhao and Kruppa 1997; BRE 2004; Wellman et al. 2011; Fike 2010; Selden et al. 2016; Kordosky 2017). Some experimental tests used a unique laboratory setting to characterize the fundamental mechanics of behavior and strength of isolated composite beams at a given temperature. In those tests, beam specimens were subjected to increasing flexural loads until structural failure occurred while the exposed surface was subjected to a constant heat. Other tests aimed at measurement of thermally induced forces and displacements of composite beam assemblies subjected to heating produced at varying rates. In such cases, beam specimens were loaded to a certain fraction of the flexural capacity at ambient temperature while heated at a specified rate or using the standard temperature-time curve with or without a cooling phase. This section presents an overview of previous experimental studies on composite beam assemblies at elevated temperatures and highlights important observations and conclusions made from those tests.

The ‘Test 1’ of the Cardington fire test program on the full-scale 8-story prototype office building (BRE 2004) in the United Kingdom was conducted on the 9 m long secondary beam supporting the composite slab of the seventh floor. No fire protection was applied to the exposed steel surfaces, and the beam-to-column connections made of a flexible end plate were not exposed to heating. Thermal load was applied using a custom-built gas furnace. The heating rate of the steel beam varied between 3 °C/min and 10 °C/min. During the heating phase, local buckling was observed at both ends of the heated test beam (inside the furnace) because thermal expansion was restrained by adjoining steel frames. Although the test beam deflected significantly (up to the ratio of span length / 40), no *runaway* (uncontrolled) displacement was observed until the lower flange temperature reached over 800 °C. The tensile failure at one of the end plate connections occurred gradually as the beam contracted during the cooling phase but did not result in structural collapse of the composite floor. Test results implied that standard fire testing of isolated members with idealized support conditions may not be able to capture the actual load-carrying capabilities of unprotected composite floor beam assemblies which can significantly contribute to the overall fire resistance of a steel framed building.

Zhao and Kruppa (1997) focused on evaluating the factors influencing the behavior and fire resistance of composite beams subjected to the International Organization for Standardization (ISO) standard ISO-834 fire (1999), including the geometry of the concrete slab, the type of shear connectors, the presence of fire protection, applied load ratios, and the level of composite action. The results of seven simply-supported beam tests indicated that the presence of fire protection on

steel beams affected the mode of failure. Fully-composite specimens with protected steel beams failed by concrete crushing at midspan. Fully-composite specimens with bare steel beams and partially-composite specimens with and without fire protection on steel beams failed by yielding of the steel beam. Three fire-resistance tests on composite beams subjected to a hogging moment at the ends (a bending moment that produces convex bending at the supports of a continuously supported beam; also called a negative bending moment) showed that local buckling of the steel beam occurred at the ends, and the influence of reinforcement steel on the hogging moment-resistance was negligible. Five, large fire-resistance tests on two-span continuous composite beams indicated that the combined effect from a hogging moment and thermal restraint resulted in local buckling of the steel beam and rupture of some shear studs near the middle support.

A joint experimental research program conducted by Purdue University and Michigan State University explored the fire resistance of slim and lightweight composite floor assemblies designed according to the U.S. practice (Wellman et al. 2011). The size of the floor assemblies was much smaller than that used in buildings because of the size limitations of the furnace; the girders were simply-supported. Of particular interest was the effect of the level of fire protection on the interior beam exposed to the ASTM E119 standard fire. Regardless of the fire protection level, the interior floor beams failed by yielding during the heating phase. The load-carrying capability of the thin composite slab was not enough to prevent the runaway deflection of the floor assembly. No failure was observed in any of the beam-to-girder connections and in the shear studs. The authors recommended protecting the secondary beams if the floor system is thin and designed with lightweight concrete slab according to the U.S. standards. Similarly, Fike (2010) tested several composite floor systems using the same gas furnace to investigate various fire protection level on the steel beams. The composite floor assembly with a normal-weight fiber reinforced concrete slab was able to develop tensile membrane action.

Selden et al. (2016) tested five partially-composite beams with flat concrete slabs at elevated temperatures using ceramic radiant heaters. The composite floor beam assemblies were designed according to the current U.S. specification for structural steel construction. The beam span length was 3.8 m and two different types of beam-to-column shear connections were used, including shear-tab and all-bolted double angles. The load-carrying capacity of the composite beam was reduced by heating. Composite beams with flat slabs failed by compressive failure of the concrete when subjected to higher loads and low heat. No connection failure was observed during the heating phase, but some shear-tab connections fractured during the cooling phase.

Researchers at Lehigh University (Kordosky 2017) examined the effect of the beam fire protection on the overall fire resistance of the composite steel frames subjected to the ASTM E119 standard

fire exposure. The floor assembly with the unprotected steel beam failed after 28 min with no visible cracks in the concrete deck. The failure time of the other floor assembly with the steel beam protected for the 2-hour fire-resistance rating exceeded that prescribed by the current design standard. Although some of the bolts used in the shear-tab connection exhibited shear failure, most stayed intact and the floor assembly did not collapse. The composite beams exceeded the failure time prescribed by the current design standards. The results of the tests were used to build and validate finite element models. A parametric study using the finite-element model validated against the test data indicated that the longer beams were able to withstand the fire and remain stable for longer durations than the shorter beams.

These studies have provided useful insight into the performance of composite floor beam assemblies subject to fire, but very few used full-scale specimens because of the size limitation of a furnace or a laboratory space. The span lengths of the tested specimens were less than 5 m with the exception of the Cardington test. Few studies evaluated the effects of restraint against thermal expansion provided by support frames and connections; however, detailing of slab reinforcement and connections was based on standard British practice. Some specimens were simply supported on the walls of a gas furnace. Other tests incorporated steel connections but used complex test protocols such as cyclic loading or relocation of applied loads during the fire tests. Lack of lateral supports around the edges of concrete slabs introduced premature failure not commonly seen in composite beams as part of floor systems. Discussion of the uncertainty in measured data owing to this loading effect was generally omitted.

### **1.3 MOTIVATION AND OBJECTIVES**

The development of performance-based methods demands a robust capability to predict the performance of structures as a complete system including connections and structural frames exposed to realistic fire conditions. The predictive tools that can be used for performance-based design need to be validated against experimental data with quantified uncertainty in measurements. Currently, there are very few test data describing the fire performance of composite floor beam assemblies with medium-to-long spans commonly used in the American construction practice. Such data cannot be generated by standard fire testing methods with furnaces.

The National Institute of Standards and Technology (NIST) has proposed the experimental research project on full-scale composite floor systems exposed to realistic, structurally significant fires. The purpose of this project is to produce the experimental data and technical information essential for both development and validation of computational models used for performance-based design of structures in fire. This research project consists of a series of fire experiments

conducted at the National Fire Research Laboratory (NFRL) on long-span composite beams (Phase I) and composite floor assemblies constructed as part of a multi-bay steel framed building (Phase II), as well as possible future work on subassemblies. The Phase I experimental tests were completed in 2018, and the Phase II study is currently in progress.

This report presents the Phase I fire experiments.

In Phase I study, a series of compartment fire experiments were conducted on 12.8 m long composite floor beam assemblies in the National Fire Research Laboratory (Bundy et al. 2016) at the National Institute of Standards and Technology (NIST).

The objectives of this study included:

- 1) design of a repeatable test fire that can be used for large-scale fire experiments to study the limit states of composite floor beam assemblies subjected to uncontrolled fires,
- 2) investigation of the performance and failure mechanisms of restrained composite beams with simple shear connections subjected to heating and cooling phases of a test fire, and
- 3) dissemination of experimental test data for the fire performance of full-scale composite floor beam assemblies designed and constructed according to American building codes and standards, which can be used to develop or validate numerical models.

This report, Part 1, presents the experimental design and the behavior of the test beam assembly at ambient temperature to compare with the fire test results presented in a subsequent report, Part 2 (Choe et al. 2019).

## **1.4 REPORT OUTLINE**

This report, Part 1, presents the test setup, specimen design and construction, and behavior of the composite beam at ambient temperature. The experimentally measured behavior and flexural moment capacity from the test conducted at ambient temperature were used as a baseline to compare with the composite beams tested under combined mechanical and fire load, which are presented in a subsequent report; Part 2 (Choe et al. 2019). The outline of this report is as follows:

- Chapter 2 describes the testing program. It presents the test matrix and a detailed discussion on the design of the specimens and the material characterization.

- Chapter 3 presents the experimental setup. It discusses the specimen boundary conditions and different aspects of both the structural (mechanical) and fire loading approaches.
- Chapter 4 describes the measurement system. It presents the details of the structural measurements, including loads, strains, and displacements, as well as fire measurements, including Heat Release Rates (HRR) and temperatures measured using fiber optics and thermocouples. It also discusses the estimated uncertainties associated with all of the measurements.
- Chapter 5 presents the behavior and capacity of the composite beam specimen from the test conducted at ambient temperature. These results were used as a baseline for comparison with the performance of the beams tested under combined mechanical and fire load, which are presented in a subsequent report; Part 2 (Choe et al. 2019).
- Chapter 6 provides the summary and conclusions of the report.
- Finally, a set of appendices at the end of this report provide drawings, calculation sets, and other useful information that complements the discussion provided throughout the report.

This page intentionally left blank

## Chapter 2

### TEST PROGRAM

---

The prototype beams used in this study incorporated the realistic span length and size of floor beams as well as simple shear connections used in steel-framed buildings in the United States. This chapter presents variables considered in the test matrix, and the design and construction of the prototype composite floor beam assemblies.

#### 2.1 TEST MATRIX

Table 2-1 shows the experimental test matrix used for both Part 1 and Part 2 of this study. All five 12.8 m long test beam assemblies were designed with the identical composite cross section but had varying support conditions. Test variables included two different beam-to-column connections that are commonly used in standard U.S. construction practice (i.e., bolted/welded double-angle and single-plate shear connections). Two of the five specimens also had slab restraint at the beam ends to evaluate the effect of the slab continuity over girders on the behavior of the composite beams. This support condition was achieved such that the axial movement of the slab ends was restrained against thermal elongation and contraction, and the slab reinforcement was anchored at the centerline of support columns.

The first test was conducted with mechanical load only, at ambient temperature, to investigate the behavior and modes of failure as well as to evaluate the ultimate moment capacity ( $M_u$ ) as a baseline to compare with the fire test results. For the compartment fire tests (Tests No. 2 through 5), all four specimens were loaded to design gravity loads required for evaluation of extreme fire effects (i.e., 1.2×dead load + 0.5×live load) as prescribed in the ASCE/SEI 7 standard (ASCE, 2016). The magnitude of resultant bending moments ( $M$ ) was equivalent to approximately 45 % of the ultimate moment capacity measured at ambient temperature in Test No.1. The undersides of the four composite beam assemblies tested under thermal load were directly exposed to a compartment fire with a heat release rate of 4 MW developed using natural gas fueled burners.

**Table 2-1 Test Matrix**

Test No.	Specimen name	Test date	Beam-to-column connection	Slab end continuity	$M/M_u$	Fire load	Specimen number used for casting
1	CB-DA-AMB	09/21/2017	Welded/bolted double angles	-	1	-	Specimen 1
2	CB-DA	12/19/2017	Welded/bolted double angles	-	0.45	4 MW	Specimen 3
3	CB-DA-SC	01/12/2018	Welded/bolted double angles	Included	0.45	4 MW	Specimen 5
4	CB-SP	02/13/2018	Single plate	-	0.45	4 MW	Specimen 4
5	CB-SP-SC	03/06/2018	Single plate	Included	0.45	4 MW	Specimen 2

## 2.2 DESIGN AND CONSTRUCTION OF PROTOTYPE COMPOSITE BEAM

### 2.2.1 Design Basis

The specimens were designed to represent composite floor beams in a 12.8 m long bay of a steel-framed building. Steel beams were assumed to be spaced at 3.05 m in a 12.8 m by 6.1 m bay. Each steel beam was partially composite with a lightweight concrete slab cast on 76 mm deep ribbed steel deck units via 19 mm steel headed stud anchors spaced at 305 mm. The slab width was 1.83 m, less than the effective width of 3.05 m determined using the ANSI/AISC 360 specification (AISC 2016), to prevent cracking along the longitudinal centerline of the specimen. For passive fire protection, each beam was designed for the 2-hour fire rating as prescribed in the building codes. A survey was conducted to incorporate common design parameters used in industry practice, including construction live loads, superimposed dead loads, beam spacing, steel deck thickness, and crack control reinforcement. Responses from six structural engineering firms are provided in Appendix B. The values of design parameters used in this study are presented in subsequent sections.

### 2.2.2 Loads

The gravity load combinations prescribed in ASCE/SEI 7 (ASCE 2016) and the design loads from the survey were considered. The nominal weight of the concrete slab of the specimen, incorporating a unit weight of lightweight concrete equal to  $18.9 \text{ kN/m}^3$ , was  $2.20 \text{ kN/m}^2$ . The nominal weight of the W18×35 steel beam was  $0.51 \text{ kN/m}$ . As specified in ASCE/SEI 7, a construction live load of  $0.96 \text{ kN/m}^2$ , superimposed dead load of  $0.48 \text{ kN/m}^2$ , and a live load of  $3.35 \text{ kN/m}^2$  were used. The calculated moment and shear demand of the specimen at ambient



temperature ( $1.2 \times \text{dead load} + 1.6 \times \text{live load}$ ) was 548 kN-m and 171 kN, respectively. During the fire tests, imposed gravity loads conformed to the ASCE/SEI 7-16 load combination for extreme fire events ( $1.2 \times \text{dead load} + 0.5 \times \text{live load}$ ). The corresponding moment and shear demand were 326 kN-m and 99.4 kN, respectively.

Figure 2-1 shows a cross section of the test beam and the steel deck. A 20-gauge galvanized steel deck with lightweight concrete was used for the slab. An 83 mm thickness of the lightweight concrete slab above the 76 mm deep steel deck was required to provide a 2-hour fire rating for the composite floor slab. The ribs of the steel deck were oriented perpendicular to the floor beams. A 6x6 W1.4xW1.4 welded wire fabric, also called welded wire mesh, (3.4 mm diameter plain steel wires in 150 mm grid) was placed in the mid-height of the concrete above the top rib as the minimum required shrinkage and temperature control reinforcement specified in Steel Deck Institute (SDI) C-2011 (SDI 2011). For two specimens CB-DA-SC and CB-SP-SC, four No. 4 reinforcing bars were placed on the top of the welded wire fabric at an average spacing of 45.7 cm on center over the support girders as crack control reinforcement.

The W18x35 steel beam, made of ASTM A992 steel, was selected to support construction loads, including the fresh concrete slab, and construction live loads, and to meet the serviceability requirement (displacement limit) for a non-composite section. The composite action between the steel beam and the slab was achieved using 19 mm diameter steel headed studs spaced at 305 mm on center. They were placed in “strong positions” as defined in ANSI/AISC 360. The total shear strength of the studs placed between the midspan and end of the steel beam was 82 % of the yield strength of the steel beam at ambient temperature. The calculated flexural capacity of the specimen (with the AISC strength reduction factor of 0.9) was 695 kN-m which is about 1.27 times the moment demand at ambient temperature. The flexural capacity was governed by the composite action developed by the steel shear studs. Refer to Appendix B for design calculations of the composite floor beam.

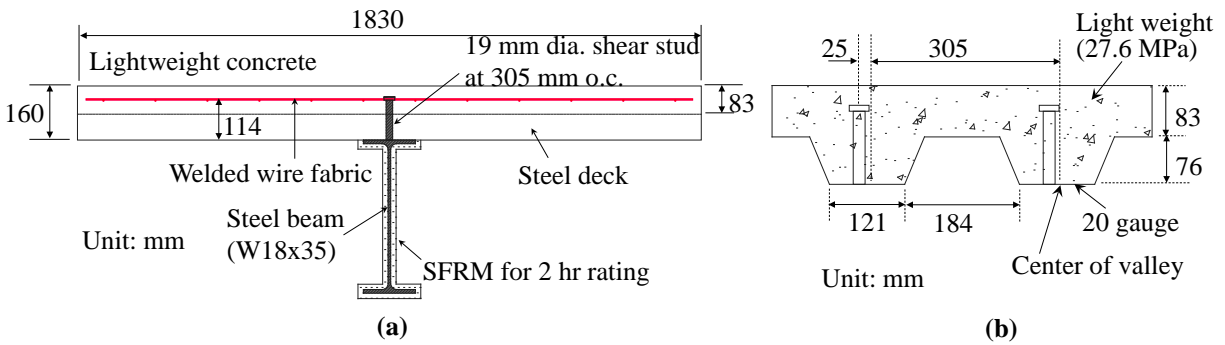


**Figure 2-1 Cross-section of (a) composite beam specimen and (b) concrete slab on steel deck. All dimensions are nominal values specified in construction drawings.**

### 2.2.3 Shear Connections

Figure 2-2 illustrates the beam end connections, either double angles or a shear tab. For double-angle connection, two L5×3×3/8 angles made of ASTM A36 steel were used. The angle legs were bolted to the beam web using three 19 mm diameter bolts, made of ASTM F3025 steel (Gr. A325), spaced at 76 mm. The top bolt was located at 114 mm from the top of the steel beam. The AISC standard bolt holes in the web were located 76 mm from the column face. The bottom flange of the steel beam was coped as recommended in the AISC manual. The angle legs on the column side were shop-welded, using an 8 mm fillet weld (E70XX electrodes), to a sacrificial plate attached to the columns. The design strength of double-angle connections was governed by weld shear, which was 267 kN (including the AISC strength reduction factor of 0.75). For the shear tab connection, a 11 mm thick plate (made of ASTM A36 steel) was bolted to the web of the steel beam and welded to the column side via a sacrificial plate. The bolt size and spacing were the same as those used in the double-angle connection. However, the steel beam was not coped. The calculated shear capacity was 242 kN (including the AISC strength reduction factor of 0.75).

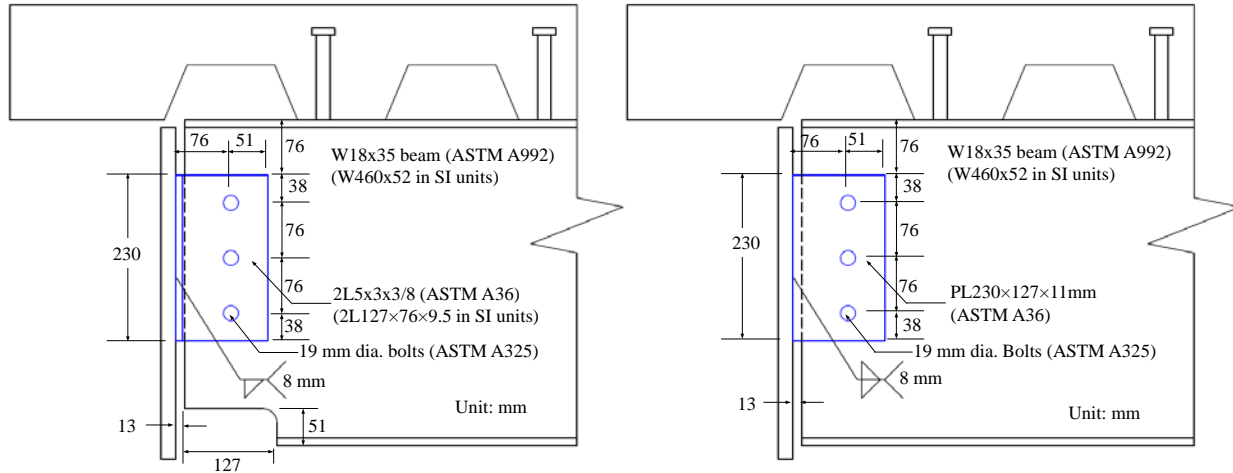


**Figure 2-2** Shear connections at the end of specimens (a) double angle and (b) single plate.

## 2.2.4 Passive Fire Protection

According to the IBC requirements, floor construction classified as Type IA, commonly found in high-rise buildings constructed with non-combustible building elements, requires passive fire protection for a 2-hour fire-resistance rating. In compliance with the current U.S. practice, the prototype composite floor beam assemblies were insulated with a Sprayed Fire Resistive Material (SFRM) having the minimum bond strength of 623 kPa required for buildings with heights ranging from 23 m to 128 m. Application of the SFRM installation was conducted at the NFRL by a manufacturer-approved contractor. The selected SFRM product was Southwest Type 5MD which was a cementitious gypsum-based material manufactured by Carboline. The manufacturer's specifications for this product indicated that the minimum density was 352 kg/m<sup>3</sup> measured in accordance with the ASTM E 605 standard (ASTM 2015).

Figure 2-3 shows photographs of the beam assemblies during the SFRM installation. Exposed steelwork including the W18×35 steel beams and the beam-to-column connections were coated with Southwest Type 5MD material. For the 2-hour restrained beam rating of floor beams, the design thickness of SFRM was 16 mm as specified in UL Directory N791 (UL 2011). The connection regions were over-sprayed to achieve the SFRM thickness of 27 mm. This is the same design thickness required for the 3-hour fire rating of W12×106 columns. The gap between the steel beam and steel deck units were also filled with the SFRM. No additional fireproofing material was installed at the underside of steel decking since the floor assembly was constructed with the 8.25 cm thick lightweight concrete cast on 7.62 cm deep galvanized, fluted deck units.

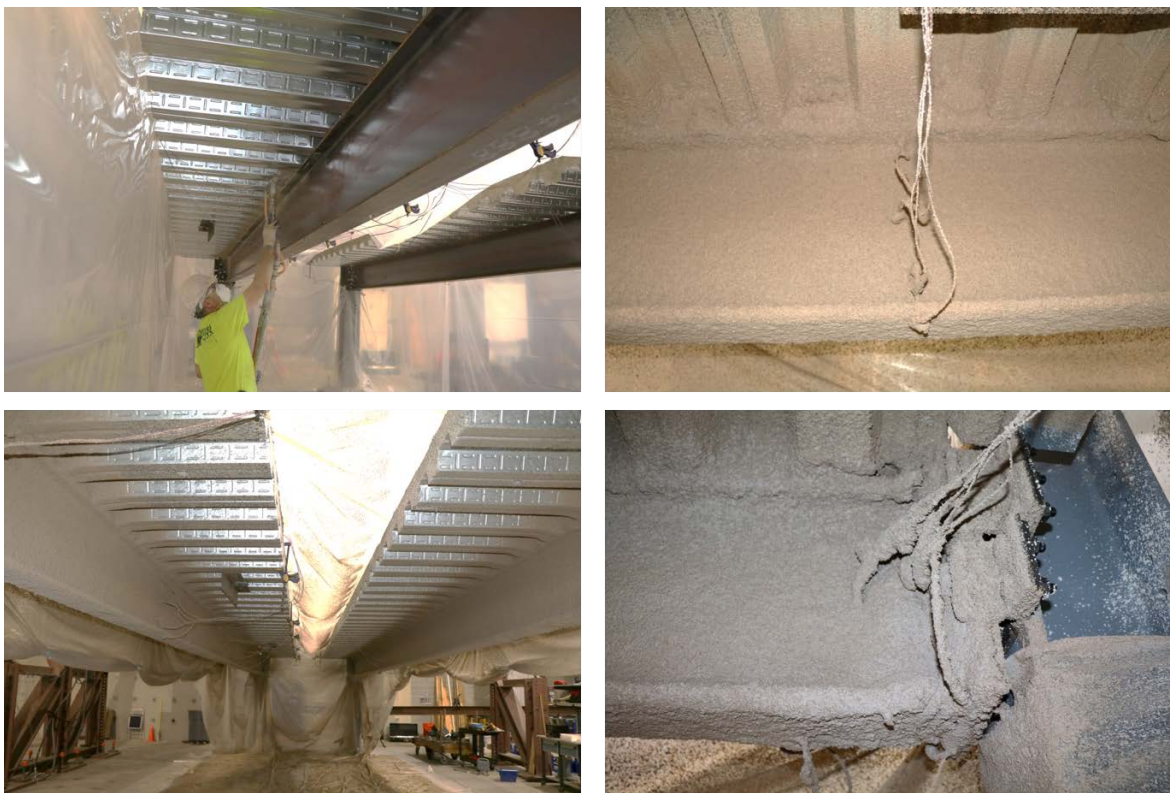


**Figure 2-3 Application of the Sprayed Fire Resistive Materials on the prototype floor beam assemblies.**

The IBC permits the minimum thickness of applied SFRM equal to the design thickness (i.e., 16 mm) minus 25 %. The contractor performed spot checks using thickness gauges during and immediately after installation and conducted necessary actions in the area of over-sprayed and under-sprayed regions to meet the thickness requirement. Prior to each fire test, the SFRM thickness was measured in accordance with the ASTM E 605 standard. Table 2-2 summarizes the final average measured thickness on the steel beam and connections and the number of measurements. The values after the  $\pm$  symbol indicate the standard deviation.

**Table 2-2 Measured thickness of the Sprayed Fire Resistive Material on steel surfaces.**

Specimen name	Final average measured thickness (mm)			Total number of thickness measurements for steel beam
	Steel beam	Connection elements	Steel beam web at 5 cm away from the edge of connections	
CB-DA	20 ± 3	28 ± 7	22 ± 3	129
CB-DA-SC	18 ± 3	26 ± 3	24 ± 1	129
CB-SP	19 ± 3	31 ± 7	24 ± 5	131
CB-SP-SC	19 ± 4	32 ± 2	24 ± 4	146

### 2.2.5 Construction of Specimen

Figure 2-4 shows photographs of the formwork of the specimens before concrete casting. Steel deck units (91 cm in width), were attached to the top of the W18×35 steel beam using power actuated fasteners (HILTI X-EDNI 19 MX). Each deck unit was connected side by side using #10 self-tapping sheet steel screws. 19 mm diameter headed shear studs (original length = 13.2 cm) were welded to the steel beam, which burned through the steel deck (Figure 2-4c). The height of the shear studs after installation was nominally 12.7 cm. Each shear stud was offset by 2.5 cm from the center of the valleys of the steel deck and positioned in the “strong direction” for horizontal shear as specified in ANSI/AISC 360. Steel welded wire fabric (6x6 W1.4xW1.4) was placed at mid-height of the topping concrete (8.3 cm) using reinforcing bar chairs, 3.8 cm in height, attached to the top ribs at a spacing of 61 cm. Full-length sheets of welded wire fabric (6.1 m) were placed first around the midspan and then two short pieces placed with lap length of 46 cm each. For the specimens with slab continuity (CB-DA-SC and CB-SP-SC), four No. 4 bars were placed on the top of the welded wire fabric with an embedded length of 76.2 cm from the slab edge (Figure 2-4d).

All five specimens were cast on the same day with two batches of concrete. All four specimens tested under fire loading were cured inside the conditioning pit for about 6 months and were cured on the laboratory floor for another 6 months. Refer to subsection 2.3.2 for the mixture design and details of concrete curing. The contractor installed SFRM on steel substrates of the specimens about 6 months prior to the fire tests.

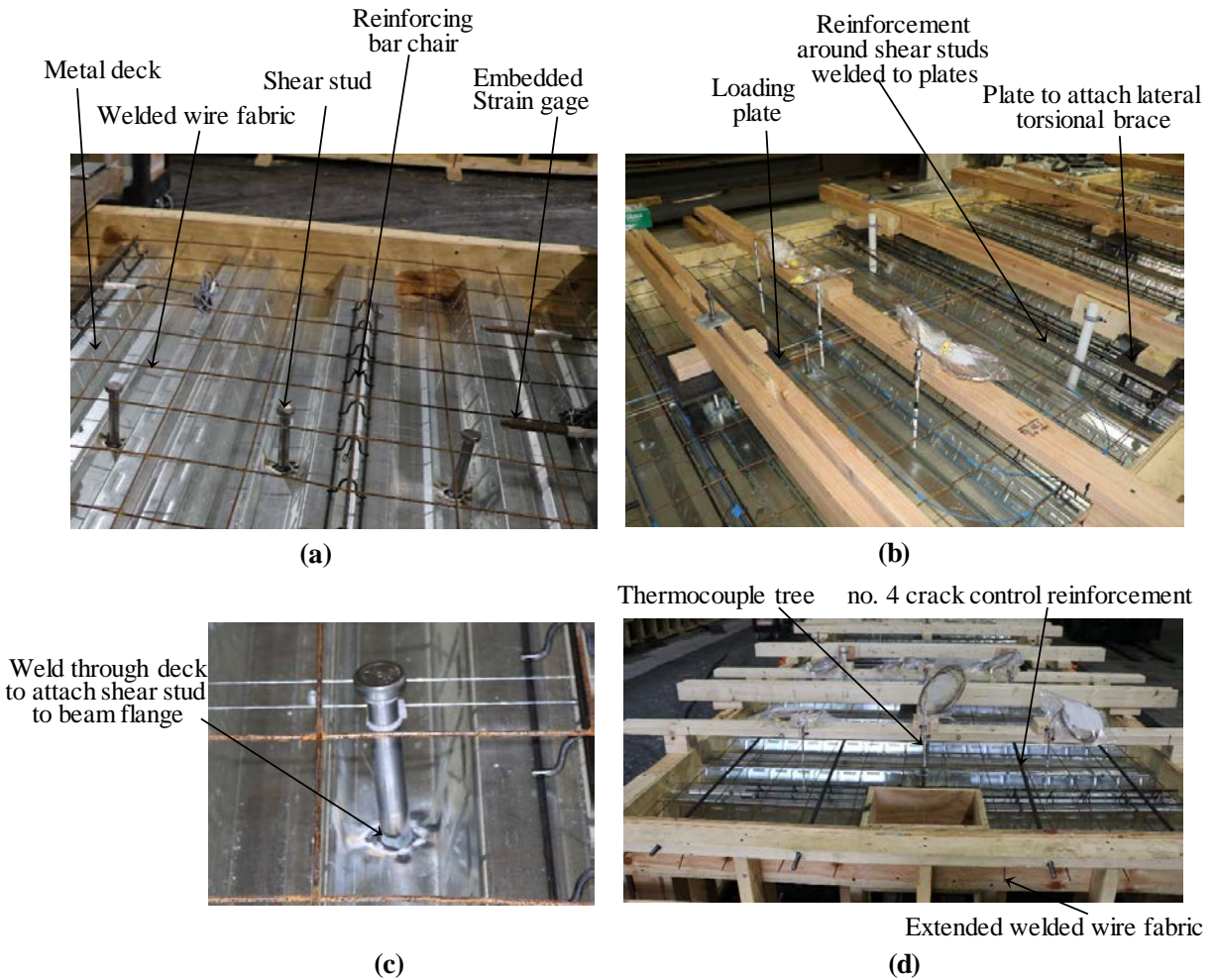


**Figure 2-4** Placement of (a) steel deck, shear stud, welded wire fabric, (b) embedded steel bearing plates, (c) a shear stud weld, (d) No. 4 reinforcing bar and welded wire fabric for slab continuity.

### **Repair of Damaged Specimen (CB-SP-SC)**

The concrete slab of CB-SP-SC was locally damaged while being cured inside the laboratory. Figure 2-5 and Figure 2-6 show photographs of the extent of damage. The slab about 85 cm from the west end exhibited through-depth fracture of concrete and complete severing of welded wire fabric. In addition, there were hairline cracks around the damaged zone, along the longitudinal centerline of the support beam and near the slab edge. This incident also caused failure of one thermocouple array (out of 24 arrays) and a fiber optic cable deployed for additional measurement of temperature in the concrete slab.

In repairing the specimen, the portion of the concrete near the west end (1.6 m in length) was cut (Figure 2-7a). Some portion of welded wire fabric embedded into undamaged concrete was



exposed to make a welded joint to new pieces of welded wire fabric placed in the formwork (Figure 2-7b). Also, new No. 4 reinforcing bars were placed. Fresh concrete was placed in the formwork, with a similar mixture to that used in the original placement (Batch 2) and a water-to-cement ratio of 0.41. Refer to subsection 2.3.2 for the mix design of the concrete used for the repair. The mean 28-day concrete cylinder strength was approximately 43.0 MPa.

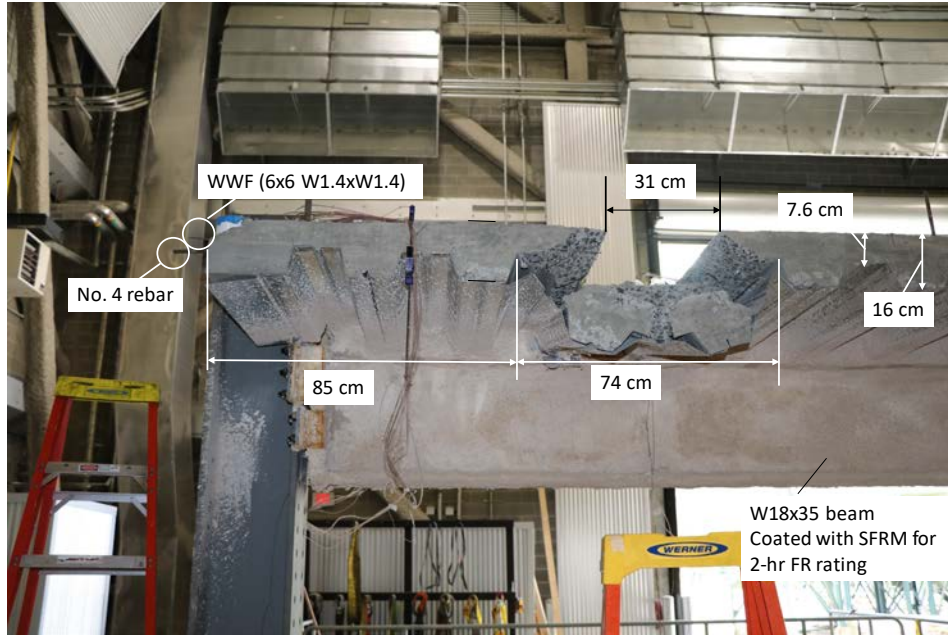


Figure 2-5 Front view of damaged concrete slab of CB-SP-SC.

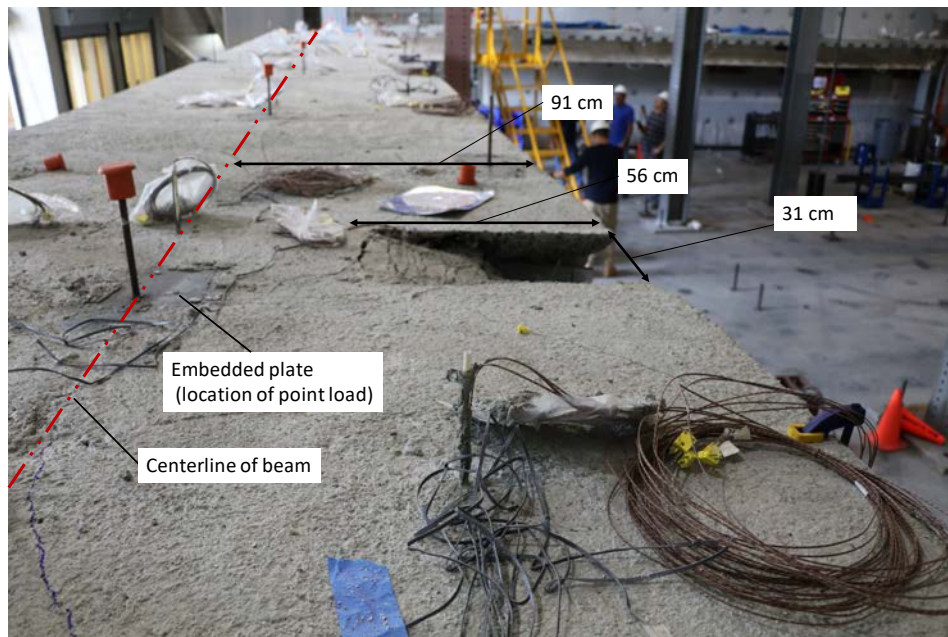
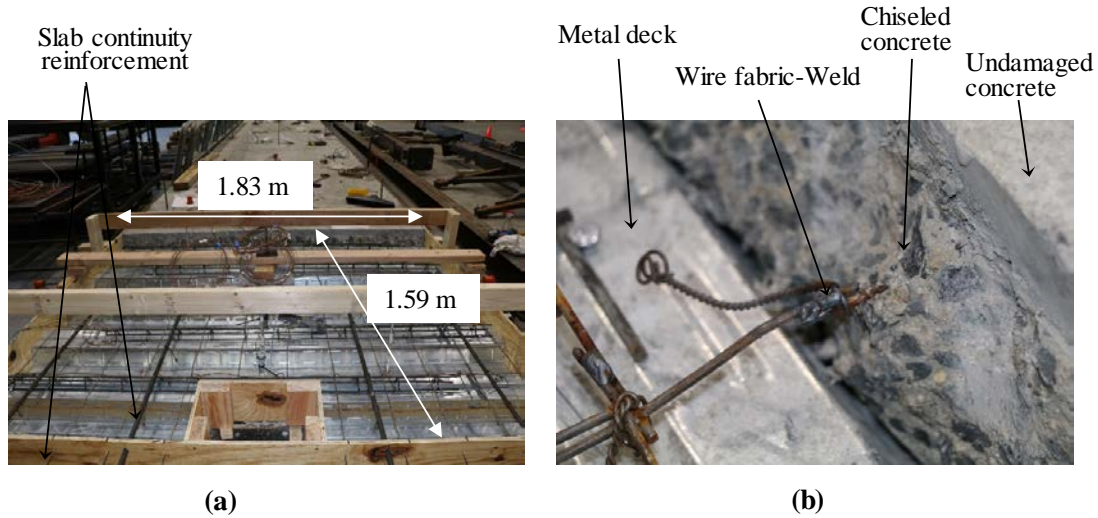


Figure 2-6 Top view of damaged concrete slab of Specimen CB-SP-SC.



**Figure 2-7 (a) Formwork for repaired concrete slab (b) wire fabric joint by welding.**

## 2.3 CONSTRUCTION MATERIALS

The following subsections describe the properties of the materials used in the construction of the specimens.

### 2.3.1 Structural Steel, Bolts, Shear Studs, Reinforcing bar, and Welded wire fabric

#### (i) Materials and material-testing specimens

Tensile coupons from steel beams, angles, shear tabs, structural bolts, shear studs, reinforcing bars, and welded wire fabric were made and loaded under tension using ASTM E8/E8M (2011) guidelines. All the steel beams used for the fire tests had the same heat number (indicated as Fire web/flange in Table 2-3) while the steel beam used for the ambient-temperature test (indicated as Ambient web/flange in Table 2-3) had a different heat number. All the flat tensile specimens, as shown in Figure 2-8, were cut by an abrasive water-jet in the NIST Center for Automotive Lightweighting (NCAL) and then ground flat on a surface grinder. These specimens contained a slight intentional taper to the center of the gauge section, as allowed by ASTM E8/E8M (2011), to bias the location of the failure section next to the center of the specimen and extensometer gauge length. Non-standard round tensile specimens from A325 bolts, Figure 2-9, and shear studs, Figure 2-10, were machined. Bolt and shear-stud specimens were not tapered. Specimens from the reinforcing bar and the welded wire fabric were tested as full section after grit blasting to remove rust. Table 2-3 summarizes the geometries used for the material testing.



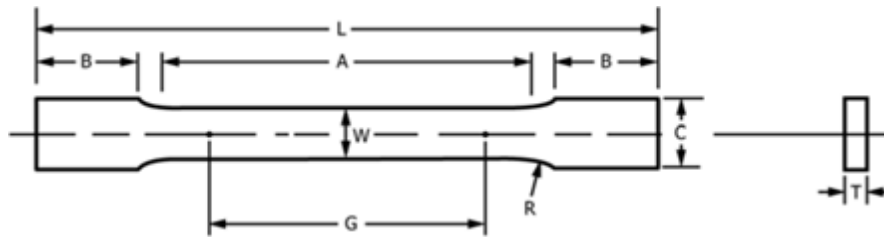


Figure 2-8 Flat tensile specimen (A=57 mm, W=12.5 mm, B=75 mm C=20 mm, R=12.5 mm).

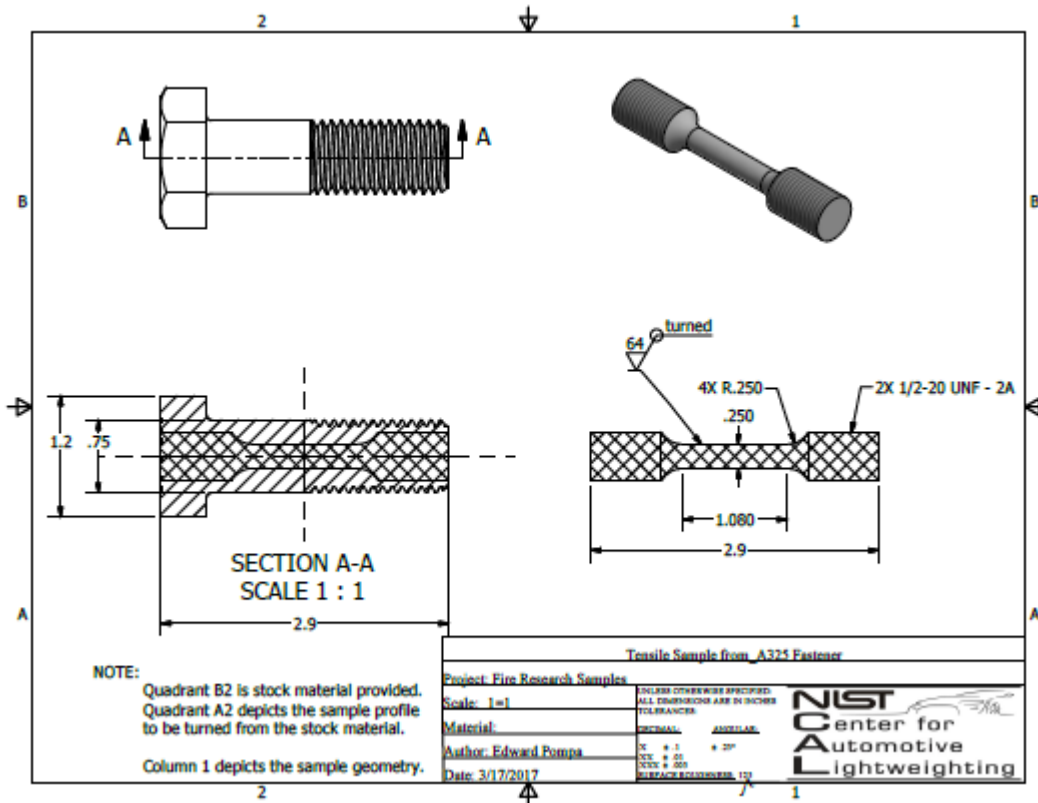


Figure 2-9 Tensile specimen machined from A325 bolt. Units = cm.

Table 2-3 Tensile specimen geometries.

Batch	Description	Specimen	Dimensions
B170310-WEL-001	Ambient web	Figure 2-8	
B170310-WEL-001	Ambient flange	Figure 2-8	
B170310-WEL-002	Fire web	Figure 2-8	
B170310-WEL-002	Fire flange	Figure 2-8	
B170313-WEL-001	L angle	Figure 2-8	
B170313-WEL-002	Shear tab	Figure 2-8	
B170313-WEL-003	A325 bolt	Figure 2-9	
B170313-WEL-004	Shear stud	Figure 2-10	
B170313-WEL-005	A615 reinforcing bar		nominal L =150 mm
B170313-WEL-006	Welded wire fabric		nominal L =150 mm

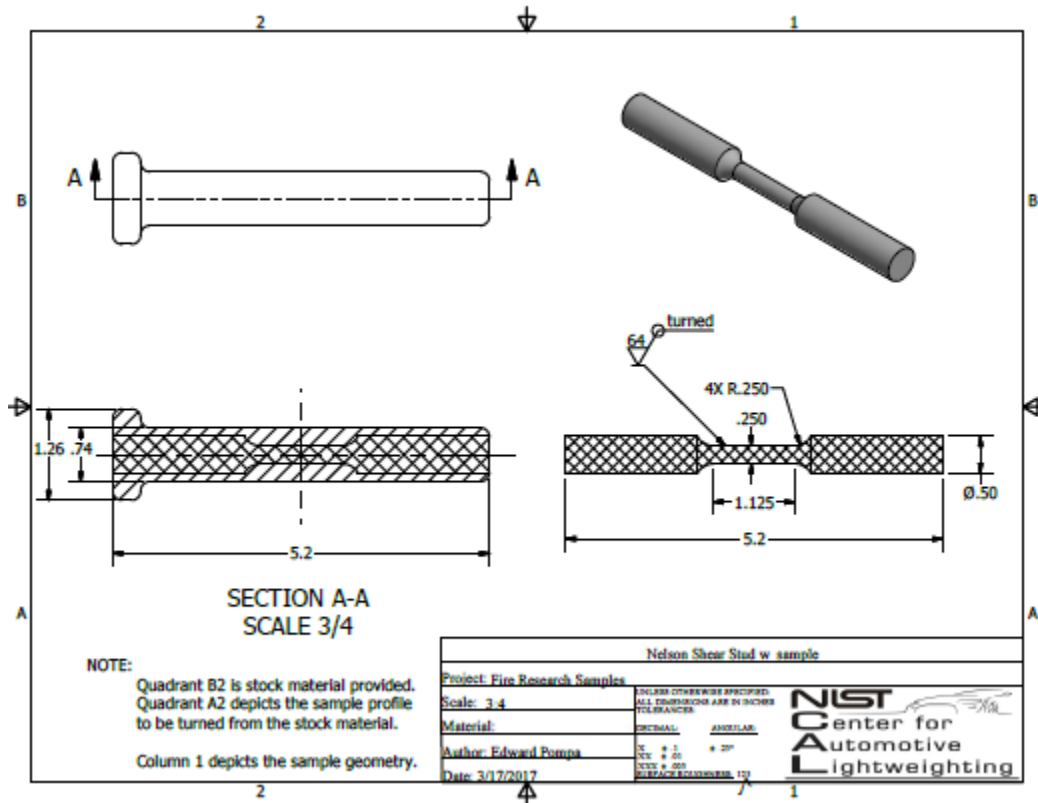


Figure 2-10 Tensile specimen machined from shear stud. Units = cm.

## (ii) Test Method

All specimens were oriented with their long axis parallel to the rolling direction. All specimens were tested in displacement control at a nominal engineering strain rate  $de/dt = 8.333 \times 10^{-5}$  mm/mm/s as specified in ISO 6892 (2009). All wide flange, reinforcing bar, and welded wire fabric specimens employed a single ASTM E83 Class B2 extensometer with a gauge length ( $G$ ) of 25 mm, which was removed after the specimen strain exceeded the uniform strain,  $e_u$ . The bolt and shear-stud specimens used a real-time Digital Image Correlation (DIC)-defined virtual extensometer with nominal gauge lengths of 20 mm and 25 mm, respectively. The bolts were first screwed into a threaded adapter, which was then hydraulically gripped. In the tests on the welded wire fabric and reinforcing bar, the displacement rate was set based on the separation of the grips, which was nominally 100 mm.

## (iii) Results

Figure 2-11a through Figure 2-11d show graphs of the engineering stress-strain diagrams for the materials listed Table 2-4. The curves terminate at the strain at which the operator removed the extensometer. One explanation for the lower repeatability of the W18x35 Fire Web material (Figure 2-11a) is that the center of the gauge section of lowest-strength specimen was about 40 mm from the flame-cut edge of the plate, which was presumably originally at the junction between the web and the flange. The specimens from the Ambient Flange section, Figure 2-11a, were cut closer to the center of the web, and their stress-strain curves are more consistent.

To analyze the reinforcing bar data, Figure 2-11d, the stresses are calculated using the nominal diameter of 12.7 mm for the non-uniform shaped reinforcing bar. The most likely source of the slightly lower values for  $E$  is that the actual diameter is slightly larger than the assumed nominal diameter of 12.7 mm. Specimens from the reinforcing bar and the welded wire fabric tended to fail away from the center of the gauge length because they were not tapered. For this reason, the failure (and necking) was often near the extensometer knife edge, so data beyond the uniform strain,  $e_u$ , is not representative. No special significance should be attributed to differences in the Young's modulus between samples. In these tests, the gauge length was too short for accurate determination of  $E$ .

Young's modulus, 0.2% offset yield strength, tensile strength, and engineering strain at tensile strength of each coupon sample are provided in Table 2-4. The total expanded uncertainty estimated using the average repeatability and reproducibility standard deviations was  $\pm 13.3\%$  of the Young's modulus,  $\pm 5.4\%$  of the yield strength,  $\pm 3.2\%$  of the tensile strength, and  $\pm 12.2\%$  of the elongation.

Figure 2-12 shows the strain rates maintained during the tensile tests as well as the upper and lower limits of the strain rates specified by ISO 6892 for the tensile tests. As shown, the strain rates of all the tests met the strain-rate requirements of ISO 6892.

**Table 2-4 Summary data for tension tests, Units of E (Young's modulus),  $S_{y0.02}$  (0.2% offset yield strength),  $S_u$  (tensile strength) are MPa. Units of  $e_{Su}$  (engineering strain at tensile strength) are mm/mm.**

<b>Specimen</b>	<b>E</b>	<b><math>S_{y0.02}</math></b>	<b><math>S_u</math></b>	<b><math>e_{Su}</math></b>
W18x35-Ambient-Web-Sample 1	212456	371	472	0.1935
W18x35-Ambient-Web-Sample 2	196141	369	474	0.1950
W18x35-Ambient-Flange-Sample 1	213183	349	465	0.1875
W18x35-Ambient-Flange-Sample 2	209808	358	466	0.1889
W18x35-Fire-Flange--Sample 1	199815	387	496	0.1880
W18x35-Fire-Flange-Sample 2	206560	388	497	0.1724
W18x35-Fire-Web-Sample 1	197098	426	513	0.1811
W18x35-Fire-Web-Sample 2	202706	437	526	0.1678
W18x35-Fire-Web-Sample 3	200151	443	533	0.1646
Shear tab-Sample 1	198722	352	487	0.2009
Shear tab-Sample 2	212545	343	485	0.1987
Bolted Angle-Sample 1	194948	381	511	0.1703
Bolted Angle-Sample 2	198490	377	511	0.1769
A325 Bolt-Sample 1	206217	900	960	0.0612
A325 Bolt-Sample 2	205374	903	961	0.0590
ASTM A615 Gr60 reinforcing bar-Sample 1	185450	467	690	0.1099
ASTM A615 Gr60 reinforcing bar-Sample 2	189031	473	740	0.1027
ASTM A615 Gr60 reinforcing bar-Sample 3	196744	466	691	0.1059
Shear stud-Sample 1	204462	412	511	0.0478
Shear stud-Sample 2	207364	404	499	0.0460
Welded wire fabric-Sample 1	206354	743	772	0.0125
Welded wire fabric-Sample 2	196834	721	752	0.0123
Welded wire fabric-Sample 3	201396	719	748	0.0108

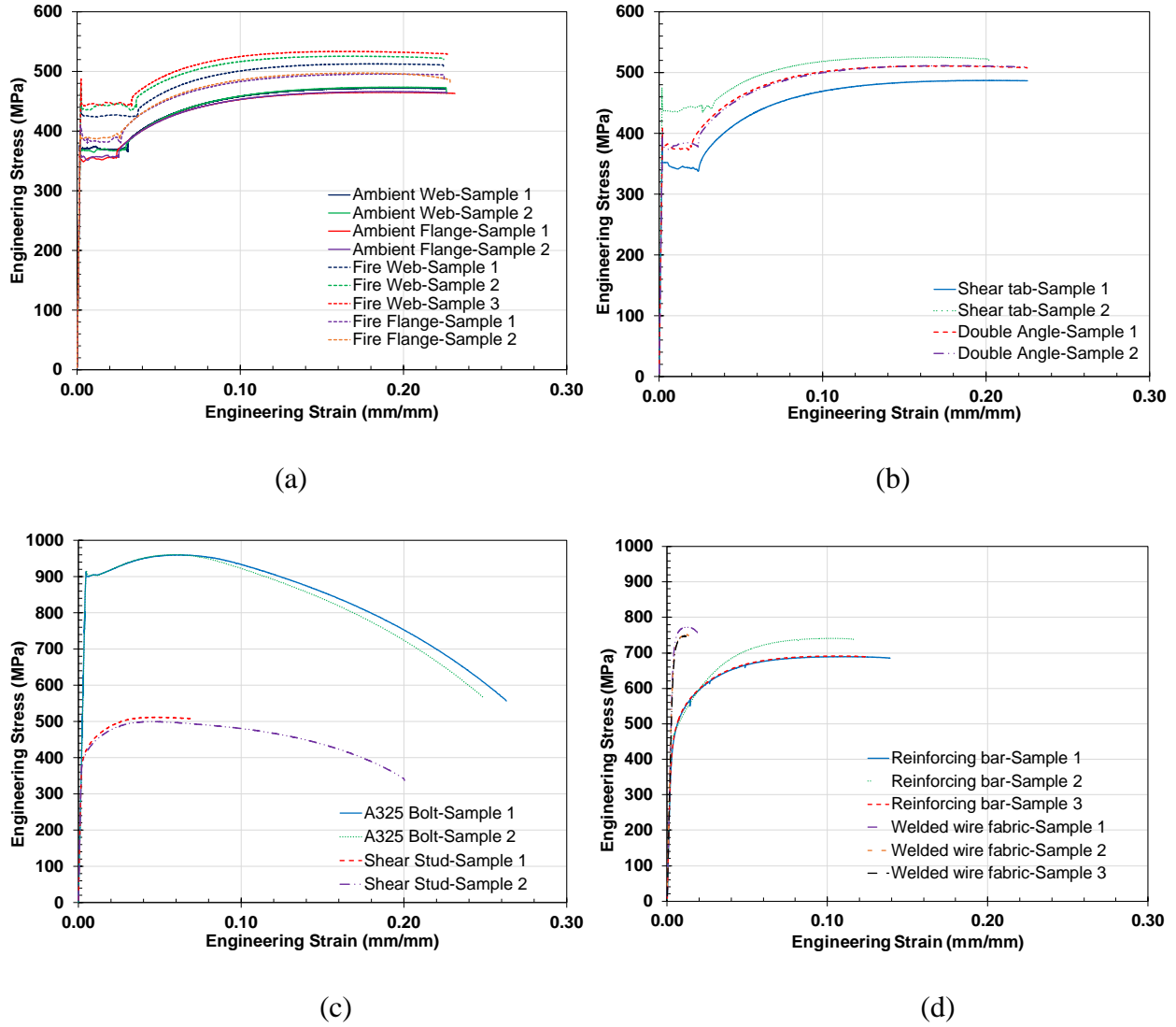
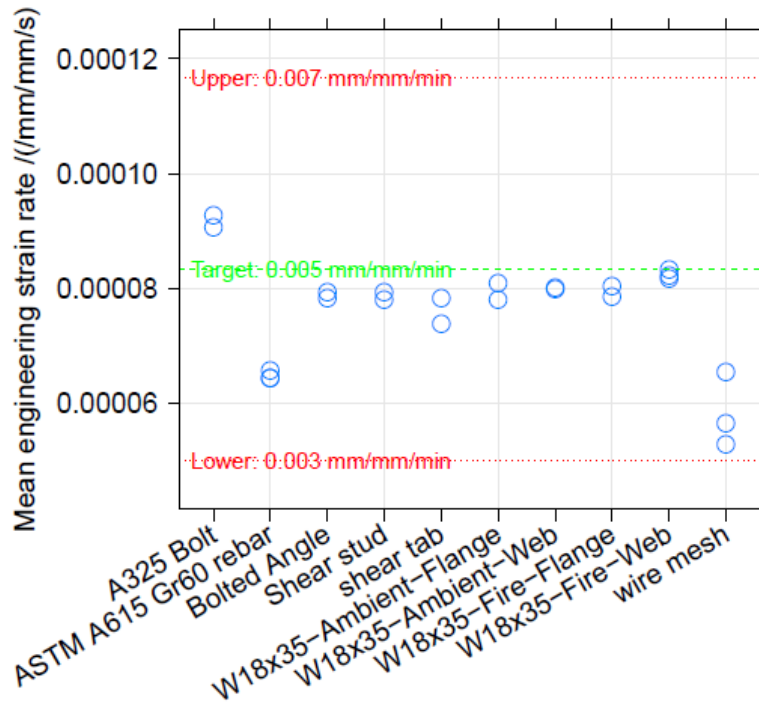


Figure 2-11 Engineering stress versus strain for (a) W18x35 steel beam, (b) shear tab and double angle, (c) bolts and shear studs, and (d) reinforcing bar and welded wire fabric.



**Figure 2-12 Average engineering strain rate during each test. Dashed colored lines denote the acceptable strain rate range in ISO 6892.**

### 2.3.2 Concrete

#### (i) Mixture design and curing

The concrete mixture was designed to provide a lightweight aggregate concrete with hardened mechanical properties typically used in current construction practice, but with a low propensity for fire-induced spalling, which would add undesired variability to the experiments. To reduce the likelihood of spalling, 2.37 kg/m<sup>3</sup> of monofilament polypropylene microfibers were used in the mix. To further reduce the chance of fire-induced spalling, expanded slate lightweight aggregate with low water-retention characteristics and high desorption was selected (Pour-Ghaz et al. 2012) to expedite the reduction of moisture in the slabs during curing. For the main concrete pour, a high slump was required because delicate fiber optic sensors were embedded in the concrete to measure strain and temperature in the slab, which limited the use of mechanical vibration during casting. For a subsequent casting to repair a damaged specimen, the slump requirement was relaxed. The concrete mixture proportions for the main pour are provided in Table 2-5. Trial batches of this mixture were cast and subjected to fire to verify the concrete performance and study fiber optic sensor installation methods (Bao et al. 2019).

**Table 2-5 Concrete mixture proportions for main pour.**

		water/cement: 0.46	Slump: 21.6±2.5 cm (8.5±1.0 inch)
Material		Saturated Surface Dry, kg (lb)	Volume, m <sup>3</sup> (ft <sup>3</sup> )
Cement:	ASTM C-150: Type I/II Lehigh	236 (520)	0.075 (2.65)
Fly ash:	ASTM C-618: Separation Technologies Class F	59 (130)	0.025 (0.88)
Aggregate:	ASTM C-33: Carolina Stalite LTWT	404 (890)	0.269 (9.51)
Sand:	ASTM C-33: Howlin Sand	621 (1370)	0.238 (8.41)
Air:	2.5%	-	0.019 (0.67)
Water:	ASTM C-1602; ASTM C-1603	136 (300)	0.136 (4.81)
Admixture:	See Below	5 (10)	0.002 (0.07)
Total		1461 (3220)	0.765 (27.00)
Unit Weight kg/m <sup>3</sup> (pcf)		1910 (119.3)	
Calculated Equilibrium Dry Density kg/m <sup>3</sup> (pcf)		1820 (113.6)	

AdmixturesFRC MONO-150 – 2.37 kg/m<sup>3</sup> (4 lb/cy)

BASF Glenium 7920 – 1.75 ± 1.75 ml/kg (3 ± 3 oz/cwt)

BASF Pozzoloth 322N – 2.33 ± 1.16 ml/kg (4 ± 2 oz/cwt)

BASF DELVO Stabilizer – 1.16 ± 1.16 ml/kg (2 ± 2 oz/cwt)

BASF RheoTEC Z-60 – 2.33 ± 1.16 ml/kg (4 ± 2 oz/cwt)

The concrete was batched at a local ready-mix concrete plant and trucked to NIST for casting. Because approximately 2.8 m<sup>3</sup> (3.7 cy) of concrete was required per specimen and the trucks held 7.6 m<sup>3</sup> (10 cy), two trucks (batches) were required to cast the five specimens. Two of the four specimens to be tested with fire loading were cast from each batch of concrete, with a mix of concrete from the two batches (half the length cast from Batch 1 and half from Batch 2) being used to cast the ambient temperature specimen. Although the mixture proportions were the same for both batches, a larger amount of high-range water reducer (BASF Glenium 7920) was needed in Batch 2 to achieve the target slump (see batch tickets in Appendices). Mechanical vibration of the concrete was only performed adjacent to embed plates and on the slab formwork. The concrete was screeded out, but no floating or hard troweling was performed.

The specimens were cast indoors (NFRL Room 125; Figure 2-13a and Figure 2-13b). Immediately after casting, the specimens were covered with wet burlap and then plastic to maintain a wet concrete surface condition (Figure 2-13c). The burlap was re-wet, as necessary, for the first 3 days of curing, after which the plastic and burlap were removed. After another 7 days, the four

specimens to be fire tested were moved to a large underground curing room (pit) with a target temperature of 30 °C and a target relative humidity of the air of 50 % (Figure 2-13d). The four specimens stayed in the curing pit for approximately five months, after which time they were moved back to the floor of the test hall, so fire protection could be applied to the steel beams. An event timeline for the curing is provided in Table 2-6.

The measured relative humidity and air temperature in the curing pit are plotted in Figure 2-14(a). Due to problems with the humidity control in the curing pit, the target relative humidity of the air was not achieved on average ( $34.5 \pm 13.1$  %), however, the target air temperature was maintained within the desired margin ( $29.2 \pm 0.9$  °C). The ambient test specimen was cured in the testing hall where the relative humidity and temperature were not measured, however, daily measurements made in the adjacent test hall (NFRL Room 113) with similar conditions to those in NFRL Room 125 are shown in Figure 2-14(b).

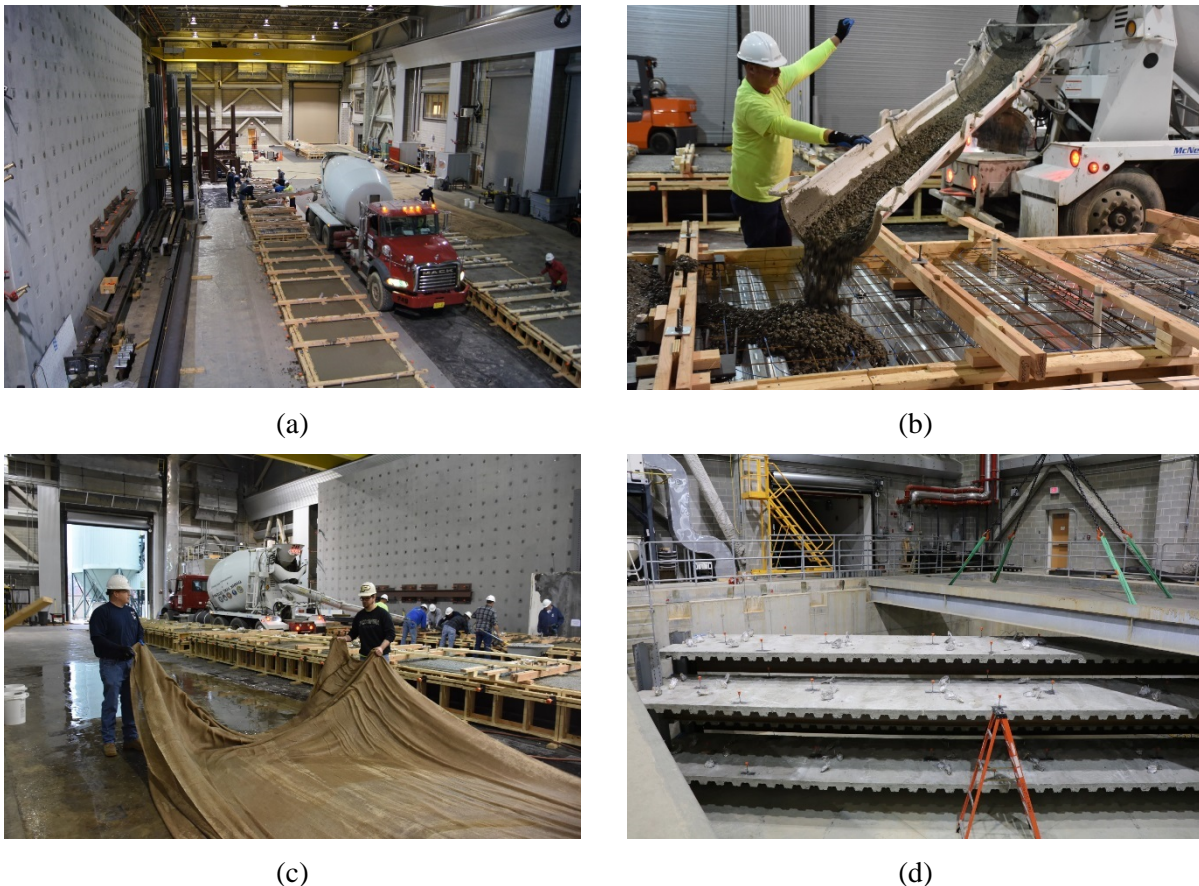


**Figure 2-13 Casting of the specimens: (a) National Fire Research Laboratory test hall; (b) concrete placement in formwork; (c) initial curing with wet burlap covered in plastic; (d) subsequent curing in underground curing pit.**



**Table 2-6 Curing event timeline.**

Event	Date	Days after casting
Concrete casting	12/6/2016	0
Removal of plastic and wet burlap	12/9/2016	3
Placement of specimens in curing pit	12/16/2016	10
Removal of specimens from curing pit	5/25/2017	170

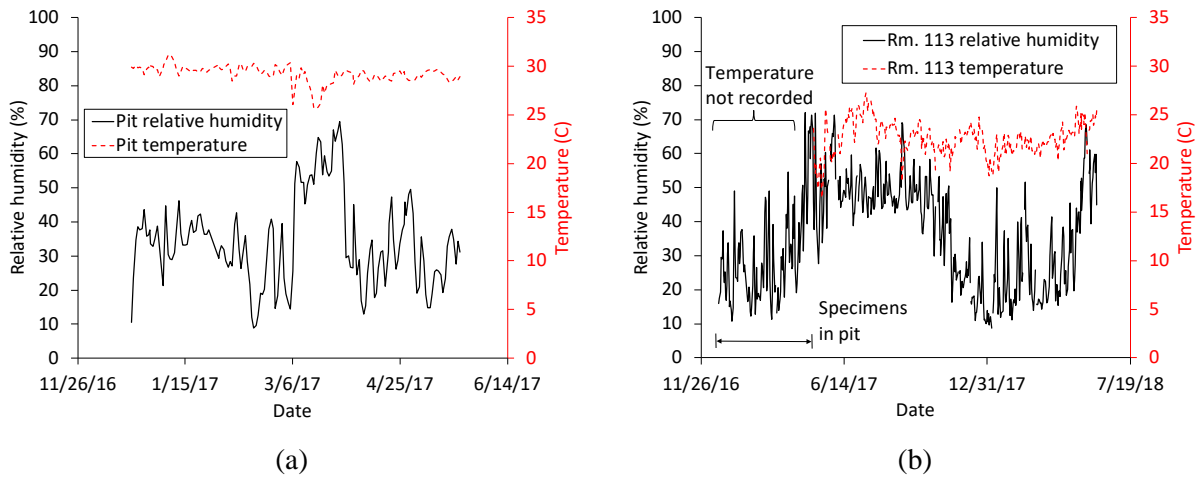


**Figure 2-14 Air temperature and relative humidity: (a) in curing pit; (b) approximate conditions in test hall.**

Two different sensor types were used to measure the relative humidity and temperature inside the slabs during curing. The first sensor type was a wireless sensor purported to be able to be placed in the formwork prior to casting (up to 150 mm from the surface) and transmit the data to a mobile phone via Bluetooth (Figure 2-15a). The manufacturer-specified accuracy of the temperature and relative humidity are  $\pm 0.4$  °C and  $\pm 3$  %, respectively. We were unable to successfully transmit data from the majority of the 15 sensors installed in the concrete and the data that were gathered varied significantly from theoretical predictions as well as from independent measurements with a second technology; therefore, the results are not discussed further in this report. The second sensor was a wired probe placed into perforated sleeves embedded in the concrete during casting (Figure 2-15b). The manufacturer specified accuracy of the temperature and relative humidity in the applied temperature range are  $\pm 0.2$  °C and less than  $\pm 2.5$  %, respectively. The temperatures measured in the specimens are shown in Figure 2-16 and the relative humidity measurements in Figure 2-17. No data were recorded immediately prior to Test 2 and Test 3. The relative humidity measurement immediately prior to Test 5 is believed to be erroneous because the seal on the probe tube had been removed and the concrete allowed to dry locally. The moisture content of the

specimens, which is related to the relative humidity, was measured separately on concrete cylinders cured under the same conditions as the slabs (discussed below).



Figure 2-15 Monitoring of relative humidity in the slab during curing: (a) embedded wireless sensors (black ovals); (b) downhole relative humidity probe.

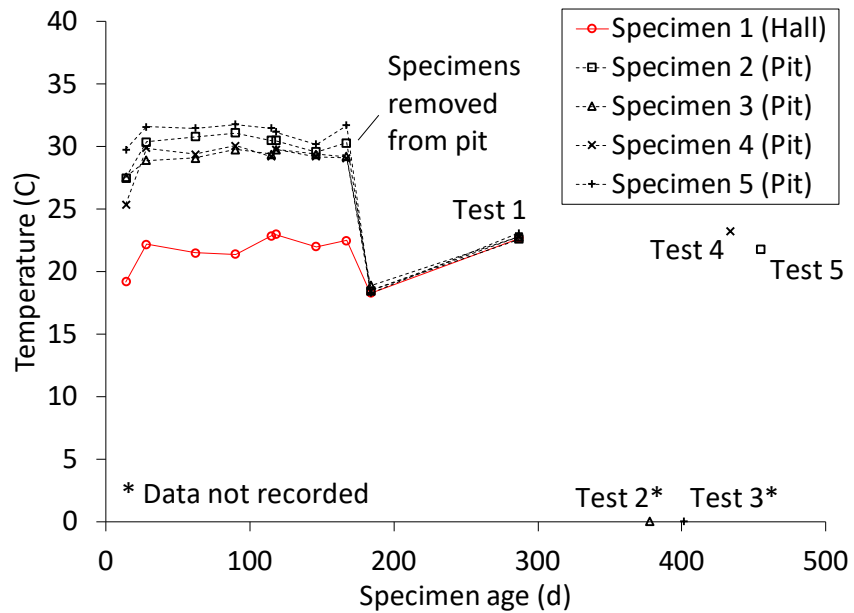


Figure 2-16 Temperature in the test specimens.

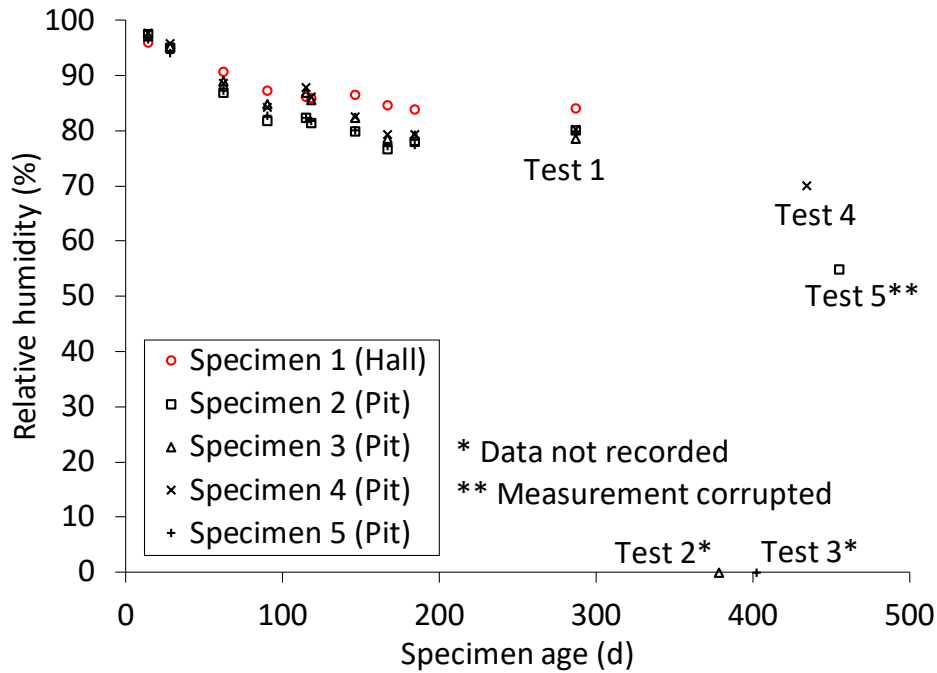


Figure 2-17 Relative humidity in the test specimens.

The mixture proportions for the concrete used to repair the specimen damaged prior to testing (CB-SP-SC) are shown in Table 2-7. They are similar to those for the main pour; however, the water/cement ratio was reduced to 0.41 to accelerate the strength gain in the concrete. The high-range water reducer was switched to Sika Visocrete 2100 and other minor adjustments to the mixture were made as shown in Table 2-7. The freshly cast repair concrete was covered with wet burlap and plastic for more than 3 days and then allowed to continue curing under the conditions in the test hall (see Figure 2-13).

**Table 2-7 Concrete mixture proportions for repair pour.**

		water/cement: 0.41	Slump: 14.0±2.5 cm (5.5±1.0 inch)
Material		Saturated Surface Dry, kg (lb)	Volume, m <sup>3</sup> (ft <sup>3</sup> )
Cement:	ASTM C-150: Type I/II Lehigh	254 (560)	0.081 (2.85)
Fly ash:	ASTM C-618: Separation Technologies Class F	64 (140)	0.027 (0.94)
Aggregate:	ASTM C-33: Carolina Stalite LTWT	404 (890)	0.269 (9.51)
Sand:	ASTM C-33: Howlin Sand	621 (1370)	0.238 (8.41)
Air:	2.5%	-	0.019 (0.67)
Water:	ASTM C-1602; ASTM C-1603	129 (284)	0.129 (4.55)
Admixture:	See Below	5 (10)	0.002 (0.07)
Total		1476 (3254)	0.765 (27.00)
Unit Weight kg/m <sup>3</sup> (pcf)		1931 (120.5)	
Calculated Equilibrium Dry Density kg/m <sup>3</sup> (pcf)		1853 (115.7)	

AdmixturesFRC MONO-150 – 2.37 kg/m<sup>3</sup> (4 lb/cy)

Sika Visocrete 2100 – 1.75 ± 1.75 ml/kg (3 ± 3 oz/cwt)

BASF Pozzoloth 322N – 2.91 ± 1.16 ml/kg (5 ± 2 oz/cwt)

BASF DELVO Stabilizer – 1.16 ± 1.16 ml/kg (2 ± 2 oz/cwt)

BASF RheoTEC Z-60 – 2.33 ± 1.16 ml/kg (4 ± 2 oz/cwt)

**(ii) Hardened concrete properties**

Table 2-8 summarizes the concrete properties measured. Where applicable, the relevant ASTM test standard used is provided in the table. The reader is directed to these standards for details on those test methods. The resistivity of the fresh concrete, as well as the surface resistivity and pulse velocity of the hardened concrete were measured for possible use in future studies; however, these measurements are not elaborated on, nor is the data reported, since they are outside the scope of this report. For the repair concrete, only a subset of the tests was performed as indicated in Table 2-8. Relevant details about the tests used to determine the thermal conductivity and specific heat of the concrete are provided below. The ‘day of test’ measurements were performed within four days of the corresponding composite beam test. Except for the measurements made at the time of casting of the concrete, all measurements were made from 102 mm × 204 mm concrete cylinders prepared according to ASTM C192 and cured alongside of the composite slab test specimens. All measurements were made at ambient laboratory temperatures; nominally 23 °C. No measurements of the concrete properties at elevated temperatures were made.

**Table 2-8 Matrix of concrete properties measured.**

Property	Casting 12/6/16	Number of cylinders				Day of test	Total
		3-day <sup>b</sup> 12/9/16	7-day 12/13/16	14-day <sup>b</sup> 12/20/16	28-day 1/3/17		
Resistivity <sup>a,b</sup>	✓	-	-	-	-	-	-
Slump (ASTM C143)	✓	-	-	-	-	-	-
Plastic unit weight (ASTM C138) <sup>b</sup>	✓	-	-	-	-	-	-
Air content (ASTM C173) <sup>b</sup>	✓	-	-	-	-	-	-
Compressive strength (ASTM C39)	-	6	6	6	6	18	42
Density (ASTM C642)	-	c	c	c	c	c	-
Pulse velocity <sup>a</sup>	-	c	c	c	c	c	-
Surface resistivity <sup>a</sup>	-	c	c	c	c	c	-
Static modulus (ASTM C469) <sup>b</sup>	-	-	-	-	-	c	-
Splitting strength (ASTM C496) <sup>b</sup>	-	-	-	-	-	4	4
Moisture content (ASTM C642)	-	-	-	-	-	4	4
Thermal conductivity <sup>b</sup>	-	-	-	-	-	2	2
Specific heat <sup>b</sup>	-	-	-	-	-	d	-
						Total	52

<sup>a</sup> Measured, but not reported here.

<sup>b</sup> Not measured for repair mix.

<sup>c</sup> Use compressive strength cylinders.

<sup>d</sup> Use microcores from thermal conductivity cylinders.

The slump, plastic unit weight, and air content of the concrete for the main pour were measured by an independent testing company. For the repair concrete, the target slump was verified by NIST staff. The measured values are reported in Table 2-9.

**Table 2-9 Fresh concrete properties.**

Batch	Slump, cm	Plastic unit weight, kg/m <sup>3</sup>	Air content, %
1	21.6	1937	2.5
2	20.1	1954	2.5
Repair	14.0	-	-

Table 2-10 summarizes the measured properties (mean and one standard deviation of six specimens) of the hardened concrete. The measurements to determine the values reported in Table 2-11 for the Batch 1 and Batch 2 concrete were made within days of the ambient specimen test (Test 1), conducted approximately nine months after casting. The measurements to determine the values for the repair concrete were made around the time of the test in which the repair concrete was used (Test 5), which was approximately four months after casting of the repair concrete. The compressive strength development over time is illustrated in Figure 2-18 and the values are provided in Table 2-11. It is notable that the Batch 2 concrete had a higher compressive strength than the Batch 1 concrete from early in the curing process. This strength stayed higher even after several months of curing. Although there was continued development of the concrete strength during the testing of the specimens (Test 1 to Test 5), the change is nominal. Therefore, the values in Table 2-10 are recommended for modeling and analysis of these test specimens.

**Table 2-10 Measured hardened concrete properties.**

Category	Description	Batch 1	Batch 2	Repair
Structural	Compressive strength, MPa	49.8 ±1.8	54.4 ±3.3	52.1 ±2.9
	Splitting tensile strength, MPa	4.6 ±0.3	4.4 ±0.2	-
	Static modulus, GPa	22.7 ±1.1	25.6 ±1.4	-
Thermal	Bulk density, kg/m <sup>3</sup>	1858 ±4.8	1871 ±4.6	1912 ±2.8
	Moisture content, % mass	7.8 ±0.1	7.5 ±0.01	7.9 ±0.1
	Thermal conductivity, W/m·K	1.77 ±0.35	1.66 ±0.17	-
	Specific heat, J/kg·K	1006 ±77	966 ±94	-

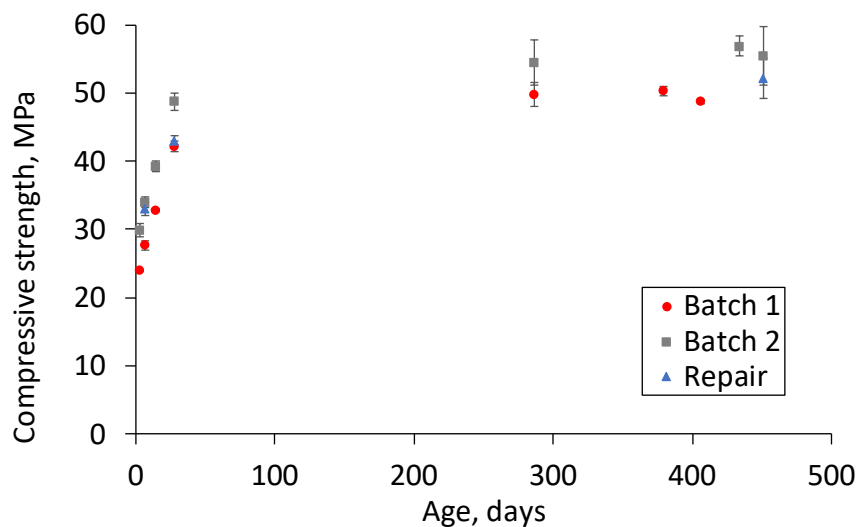


**Figure 2-18 Compressive strength development (error bars are standard deviation)**

**Table 2-11 Compressive strength development.**

	Compressive strength, MPa								
	3-days	7-days	14-days	28-days	Test 1 286-days	Test 2 379-days	Test 3 406-days	Test 4 434-days	Test 5 451-days <sup>a</sup>
Batch 1	24.0 ± 0.1	27.7 ± 0.7	32.8 ± 0.2	42.1 ± 0.8	49.8 ± 1.8	50.3 ± 0.6	48.7 ± 0.2	-	-
Batch 2	29.9 ± 1.0	34.0 ± 0.8	39.2 ± 0.8	48.7 ± 1.3	54.4 ± 3.3	-	-	56.9 ± 1.5	55.4 ± 4.3
Repair	-	32.9 ± 1.0	-	43.0 ± 0.6	-	-	-	-	52.1 ± 2.9

<sup>a</sup> The repair concrete was 127 d old at the time of Test 5.

The thermal conductivities of the concretes at ambient temperature were determined using the transient plane source (TPS) method (Gustafsson 1991; Log and Gustafsson 1995) with a commercially-available measurement system. Additionally, the heat capacities (specific heat) of the concretes at ambient temperature were measured using a gold pan heat capacity cell connected to the TPS measurement system. The procedure reported here was previously used by Bentz et al. (Bentz et al. 2011).

For thermal conductivity measurements, a 14.67 mm radius probe (Ni foil encased in Kapton) was sandwiched between two 45 mm thick slices of a 102 mm diameter hardened concrete cylinder. After an equilibration time of at least 45 min, measurements were obtained using a power of 0.3 W applied for a measurement time of 10 s. The measured response of points 100 to 200 of those

sampled during the 10 s was analyzed using the built-in software to estimate the thermal conductivity of the specimens. To account for heterogeneity of the concrete, the cylinder slices were rotated 45-degrees after each measurement to capture a representative average response from the cement paste and aggregates. A minimum of six measurements were made for each batch of concrete. According to the manufacturer's specifications, thermal conductivity measurements made in this way are reproducible within  $\pm 2$  % standard uncertainty.

For the heat capacity measurements, approximately 1.0 g of material from the cylinders was ground to a powder using a mortar and pestle and placed in the heat capacity unit, which consisted of a Kapton probe attached to the base of a gold pan/lid. The gold pan with its lid was surrounded by polystyrene insulation to minimize energy loss. First, a reference measurement was made with an empty pan, followed by the measurement with the specimen placed in the pan. A power of 0.1 W was applied for a measurement time of 80 s and points 100 to 200 of those sampled in the 80 s were used in the analysis. Knowing the mass of the specimen, its heat capacity in units of J/(kg•K) could be determined. According to the manufacturer, heat capacity measurements made in this way are reproducible within  $\pm 2$  % standard uncertainty.



## Chapter 3

### EXPERIMENTAL SETUP

---

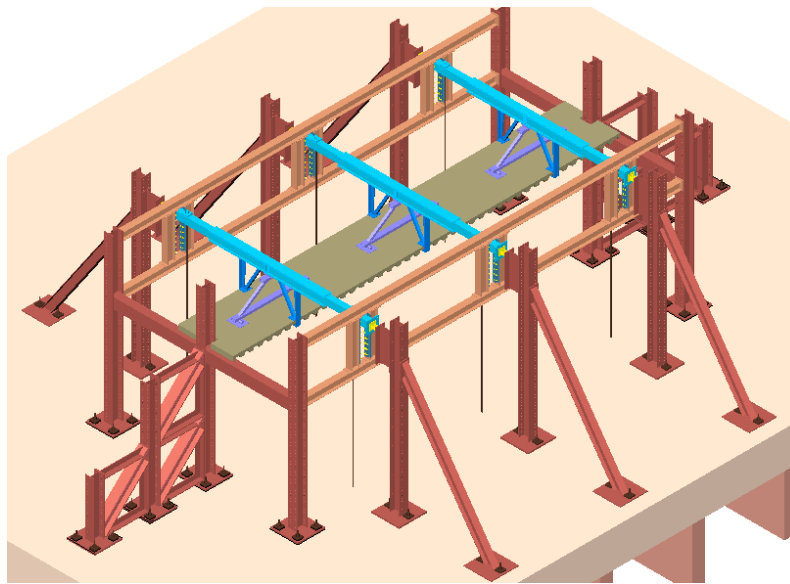
---

#### 3.1 STRUCTURAL SETUP

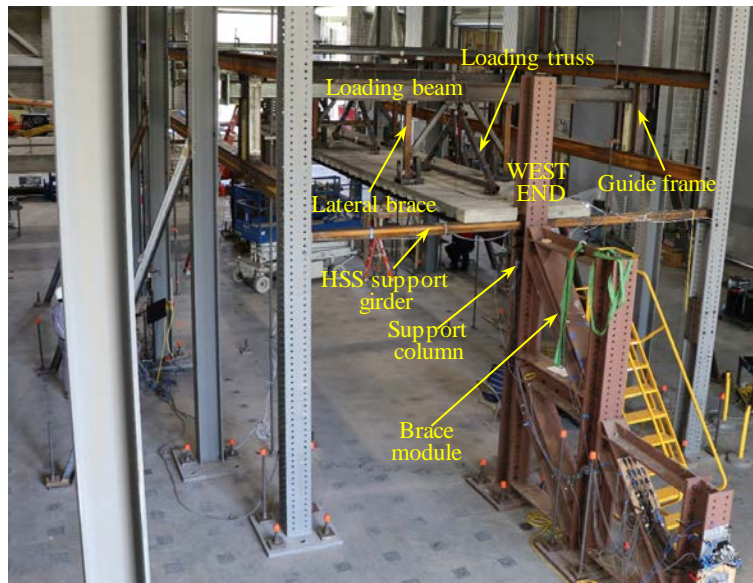
Figure 3-1 shows the test setup. Each composite beam specimen was attached to the W12x106 columns using either double-angle or the single plate shear (shear-tab) connections. Both connections were bolted to the beam web and welded to a 9 mm thick sacrificial plate on the face of the column flange. The connection assemblies were bolted to the column flange together with a 45 mm thick bearing plate to prevent flange local buckling of the columns during the fire test (Figure 3-2). The top surface of the slab was at the elevation of 3.93 m from the strong floor. The length of the steel beams was 12.3 m. The center-to-center distance between the bolt lines on the web of the steel beam was 12.2 m.

The slab and embedded reinforcement were extended to the centerlines of the columns. The extended slab edge was vertically supported by an HSS 5x5x1/2 (a 127 mm square hollow structural section with a wall thickness of 13 mm) girder (Figure 3-2a). For specimens CB-DA-SC and CB-SP-SC, some portion of the welded wire fabric and No. 4 reinforcing bars (with the embedded length of 760 mm) were also extended beyond the slab edge to anchor them with stiffened box-shaped steel stubs consisting of HSS 10x10x5/8 and HSS 8x3x3/8 sections to simulate the slab continuity condition (Figure 3-3). The extended ends of the reinforcing bars were bolted to a stiffened box-shaped stub using high strength nuts; the extended pieces of welded wire fabric were welded to the stiffened box-shaped stub. Load cells were placed between the nut and the stiffened stub to measure tensile loads induced in the reinforcing bars during the fire test.

The W12x106 columns were laterally braced using a set of brace modules made of the same wide-flange sections (Figure 3-1). The base plates of columns and brace modules were anchored to the strong floor using high strength steel bars with a total clamping force of 5400 kN. The lateral stiffness of the column attached to brace modules was 190 kN/mm for a lateral force pushing the column away from the test compartment and 170 kN/mm for a lateral force pulling the column toward the test compartment, as described in Section 3.1.2.



(a)



(b)

**Figure 3-1 (a) A 3D schematic and (b) photograph of the structural test setup (fire compartment walls are not shown).**

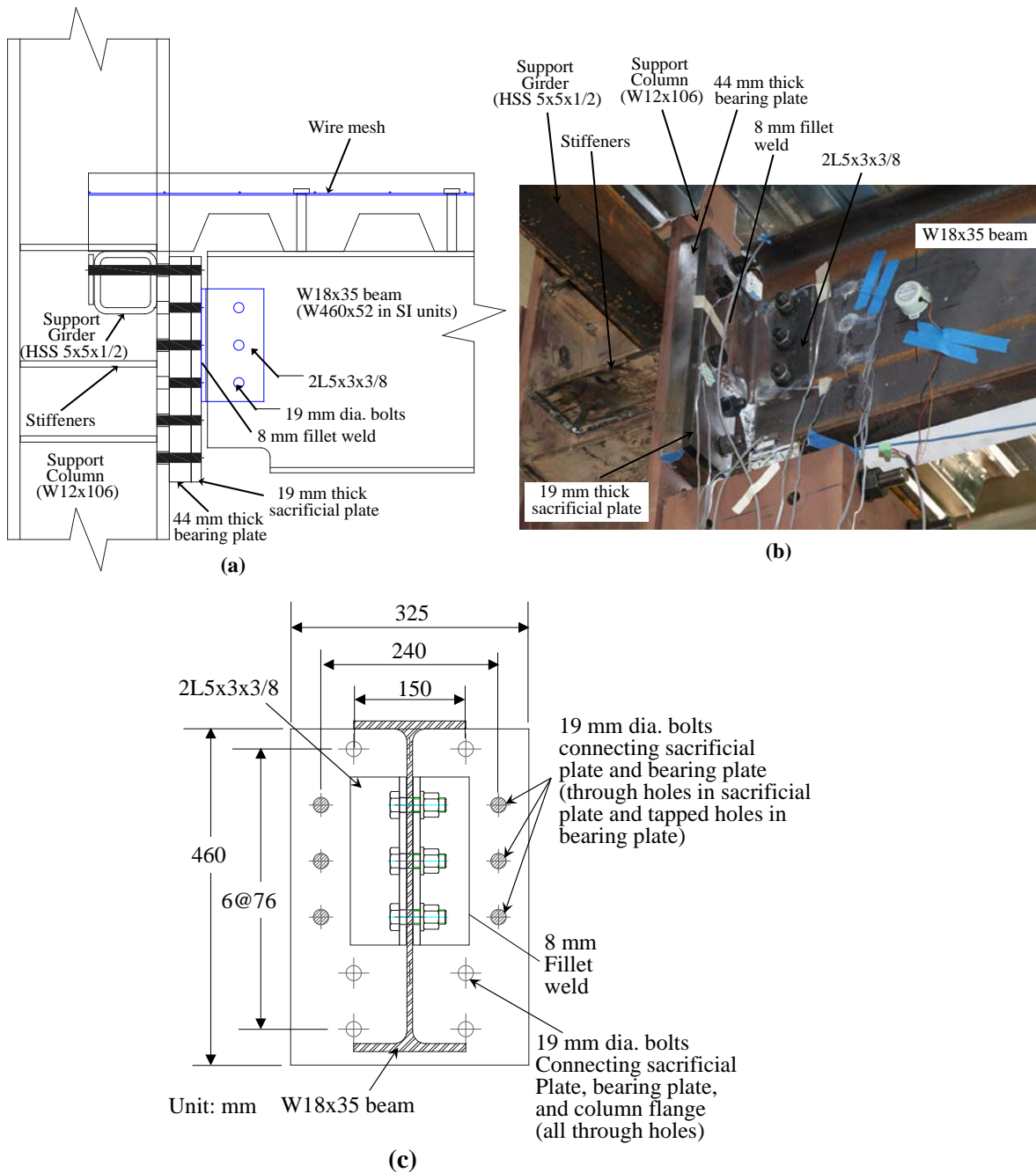


**Figure 3-2 (a) Connection and slab end support conditions for specimen without slab continuity-side view, (b) beam-to-column connection, (c) connection of sacrificial and bearing plates to column.**

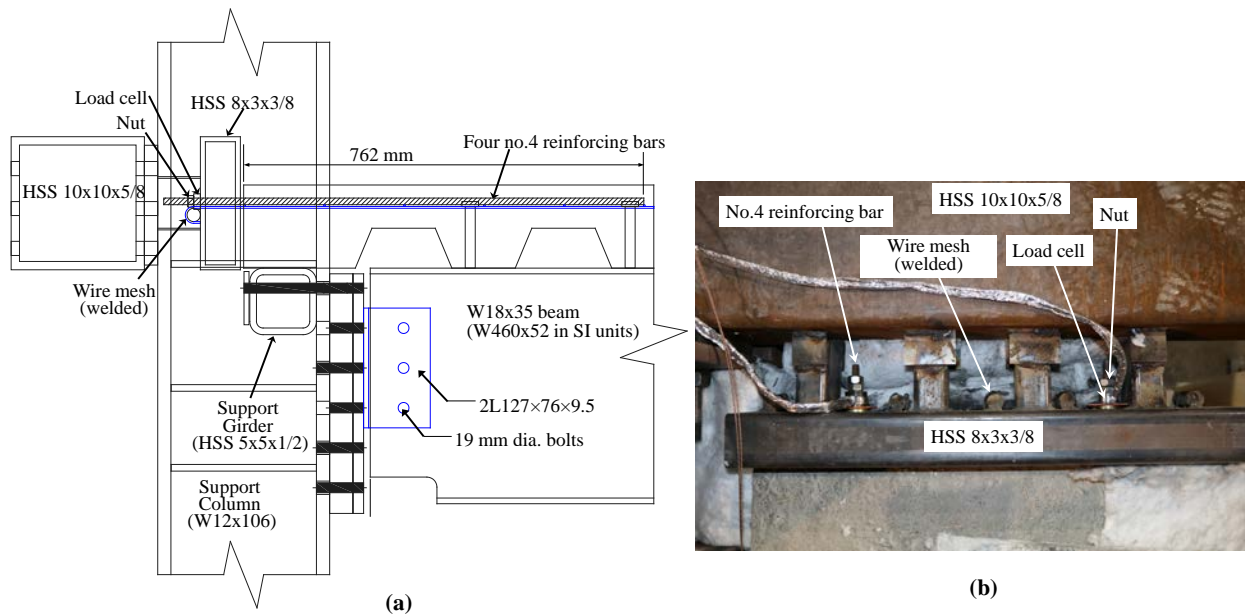


**Figure 3-3 (a) Connection and slab end support conditions for specimen with slab continuity (elevation view), (b) photograph of anchored slab (top view).**

### 3.1.1 Mechanical Loading

Mechanical loading was applied to the top of the slab at six loading points along the longitudinal centerline of the specimen. Three loading beams made of HSS shapes were used to apply six equally distributed point loads as shown in Figure 3-4. Each loading beam was pin-connected to a triangular-shaped loading truss, made of structural steel tubes, to equally transfer the forces at each contact point on the specimen. The ends of a loading beam were connected to two hydraulic actuators (each mounted in the basement) via high-strength tension bars; therefore, a total of six hydraulic actuators were used. The loading beams were also mechanically guided such that they could move vertically only. Steel roller bearings were used at each loading point on top of the slab and at the lateral braces of the slab to minimize friction effects (Figure 3-5a through Figure 3-5c).

Since the long-span composite beam specimen was vertically supported by the simple shear connection to the columns, it could be susceptible to rotation about the longitudinal axis (i.e., twisting), which cannot be seen as common behavior of composite beams as part of the floor system. To prevent the premature failure associated with torsional instability of the specimen, the side edges of the 1.83 m wide slab were laterally braced at the projected locations of the loading beams (Figure 3-5d).

In addition, the coupled actuators automatically adjusted the load and displacement such that a moment induced by torsional instability of the specimen was counter-balanced. During the test, the levelness of the loading beams was maintained using displacement control of the coupled actuators, and the total gravity loads remained constant using force control of the same actuators. Figure 3-6 shows the cross-section view of the specimen with the loading system. The two actuators (actuator 1 and actuator 2) attached to the same loading beam were programmed to maintain the horizontal level with displacement control ( $\delta_1 = \delta_2$ , where  $\delta_1$  and  $\delta_2$  are displacement of the actuator 1 and actuator 2, respectively) during the test. Simultaneously, mechanical loads applied using the two actuators ( $P_1$  and  $P_2$ ) were controlled such that the value of  $P_1 + P_2$  remained a constant (force control). The total load on the load beam (i.e.,  $P_1 + P_2$ ) was equally distributed to two loading points on the specimen via the pin-connected loading truss. The magnitude of the force at each contact point on the specimen was approximately  $0.5 \times (P_1 + P_2)$ .

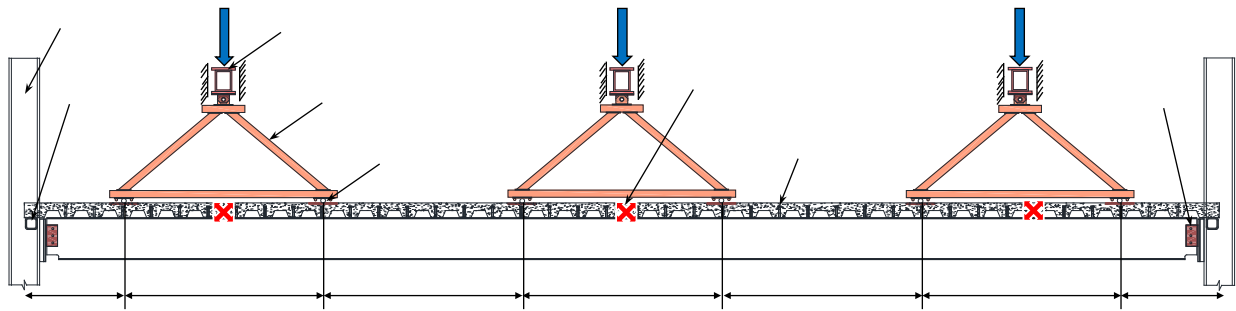


**Figure 3-4 (a) Mechanical loading system (lateral brace system not shown)**

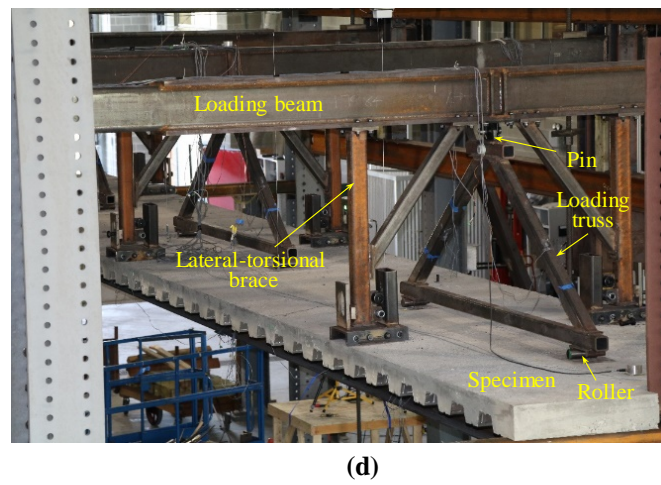
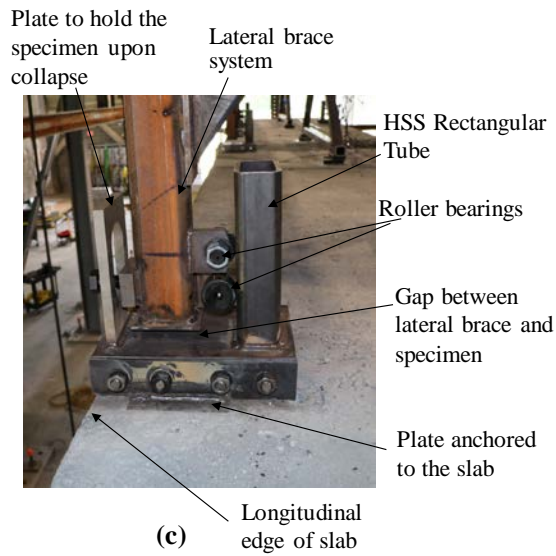
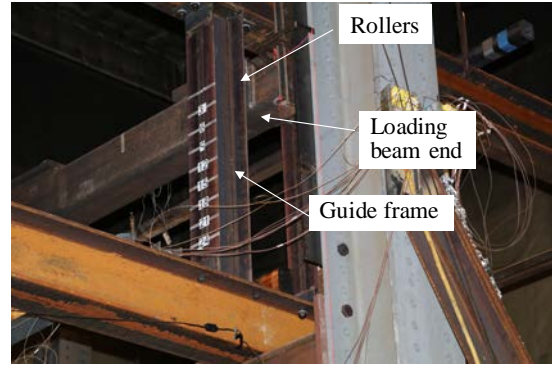
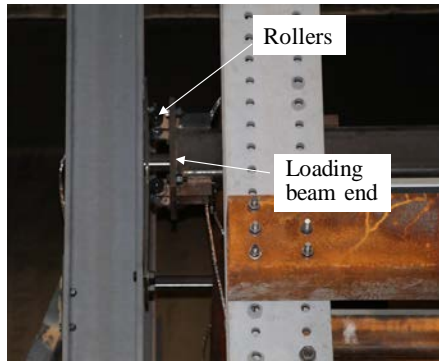


**Figure 3-5 (a) Rollers at the end of loading beams, (b) guide frame, (c) lateral-torsional brace to specimen, (d) loading truss.**



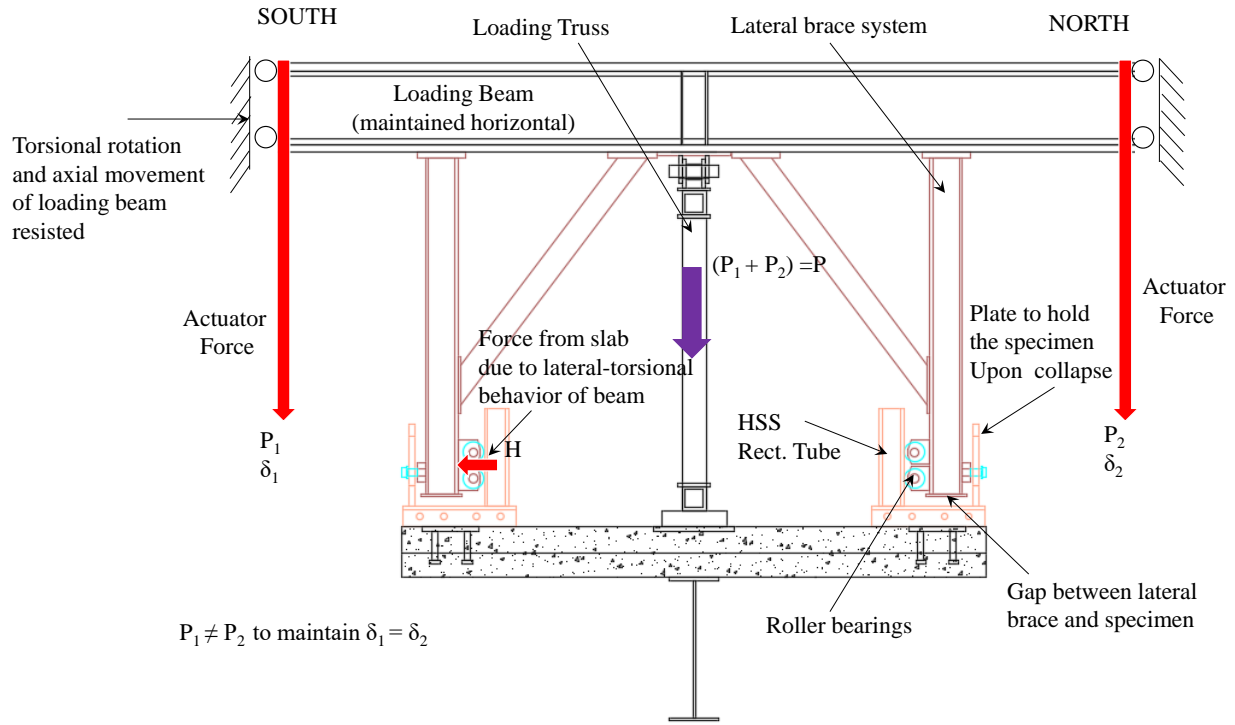


**Figure 3-6 Cross-section view of the specimen with loading system.**

### 3.1.2 Lateral Support Stiffness

The lateral stiffness of the column brace module was measured prior to the tests. Figure 3-7 shows a schematic of the test setup and the location of strain gauges used in the lateral stiffness test. Figure 3-8 shows photograph of the test frame and the sensors used in the test. The base plates of the column and attached brace modules were anchored to the laboratory strong floor using twelve 3.5 cm diameter high strength bars with a post-tension force of 445 kN each. Two 222-kN hydraulic actuators mounted on the strong wall were used to pull and push the braced column at an average height of 354 cm. This height was similar to the location of the middle bolt of the composite beam assemblies tested under fire conditions. The linear displacement sensor was mounted on the column flange at the height of 354 cm to measure the lateral displacement of the braced column during the test. In addition, a laser tracker system was used to measure lateral movement of three targets attached to the flange and web of the column at the same height. Three slip sensors were mounted on the floor to measure any slip at the base plate of the column during the lateral loading. A total of eight linear strain gauges were mounted on the primary diagonal brace members to record the linear relationship of the lateral load versus axial strains in the braces. The measured relationship was used to quantify the axial restraint force in the composite floor beam assemblies subjected to fire. Table 3-1 summarizes the measured values of the lateral stiffness and the ratio of the lateral load to axial strains in the braces.

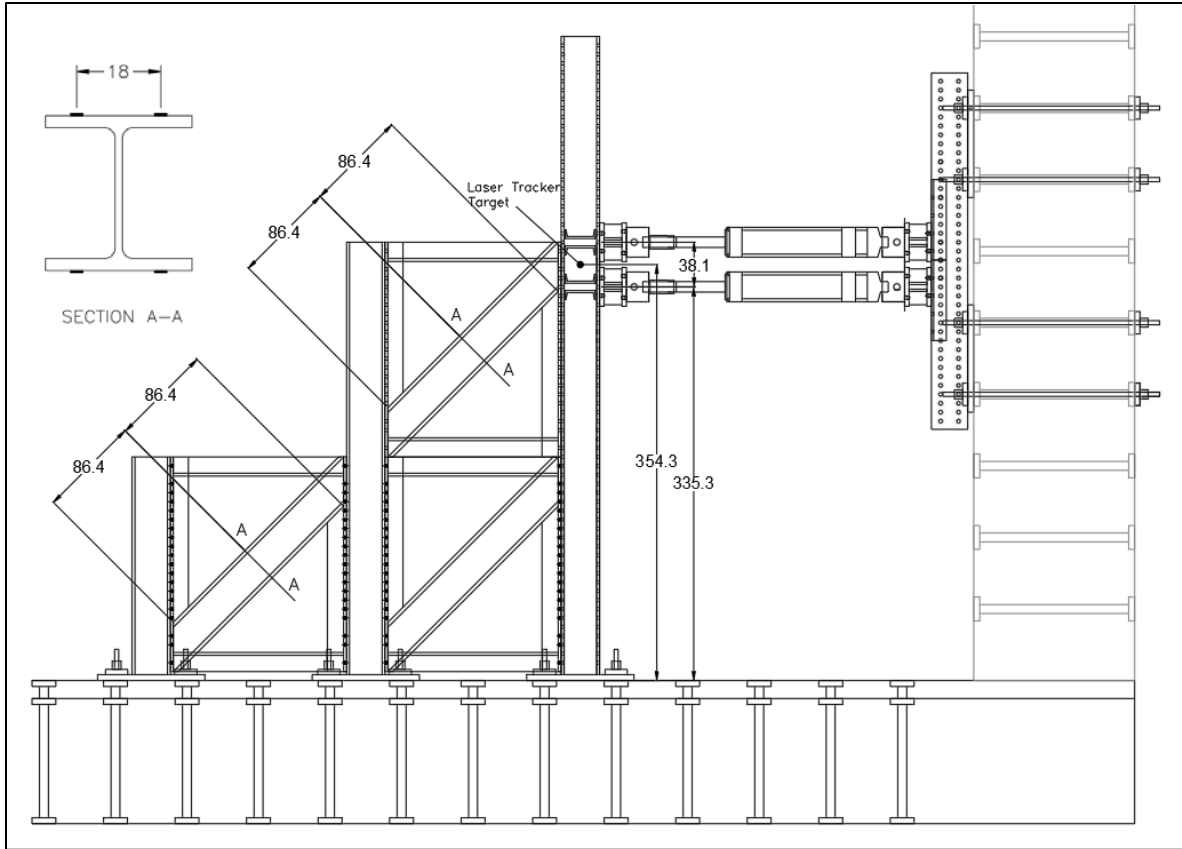


**Figure 3-7 Setup for lateral stiffness test of braced columns (units in cm).**



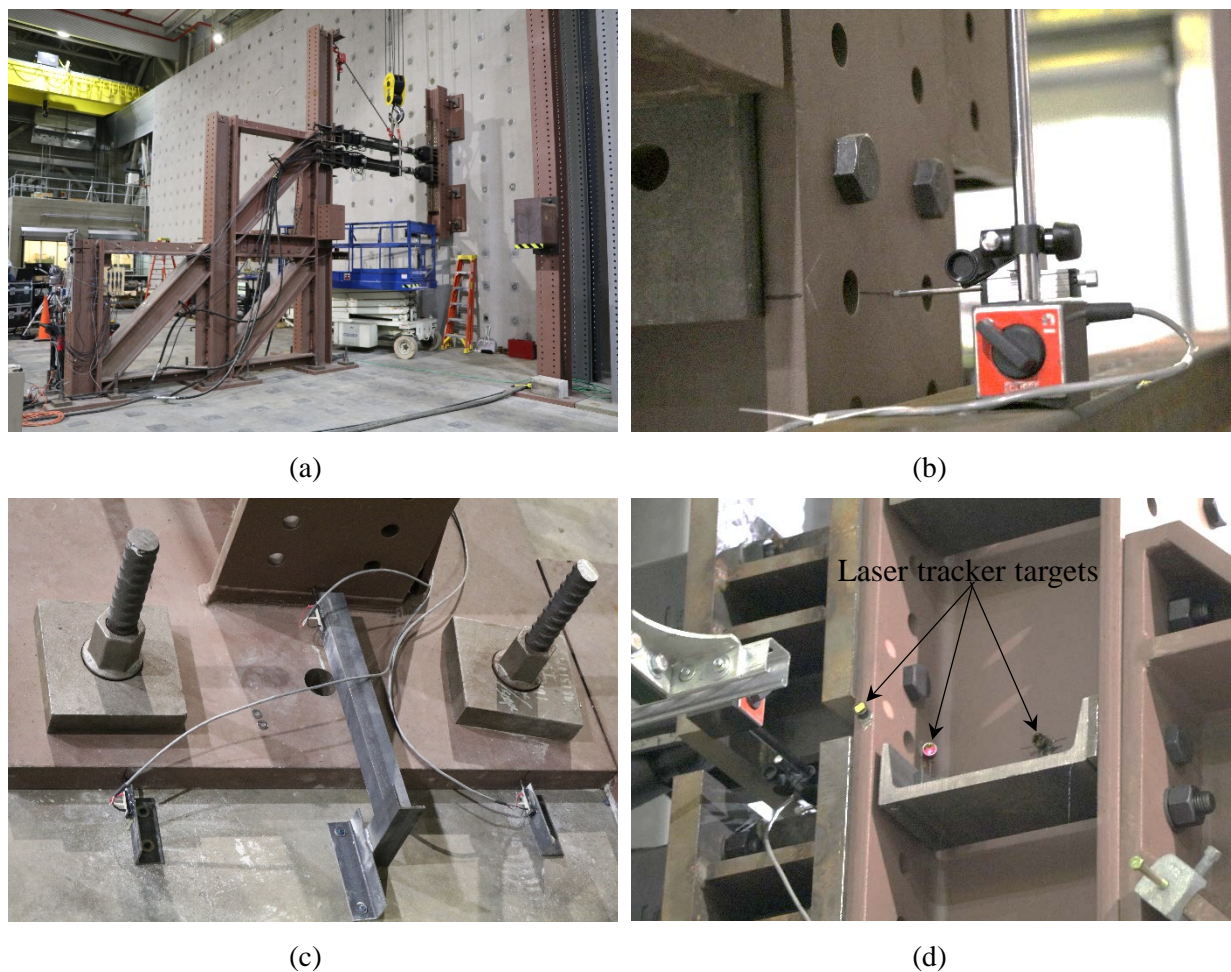


**Figure 3-8** Photographs of (a) the lateral stiffness test setup, (b) displacement sensor, (c) slip sensor, and (d) targets for laser tracker system.

**Table 3-1** Results from the lateral stiffness test.

	Measured lateral stiffness, kN/mm		Measured ratio of lateral load to axial strain in column braces, kN/(mm/mm*10 <sup>-6</sup> )
	Actuator load in compression	Actuator load in tension	
Mean	190	170	3.90
Standard deviation	10 (5 %)	5 (3 %)	0.24 (6%)

## 3.2 FIRE CONDITIONS

### 3.2.1 Fire Load Development

The fire resistance of a structural assembly in prescriptive building codes is rated based upon the assembly's performance in a furnace environment as specified in a test standard such as ASTM E119 (2018) or ISO 834 (2014). The standard furnace, either gas- or oil-fired, is required to increase the temperature of the environment according to the time-temperature relation shown as the solid black line in Figure 3-9. In the current study, the fires to which the composite beams were exposed were not intended to replicate the standard fires, but to represent realistic yet extreme conditions that had the potential to threaten the structure. The Heat Release Rate (HRR) selected was based upon knowledge gained in previous full-scale fire experiments, one conducted at NIST using three workstations as the fuel (Hamins et al. 2008), and another at Cardington using wood pallets for fuel (BRE 2004). The previous full-scale fires at NIST were conducted in a room that was 10.7 m deep, 7 m wide, and 3.4 m high. The room was fully enclosed except for windows along one of the 7 m walls, providing a total area of 4.8 m<sup>2</sup> for ventilation. The framing structure was not mechanically loaded. Two experiments were run using similar fuel packages, each with three identical workstations with a total mass of 1670 kg (17 MJ/kg). A jet fuel spray with a 2 MW heat release rate was applied for the first ten minutes of the tests. The spray burner caused rapid ignition of the combustibles throughout the compartment but contributed only a fraction of the total experimental heat release. The heat release rates and upper layer temperatures averaged over two positions for the duplicate experiments are shown in Figure 3-9.

The test at Cardington was conducted in an eight-story steel structure as part of a European collaborative study (EC FP5 HPRI-CV5535). The fire room in Test 7 was 11 m wide by 7 m deep and one story (4.1 m) high. A single vent ran along the width of the room. Wood cribs uniformly distributed across the floor were used as the fuel, providing 40 kg/m<sup>2</sup> mass load on the fire floor (700 MJ/m<sup>2</sup> energy load). Unlike the NIST experiments, the floor above the fire room in the Cardington test was structurally loaded using sandbags to 30 % of the design strength. The average of the upper layer compartment temperatures measured during Test 7 is shown in the Figure 3-10.

The key parameters which dictate the thermal environment in a fire are the room geometry, ventilation, and fuel load. The bay for the current structural fire experiments had a floor area of 2 m by 12.8 m and a height of 3.7 m. Natural gas was used as the fuel in the composite beam fire experiments because:

- natural gas allows independent and rapid control of HRR during an experiment;

- NIST has extensive experience with high accuracy flow rate measurements and independent means of HRR calculation when using natural gas;
- the major constituent of natural gas ( $\text{CH}_4$ ) has the lowest tendency to soot of any hydrocarbon, providing the best environment for optical measurements of displacement;
- natural gas fires are well suited for simulation; and
- natural gas provides a baseline for comparison to future solid fuel fires.

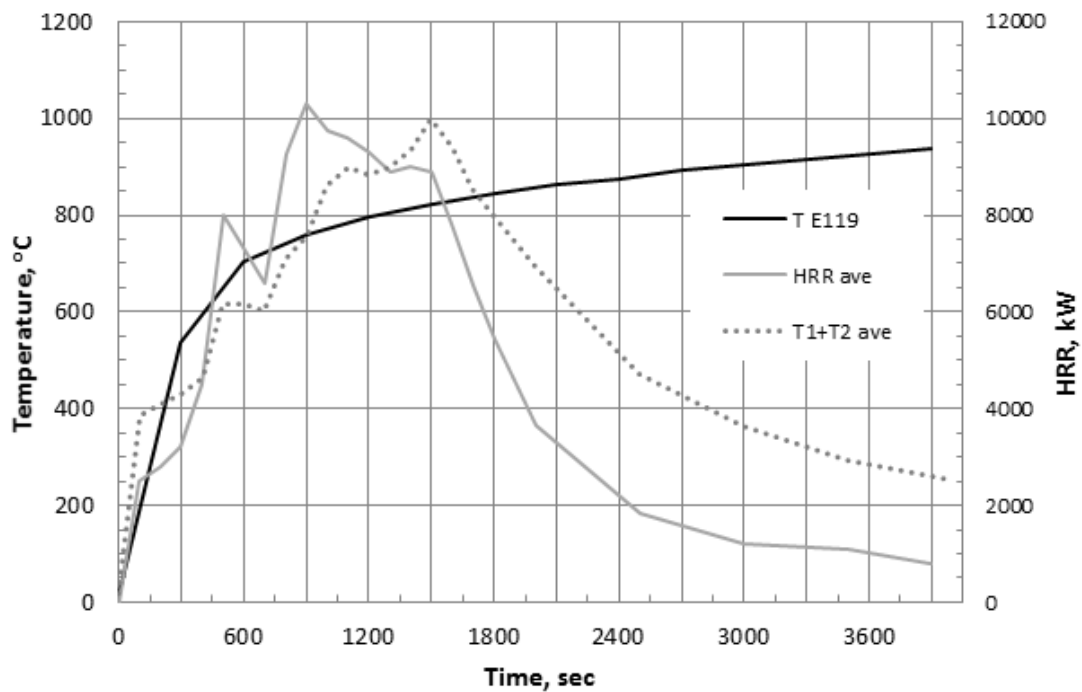
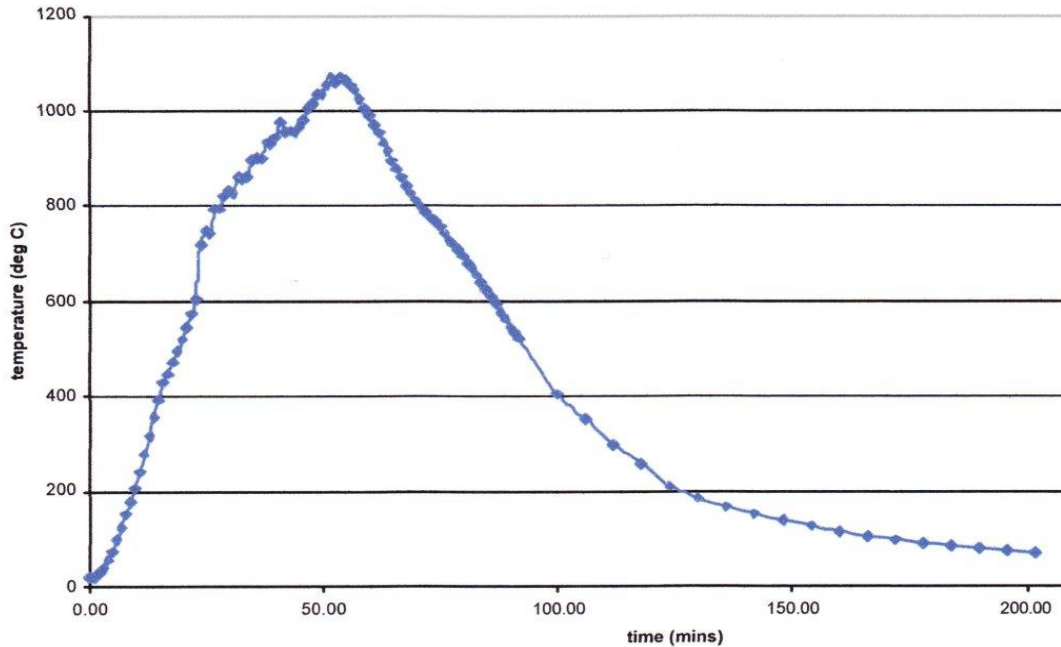


Figure 3-9 Average HRR and nominal temperature of NIST full-scale office fire experiments (Hamins et al. 2008) with time-temperature curve from ASTM E119.



**Figure 3-10 Average compartment time-temperature response in Cardington Test 7 (BRE 2004).**

Three burners (1 m x 1.5 m) with a rating up to 4000 kW each were used to simulate the fire throughout the test room. The enclosing walls of the compartment were constructed of 22-gauge sheet steel on steel studs protected by two layers of 25 mm thick ceramic fiber blanket on the side exposed to the fire.

The fire in the composite beam study was designed to maximize the upper layer temperature, to minimize the level of smoke, and to avoid excess fuel feeding a fire external to the bay. The ventilation was controlled by the total vent area,  $A_{vent}$ , and the height of the vent,  $H$ . In wood crib fires, when  $A_{vent}\sqrt{H}$  is greater than  $10 \text{ m}^{5/2}$ , an over-ventilated condition exists (Kawagoe 1958). Table 3-2 compares the room geometry and fire parameters in the current composite beam study to the design of the Cardington and previous NIST study. It appears that the fire in the Cardington test may have been over-ventilated, while the fire in the NIST 2008 study was under-ventilated. The value of  $A_{vent}\sqrt{H}$  in the current experiment suggests that this fire would have been under-ventilated; however, the correlation for wood crib fires is not directly applicable to natural gas fires.

When scaled with the room volume, the vent area in the composite beam study, 0.062/m, was slightly greater than the vent area/volume used in the Cardington fire. Calculations using the NIST Fire Dynamic Simulator (FDS, discussed in a subsequent section) support the hypothesis that most

of the heat content of the natural gas was released within the test compartment with little excess air.

Surveys (e.g., EUR 26698 EN's Table 1.4.2, Vassart 2014) have found that the fuel loads in commercial and public spaces vary greatly with the designated purpose of the space. A standard office contains in the range of 420 MJ/m<sup>2</sup> to 655 MJ/m<sup>2</sup> of combustible material; a shopping center is in the range of 600 MJ/m<sup>2</sup> to 936 MJ/m<sup>2</sup>; and a library can have fuel loads up to 2340 MJ/m<sup>2</sup>. The previous NIST experiment at a load of 400 MJ/m<sup>2</sup> was conducted with only three workstations in a space that more typically would have had six workstations. In the more typical case, the energy content would have been 800 MJ/m<sup>2</sup>, about equal to the fuel load in the Cardington tests and a bit above the survey levels for typical office layouts. Because the current experiments represented an extreme fire condition, the capability for an equivalent fuel load of 1.6 times (the value 1.6 is a typical safety factor used for other loads in structural design practice) the energy content more typical of a modern office, or about 1200 MJ/m<sup>2</sup> for a two-hour fire, was built into the fire design, with the possibility to go higher for longer exposure times if necessary to attain significant structural failure.

The average HRR in the NIST 2008 fire was 4300 kW, slightly below the estimated average in the Cardington test. The HRR in the composite beam pre-experiment design simulation ramped up to 4000 kW in 10 min, was held steady for 3 hr, and then decreased linearly to zero over the next 60 min. The peak intensity of the fire on a volumetric basis was 42 kW/m<sup>3</sup>, similar to the value of 40 kW/m<sup>3</sup> in the NIST 2008 test. Since HRR was not measured directly in the Cardington work, the HRR<sub>peak</sub>/vol. cannot be compared to the present study.

Refer to Table 3-2 for the detailed comparison of key geometric and thermal parameters of the previous studies done at NIST and Cardington to those proposed to be used in the composite beam study. Note that the fires proposed for the current study were not intended to represent a specific "Design Fire Scenario" in the sense of one to be used in Performance-based Engineering, or equivalent prescriptive design; rather, the fires were designed to provide insight into the ultimate limits of a conventionally designed composite beam engulfed in fire for a period beyond its standard 2-hour rating.

**Table 3-2 Key geometric and proposed thermal parameters for composite beam study**

Parameter	NIST	Cardington	Composite Beam Study
depth x width x height	10.7 m x 7 m x 3.36 m	11.0 m x 7.0 m x 3.1 m	2 m x 12.8 m x 3.7 m
floor area	74.9 m <sup>2</sup>	77.0 m <sup>2</sup>	25.6 m <sup>2</sup>
volume	252 m <sup>3</sup>	239 m <sup>3</sup>	95 m <sup>3</sup>
vent opening area	4.8 m <sup>2</sup>	11.4 m <sup>2</sup>	5.9 m <sup>2</sup>
$A_{vent}\sqrt{H}$	6.9 m <sup>5/2</sup>	12.8 m <sup>5/2</sup>	6.4 m <sup>5/2</sup>
vent area/vol.	0.02/m	0.05/m	0.062/m
fuel package	3 work stations plus 40 L of jet fuel	wood cribs	3 natural gas burners, 1 m x 1.5 m each
fuel load	400 MJ/m <sup>2</sup>	720 MJ/m <sup>2</sup>	1781 MJ/m <sup>2</sup>
average HRR	~4300 kW	~4600 kW (est.)	3167 kW
peak HRR/vol.	40 kW/m <sup>3</sup>	unknown	42 kW/m <sup>3</sup>
upper layer temperature	~1050 °C	~1050 °C	~1000 °C
fire duration	67 min	200 min	180 min; 60 min cooling period

### 3.2.2 Fire Simulation

#### Predicted surface temperatures and heat fluxes

The NIST Fire Dynamic Simulator (FDS) Version 6.5.3 (McGrattan et al. 2013), a computational fire model, was used to examine the influence of varying the geometric and thermal parameters listed in Table 3-2 on the fire behavior and the beam temperatures. The HRR was varied between 2500 kW and 5000 kW, resulting in heat release rates per unit volume between 25 kW/m<sup>3</sup> and 50 kW/m<sup>3</sup> and in fuel loads between 600 MJ/m<sup>2</sup> and 2600 MJ/m<sup>2</sup>. The vent openings were varied between 4 m<sup>2</sup> and 6 m<sup>2</sup> (14 % to 22 % of floor area). The effect of two different SFRM insulating materials on the steel beam temperatures was also investigated. The fuel was methane and delivered through three 1 m by 1.5 m burners placed on the floor along the centerline of the composite beam. The dimensions of the test compartment were fixed, except as noted in this section.

A number of different fire scenarios were modeled. The FDS input file for one of these case (Case 5be) is available on the github repository for FDS (<https://github.com/firemodels/fds>). It is provided in Appendix C of this report as well. Results from that simulation, done with 5 cm grid spacing, are shown in Figure 3-11 through Figure 3-17.

The outline of the compartment with a representative fire can be seen in Figure 3-11. Figure 3-12 and Figure 3-13 are views of, respectively, the surface temperatures and the heat fluxes on the interior walls looking upward from below the burner surface (black squares) 120 min after ignition. The ceiling, the exposed surface of the SFRM, and the upper 50% of the chamber walls are at temperatures between 900 °C and 1000 °C. The gauge heat fluxes approach 150 kW/m<sup>2</sup> on the ceiling and on the exposed surface of the SFRM protecting the beam lower flange and remain above 100 kW/m<sup>2</sup> throughout the top two-thirds of the interior chamber.

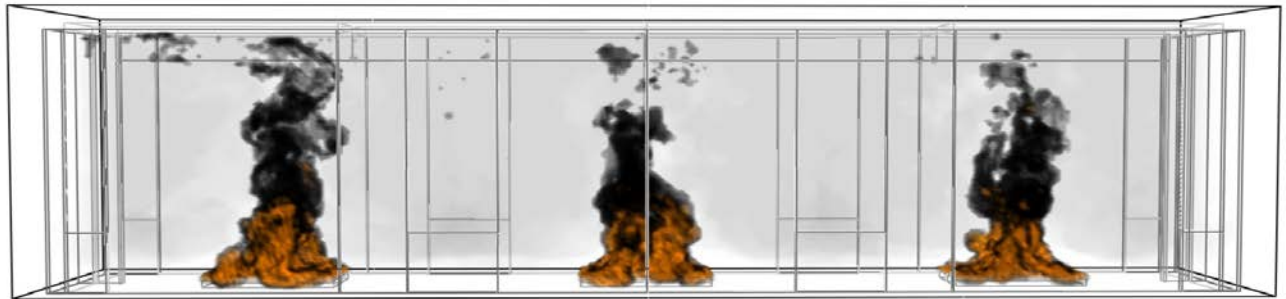


**Figure 3-11 Representative fire behavior showing simulated local heat release and soot.**

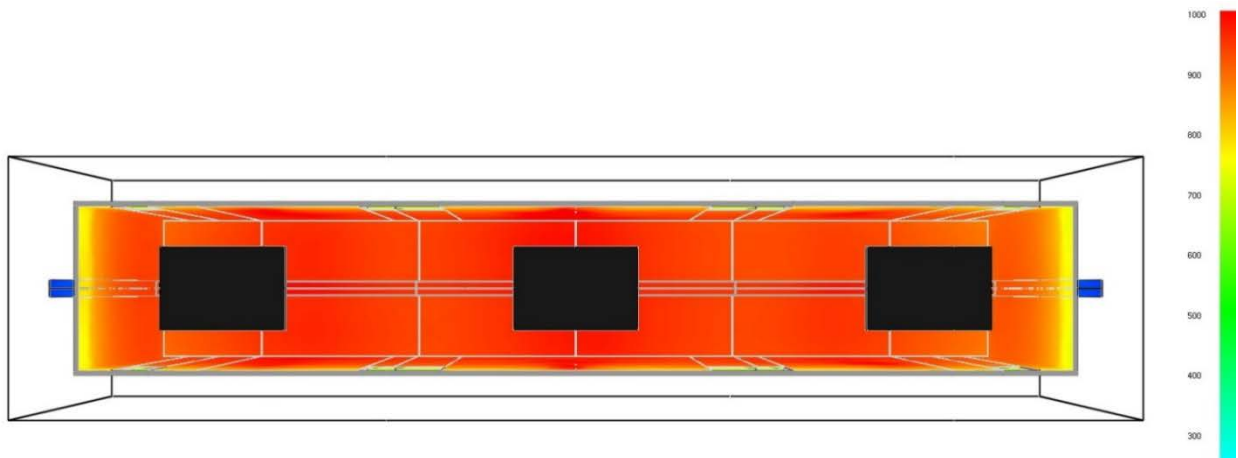


**Figure 3-12 Interior wall surface temperatures (in degree Celsius) viewed from below 120 min after ignition.**



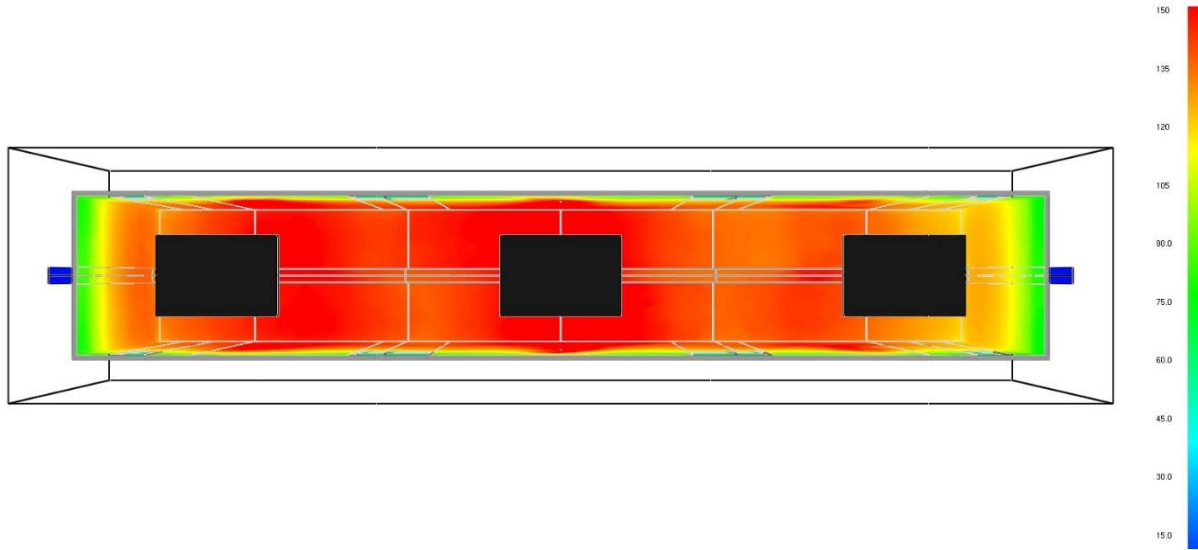


**Figure 3-13 Interior wall heat fluxes ( $\text{kW/m}^2$ ) viewed from below 120 min after ignition.**

Figure 3-14 is an image of the exterior wall temperatures 120 min after ignition. Most of the exterior wall temperatures exceed  $300\text{ }^\circ\text{C}$ ; the temperature on top of the concrete slab is uniformly around  $250\text{ }^\circ\text{C}$ . Temperatures on the floor (viewed through the vents) are predicted to exceed  $750\text{ }^\circ\text{C}$ . External burning can be seen exiting the smaller vents at either end of chamber.

The average temperature of the hot gas layer (HGL) is plotted in Figure 3-15 as a function of time. A maximum temperature of  $980\text{ }^\circ\text{C}$  is attained just before the cooling period begins. The temperature of the lower beam flange, averaged along the beam's length, is shown as the orange line in Figure 3-15. The average temperature exceeds  $600\text{ }^\circ\text{C}$  about  $7200\text{ s}$  (2 hr.) after ignition and reaches its peak value of  $815\text{ }^\circ\text{C}$  at  $12\ 600\text{ s}$ , during the cooling period. Also plotted is the temperature of the columns, which are protected by being outside the compartment walls so that the support system will be undamaged for subsequent tests.

Figure 3-16 shows how the temperatures evolve with time and distance along the lower beam flange. The heating from the fire appears relatively uniform. The highest temperatures are in the central portion of the beam, reaching a peak of  $850\text{ }^\circ\text{C}$  at  $12\ 600\text{ s}$ , which is  $60\text{ }^\circ\text{C}$  hotter than near the connections.



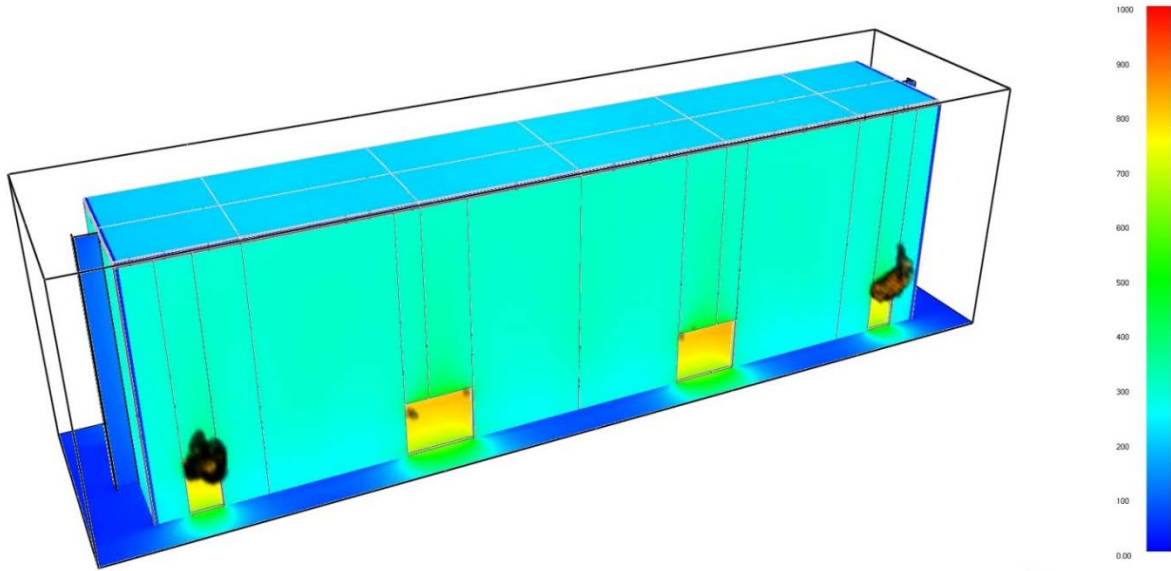


Figure 3-14 Exterior wall temperatures (in degree Celsius) 120 min after ignition

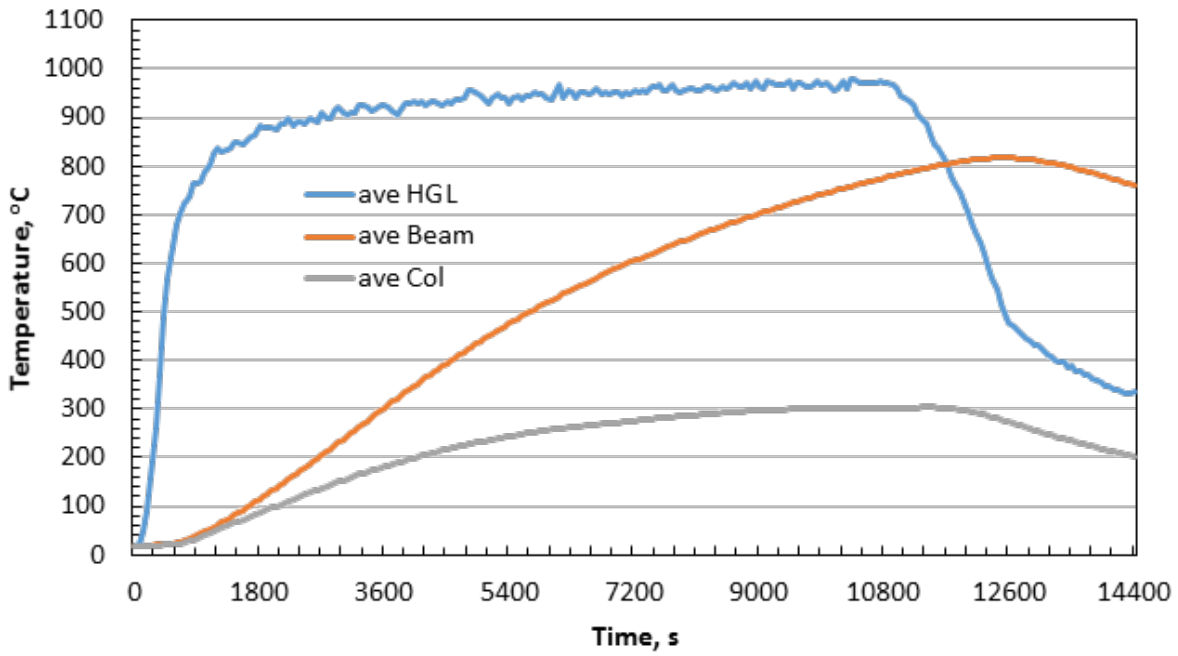


Figure 3-15 Average temperatures of hot gas layer (blue), spatial average along lower flange of steel beam (orange), and average temperature of columns near beam connection (gray) for case 5Be.

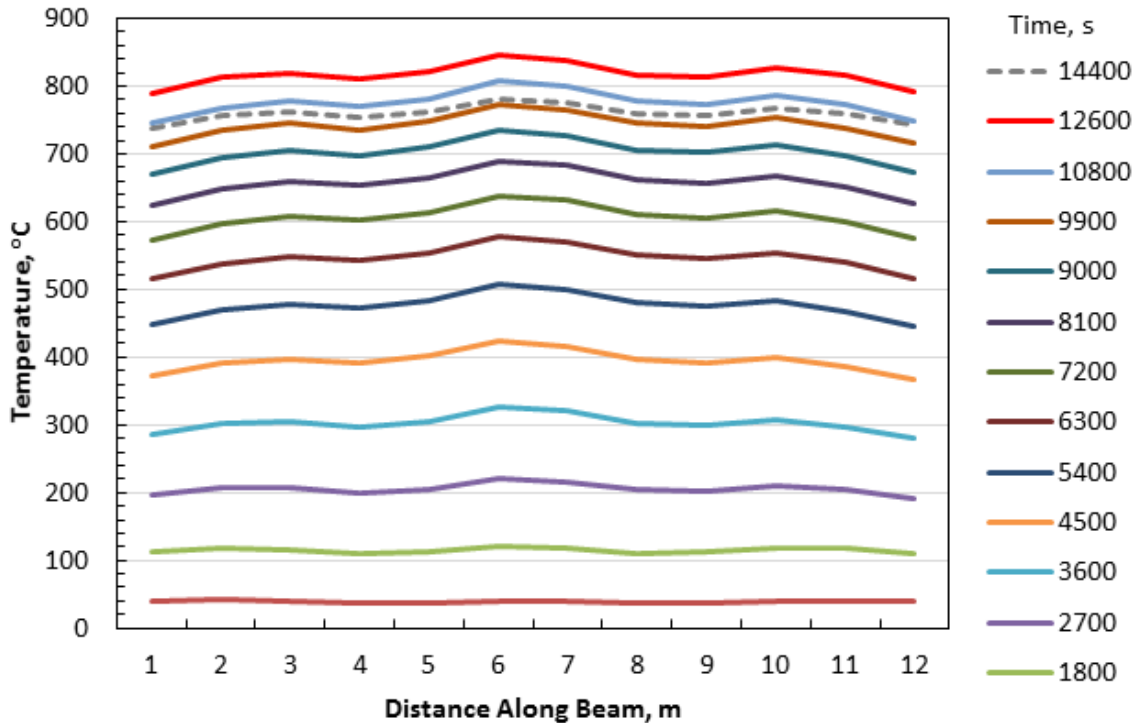


Figure 3-16 Temperatures along lower flange of steel beam (case 5Be).

### Sensitivity to variation in FDS input parameters

Several cases were run with FDS to examine the effects of: (1) refining the mesh in the vicinity of the beam, (2) changing compartment geometry, (3) increasing ventilation, (4) changing the wall materials, and (5) changing the SFRM properties.

- 1) The base-line calculations were performed with a uniform mesh size of 0.05 m and 1.4 million cells. The mesh size was reduced from 0.05 m to 0.025 m, first over the entire chamber height (2.7 million cells) and second over only the top 0.7 m near the ceiling (1.8 million cells). In both cases, the upper layer gas temperature variation was barely perceptible during the first 6000 s of the fire. The temperature of the steel beam flange was essentially unchanged in the center of the span but was lowered as much as 20 °C near the ends. These variations in temperatures accord with previous findings that a finer mesh predicts lower flame height, resulting in lower beam and upper layer temperatures.
- 2) Two variations to the compartment geometry were considered: decreasing the height of the room and allowing for sag in the composite beam. Cutting the height of the room in half to 1.9 m (all other dimensions unchanged) would make construction and operation of the

laboratory experiments more convenient while maintaining or increasing safety. However, reducing the height by this much was found to lead to an unacceptable degree of non-uniformities in heat flux and temperature distribution across the beam and underside of the concrete slab. Hence, the approach was not considered viable. The impact of sag was estimated by assuming that the composite beam was permanently deformed in a parabolic shape with the center point 0.6 m below the connections, which were maintained at full height (3.7 m). The temperature and heat flux distribution on the composite beam remained qualitatively the same with or without sag, although in the region with the most sag, the heat flux was about 5 % higher. This relatively small effect suggests that assuming the geometry remains unchanged within the FDS calculation is unlikely to have more than a second-order effect on the temperature of the beam.

- 3) The end vents were increased in size from 0.45 m to 0.85 m, for a total open area increase of about 1/3. This change resulted in a drop in the average upper layer gas temperature 6000 s after ignition of about 40 °C. At the same time, the temperature at the ends of the steel beam increased about 10 °C, while the temperatures in central portion of the span were not impacted. The conclusion is that increasing the vent opening caused a shift in the outer fire plumes toward the ends of the chamber, but, overall, the increase in air flow tended to cool the upper layer.
- 4) Different insulating materials used for the walls of the enclosure and the SFRM were investigated. The walls were simulated as (a) concrete sheet, (b) steel sheet with a single layer of 25 mm ceramic fiber blanket, and (c) steel sheet with a 50 mm layer of ceramic fiber blanket. The 50 mm layer of the ceramic fiber blanket produced upper layer gas temperatures slightly over 1000 °C at 7200 s into the simulation, which was about 50 °C hotter than in the baseline calculations. The temperature on the outside wall (facing into the laboratory) 2.5 m above the floor was found to be 100 °C lower with the 50 mm layer of ceramic fiber blanket when compared to the 25 mm layer, as seen in Figure 3-17. Figure 3-18 graphically shows how much more effectively the 50 mm insulation layer, on the right, reduces the external temperature throughout the surface of the wall with only 25 mm of insulation, on the left. The black areas represent regions that exceed 300 °C.
- 5) The original calculations were done assuming that the fire-resistant material for the steel beam would be SFRM A, sprayed according to the manufacture's specification for a 2-hour rating. Subsequently, SFRM B was selected for the experiments and was applied to the steel beam according to the manufacturer's specification for a 2-hour rating. With SFRM A the average lower flange temperature was calculated using thermal properties reported

in Hamins et al. (2008) to reach 600 °C in 3600 s, with a peak temperature near 950 °C at the start of the cooling period. These temperatures compare to 600 °C about 7200 s after ignition, and a peak value of 815 °C during the cooling period for the SFRM B protected specimen, calculated using the thermal properties reported in Kodur and Shakya (2013).

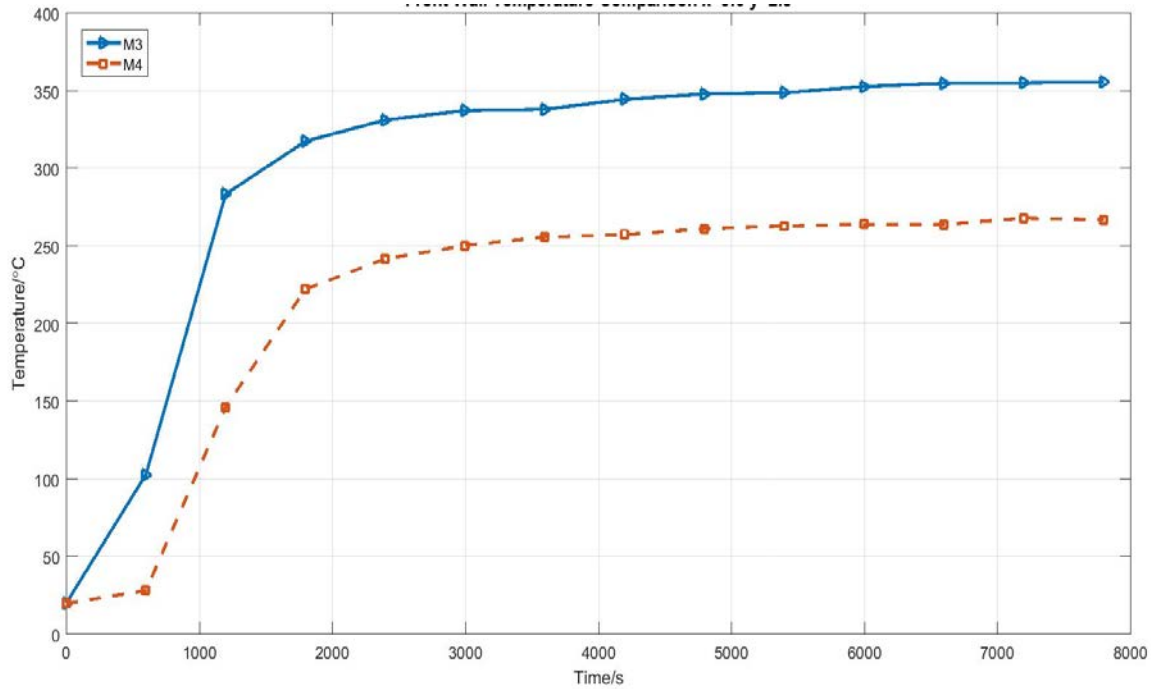


**Figure 3-17 Laboratory-side wall temperature of at  $x=9.0$ ,  $y=2.5$  comparing 25 mm of ceramic fiber blanket (blue curve) to 50 mm of ceramic fiber blanket (red-dotted curve).**

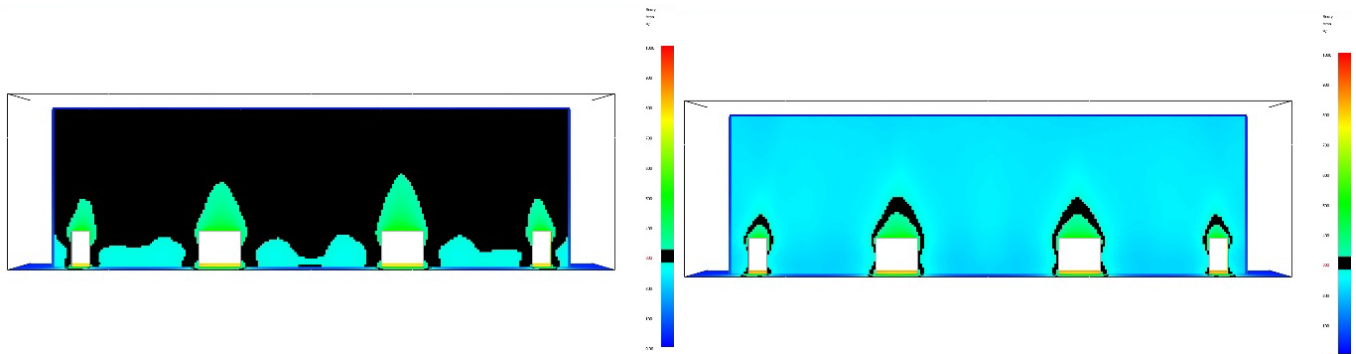


**Figure 3-18 Temperature of front wall (outside) with temperatures of 300 °C and higher shown in black; 25 mm insulation on left compared to 50 mm on right.**

## Chapter 4 MEASUREMENT SYSTEM

This chapter describes the measurement system. It presents the details of the structural measurements, including loads, strains and displacements, as well as the fire measurements, including Heat Release Rates (HRR) and temperature. It also discusses uncertainties associated with the measurements.

Various instruments were used to characterize measurands including: (1) mechanical loading applied using hydraulic actuators, (2) fire loading (Heat Release Rate, heat flux, gas temperature), (3) temperatures of the specimens, and (4) structural responses of the specimens to gravity and fire loading (displacement, rotation, strains, and forces). The sensors used for these measurements are listed in Table 4-1 and detailed descriptions are provided in the following subsections. The locations of the sensor for each experiment are provided in the results section for each individual experiment.

**Table 4-1 Sensors used in the experiments.**

Sensor Description	Manufacturer	Model	Full Scale Value	Remarks
Load cell	MTS	201.35TS	240 kN (T) 365 kN (C)	T=tension; C=Compression
Load cell	Omega	LCWD-20K LCWD-50K	90 kN 220 kN	Tensile loads on reinforcing bars
Strain gauge	Tokyo Measuring Instruments Lab.	FLA-6-11-5LT FLA-5-11-5LT FLM-60-11-5LT EGP-5-120	50000 $\mu\epsilon$ 50000 $\mu\epsilon$ 50000 $\mu\epsilon$ 5000 $\mu\epsilon$	
Potentiometer	MTS	201.35TS	760 mm	
String potentiometer	UniMeasure	PA-5 PA-10 PA-25 PA-30	130 mm 250 mm 635 mm 760 mm	
Linear position sensor	BEI	9615 9610	38 mm 25 mm	
Inclinometer	Meas. Specialties	ACCUSTAR®-EA G-NSDMG-023	$\pm 60^\circ$ $\pm 30^\circ$	
HRRburner	NIST	-	20 MW	Heat release rate (HRR) from gas mass flow
HRR	NIST	-	20 MW	Heat release rate (HRR) from calorimeter

Sensor Description	Manufacturer	Model	Full Scale Value	Remarks
Thermocouple	Omega	GG-K-24-SLE	1250°C	
		XC-K-24	870°C	
		TJ36-CAXL-38U-36	1250°C	
		TJ36-CAXL-14U-24	1250°C	
		INC-K-MO-3.0MM	1250°C	
Heat flux	Medtherm	64-20-18		Gardon Gauge
Plate Thermometer	Pentronic	-	-	Adiabatic surface temperature

## 4.1 STRUCTURAL MEASUREMENTS

### 4.1.1 Forces

Six hydraulic actuators (model: MTS 201.35TS) were used to apply gravity loading on the specimens. Each actuator has a built-in load cell (model: MTS 661.22D-01). Refer to Figure 4-1a. For specimens with slab end continuity (CB-DA-SC and CB-SP-SC), load cells (model: Omega LCHD-20K and LCHD-50K) were installed around the embedded No. 4 reinforcing bars anchored at the location of girders to measure tensile loads during the experiments. A photograph of load cells mounted near the end of the reinforcing bars is shown in Figure 4-1b.

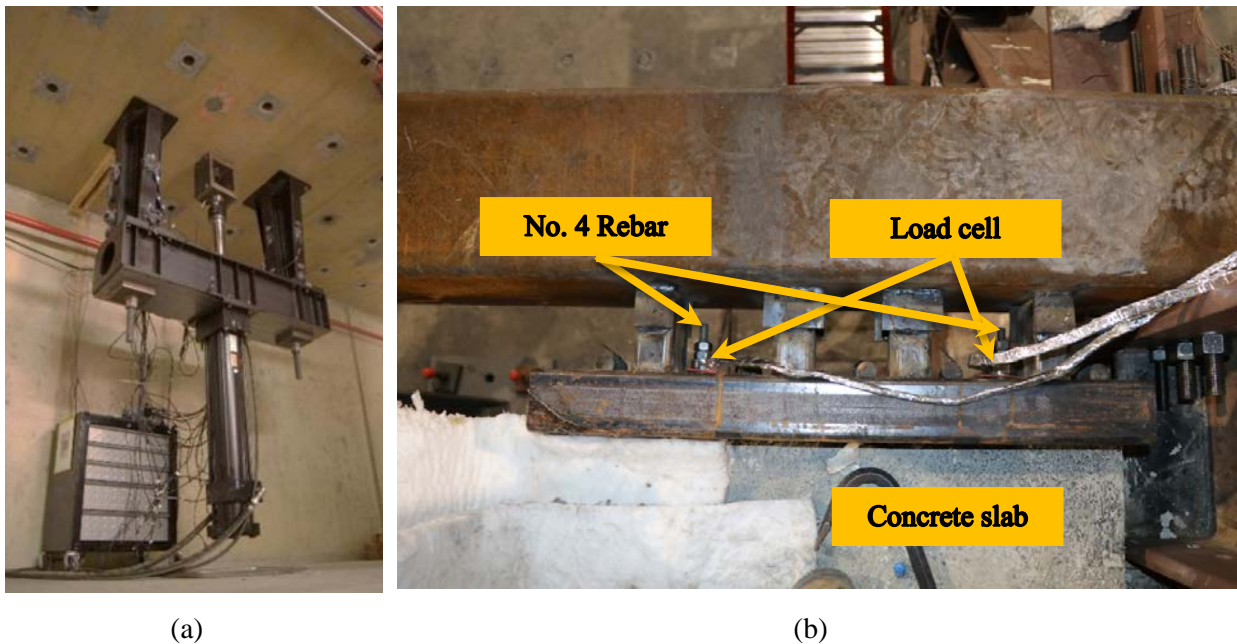


**Figure 4-1 (a) Hydraulic actuator mounted on yoke located underneath strong floor; (b) load cells mounted around the reinforcing bars (top view).**

### 4.1.2 Strains

Linear strain gauges were mounted at various locations including on the concrete slab and W18x35 floor beams of the specimens, loading frames, and braced modules attached to W12x106 columns. FLA-5-11-5LT gauges were attached to both loading frames and floor beams; FLA-6-11-5LT gauges were mounted on brace modules; FLM-60-11-5LT were mounted on top of the concrete slab; EGP-5-120 embedment gauges were installed inside the concrete slab. The manufacturer-specified operating temperature of FLA-5-11-5LT and FLA-6-11-5LT is in the range of -196 °C to 150 °C; that of FLM-60-11-5LT is in the range of -20 °C to 80 °C; and that of EGP-5-120 is in the range of -5 °C to 50 °C. In this study, all strain measurement took place at temperatures lower than 50 °C.

### 4.1.3 Displacements

Displacements of the specimens were measured using linear displacement transducers (potentiometers). String potentiometers were connected to the top of the concrete slab at four locations along the specimen length. The potentiometers were positioned approximately 2 m above the slab and protected from excessive heating using aluminum foil and ceramic fiber blanket (Figure 4-2a,b). For the ambient specimen (CB-DA-AMB), additional displacements were measured, including the vertical and lateral displacements of the specimen at midspan, the slip between the steel beam and the slab, and the gap closure between the beam web (at ends) and sacrificial plate attached to the column flange (Figure 4-2c).



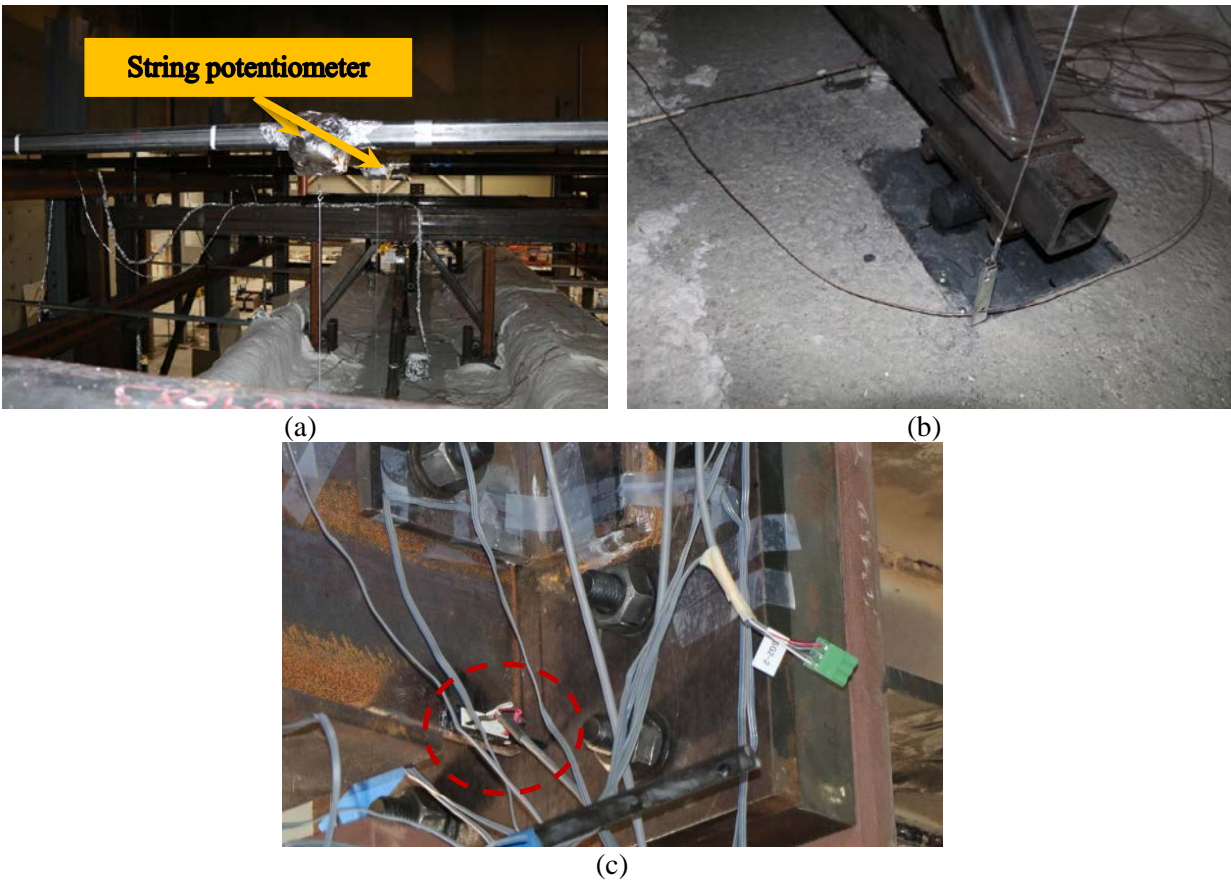


**Figure 4-2 (a) Measurement of vertical displacement using string potentiometers; (b) attachment to the concrete slab; (c) gap measurement at beam end.**

#### **4.1.4 Rotations**

Linear rotation transducers were used at several locations (Figure 4-3). Dual-axis inclinometers (Measurement Specialties model G-NSDMG-023) were attached to top of the slab along the centerline at the east and west ends for all specimens and on top of the loading beam for the ambient specimen only. Single-axis inclinometers (Measurement Specialties model ACCUSTAR-EA) were used to measure rotations of the loading frames for all tests and that of the web of W18x35 beam at each end for the ambient test only.



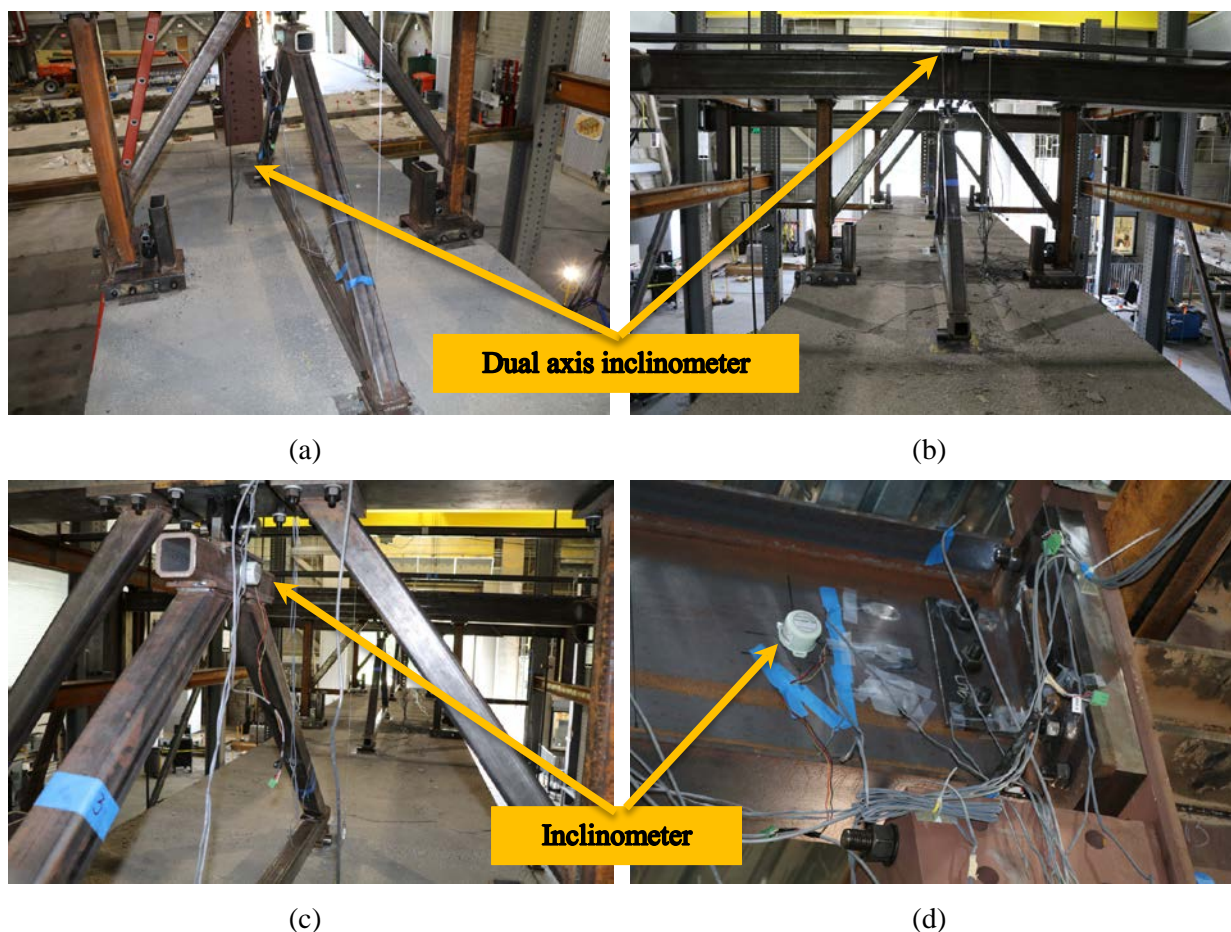


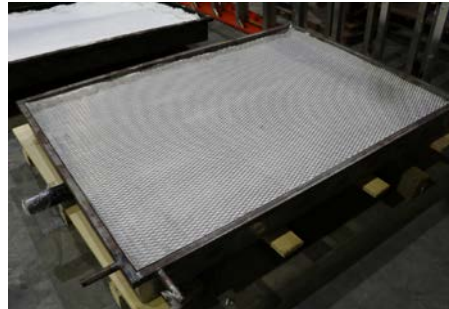
**Figure 4-3 Inclinometers: (a) along centerline of the slab at east and west ends; (b) on top of the loading beam; (c) on the loading truss; (d) on the web of the beam at east and west ends.**

## 4.2 FIRE MEASUREMENTS

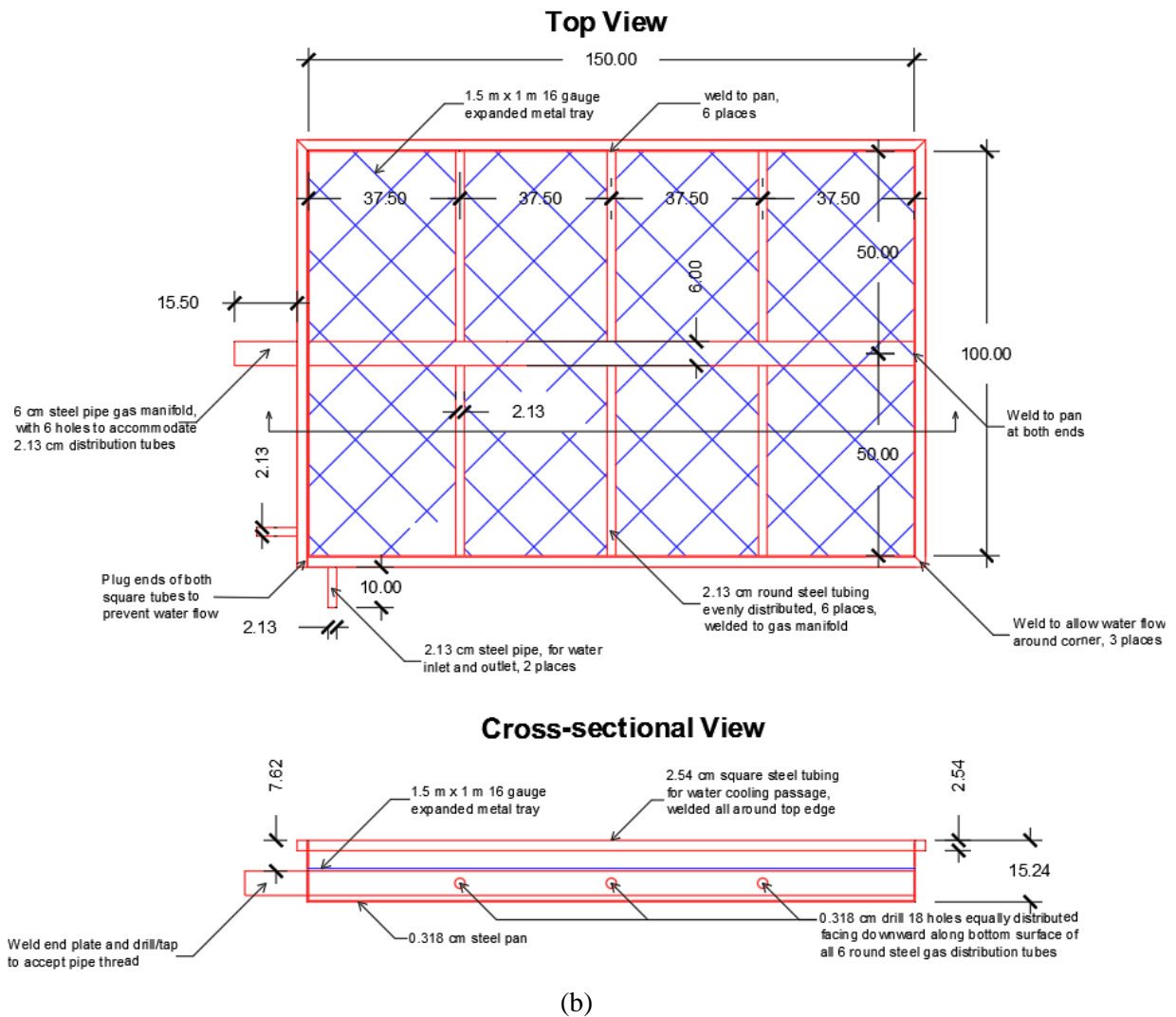
### 4.2.1 Natural Gas

Three 1 m by 1.5 m gas burners (Figure 4-4) were used to create controlled fire conditions in the compartment. A gas fuel delivery control and measurement system was used to supply the burners. The fuel delivery system is capable of providing natural gas flow for fires up to 20 MW in size. The fuel delivery system is capable of providing natural gas flow for fires up to 20 MW in size. The 12.7 cm gas supply line pressure was 138 kPa. A pneumatic actuated ball valve was computer controlled using an analog output signal. A balancing valve was located upstream of each of the three burners to distribute the fire inside the compartment. The burner heat release rate was calculated using the measured mass flow and composition of the natural gas (Bryant et al. 2015). The gas mass flow rate was determined using a positive displacement rotary volume flow meter, pressure transducer, and thermistor. The carbon monoxide mass yield was less than 3 % and the effect of combustion efficiency was factored into the uncertainty of HRR. The composition of natural gas was measured using a gas chromatograph with a sampling period of 3 min. The main

components of the natural gas used during this test series was methane (89 % to 94 %), ethane (4 % to 9 %), and propane (0.2 % to 1 %). The Ideal Gross Heating Value was calculated using the method described in ASTM D3588-98 (2017).



(a)



(b)

**Figure 4-4 (a) Burner; (b) drawing of gas burner assembly, units in cm. All dimensions have a standard uncertainty of  $\pm 0.5$  cm.**

## 4.2.2 Calorimeter

The large-scale oxygen consumption fire calorimeter (Bryant et al. 2003) in the National Fire Research Laboratory allows one to measure the energy given off by a fire (heat release rate) with relatively high accuracy and a well-characterized uncertainty. In the largest test bay, the calorimeter consists of a 15.2 m by 13.7 m canopy-style smoke collection hood (see Figure 4-5), a 2.42 m diameter exhaust duct instrumented for mass flow measurements and a gas sampling system for measuring exhaust gas composition. The smoke collection hood is located 12.5 m above the test floor and is equipped with 6 m retractable side curtains.

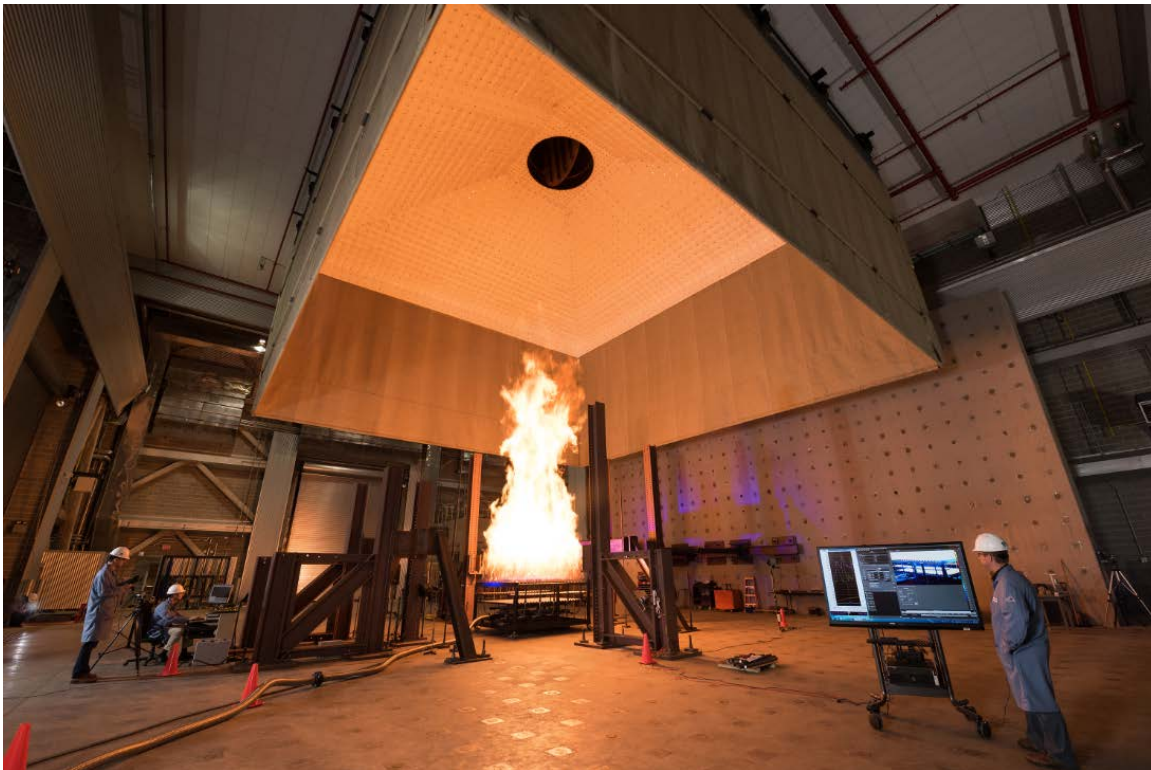


Figure 4-5 Photograph of the testing area showing the strong floor, strong wall, and exhaust hood.

## 4.2.3 Thermocouples

Temperatures were measured using K-type thermocouples for which the lead wires were shielded with fiberglass, ceramic fiber, Inconel, or stainless steel.

Glass-sheathed thermocouples (Omega model GG-K-24-SLE) were mounted near the surfaces of the W18x35 beams (Figure 4-6a) using peening and then covered with ceramic adhesive (Choe et al.



2018) and were embedded into the concrete slab (Figure 4-6b). Since the bead of each thermocouple was embedded in a base material, the effects of radiation on the bead was negligible. Ceramic fiber insulated thermocouples (Omega model XC-K-24) were mounted to the exposed steel decking. Thermocouple beads were insulated with high temperature cement (Omega model CC HIGH TEMP).

Inconel sheathed thermocouples (Omega model INC-K-MO-3.0MM) were used to measure the steel beam temperatures as shown in Figure 4-6c.

Super OMEGACLAD sheathed thermocouples (Omega model TJ36-CAXL-14U-24; TJ36-CAXL-38U-36) were used to measure the upper layer gas temperatures i) 25 mm and 230 mm below the slab and ii) 810 mm below the slab, mounted on the enclosing walls of the fire compartment (Figure 4-6d).

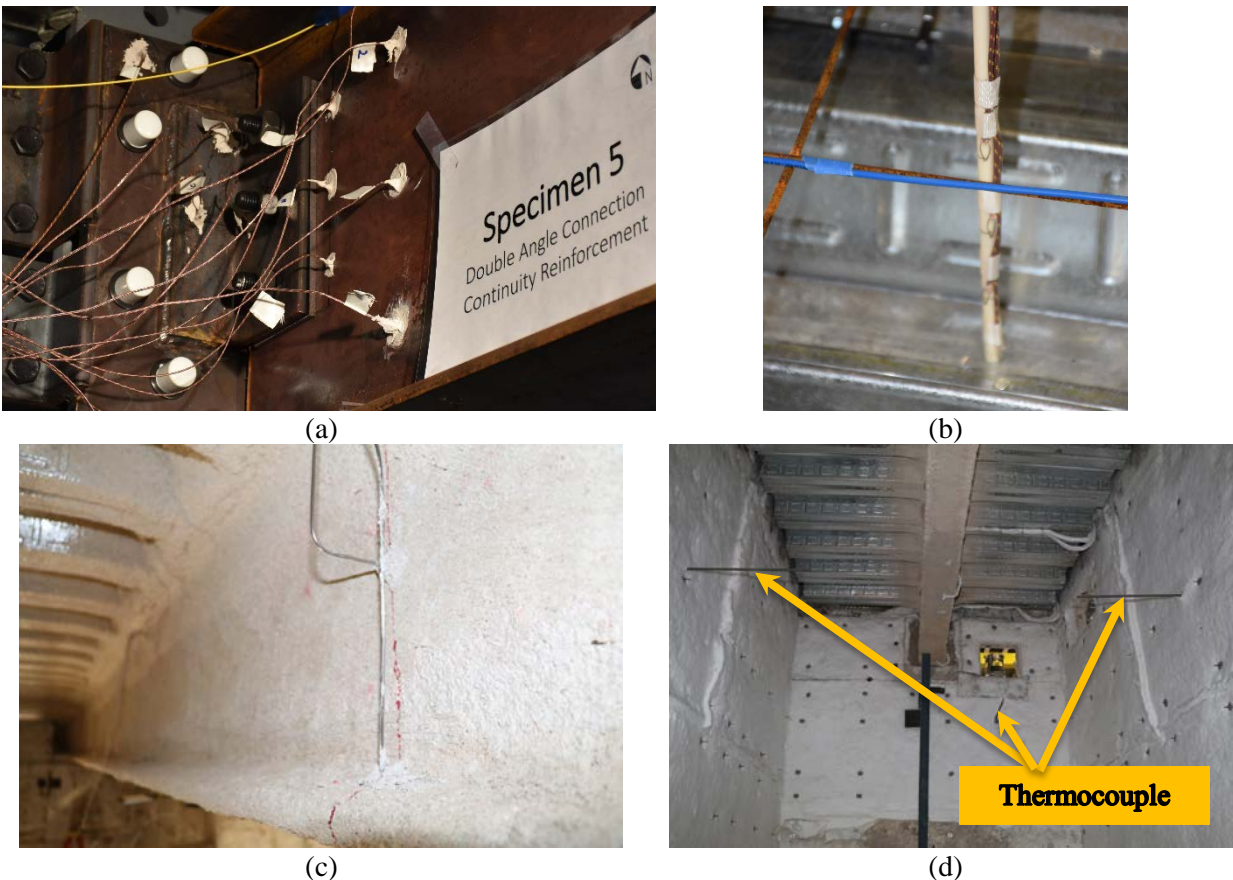


**Figure 4-6 Thermocouples: (a) peened into drilled holes and covered with ceramic adhesive (prior to application of SFRM); (b) bare bead thermocouples attached to ceramic rod in slab prior to concrete casting; (c) Inconel sheathed thermocouples used to measure the temperature of the steel beam; (d) super OMEGACLAD sheathed thermocouples used to measure the temperature of the compartment.**

#### 4.2.4 Heat Flux Gauges

A Gardon gauge (Medtherm model 64-20-18) was placed on the east wall 410 mm below the bottom flange of the specimen (Figure 4-7). The diameter of this gauge was 25.4 mm. It was placed in a steel pipe (inside diameter = 25.4 mm) and water-cooled during the fire tests.



Figure 4-7 Gardon gauge mounted on the east wall.

#### 4.2.5 Plate Thermometers

Plate thermometers (PT) were placed around midspan of the specimen and the east connection (Figure 4-8) and were used to measure adiabatic surface temperature. They consisted of a glass-sheathed, K-type, 24-gauge, thermocouple (Omega model GG-K-24) welded to an Inconel plate with dimensions of 100 mm × 100 mm × 0.7 mm with insulating material on the back. Reference gas temperature was measured using a thermocouple (Omega model XC-K-24) next to the plate thermometer.



**Figure 4-8 Location of plate thermometers: (a) east connection; (b) mid-span of the beam.**

### 4.3 DATA ACQUISITION SYSTEM

Measurements were acquired using a National Instruments cDAQ-9188 data acquisition (DAQ) chassis (shown in Figure 4-9) populated with the following I/O-Modules: NI-9213 (temperature) NI-9237 (voltage from bridge circuitry of strain gauges and load cells), and NI-9205 (voltage from resistive-based sensors including potentiometers). For the ambient test, strains were acquired using NI PXIe-1082 data acquisition chassis populated with the NI PXIe-4330 modules.

An in-house software developed in LabVIEW™ was used to allocate channels and control data acquisition. During the tests, data were recorded at 1 Hz along with the standard deviations from the averaging process.

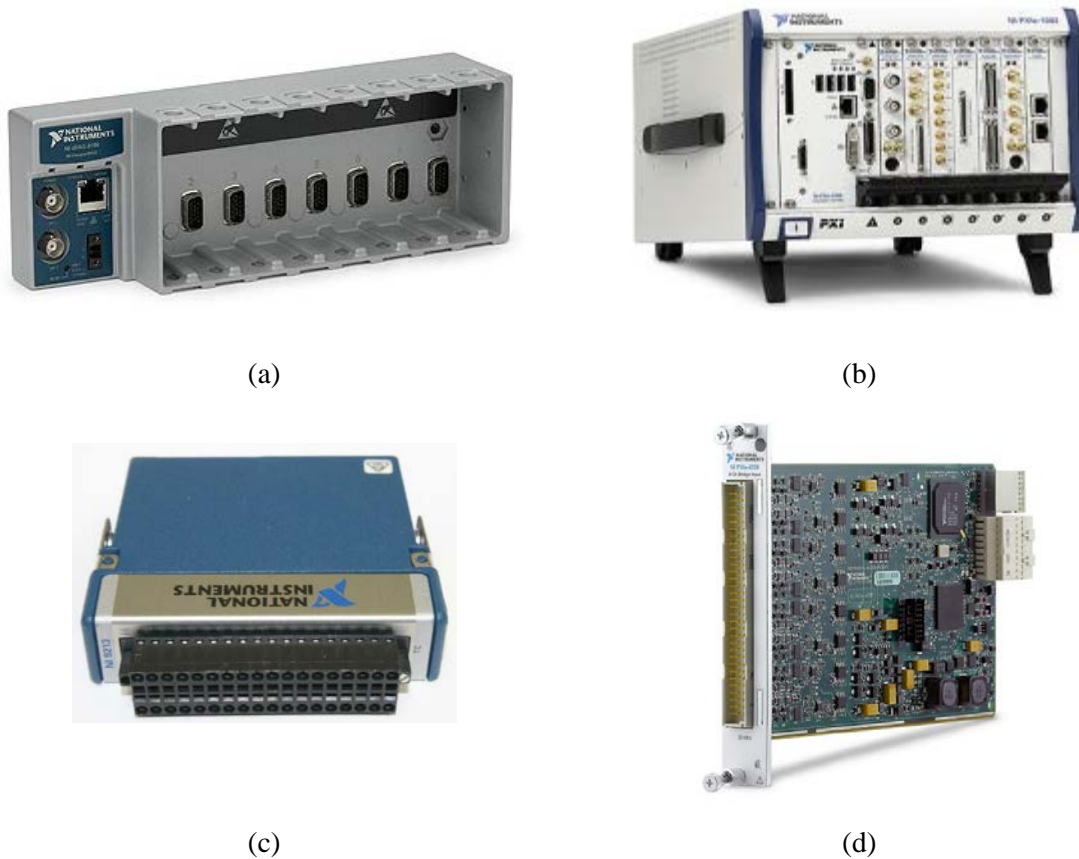


**Figure 4-9 Data Acquisition hardware: (a) cDAQ-9188; (b) NI PXIe-1082; (c) NI-9213; (d) NI PXIe-4330.**

## 4.4 FIBER OPTIC MEASUREMENTS

Optical fibers were used to measure strain in the concrete with both distributed (ambient only) and grating-based (ambient and elevated temperature) sensors. Temperature in the concrete as well as temperature on the surface of the steel beam was measured during the fire experiments using two distributed fiber optic sensing modalities: pulse pre-pumped Brillouin optical time domain analysis (PPP-BOTDA) and optical frequency domain reflectometry (OFDR).

### 4.4.1 Distributed Fiber Optic Sensors

Telecommunication-grade, single-mode optical fiber cable with a polymer sheath and aramid yarn was used as a distributed temperature sensor. Figure 4-10 shows the structure of the optical fiber cable for temperature measurement (Bao et al., 2017). The optical fiber has a tight polymer buffer (diameter: 900  $\mu\text{m}$ ), a polymer outer coating (outer diameter: 242  $\mu\text{m}$ ), a polymer inner coating (outer diameter: 190  $\mu\text{m}$ ), a silica (glass) cladding (outer diameter: 125  $\mu\text{m}$ ), and a silica (glass)

core (diameter: 8.2  $\mu\text{m}$ ). The polymer buffer and coatings protected the glass from mechanical impact and abrasion as well as from undesired environmental exposure. The same optical fiber without the sheath and aramid yarn was used as a distributed strain sensor. The buffer and coatings burn off at approximately 300  $^{\circ}\text{C}$ ; however, the glass core and cladding can sustain temperatures above 1000  $^{\circ}\text{C}$ .

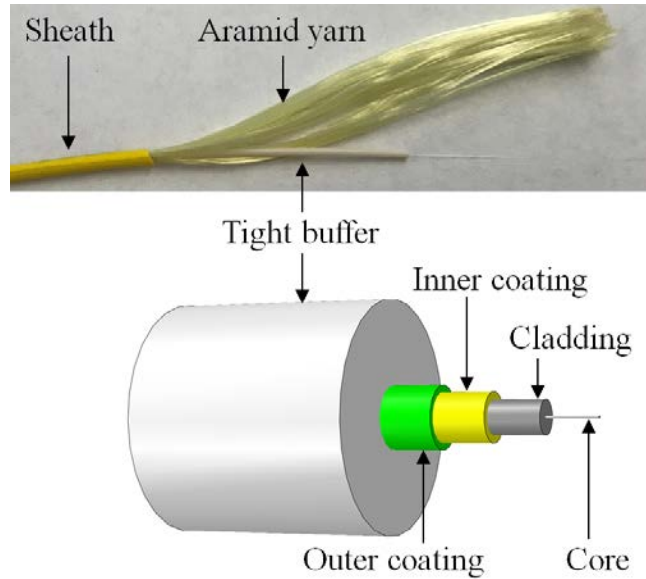


**Figure 4-10 Schematic view of an optical fiber cable.**

For the temperature sensor, the optical fiber (tight buffer) could move longitudinally in the sheath with negligible friction. Therefore, the distributed temperature sensor theoretically measures Brillouin frequency shifts due to temperature changes only. Once calibrated, the sensor can be used to evaluate temperature changes from the measured Brillouin frequency shifts. For the strain sensor, the optical fiber without the sheath and aramid yarns is bonded with the concrete (Fan et al. 2019), and it can measure Brillouin frequency shifts due to the combined temperature and strain effects before the tight buffer and coatings start softening at approximately 60  $^{\circ}\text{C}$ . To differentiate the contribution of temperature and strain, a distributed temperature sensor, deployed close to the strain sensor, is used for temperature compensation (Fan et al. 2018).

### **Sensing modalities**

The distributed fiber optic sensors provided high spatial resolution; however, measurements were only made at select time intervals during each test.



(i) **Pulse pre-pumped Brillouin optical time domain analysis (PPP-BOTDA)**

Pulse pre-pumped Brillouin optical time domain analysis (PPP-BOTDA) measurements were made using a Neubrescope Model NBX7020. PPP-BOTDA measures stimulated Brillouin backscattering light at any point along the length of an optical fiber using a pulsed pump wave and a counter-propagating continuous probe wave. When the frequency difference between the pump and probe waves matches the Brillouin frequency, the probe wave is amplified, and the frequency difference is referred to as the Brillouin frequency. The Brillouin frequency depends on the optical properties of the fiber, which change with the strain and temperature applied on the optical fiber. For a relatively small change of strain  $\Delta\varepsilon$  and temperature  $\Delta T$  with respect to their calibration values, the Brillouin frequency shift  $\Delta\nu_B$  can be linearly related to the strain and temperature changes (Bao et al. 2016):

$$\Delta\nu_B = C_\varepsilon\Delta\varepsilon + C_T \Delta T = C_\varepsilon\Delta\varepsilon + (C_T + C_\varepsilon\alpha)\Delta T \quad (4.1)$$

where  $C_\varepsilon$ ,  $C_T$ , and  $\alpha$  denote the strain coefficient, temperature coefficient, and the coefficient of thermal expansion of surrounding material, respectively.

A 2 cm spatial resolution was obtained using a pulse bandwidth of 0.2 ns (Kishida et al. 2014). The sampling and spatial resolutions in this study were 1 cm and 2 cm, respectively. In other words, data points were sampled at every 1 cm and the Brillouin frequency shifts of two points spaced at no less than 2 cm could be distinguished.

(ii) **Optical frequency domain reflectometry (OFDR)**

Optical frequency domain reflectometry (OFDR) measurements were also taken using a Luna OBR 4600 - a type of optical backscatter reflectometry. This technique uses swept wavelength homodyne interferometry to measure the Rayleigh backscatter throughout the length of a single mode fiber. The Rayleigh backscatter is a property of the optical fiber and is caused by radius and density fluctuations and thus index profiles throughout the length of the fiber (Soller et al. 2005); Kreger et al. (2007). Strain and temperature measurements can be obtained based upon spectral shifts in the Rayleigh spectrum in reference to a baseline. The spectral shift,  $\Delta\nu_R$ , is related linearly to temperature and strain by calibration coefficients  $K_\varepsilon$  and  $K_T$  (Froggatt and Moore 1998; Kishida et al. 2014):

$$\Delta\nu_R = K_\varepsilon\Delta\varepsilon + K_T\Delta T \quad (4.2)$$

## Sensor calibration

The sensitivity of Brillouin frequency to temperature and strain was experimentally calibrated (Bao and Chen 2016). The optical fiber was passed through an electric tube furnace where the temperature was monitored using a calibrated type-K thermocouple. The furnace temperature was linearly increased from 22 °C to 300 °C in 100 °C intervals. A translation stage was used to apply elongation in the optical fiber. Spatially-distributed Brillouin gain spectra were measured along the length of the optical fiber using the Neubrescope. Within a range of 22 °C to 300 °C, the effect of temperature on the temperature and strain calibration coefficients is negligible (Bao and Chen 2016). Therefore, the temperature and strain calibration coefficients in this study were determined under zero strain at a reference room temperature.

The strain sensors were calibrated using an Instron 5965 with a 100 N load cell at room temperature. A fiber optic cable of length L was selected, and probes were spliced onto each end for strain measurement. Protective sleeves were bonded to the splice point to strengthen the fiber at this location, and the fiber was clamped onto the load frame for a tension test. An initial load was placed onto the fiber to remove any slack and the fiber length was measured. The displacement was controlled by the load frame and the fiber was loaded at intervals of 0.5 N. Measurements were taken using a Neubrescope 7020 and a Luna 4600 and the load and displacement were noted. The strain was determined by dividing the change in length by the original fiber length and was correlated with the signal obtained from each measurement device.

Linear regression was used to identify the strain and temperature coefficients for each fiber as summarized in Table 4-2. Values reported as N.A. were not used. It can be seen from Table 4-2 that the difference in calibration coefficients of various fibers is within 6 %. Therefore, a strain coefficient of 53 GHz/ $\epsilon$  and a temperature coefficient of 0.001 GHz/°C are used.

**Table 4-2 Summary of strain coefficients used for flexural testing.**

Optical Fiber	Strain Coefficient (GHz/ $\epsilon$ )		Temperature Coefficient (GHz/°C)		Sensor Application
	Neubrescope	Luna	Neubrescope	Luna	
Pink	$50 \pm 2.5$	$-160000 \pm 1480$	$(9.49 \pm 0.442) \times 10^{-4}$	$-1.58 \pm 5.02 \times 10^{-2}$	Temperature
Blue	$53 \pm 0.79$	$-161000 \pm 38.1$	$(10.1 \pm 0.389) \times 10^{-4}$	$-1.50 \pm 1.67 \times 10^{-3}$	Temperature
Thin Yellow	$50 \pm 1.2$	$-157000 \pm 3960$	N.A.	$-1.53 \pm 9.55 \times 10^{-3}$	Strain
Thick Yellow	N.A.	$-140000 \pm 2050$	N.A.	$-1.46 \pm 2.37 \times 10^{-2}$	Temperature

## Sensor installation

The distributed fiber optic sensors were embedded in the concrete slab and attached on the surface of the steel girder along the length. Figure 4-11 shows the top view of the distributed fiber optic sensors in the concrete slab. The distributed fiber optic sensors were deployed along the longitudinal direction (beam length) and the transverse direction (beam width). The longitudinal and transverse distributed fiber optic sensors are designated as L-DFOS and T-DFOS, respectively. As depicted in Figure 4-11a, the L-DFOS sensors are along the centerline of the concrete slab. In each specimen, two T-DFOS sensors, designated T-DFOS-1 and T-DFOS-2, were deployed with a spacing of 152 mm in the longitudinal direction. Figure 4-11b differs from Figure 4-11a in that the length and position of the Fiber Bragg Grating (FBG) sensor were slightly different. Photographs of the installed DFOS prior to concrete casting are shown in Figure 4-12.

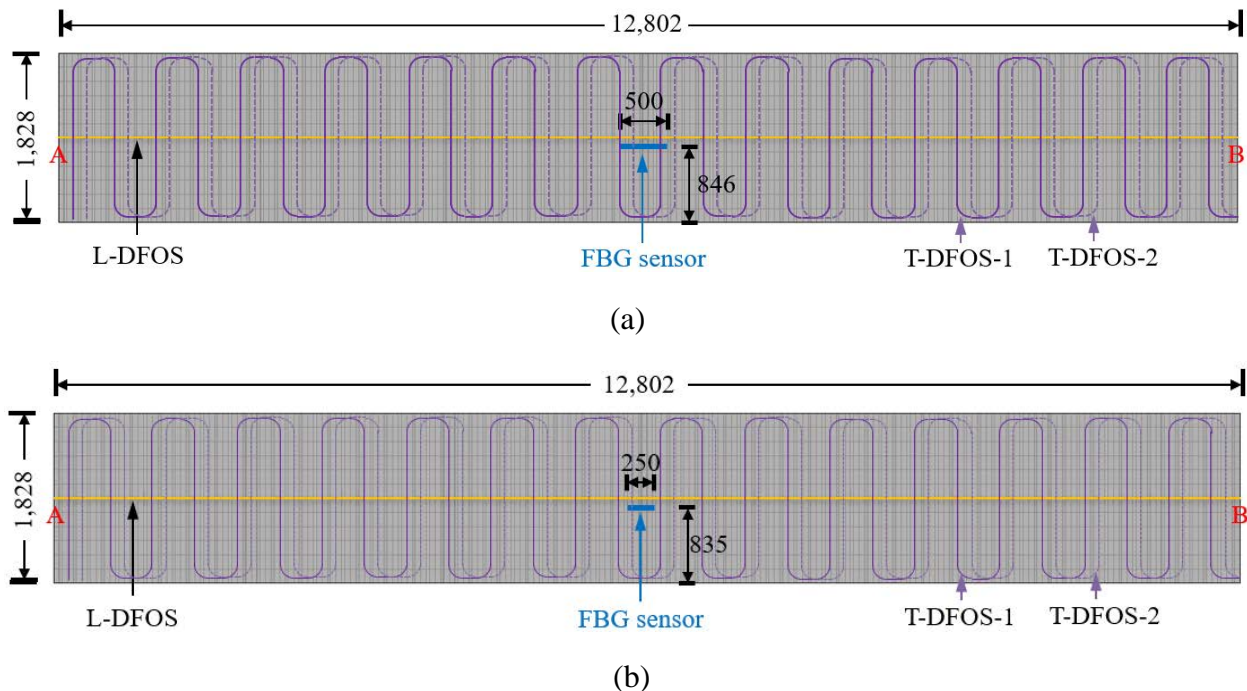


**Figure 4-11 Top view of the locations of distributed fiber optic sensors (DFOS) and Fiber Bragg Grating (FBG) sensors in the concrete slab. The length and locations of the FBG sensors in (a) CB-DA-AMB are different from those in (b) CB-DA and CB-DA-SC (units in mm).**

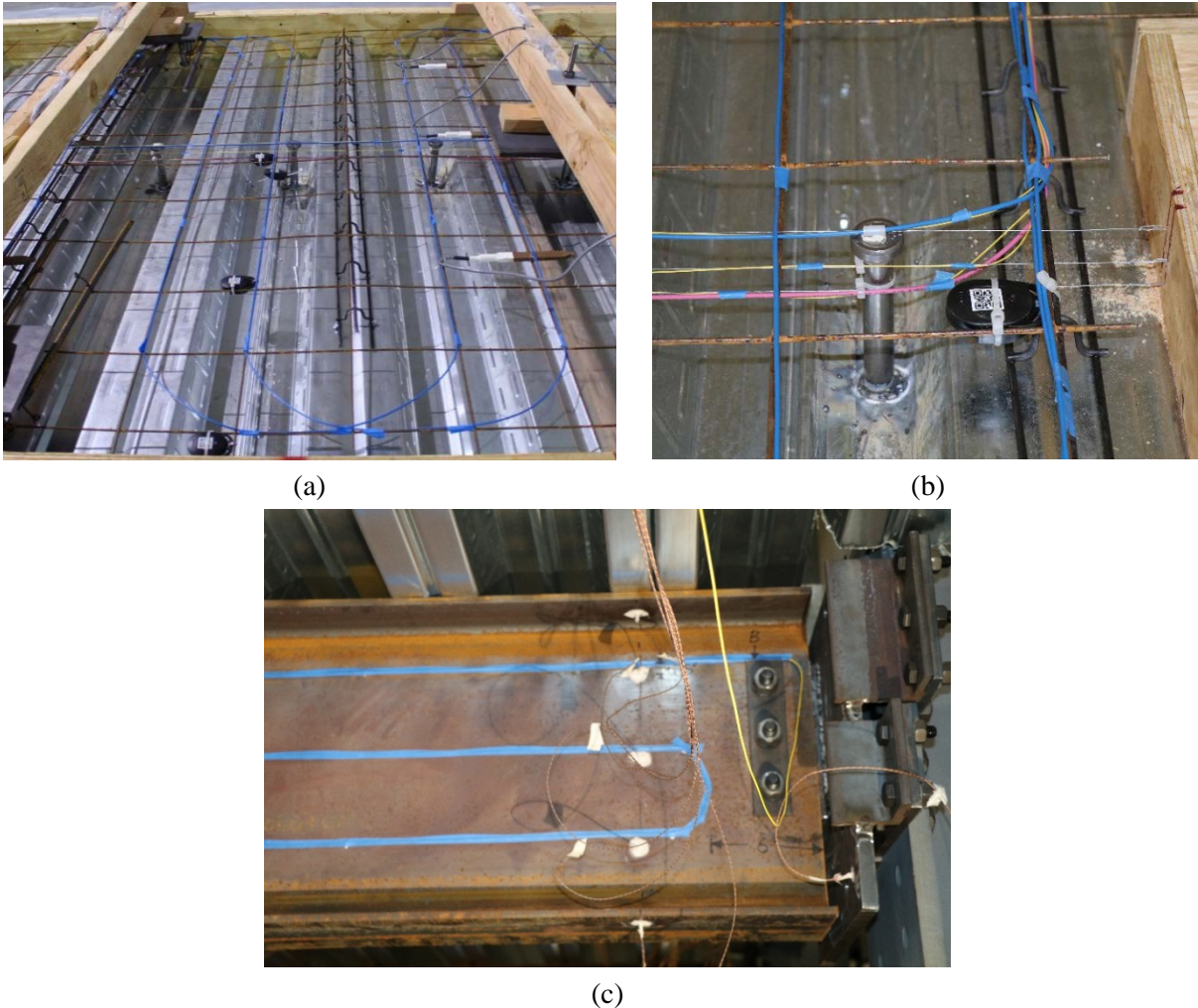


**Figure 4-12 Photographs of installed distributed fiber optic sensors: (a) transverse (T-DFOS) temperature sensors (blue), (b) longitudinal (L-DFOS) temperature (blue and pink) and strain (yellow, thin), and (c) temperature sensor on web of steel beam (blue tape over thick yellow optical fiber).**

Figure 4-13 shows the elevation of the fiber optic sensors in the concrete slab. There are five paths of L-DFOS, which are designated L-DFOS-1 to L-DFOS-5. The L-DFOS-1 and L-DFOS-5 measured the temperature distributions, and the other three paths of distributed fiber optic sensors (L-DFOS-2, L-DFOS-3, and L-DFOS-4) measured the combined effect of temperature and strain. The L-DFOS-1 and L-DFOS-2 were co-located, L-DFOS-4 and L-DFOS-5 were co-located, and L-DFOS-3 was deployed at approximately the center between L-DFOS-1 and L-DFOS-5. The temperature measurement from L-DFOS-1 and L-DFOS-5 were respectively used for temperature compensation of the measurement results from L-DFOS-2 and L-DFOS-4. The average results from L-DFOS-1 and L-DFOS-5 were used for temperature compensation of the measurement results from L-DFOS-3. The longitudinal distributed fiber optic sensor was continuously passed back and forth to form a loop.

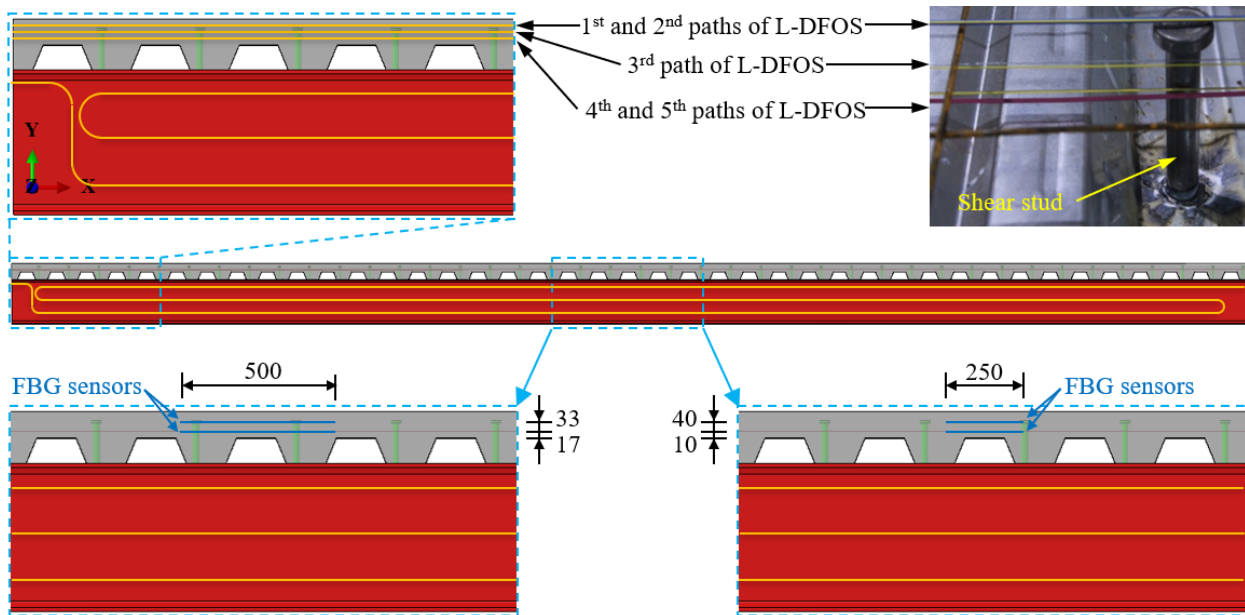


**Figure 4-13** Side view of the locations of distributed fiber optic sensors (DFOS) and Fiber Bragg Grating (FBG) sensors in the concrete slab. The length and locations of the FBG sensors in CB-DA-AMB (left) are different from those in CB-DA and CB-DA-SC (right) (units in mm).

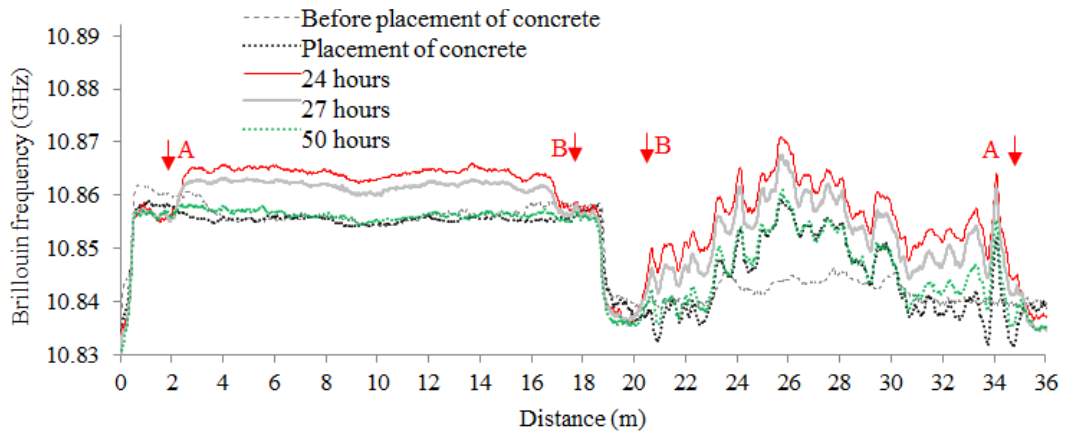
### Early age behavior (DFOS measurements)

Figure 4-14a plots the absolute Brillouin frequency distributions along the 1<sup>st</sup> path (temperature from point A to B in Figure 4-11) and 2<sup>nd</sup> path (temperature plus strain from B to A in Figure 4-11) of the longitudinal distributed sensors in specimen CB-DA before and after concrete placement. Taking the Brillouin frequency at the time of concrete placement as the reference, the Brillouin frequency shifts along these paths after 24 h, 27 h and 50 h are shown in Figure 4-14b.

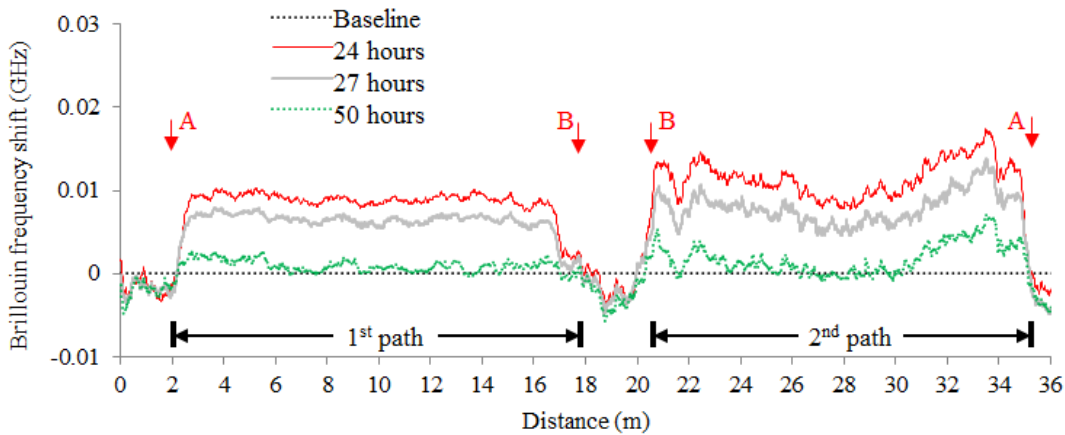
Using the calibrated temperature sensitivity coefficients in Table 4-2, the Brillouin frequency distributions are converted into temperature distributions along the centerline of the specimen for L-DFOS-1 (Top) in Figure 4-15; temperature only sensor. The temperature distributions are nearly uniform along the length of the specimen. The measured temperature increase, due to exothermic hydration reactions in the concrete, was largest at 24 h and then decreased. It is noted that peak temperature occurred about 10 h after casting, however, no DFOS measurements were taken at that time.

After temperature compensation using the Brillouin frequency shift of the L-DFOS-1 (the temperature distribution in L-DFOS-5 was faulty, so it was assumed that the temperature through the depth was the same as L-DFOS-1), the strain distributions along L-DFOS-2 (Top) to L DFOS 2 (Bottom) were determined and are shown in Figure 4-16. The strain distributions along the

specimen follow similar shifts in amplitude to the temperature in the concrete over time, however, the influence of the bending of the specimen can be seen in the curvature of the traces. The amplitude varied through the depth of the slab likely because of the varying distance of the sensors from the bending neutral axis in the specimen, however, other mechanisms related to differential shrinkage may have contributed to the observed behavior.



(a)



(b)

**Figure 4-14 Distributed fiber optic sensor (DFOS) measurements in L-DFOS-1 and L-DFOS-2 along the centerline of specimen CB-DA during the first 50 h after casting: (a) absolute Brillouin frequency distributions, (b) relative Brillouin frequency shifts.**



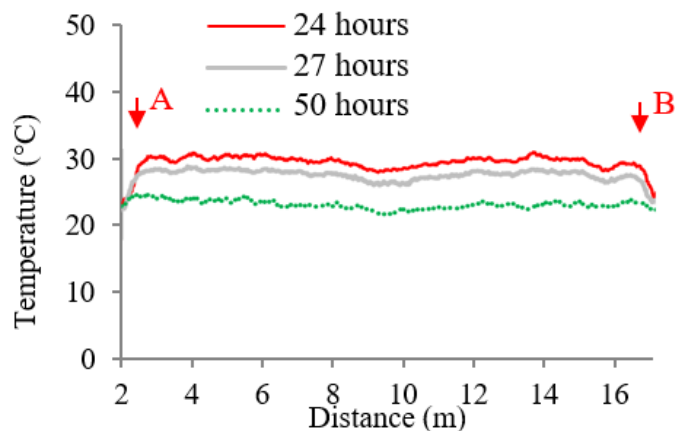


**Figure 4-15** Distributed fiber optic sensor (DFOS) measurements of temperature distribution in L DFOS 1 of specimen CB-DA during the first 50 h after casting.

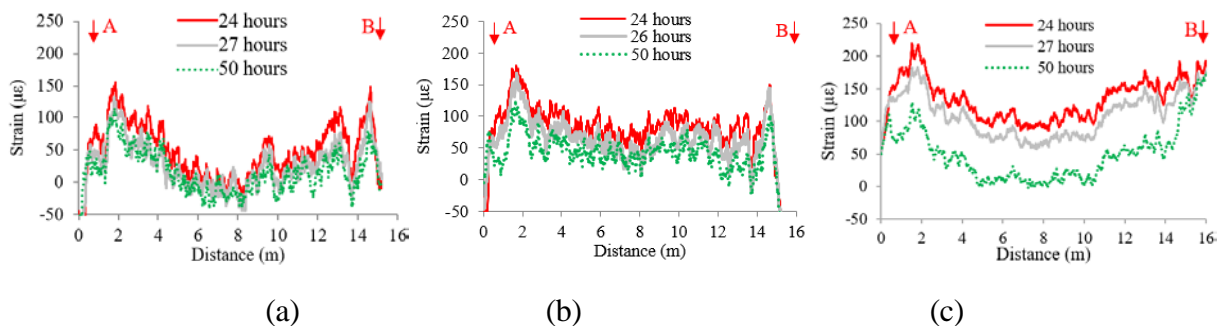


**Figure 4-16** Distributed fiber optic sensor (DFOS) measurements of strain distribution along the centerline of specimen CB-DA during the first 50 h after casting: (a) L DFOS 3 (Top), (b) L-DFOS-3 (Middle), and (c) L-DFOS-4 (Bottom).

#### 4.4.2 Fiber Bragg Grating Sensors

Fiber Bragg Grating (FBG) strain sensors were embedded in the concrete deck in specimens CB-DA-AMB, CB-DA, and CB-DA-SC. These sensors measure an average change in strain over their gauge length and require temperature compensation from other sensors (thermocouples) in the slab. The FBG sensors have a measurement standard uncertainty of  $\pm 3.1 \mu\epsilon$ ; a result of the uncertainty in the fiber optic system reading the reflected wavelengths from the FBG's and from the uncertainty in the thermocouples used for the thermal compensation. Two different forms of FBG sensors were employed: for the ambient temperature slab (CB-DA-AMB), the FBGs had a gauge length of 50 cm and the FBG was encased in a polyethylene tube. The FBGs in specimens CB-DA and CB-DA-SC, which were subjected to fire testing, had a gauge length of 25 cm and were encased in a polytetrafluoroethylene tube for protection at temperatures up to 300 °C. Both fibers were coated in polyimide to improve durability. Steel cylinders mechanically attached to the

optical fiber marked the ends of the measurement region (gauge length) and transferred strain from the concrete to the sensor. Two sensors were installed in parallel in the concrete near the midspan of the beam to measure both axial strain and bending in the deck. The FBG sensors were installed near ceramic-encased resistive strain gauges (CB-DA-AMB only) and distributed fiber optic sensors to facilitate comparison of the strain measurements. The locations of the sensors are shown in Figure 4-11 and Figure 4-13. Figure 4-17 shows the installed sensors in specimen CB-DA-AMB, with the red arrows indicating the two FBG sensors before the concrete pour. Figure 4-18 and Figure 4-19 show close-ups of specimens CB-DA and CB-DA-SC, with one of the thermocouples used for temperature compensation of the FBG visible in Figure 4-19. A Smartec MuST Dynamic Reading Unit and Micron Optics Enlight software were used to read and record measurements. Measurements were taken at a rate of one measurement per minute for the initial curing, and ten measurements per second for the load testing.



**Figure 4-17 Fiber Bragg Grating sensors in CB-DA-AMB indicated by red arrows.**



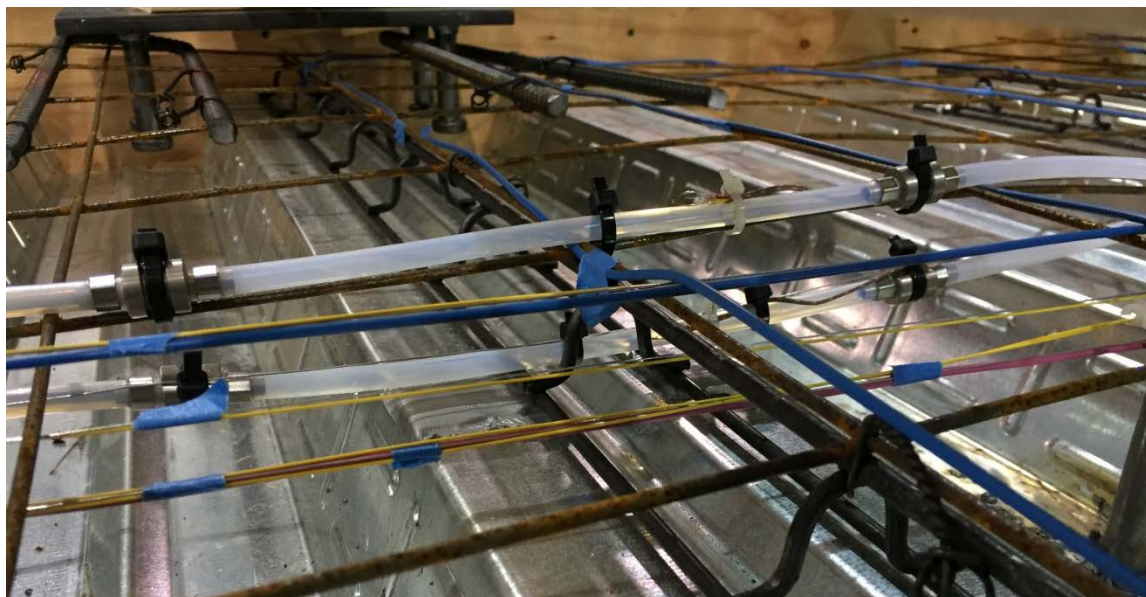


**Figure 4-18 Fiber Bragg Grating sensors in CB-DA.**



**Figure 4-19 Fiber Bragg Grating sensors in CB-DA-SC with thermocouple indicated by red arrow.**

### **Early age behavior (FBG measurements)**

After the pouring of the concrete on December 6, 2016 all six FBG sensors recorded strain continuously for the initial week of concrete curing. Figure 4-20 shows the strain measured by the FBGs at the two sensor locations in the concrete slab (Top and Bottom) in specimens CB-DA-AMB, CB-DA, and CB-DA-SC over the first week of concrete curing. After an initial increase in strain due to early thermal activity in the material, the concrete experienced a drop-in strain over the 7 days as shrinkage of the concrete occurred. In the first week after casting, several events caused jumps in the strain that are believed to be temperature related. The first occurred on

12/8 and the next two events on 12/9 and 12/12. On these dates the high bay doors were open in the lab causing a reduction in temperature in the concrete as seen in Figure 4-21. This temperature change is responsible for the drops in strain in Figure 4-20.

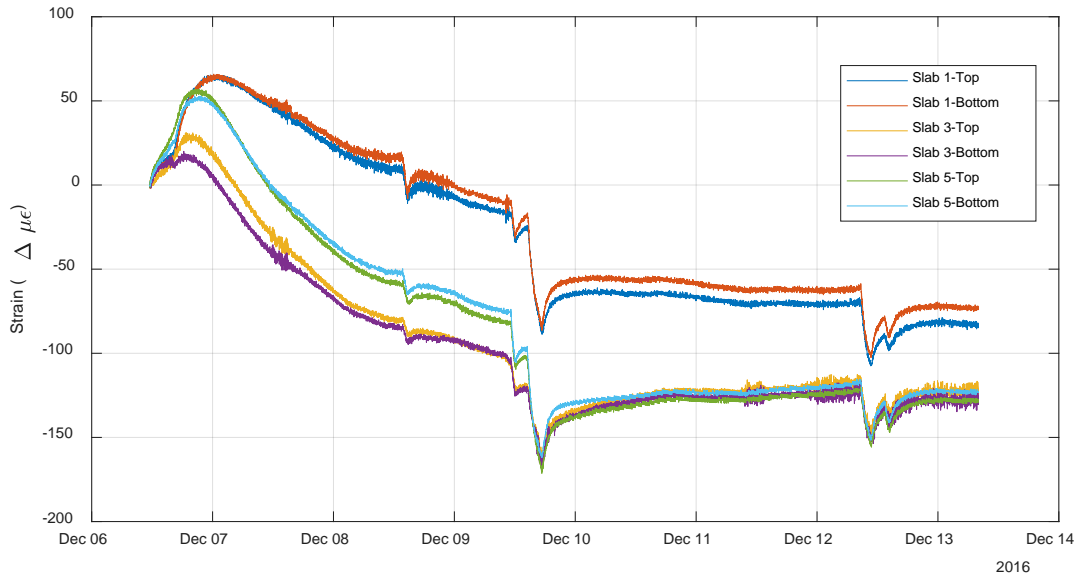


**Figure 4-20 Fiber Bragg Grating strain during first week of concrete curing.**

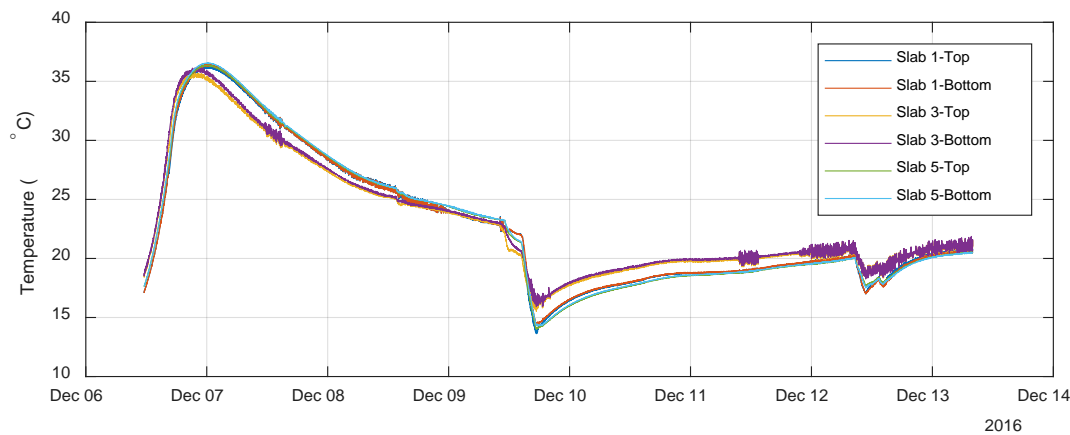


**Figure 4-21 Fiber Bragg Grating thermocouple temperature during first week of concrete curing.**

Figure 4-22 shows the continuing development of the concrete through six months. CB-DA-AMB was in the testing hall and subject to ambient temperature and humidity, while the other slabs were in a temperature and humidity-controlled environment (see Section 2.3.2). FBG measurements were taken for one hour at each interval of monitoring to capture long-term strain development in

the material. The shrinkage appears to stabilize after six months for CB-DA-AMB, although CB-DA and CB-DA-SC still have some strain left to experience.

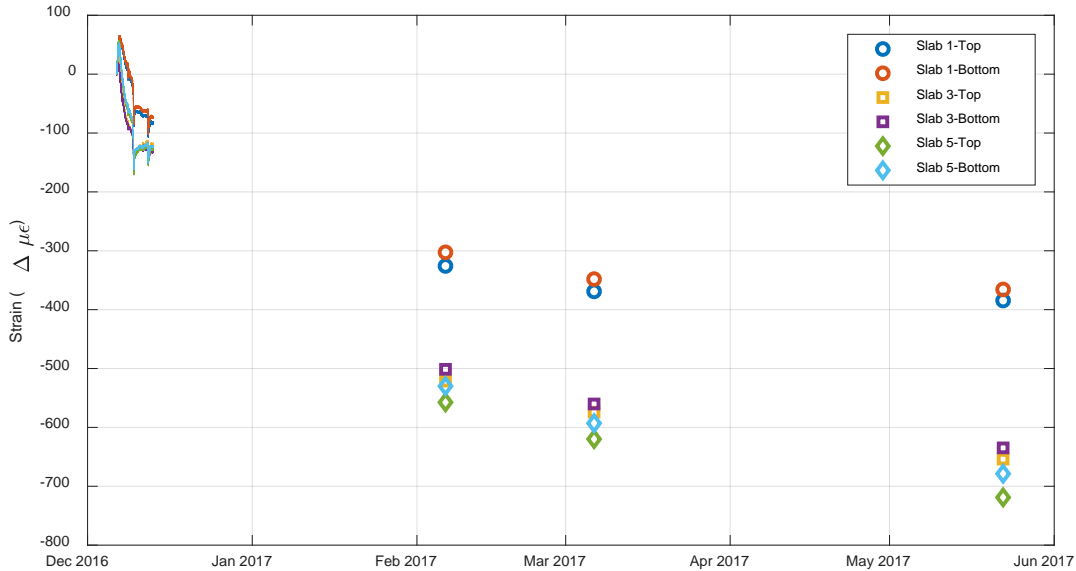


**Figure 4-22 Fiber Bragg Grating strain development over first six months after casting (CB-DA-AMB = Slab 1; CB-DA = Slab 3; CB-DA-SC = Slab 5).**

#### 4.5 MEASUREMENT UNCERTAINTY

Table 4-3 summarizes the estimated uncertainties of the measurements including force, temperature, displacement, rotation, strain, heat flux, and heat release rates. The component standard uncertainties, combined standard uncertainty, and total expanded uncertainty were estimated for each measurand. The component standard uncertainty was evaluated either as Type-A or Type-B uncertainties. As defined by Taylor and Kuyatt (1994), Type-A uncertainty was evaluated using statistical analysis of the measurements. Type-B uncertainty was estimated using scientific judgment based on past experience, manufacturer’s specifications, and previous data. The combined standard uncertainty was calculated as the square root of the summations of the squares of each component standard uncertainty, referred to as root-sum-of-squares method. The expanded uncertainty was computed by multiplying the combined uncertainty by a coverage factor of 2 corresponding to an interval with approximately a level of confidence of 95 %.

The uncertainty components included resolution, bias, installation, repeatability and random errors. The resolution is the ability of the measurement instrument to exhibit changes in the data. Bias resulted from calibration of the sensor and other known repeatable errors. The uncertainties

due to resolution and bias were derived from instrument specifications (Type-B). Uncertainty due to installation method was estimated based on engineering judgment (Type-B). Random error, which resulted from random, unpredictable variations in the measurement process and environment was estimated as Type-A using the standard deviations of the residuals from the mean value of the measurements under a steady-state period. It was estimated as Type-B in the absence of data for statistical analysis.

The resistive-based sensors used in this experimental program, such as load cells, strain gauges, position transducers, and inclinometers have a linear calibration factor at close to ambient temperatures. The load cells and position transducers were protected against excessive radiant heat from the fire or placed in the cool zone where the temperature was less than 35 °C during the test. Thermocouples were attached to the inclinometers placed on unexposed surfaces of specimens and loading frames (e.g., top of the slab near support columns and loading trusses) to monitor whether the temperature exceeded the specified operating temperature. Some inclinometers were exposed to a temperature higher than 85 °C, the maximum operating temperature, when the concrete fractured as hot gas or flame leaked through concrete cracks during the fire test. This point was marked on the data plots. The estimated total expanded uncertainty of the rotation measured by the inclinometer increased to  $\pm 29\%$  at temperatures up to 85 °C from  $\pm 9\%$  at 25 °C.

The uncertainty due to installation of the resistive-based sensors was estimated considering misalignment and quality of the mounting method of the sensors (refer to Section 4.1 for the details of the mounting methods). Friction between the steel surfaces of the loading system was considered in the estimation of the installation error of the actuator load measurement. A maximum misalignment of about 5 degrees was considered conservatively for load cells of reinforcing bars, strain gauges, inclinometers, and displacement transducers with stroke length less than 50 mm. The vertical displacement of the specimen was measured at four different points along the length of the specimen using position transducers mounted 1.83 m above the concrete slab. When the specimen deflected during the tests, the strings attached to the specimen tilted from the original position normal to the undeformed concrete slab. The error due to this installation method was estimated conservatively using a maximum tilt angle of 6 degrees.

The combined standard uncertainty of the resistive-based sensors includes a component related to the random effects. For example, the two actuators connected to each loading beam (Figure 3-1) were programmed to apply a constant total load of 36 kN during the fire test. A maximum variation in a total load using these actuators was  $\pm 3\%$  over the test period, which resulted in a total expanded uncertainty of  $\pm 8\%$ . The uncertainties due to random effects of the remaining resistive-based sensors were estimated from the standard deviation of the measurements taken when a

steady-state of load was simulated by applying a constant load (about 45 kN per actuator at which the specimen remained elastic) for a period of about 10.5 min during Test 1 (CB-DA-AMB).

Glass-insulated thermocouples and Inconel-sheathed thermocouples were used to measure temperatures of the steel components. The glass-insulated thermocouples were attached to the steel beam by peening and to the connections by welding. In the peening method, the thermocouple with pre-made junction was placed into a small blind hole drilled in the steel and then the edges of the hole were peened by use of a punch. Incompletely closed holes would partially expose the thermocouple to either hotter or cooler surrounding air temperature. In the welding method, the thermocouples, without pre-made junction, were welded to the steel surface followed by protection of the welded junctions of the thermocouples using a high temperature cement. The component standard uncertainty due to peening and welding methods were estimated to be  $\pm 2\%$  (Choe et al. 2018). During the first three fire tests, glass insulation of thermocouple lead wires that were exposed to the flame burned off around 10 min after ignition, making temperature readings unreliable. For the last fire test specimen, thermocouple lead wires were embedded under a layer of sprayed fire resistive material (SFRM) on the steel beam that resulted in reliable steel beam temperatures. For the last three fire test specimens, Inconel-sheathed thermocouples were added to measure the steel beam temperatures. The Inconel-sheathed thermocouples were inserted through the SFRM and rested inside the holes drilled on the webs and flanges of the steel beam. However, when the specimen was subjected to large displacements, the sheathed thermocouples separated from the steel beam, which resulted in higher (gas) temperature measurements. The uncertainties due to that effect are not presented in this report. Details of temperature measurement challenges and comparisons are presented in the companion report (Part 2) discussing the results of the fire tests (Choe et al. 2019).

Thermocouple trees made of glass insulated thermocouples attached to ceramic tubes were used to measure the temperature in the concrete slab of the specimens. The uncertainties due to that installation method were estimated by immersing the thermocouple trees in a water bath with water temperatures measured using thermocouple trees and Inconel sheathed thermocouples (as a reference). The difference between the temperatures measured by those two sensors was used to estimate the uncertainties due to the installation method of the glass insulated thermocouples in concrete. The uncertainties due to random effects of steel, concrete, steel deck, and gas temperature measurements were estimated using the standard deviation of the residuals from a best fit curve of the gas temperature time history obtained during the fire test of the specimens.

The natural gas mass flow rate and the composition of the natural gas was used to calculate the heat release rate at the burner. The total expanded uncertainty of the burner heat release rate was

estimated to be  $\pm 2\%$  (Hoehler et al. 2019). The heat release rate at the 13.7 m by 15.2 m exhaust hood was measured using the principle of oxygen consumption calorimetry (Bryant et al. 2004) to characterize the total burning influenced by any change in fuel, ventilation, and compartmentation during the test. The uncertainties of the calorimeter heat release rate measurement were estimated using a natural gas burner reference fire. The total expanded uncertainty of the calorimeter heat release rate measurement was estimated to be 15% (Hoehler et al. 2019).

**Table 4-3 Uncertainty in the experimental data**

Measurement / Component	Estimation Method of Uncertainty	Component Standard Uncertainty	Combined Standard Uncertainty	Total Expanded Uncertainty(k=2)
Actuator Load				
Resolution	Type B	$\pm 0.1\%$	$\pm 3.8\%$	$\pm 8\%$
Bias	Type B	$\pm 1\%$		
Installation	Type B	$\pm 2\%$		
Random (N=4000)	Type A	$\pm 3\%$		
Load cells at reinforcing bars				
Resolution	Type B	$\pm 0.1\%$	$\pm 5.2\%$	$\pm 11\%$
Bias	Type B	$\pm 0.8\%$		
Installation	Type B	$\pm 5\%$		
Random (estimate)	Type B	$\pm 1\%$		
Displacement (String Potentiometer)				
Resolution	Type B	$\pm 0.1\%$	$\pm 2.1\%$	$\pm 5\%$
Bias (linearity)	Type B	$\pm 0.2\%$		
Bias (repeatability)	Type B	$\pm 0.1\%$		
Installation	Type B	$\pm 2\%$		
Random (N=600)	Type A	$\pm 0.4\%$		
Gap between beam web and column sacrificial plate (BEI linear position sensor)				
Resolution	Type B	$\pm 0.1\%$	$\pm 2.1\%$	$\pm 5\%$
Bias	Type B	$\pm 2\%$		
Installation	Type B	$\pm 1\%$		
Random (N=600)	Type A	$\pm 0.4\%$		
Slip between beam and slab (TR50)				
Resolution	Type B	$\pm 0.1\%$	$\pm 2.3\%$	$\pm 5\%$
Bias (linearity)	Type B	$\pm 0.2\%$		
Bias (repeatability)	Type B	$\pm 0.2\%$		
Installation	Type B	$\pm 1\%$		
Random (N=600)	Type A	$\pm 0.8\%$		
Rotation (Ambient, 25 °C)				
Resolution	Type B	$\pm 0.3\%$	$\pm 4.4\%$	$\pm 9\%$
Bias	Type B	$\pm 3\%$		
Installation	Type B	$\pm 1\%$		
Random (estimate)	Type B	$\pm 3\%$		

Measurement / Component	Estimation Method of Uncertainty	Component Standard Uncertainty	Combined Standard Uncertainty	Total Expanded Uncertainty(k=2)
Rotation (-40 °C to 85 °C)				
Resolution	Type B	± 0.3 %	± 14.3 %	± 29 %
Bias (calibration)	Type B	± 13%		
Temperature drift	Type B	± 5 %		
Installation	Type B	± 1 %		
Random (estimate)	Type A	± 3 %		
Strain (Steel)				
Resolution	Type B	± 0.1 %	± 2.3 %	± 5 %
Calibration	Type B	± 0.5 %		
Installation	Type B	± 1 %		
Random (N=600)	Type A	± 2 %		
Strain (Concrete-embedded)				
Resolution	Type B	± 0.1 %	± 1.2 %	± 3 %
Calibration	Type B	± 0.5 %		
Installation	Type B	± 1 %		
Random (N=600)	Type A	± 0.2 %		
Strain (Concrete-surface)				
Resolution	Type B	± 0.1 %	± 1.5 %	± 3 %
Calibration	Type B	± 0.5 %		
Installation	Type B	± 1 %		
Random (N=600)	Type A	± 0.9 %		
Steel Temperature (glass sheathed TC)				
Resolution	Type B	± 0.1 %	± 2.2 %	± 5 %
Bias	Type B	± 0.4 %		
Installation	Type B	± 2 %		
Random (N=300), 700 °C	Type A	± 0.6 %		
Concrete Temperature (glass sheathed TC)				
Resolution	Type B	± 0.1 %	± 3.1 %	± 7 %
Bias	Type B	± 0.4 %		
Installation	Type B	± 3 %		
Random (N=300), 600 °C	Type A	± 1.2 %		
Steel deck Temperature (Nextel braided TC)				
Resolution	Type B	± 0.1 %	± 2.4 %	± 5 %
Bias	Type B	± 0.4 %		
Installation	Type B	± 2 %		
Random (N=300), 1000 °C	Type A	± 1.3 %		
Gas Temperature (Super OMEGAGLAD TC)				
Resolution	Type B	± 0.1 %	± 1.6 %	± 4 %
Bias	Type B	± 0.4 %		
Installation	Type B	± 1 %		
Random (N=3000), 1000 °C	Type A	± 1.2 %		
Temperature (Plate thermometer)				
Resolution	Type B	± 0.1 %	± 2.2 %	± 5 %
Bias	Type B	± 0.8 %		
Installation	Type B	± 2 %		
Random (estimate)	Type B	± 0.5 %		
Burner Heat Release Rate				
Resolution	Type B	± 0.2 %	± 0.8 %	± 2 %
Bias	Type B	± 0.6 %		
Random	Type B	± 0.5 %		
Calorimeter Heat Release Rate				
Resolution	Type B	± 0.1 %	± 7.4 %	± 15 %
Bias	Type B	± 4.5 %		
Random	Type B	± 5.9 %		
Dimensions, larger than 0.5 m				

Measurement / Component	Estimation Method of Uncertainty	Component Standard Uncertainty	Combined Standard Uncertainty	Total Expanded Uncertainty(k=2)
Resolution	Type B	± 2 mm	± 13 mm	± 27 mm
Bias	Type B	± 2 mm		
Random	Type B	± 13 mm		
Dimensions, smaller than 0.5 m				
Resolution	Type B	± 2 mm	± 4 mm	± 8 mm
Bias	Type B	± 2 mm		
Random	Type B	± 3 mm		

N=Number of samples



## Chapter 5

### TEST 1- STRUCTURAL BEHAVIOR AT AMBIENT TEMPERATURE

---

---

This chapter presents the behavior and capacity of the composite beam specimen tested at ambient temperature (CB-DA-AMB). These results were used as a baseline performance when compared to the beams tested under combined mechanical and fire load, which are presented in a subsequent report, Part 2 (Choe et al. 2019).

#### 5.1 INSTRUMENTATION

Figure 5-1 shows the instrumentation layout for Specimen CB-DA-AMB. Details about the sensors are presented in Chapter 4. Linear displacement transducers were used to measure the global behavior of the specimen, including: the vertical displacement of the concrete slab at the locations of point loads (VD3, VD4, VD5, VD6), the vertical and lateral displacement of the bottom flange of the W18×35 steel beam at midspan (VD1 & LD1), the axial displacement of the steel beam relative to that of the concrete slab (SlipE, SlipW), and the gap-closure distance between the end section of the steel beam and the flange of the steel column (GapE, GapW). Rotation transducers were mounted on the top of the concrete slab (RotSlabW<sub>x</sub>, RotSlabW<sub>y</sub>, RotSlabEx, RotSlabEy) and on the web of the steel beam (RotBeamW, RotBeamE) to measure the end rotation of the specimen. Linear strain gauges were mounted across the beam section at midspan and at 2.3 m away on west and east sides of the midspan to characterize the section behavior of the specimen subjected to varying flexural loads (Figure 5-1c,d). They were also mounted on the surface of the supporting angles at the beam ends to measure the connection behavior (Figure 5-1e).

Specimen CB-DA-AMB was subjected to a uniform floor load simulated by applying six equally-spaced point loads along the centerline of the beam (Figure 3-1). Refer to Section 3.1.1 for details of the mechanical loading setup. The ends of each loading beam spanning the north-south direction were connected to two coupled hydraulic actuators (mounted at the basement) via high-strength tension bars (Figure 3-6). A total of six actuators were used to measure applied forces (LoadNE; LoadSE; LoadNM; LoadSM; LoadNW; LoadSW) and displacements (DispNE; DispSE; DispNM; DispSM; DispNW; DispSW). The actual load transfer to each of six contact points on the top of the concrete slab was estimated using strain gauges and rotation transducers mounted on three loading trusses (Figure 5-1f).

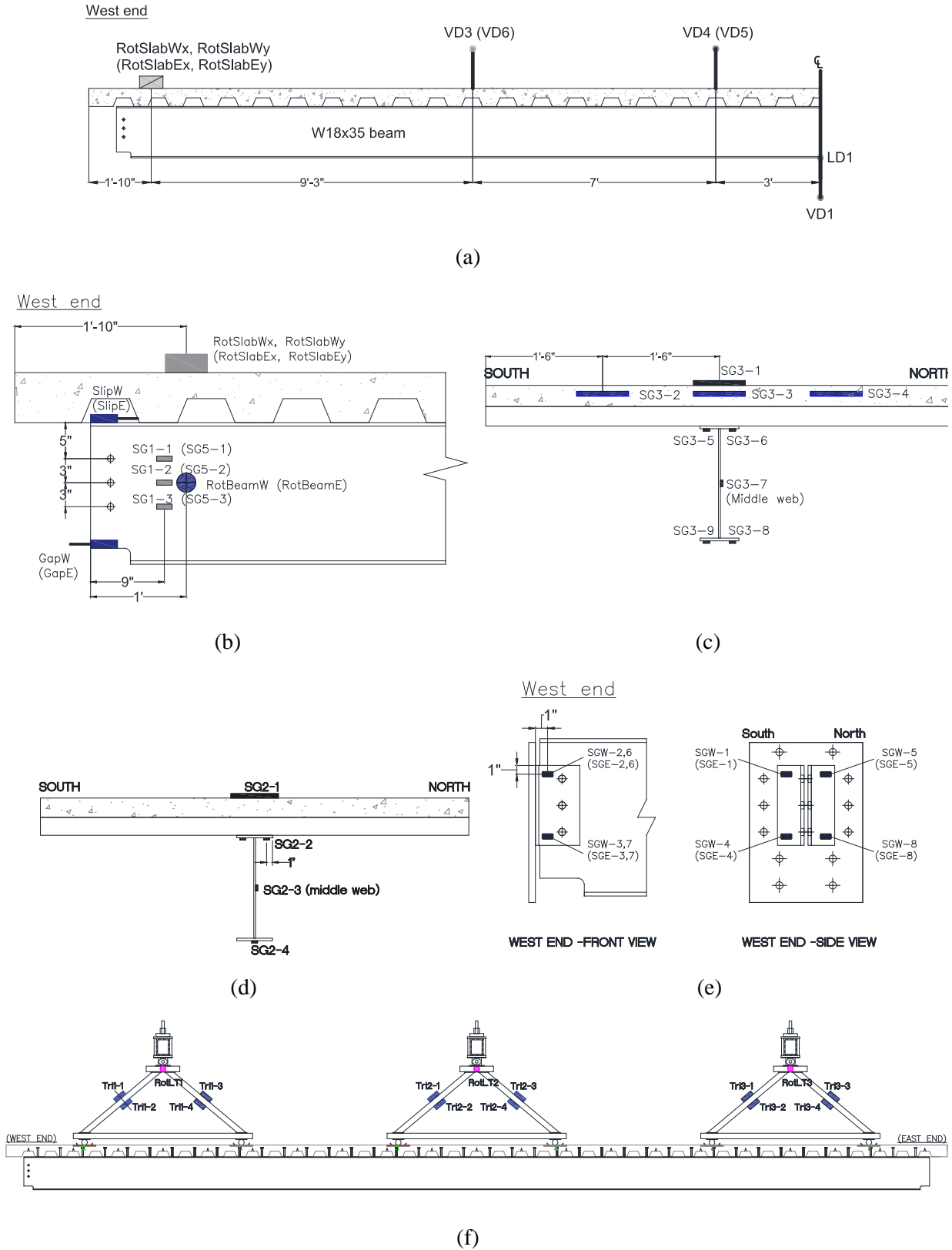
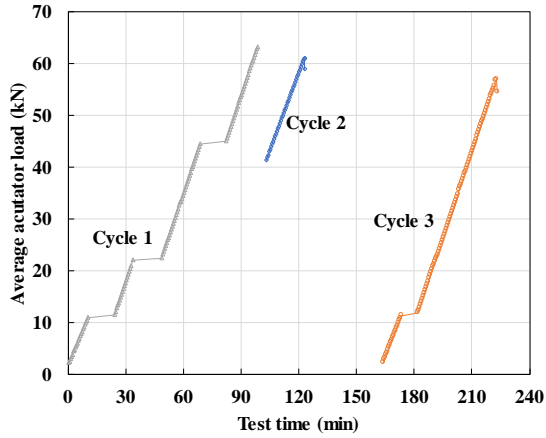


**Figure 5-1 Instrumentation layout for Specimen CB-DA-AMB.**

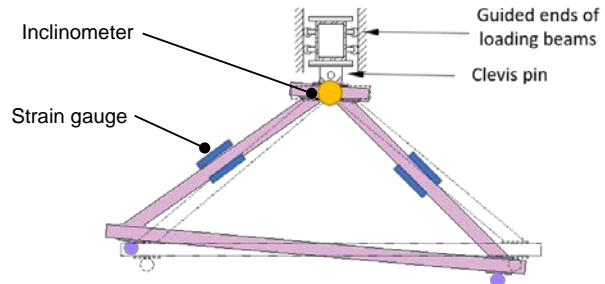
## 5.2 MECHANICAL LOADING

To simulate uniform floor loads on the specimen, two actuators connected to the same loading beam were programmed such that the summation of actuator loads acting on the center of the loading beam was increased at a rate of 2.2 kN/min. The individual point load at each of the six loading points was then increased at an average rate of 1.1 kN/min. To prevent twisting of the specimen while loaded, two actuators were coupled using displacement control so that the actuator stroke (displacement) increased at the same rate. Figure 5-2a shows the applied point load versus time relationship. As shown, three cycles of loading (Cycle 1, Cycle 2, and Cycle 3) were applied to capture the full sequence of failure of the composite beam specimen connected to the steel columns via the welded/bolted double-angle connection. The mechanical loading was paused at 11 kN, 22 kN and 44 kN (i.e., load plateaus shown in Figure 5-2a) to make strain measurements using fiber optics.

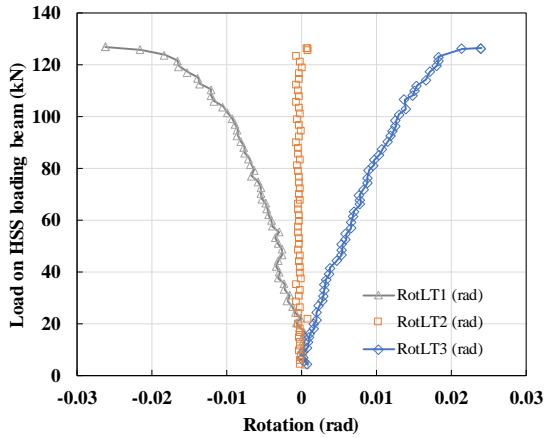
As the specimen bent downward in response to increasing mechanical loads, the rotation of the trusses attached to the east and west loading beams increased (Figure 5-2b). This resulted in variations in applied point loads. Figure 5-2c shows the average applied load on the loading beams versus the rotation of trusses measured during Cycle 1. Figure 5-2d shows the distribution of six-point loads with respect to a fraction of the maximum point load measured during Cycle 1. The variation in point loads was estimated in the range of 2 % to 4 % during Cycle 1; however, it increased to nearly 20 % during Cycle 3. Provided that the specimen was simply supported, the point load variation of 20 % resulted in about 2 % difference in the maximum bending moment (at midspan) when calculated using six-point loads with the same magnitude each.



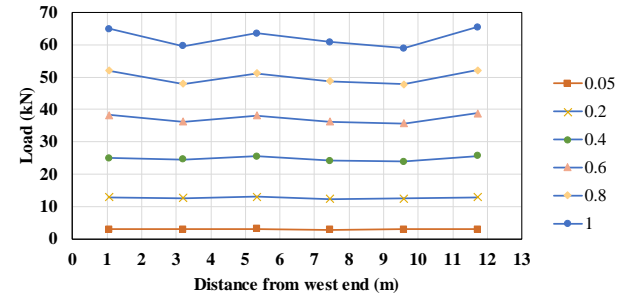
(a)



(b)



(c)



(d)

**Figure 5-2 (a) Point-load versus time relationship; (b) loading truss; (c) rotation of loading trusses; and (d) distribution of six point loads during Cycle 1 at various load levels defined as the applied point load normalized by a peak value.**

## 5.3 RESULTS AND DISCUSSION

### 5.3.1 Global Behavior

Figure 5-3 shows the point load versus the vertical and lateral displacements measured at the bottom flange of the W18×35 steel beam at midspan, the change in the vertical displacement profile of the concrete slab during Cycle 1, and the maximum vertical displacement corresponding to the peak load of each cycle. The lateral displacements plotted in the figure are the corrected values considering the effect of the vertical displacement of the specimen on the lateral displacement measurements. The flexural capacity, indicated as peak value of loads measured in

each cycle, decreased with increasing number of loading cycles (Figure 5-3a). Some key observations made in each loading cycle are summarized below.

- Cycle 1: The specimen exhibited linear elastic behavior until the point load reached approximately 45 kN. In this regime, the vertical displacement of the specimen was symmetric with respect to its midspan. A maximum lateral displacement of 1.3 mm, towards south, was measured during Cycle 1 (Figure 5-3b). When the point load increased to a peak value of  $63 \text{ kN} \pm 4\%$ , the shear stud at the west end failed, resulting in a sudden increase in the vertical displacement on the west side (Figure 5-3c). The value after  $\pm$  symbol indicates the standard deviation of point loads measured at six loading points.

Figure 5-3e shows the beam end rotations along the strong axis measured using the inclinometers attached to the beam webs (Figure 5-1b). As shown, from the start of the test, the west end experienced more end rotation than the east end. The rate of change in rotation with the applied load calculated between the average point loads of 5 kN and 45 kN, a linear region, were  $1/1500 \text{ rad/kN}$  and  $1/2400 \text{ rad/kN}$ , respectively. Provided that Figure 5-2d shows a symmetric loading about midspan of the beam, larger beam rotation in the west might have been resulted from the lower concrete strength ( $49.8 \pm 1.8$ ) MPa in the west half of the specimen measured on the day of the test relative to the concrete strength ( $54.4 \pm 3.3$ ) MPa in the east half as detailed in Section 2.3.2. At the peak load of  $63 \text{ kN} \pm 4\%$  during Cycle 1, the beam rotations reached 0.094 rad and 0.036 rad in west and east ends, respectively. The point load was relaxed to approximately 40 kN.

- Cycle 2: The point load was ramped up at a rate similar to Cycle 1. The vertical displacement increased noticeably when the load exceeded 60 kN. At a peak value of  $61 \text{ kN} \pm 5\%$ , the west half of the beam exhibited substantial composite failure, with visible delamination of steel deck units. The specimen was unloaded immediately afterwards. The specimen exhibited asymmetric vertical displacements with respect to its midspan (Figure 5-3d)
- Cycle 3: The point load was ramped up at a rate similar to Cycle 1. With existing composite failure on the west side, the lateral displacement increased with increasing loads (Figure 5-3b). The measured peak load was about  $57 \text{ kN} \pm 10\%$  at which the specimen collapsed by weld fracture failure (unzipping) of the west angle connection. The corresponding vertical displacement near midspan was approximately 360 mm, equivalent to  $L/30$  where  $L$  is the beam span length (Figure 5-3d).

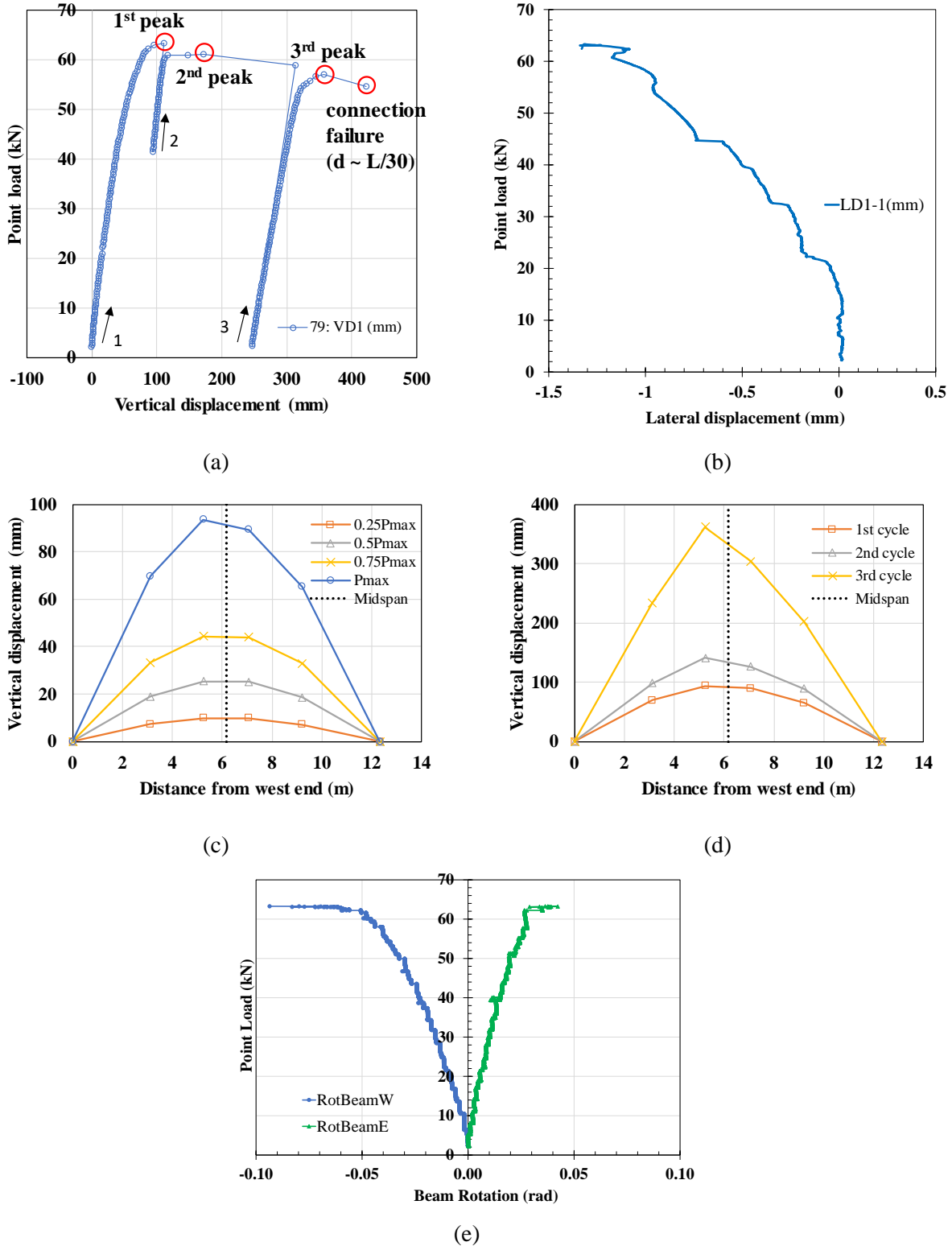
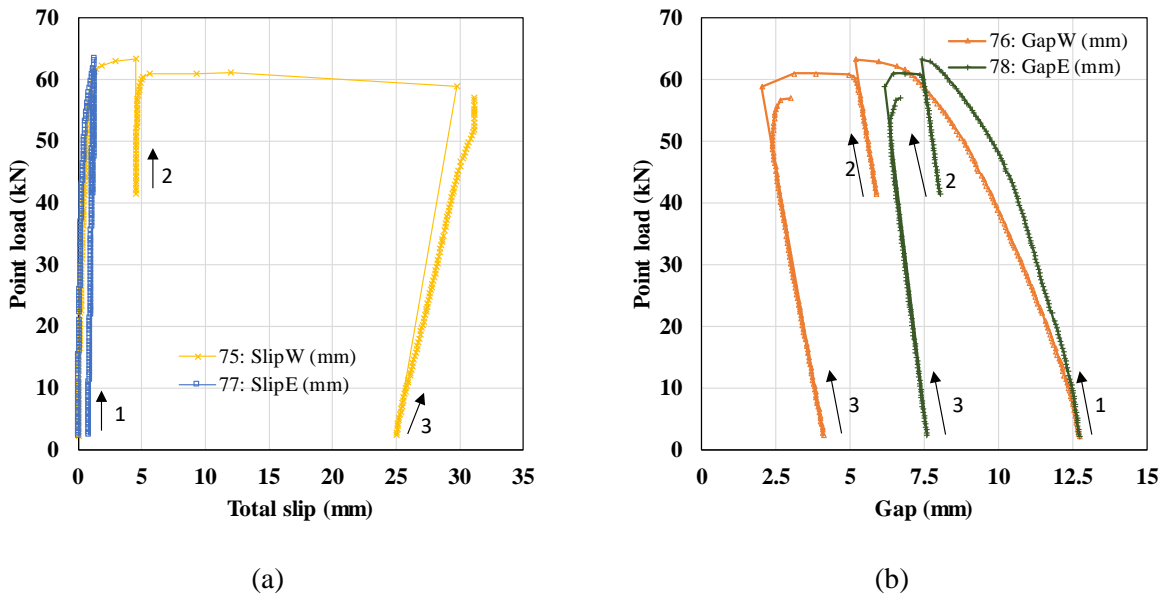


Figure 5-3 (a) Point load versus vertical displacement at midspan, (b) point load versus lateral displacement during Cycle 1, (c) vertical displacement profile of the concrete slab during Cycle 1, (d) the maximum vertical displacement measured at the peak load of each cycle, and (e) beam rotation during Cycle 1.

### 5.3.2 End Slip and Gap Closure

Figure 5-4 shows (a) the slip of the concrete slab relative to the end of the steel beam and (b) the change in gap distance between the column sacrificial plate and the bottom coped web as the specimen underwent multiple cycles of flexural loading. Those relative displacements (between two planes) were measured using spring-loaded displacement sensors at the locations shown in Figure 5-1b. The west end slip displacement increased to approximately 5 mm when the shear stud at the west end failed in Cycle 1. During Cycle 2, this value increased to nearly 30 mm (Figure 5-4a), accompanied with the horizontal interaction failure between the concrete slab and the steel beam. However, the east end slip displacement remained below 0.85 mm until the specimen failed by connection failure in Cycle 3.

The initial gap distance from the coped bottom flange of the steel beam to the sacrificial plate attached to the column flange was about 13 mm in accordance with AISC manual. As shown in Figure 5-4b, the gap distance varied as the test beam was subjected to increasing flexural loads in each cycle of loading. The gap closure at the west end was greater than the east as the west half of the beam lost the composite action. The gap distance at both ends never decreased to zero; namely, there was no bearing of the steel beam on the support column.



**Figure 5-4 (a) Slip between concrete slab and steel beam and (b) gap distance between sacrificial plate and beam web.**

### 5.3.3 Cross-Sectional Behavior

The section behavior of the specimen was measured using strain gauges attached at various sections along the length of the beam. Refer to Figure 5-1 for location of strain gauges. Figure 5-5a and Figure 5-5b show the applied point load as a function of axial strains of the specimen measured during Cycle 1 at sections 3 and 1, respectively. At midspan, subjected to positive flexure, the concrete slab was in compression, whereas the steel beam was in tension. The neutral axis was in the top flange of the W18×35 steel beam (i.e., near-zero strain) until the point load reached 48 kN. This result was consistent with design of a partially composite beam using the AISC 360 specification. As shown in Figure 5-5b, the web of the steel beam (near connection region) was in compression because of the restraint provided by the double-angle connection. Although strain values were small, the result showed that the beam web next to the double-angle connection was subjected to combined axial loads and negative moments.

As the point load exceeded 48 kN, however, the cross section at midspan exhibited inelastic behavior attributed to lateral-torsional buckling (Figure 5-5a). As the point load increased from 48 kN to 55 kN, the south side of the bottom flange (SG3-9) was subjected to excessive tension leading to local yielding. Strain hardening appeared at the point load beyond 55 kN. Conversely, the north side of the bottom flange (SG3-8) exhibited no increase in tensile strains and remained elastic, indicating the presence of compressive force. It was thought that an erection tolerance of lateral braces (Figure 3-6) to the concrete slab allowed a slight tilt of the concrete slab less than 0.5 degree when loaded. In addition, although the top flange was restrained, the steel beam was still susceptible to web torsional buckling because of the presence of compressive forces at the beam ends (i.e., the axial restraint provided by the angle connections). Twisting of the beam at midspan was not visible when this occurred. Even after local yielding of the bottom flange, the specimen continued to resist the applied loads until the shear stud at the west end fractured.

Figure 5-5c and Figure 5-5d show the applied point load versus axial strains measured at sections 2 and 4, located at 2.13 m west and east of midspan, during Cycle 1, respectively. After a point load of about 26 kN, a change in the load versus strain gradient was observed in the bottom flange of the steel beam at section 2 indicating increase of compressive forces that leads to lateral torsional behavior of the beam.

Figure 5-5e shows the strain in the mid-section measured at various load levels during the first cycle. The y-axis of the plot indicates the section depth measured from the bottom flange of the W18×35 steel beam. As shown, the steel beam was in tension and the concrete slab was in compression during the first cycle, indicating that the neutral axis was located within the top



flange. The maximum compressive strain, in concrete, and the maximum tensile strain, in steel, were 0.07 % and 0.3 % at the peak load of the first cycle, respectively.

Figure 5-5f shows the strain distribution in the mid-section at each peak load of loading cycles. The neutral axis, where the strain is zero, shifted downward to the steel beam section as the horizontal shear failure propagated toward the midspan. At the end of the third cycle of loading, the specimen lost the horizontal shear interaction (between the concrete slab and the steel beam) which was indicated by non-linear strain versus section depth shown in Figure 5-5f. The top flange of the steel beam exhibited a compressive strain of 0.2 %, and the bottom flange failed by yielding with the maximum strain of 0.6 %.

The peak moment applied to the test specimen was calculated using the midspan strain measurements shown in Figure 5-5a for the peak load of 63 kN during Cycle 1. A bi-linear strain distribution that occurs in the presence of slip between steel and concrete was considered in the moment calculation. A Modified Hognestad (Macgregor and Wight 2005) stress-strain model was used for the concrete and an elastic-perfectly plastic model was used for the steel. The measured properties of the steel beam and concrete detailed in Section 2.3 were used for the material properties. The peak moment calculated using the measured strains at the midspan was 665 kN-m which was about 80% of the moment capacity of the composite beam calculated in accordance with AISC 360 (AISC 2016) using the material properties measured from the standard testing methods (refer to Section 2.3).

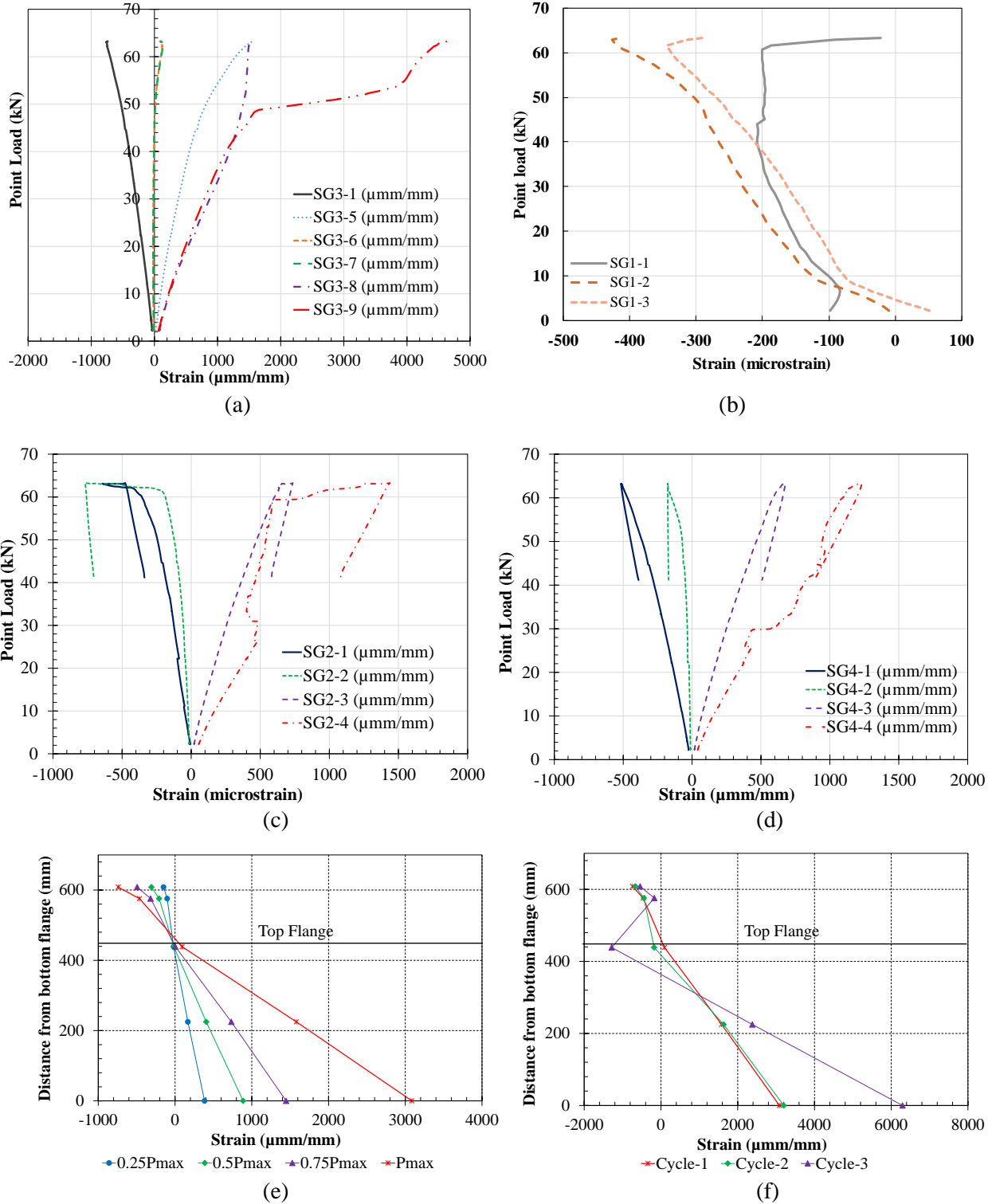


**Figure 5-5 (a) Strain at midspan during first cycle, (b) strain at beam web near west connection, (c) strain at section 2 (2.13 m west of midspan), (d) strain at section 4 (2.13 m east of midspan), (e) strain distribution in the mid-section at different load levels during first loading cycle, and (f) strain distribution in the mid-section at each peak load of loading cycles.**

### 5.3.4 Connection Behavior

The performance of the steel angle connections was measured using strain gauges as shown in Figure 5-6a and Figure 5-6b. The load cycle numbers and direction arrows are shown in black in these plots. As shown in Figure 5-6a, the top of the angle leg on the column side exhibited compressive strains during the test indicating prying of the attached angles. When fracture at the weld return was initiated at about 45 kN during the third cycle, the compressive strains started decreasing in both connections. The angles at the east end developed more ductile behavior than the west end. The maximum compressive strain was 0.83 % at the east connection prior to the initiation of weld fracture. Figure 5-6b shows the strains in the angle legs bolted to the beam web. As shown, there was no significant increase in strains (less than 0.05 %) during the first cycle, and then tensile stresses, indicated by positive slopes in strain data, were developed during the last two cycles until weld fracture occurred.

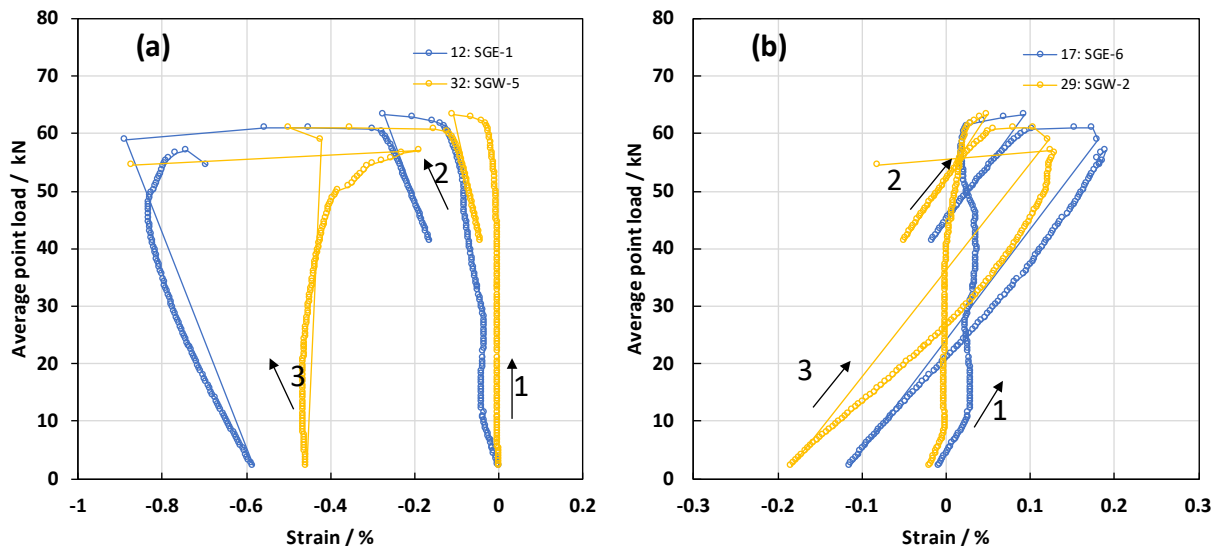


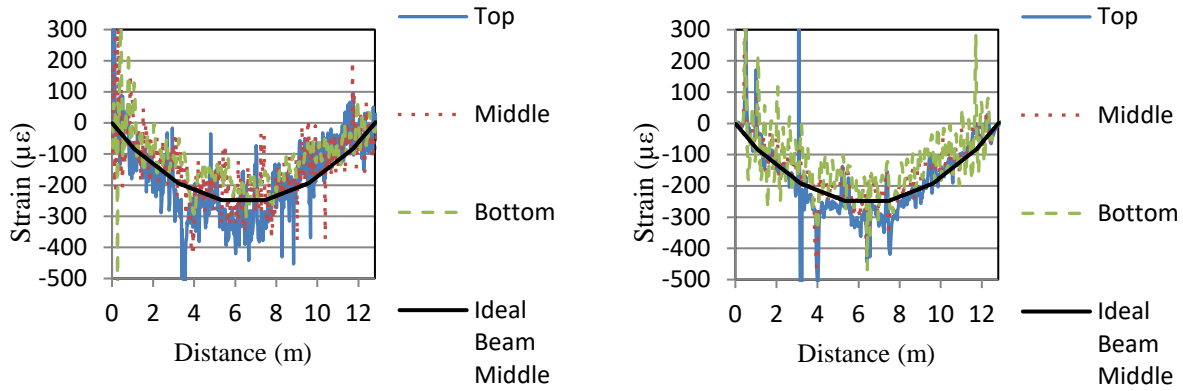
Figure 5-6 (a) strains in the top of the angle legs welded to the sacrificial plate and (b) strains in the top of the angle legs bolted to the beam web.

### 5.3.5 Fiber Optic Strain Measurements

#### Distributed fiber optic sensors

A typical strain profile with an overlaid theoretical solution of an ideal fully composite beam with no strain discontinuity due to shear studs is shown in Figure 5-7. The material properties used for the theoretical solution were a concrete density of 1865 kg/m<sup>3</sup>, a concrete compressive strength of 45.4 MPa, and a modulus of elasticity of concrete of 21.3 MPa. The yield stress and modulus of

elasticity used for the steel beam were 344.7 MPa and 200 GPa, respectively. Based on these material parameters, the neutral axis depth was calculated for an ideal beam to be 141 mm from the top surface and the moment of inertia about the strong axis was  $7.77 \times 10^8 \text{ mm}^4$ . The remainder of the DFOS data processing was not complete at the time of writing this report.



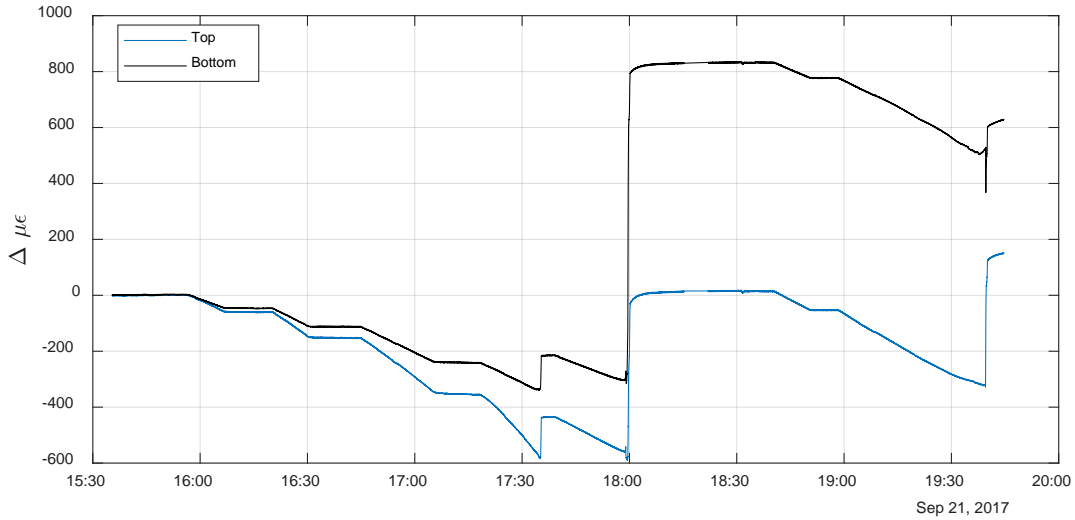
(a) Strain from Neubrescope at 44.5 kN/actuator

(b) Strain from Luna at 44.5 kN/actuator

**Figure 5-7 Strain measurements under ambient temperature with overlaid theoretical solution.**

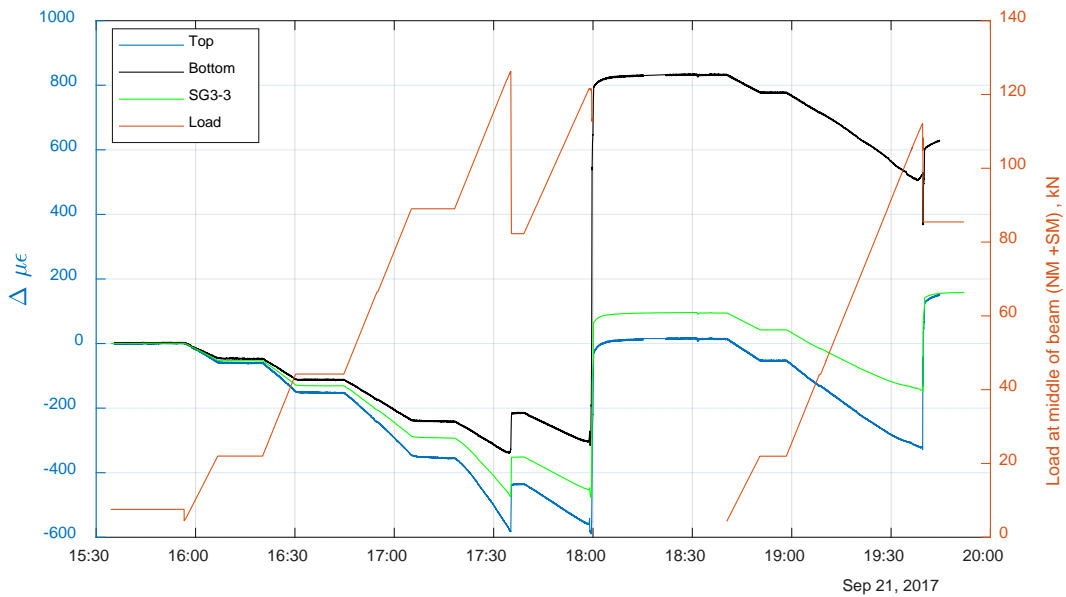
### Fiber Bragg grating sensors

Figure 5-8 shows the change in strain measured by the Fiber Bragg Grating (FBG) sensors during the testing of CB-DA-AMB. There were two main phases: first, loading through the elastic range into the initiation of plastic behavior and cracking from the time of 15:30 to 18:00, and second, re-loading the beam to failure. After the initial loading, the bottom sensor experienced a large unloading of the compression strain and a jump to  $\approx 825 \mu\epsilon$ . While no crack was observed to cross the sensor (inspected after the test), there were wide ( $> 5 \text{ mm}$ ) transverse cracks in the concrete within 0.5 m to the east and west of the sensor that may have led to the observed reduction in the compression strain. Additionally, a thin ( $\approx 0.1 \text{ mm}$  wide) longitudinal crack in the concrete was observed directly above the FBG sensor after completion of the test.



**Figure 5-8 Fiber Bragg Grating strain from CB-DA-AMB specimen.**

Figure 5-9 shows the same plot of the FBG strain during the test with the loading at the midspan superimposed on the right y-axis, highlighting the reduced capacity of the beam after damage occurred during the first loading at 18:00. The loading shown is only the load at midspan: the total load on the beam is roughly three times the load applied at the mid-span. Figure 5-9 also includes strain from SG3-3, a strain gauge embedded in the concrete nearby. SG3-3 is located at a depth in-between the FBG sensors in the concrete (Figure 5-9) and the measured strain from SG3-3 is consistently between the measured strains from the top and bottom FBGs.



**Figure 5-9 Fiber Bragg Grating strain with applied load and SG3-3 shown for comparison.**

After the loading was initiated near 16:00, the sensors show the corresponding strain development for the increasing load. The top sensor reads the largest (compression) strain, as it is furthest away from the neutral axis of the composite specimen. The bottom sensor reads the least strain, while SG3-3 reads a value in between. After unloading the beam at 18:00, SG3-3 returns to +95  $\mu\epsilon$ , rather than back to zero strain. This tension indicates that either there is a crack in the concrete or that there is some different structural condition for the concrete in the middle of the beam after the events and unloading at 18:00.

Figure 5-10 focuses on the event near 18:00. The sensors read a small jump (or ‘pop’) at 17:59, just before the large change in strain associated with reduction of the applied load on the beam. There is a time delay ( $\approx 30$  s) between the FBGs returning to a steady measurement after unloading. The source of the ‘pop’ is unknown but is possibly delamination of the concrete from the steel decking. Figure 5-11 zooms in on the final event in the concrete around 19:39 prior to termination of the experiment. Here too, a rapid increase in tension strain is observed due to changing strain states in the concrete; likely the large cracks observed adjacent to the FBG sensors after the test.

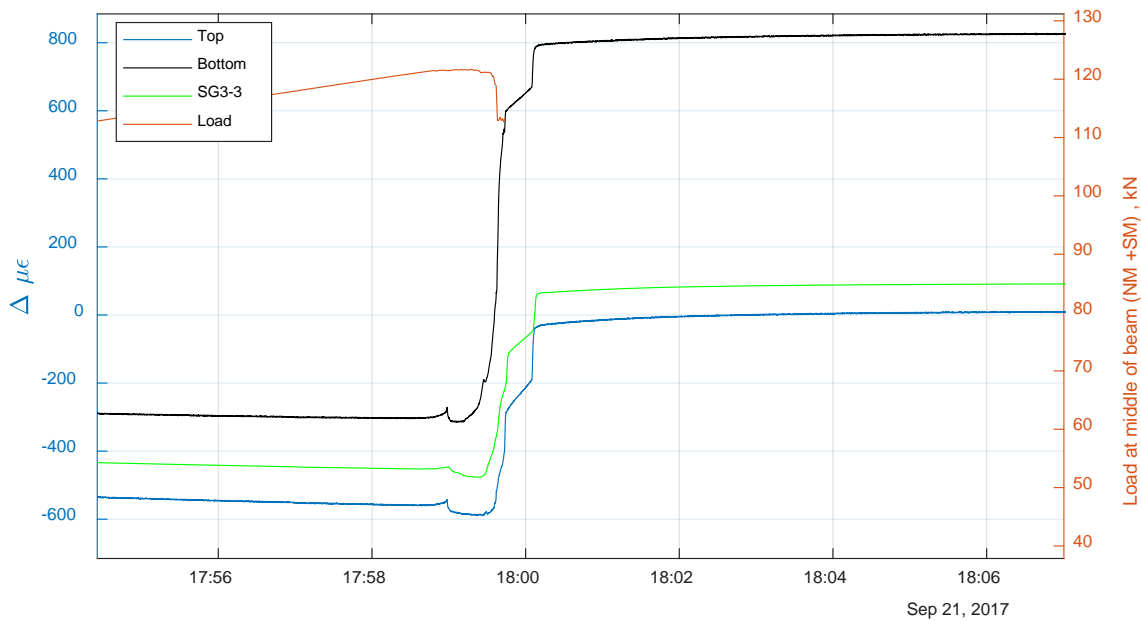


**Figure 5-10 First cracking measured by Fiber Bragg Grating sensor.**

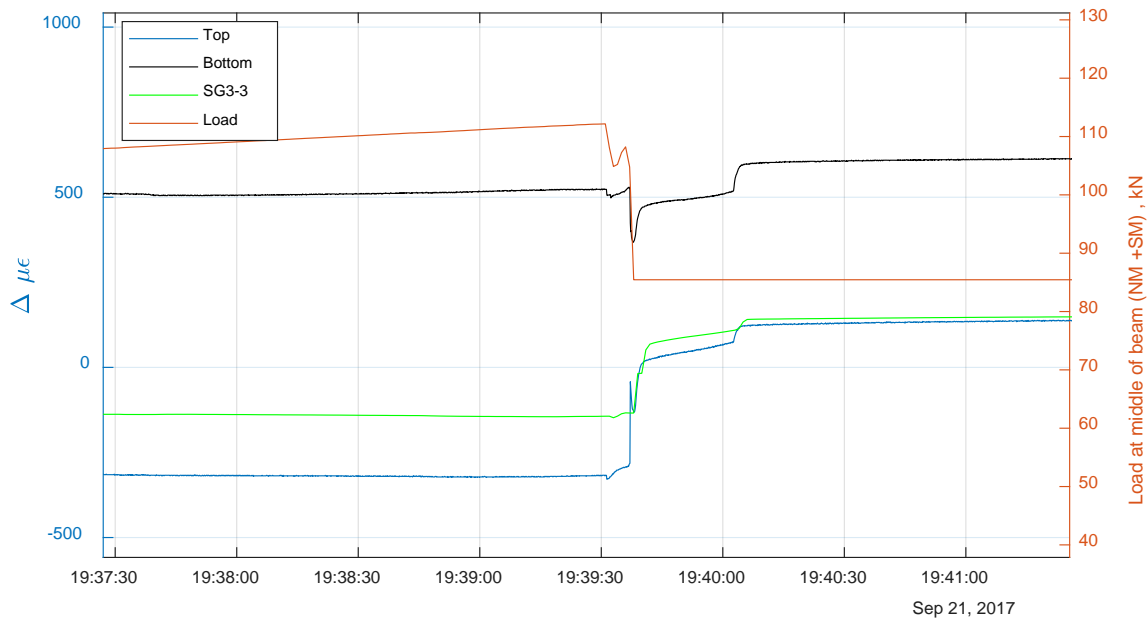


**Figure 5-11 Final cracking measured by Fiber Bragg Grating sensor.**

### 5.3.6 Post Test Investigation of Failure Modes

Figure 5-12 and Figure 5-13 show photographs of the specimen taken after the test representing different failure modes of the specimen during the test. During Cycle 1, when the test specimen was subjected to a monotonically increasing bending moment about its strong axis, the specimen exhibited failure at the interface between the shear studs and the concrete at the west end. The load-displacement curve started plateauing at an average point load of about 63 kN when the shank of the first shear stud fractured as shown in Figure 5-12a. During Cycle 2, when the specimen was unloaded to about 40 kN and reloaded again, as the first shear stud had already fractured at the west end, the remaining shear studs in the west half of the specimen had to transfer the total shear between the concrete and steel in that region. Hence, the composite interaction failure quickly propagated from west end toward the midspan. As in Figure 5-12b that shows the west end of the specimen after concrete removal, shear studs deformed towards the west, in the direction of compressive forces from the concrete slab subjected to flexural loading. Figure 5-12c and Figure 5-12d show the cut sections of the concrete slab at midspan and at the east end, respectively. As shown, concrete breakout around the shear stud occurred in the west half of the specimen while no concrete breakout was observed in the east half of the specimen. As the west half of the beam lost the continuity between the beam and slab, plastic hinging formed in the critical section at the west support of the middle loading truss (about 1 m from the beam centerline). This region was subjected to the maximum bending moment and the bearing stress from the point load. The beam

failed by yielding and a flexural crack was developed through the depth of the concrete slab (Figure 5-12e). Figure 5-12f shows the deflected shape of the specimen. Crushing of concrete in the top of the slab was not observed. Figure 5-13a and Figure 5-13b show the connections at the west and east ends, respectively. During Cycle 3, the legs of the west angles welded to the column sacrificial plate were completely detached at the peak load of 57 kN, which was the same as the limit state of angle connections (i.e., weld shear) designed using the AISC design table. Figure 5-13b shows deformed angle legs on the column face and weld fracture at the top of the angle legs at the east angle connection.





(a)



(b)



(c)



(d)



(e)



(f)

**Figure 5-12 (a) fracture of first shear stud at west end, (b) west side of specimen after concrete removal, (c) cut-section of concrete slab at midspan, (d) cut-section of concrete slab at east end, (e) exposed concrete at 1 m left of beam centerline, (f) deflected specimen after the test.**

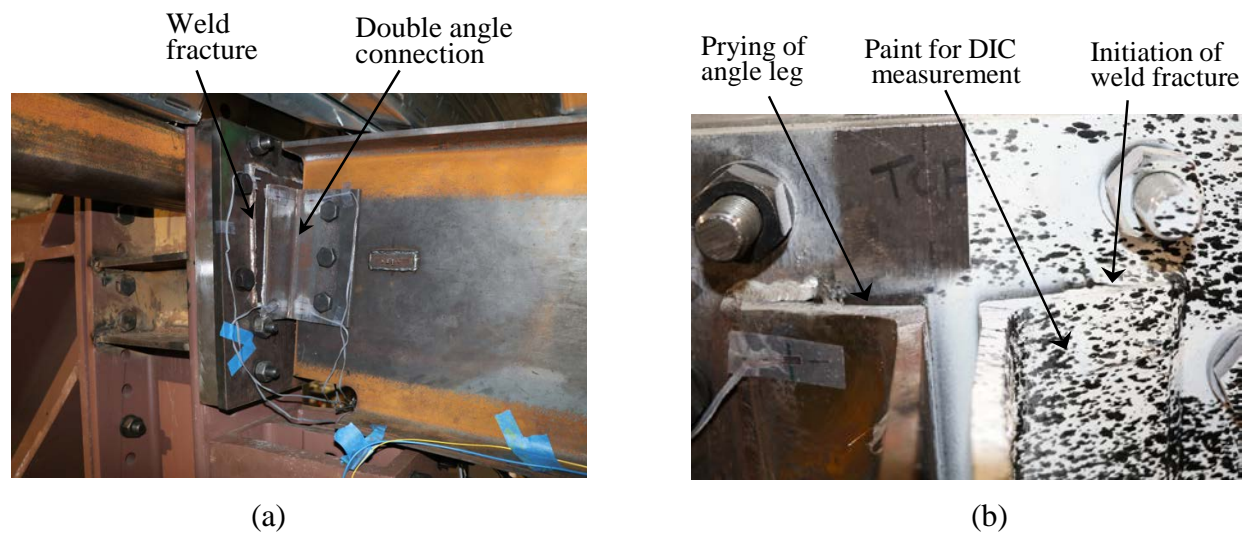


**Figure 5-13(a) west connection after the test and (b) east connection after the test. Paint pattern on right side of image (b) was used for Digital Image Correlation measurements (not reported here).**

## Chapter 6

### SUMMARY AND CONCLUSIONS

---

A series of compartment fire experiments was conducted on 12.8 m long composite floor beam assemblies resisting gravity loads to study the performance and limit states under realistic fire conditions. The specific objectives for this study were (a) to create realistic, structurally significant fire conditions using natural gas fueled burners to study the failure mechanisms of full-scale beam assemblies and (b) to produce data that can be used to guide the development or validation of numerical models and design tools used for performance-based design of similar structures in the event of fire. This report (Part 1) describes details of the experimental design, including design and construction of the composite beam specimens and mechanical loading system, design of a test fire, measurement systems, and the ambient capacity and behavior of the composite beam specimen. The Part 2 (Choe et al. 2019) presents the results of four compartment fire experiments conducted at the NIST National Fire Research Laboratory.

Design and construction of the 12.8 m long composite beam specimens followed the U.S. construction practice. Specimens consisted of a lightweight aggregate concrete slab on 76 mm deep ribbed steel decking and a W18×35 steel beam. The composite action was 82 % of the yield strength of the W18×35 beam. The steel beams of the four fire test specimens were sprayed with fire resistive material for 2-hour fire-resistance rating. Test variables used in this test program included (1) two types of simple shear connections (welded-bolted double-angle versus shear-tab connections) and (2) the presence or absence of slab continuity over the girders.

Mechanical loading was applied at six points along the specimen to simulate a uniform floor load. A loading system was designed to apply mechanical loads using hydraulic actuators while providing lateral braces to the side edges of the concrete slab. A 4 MW compartment fire was developed using natural gas burners to simulate realistic and structurally significant fire loading for the subsequent test series. The fire was designed to develop an upper layer gas temperature of about 1000 °C without any combustion outside of the compartment. A variety of sensor, including fiber optics, were implemented to characterize the thermal and structural responses of the specimens. Prior to the fire experiments, the first test reported herein was conducted to study various modes of failure of the long-span composite beam with double-angle connections at ambient temperature.

The ambient temperature test indicated that the composite beam specimen failed by a shear stud near the west end, followed by concrete breakout failure and yielding of the steel beam. A peak load capacity of 378 kN was achieved at a corresponding midspan deflection of approximately 100

mm. The corresponding measured moment capacity was approximately 80% of the flexural strength calculated in accordance with AISC 360. The double-angle connection at the west end failed by weld fracture, which caused collapse of the composite beam. The lower measured moment capacity suggests that the AISC equations for the calculation of flexural strength of long-span composite beams may not be conservative in this specific case, although further study is needed. The ambient behavior of the composite beam specimen presented herein will serve as a baseline to compare with the composite beam assemblies tested under combined mechanical loads and fire exposure, which are presented in a subsequent report; Part 2 (Choe et al. 2019).

## REFERENCES

---

---

- Almand, K.H., (2004). NIST-SFPE Workshop for Development of a National R&D Roadmap for Structural Fire Safety Design and Retrofit of Structures: Proceedings. NIST Interagency/Internal Report (NISTIR) – 7133
- Almand, K. (2012). Structural Fire Resistance Experimental Research – Priority Needs of U.S. Industry. Grant/Contract Reports (NISTGCR) - 12-958
- American Institute of Steel Construction (AISC). (1999). *Load and resistance factor design specifications for structural steel buildings*. Chicago, IL.
- American Institute of Steel Construction (AISC). (2002). “Seismic provisions for structural steel buildings.” *ANSI/AISC 341-02*, Chicago, IL.
- American Institute of Steel Construction AISC (2010). “Specification for structural steel buildings,” Specification ANSI/AISC 360-10, American Institute of Steel Construction (AISC), One East Wacker Drive, Suite 700, Chicago, IL 60601-1802.
- ASCE. (2016). “Minimum design loads and associated criteria for buildings and other structures.” *ASCE/SEI 7-16*, Reston, VA.
- ASCE. (2007). “Minimum design loads for buildings and other structures.” *ASCE/SEI/SFPE 29-05*, Reston, VA.
- ANSI/AISC-360 (2017). Steel Construction Manual. American Institute of Steel Construction
- ASCE MOP 138-2018. Structural Fire Engineering. Prepared by the Fire Protection Committee of the Structural Engineering Institute of ASCE
- ASTM International (2009a). Standard specification for high-yield-strength, quenched and tempered alloy steel plate, suitable for welding. *Standard A514/A514M-05*, ASTM International, W. Conshohocken, Pa. doi:10.1520/A0514\|do5(A)0514M-05R09.
- ASTM International (2009b). Standard terminology relating to methods of mechanical testing. *Standard E6-09b*, ASTM International, W. Conshohocken, Pa. doi:10.1520/E0006-09B.
- ASTM International (2009c). Standard test methods for elevated temperature tension tests of steelic materials. *Standard E21-09*, ASTM International, W. Conshohocken, Pa. doi:10.1520/E0021-09.
- ASTM International. (2010). "Standard Specification for Structural Bolts, Steel, Heat Treated, 120/105 ksi Minimum Tensile Strength." *ASTM A325-10e1*, ASTM International, West Conshohocken, PA. doi: 10.1520/A0325.
- ASTM International (2011). “Standard specification for structural steel shapes”. *Standard A992/A992M-11*, ASTM International, W. Conshohocken, Pa. doi:10.1520/A0992\_A0992M-11.
- ASTM E605/E605M-93 (2015) e1. Standard Test Methods for Thickness and Density of Sprayed Fire-Resistive Material (SFRM) Applied to Structural Members, ASTM International, West Conshohocken, PA, 2015, [https://doi.org/10.1520/E0605\\_E0605M-93R15E01](https://doi.org/10.1520/E0605_E0605M-93R15E01)

- ASTM International (2018), “ASTM Standard E119-18ce Standard Test Methods for Fire Tests of Building Construction and Materials”, *Standard E119-18ce*, ASTM International, West Conshohocken, PA, doi: 10.1520/E0119-18CE01.
- ASTM International. (2012a). "Standard Specification for Carbon Structural Steel." *Standard A36/A36M-12*, ASTM International, West Conshohocken, PA. doi: 10.1520/A0036\_A0036M-12.
- ASTM International. (2012b). "Standard Specification for Structural Bolts, Alloy Steel, Heat Treated, 150 ksi Minimum Tensile Strength." *Standard A490-12*, ASTM International, West Conshohocken, PA. doi: 10.1520/A0490-12.
- ASTM International. (2012c). "Standard Specification for Structural Bolts, Alloy Steel, Heat Treated, 150 ksi Minimum Tensile Strength." *Standard A992/A992M-11*, ASTM International, West Conshohocken, PA. doi: 10.1520/A0992\_A0992M-11.
- ASTM International (2012d). “Standard specification for structural steel with improved yield strength at high temperature for use in buildings”. *Standard 1077/1077M-12*, ASTM International, W. Conshohocken, Pa. doi:10.1520/A1077\_A1077M-12.
- ASTM International. (2013), "Standard Specification for High-Strength Low-Alloy Columbium-Vanadium Structural Steel." *Standard A572/A572M-13a*, ASTM International, West Conshohocken, PA. DOI: 10.1520/A0572\_A0572M.
- ASTM International (2018). “Standard Test Methods for Fire Tests of Building Construction and Materials”, *Standard E119-18*, ASTM International, W. Conshohocken, Pa.
- ASTM International. Standard test methods for tension testing of steelic materials [metric]. Standard E8/E8M-09, ASTM International, W. Conshohocken, Pa, 2011. doi:10.1520/E0008\E0008M-11.
- British Standards Institution (1990). “Specification for weldable structural steels”. *Technical Report BS 4360:1990*, British Standards Institution. Status: superseded, Withdrawn June 1994. URL: <http://shop.bsigroup.com/en/ProductDetail/?pid=000000000011122236>.
- Brockenbrough, R. L. and Johnston, B. G. (1968). Steel design manual. Technical Report ADUSS 27-3400-01, United States Steel Corporation. Some data appear in Holt (1964).
- Bundy, M., Hamins, A., Johnsson, E. L., Kim, S.C., Ko, G. H., and Lenhart, D. B. (2007). “Measurements of Heat and Combustion Products in Reduced-Scale Ventilation-Limited Compartment Fires.” NIST Technical Note TN-1483, National Institute of Standards and Technology, Gaithersburg, MD.
- Bao, Y., Chen, G. (2016). “Temperature-dependent strain and temperature sensitivities of fused silica single mode fiber sensors with pulse pre-pump Brillouin optical time domain analysis.” *Measurement Science and Technology*, 27(6), 65101–65111.
- Bao, Y., Hoehler, M.S., Smith, C.M., Bundy, M., Chen, G. (2017). “Temperature measurement and damage detection in concrete beams exposed to fire using PPP-BOTDA based fiber optic sensors.” *Smart Materials and Structures*, 26(10), 105034.
- Bao, Y., Hoehler, M. S., Smith, C. M., Bundy, M., and Chen, G. (2019). “Temperature Measurement in Steel-Concrete Composite Slab Specimens Subjected to Fire Using



Brillouin Scattering Based Distributed Fiber Optic Sensors.” ASCE Journal of Structural Engineering.

- Bao, Y., Tang, F., Chen, Y., Meng, W., Huang, Y., Chen, G. (2016). “Concrete pavement monitoring with PPP-BOTDA distributed strain and crack sensors.” *Smart Structures and Systems*, 18(3), 19p.
- Bentz, D., Peltz, M., Durán-Herrera, A., Valdez, P., and Juárez, C. (2011). “Thermal properties of high-volume fly ash mortars and concretes.” *Journal of Building Physics*, 34(3), 263–275.
- BRE (2004). Client Report: Results and observations from full-scale fire test at BRE Cardington, 16 January 2003, Client report number 215-741.
- British Steel (1999). The behaviour of multi-storey steel framed buildings in fire. British Steel, Rotherham, UK
- Bundy, M., Hamins, A., Gross, J., Grosshandler, W., and Choe, L. (2016). Structural fire experimental capabilities at the NIST National Fire Research Laboratory, *Fire Technology*, 52(4), 959-966.
- Bryant, R.A. (2003). NIST 3 Megawatt Quantitative Heat Release Rate Facility. Special publication (NIST SP) - 1007
- Bryant, R.A., Bundy, M.F., Zong, R. (2015). Evaluating Measurements of Carbon Dioxide Emissions Using a Precision Source – a Natural Gas Burner. *Journal of the Air & Waste Management Association*. Volume 65, Issue 7. <https://doi.org/10.1080/10962247.2015.1031294>
- Bryant, R., Ohlemiller, T. J., Johnson, E. L et al. (2004). “The NIST 3-megawatt quantitative heat release rate facility.” NIST SP 1007, Gaithersburg, MD.
- Bundy, M.F., Hamins, A., Johnsson, E.L., Kim, S.C., Ko, G.H. and Lenhart, D.B. (2007). Measurements of Heat and Combustion Products in Reduced-Scale Ventilation-Limited Compartment Fires, National Institute of Standards and Technology, NIST TN 1483.
- Bundy, M., Hamins, A., Gross, J., Grosshandler, W., and Choe, L. (2016). “Structural fire experimental capabilities at the NIST National Fire Research Laboratory,” *Fire Technology*, 52(4), 959-966.
- Choe, L. (2011). “*Structural mechanics and behavior of steel members under fire loading*”, Ph.D. Thesis. Purdue University, West Lafayette, IN., December.
- Choe, L., Ramesh, S., Hoehler, M., Seif, M., Gross, J., Zhang, C. and Bundy, M. (2018). National Fire Research Laboratory Commissioning Project: Testing Steel Beams under Localized Fire Exposure. NIST Technical Note 1983.
- Choe, L., Ramesh, S., Hoehler, M., Seif, M., Bundy, M., Reilly, J., and Glisic, B. (2019). “Compartment Fire Experiments on Long-Span Composite-Beams with Simple Shear Connections. Part 2: Test Results.” NIST Technical Note TN-2055, National Institute of Standards and Technology, Gaithersburg, MD.
- Cooke, G. (1988). An introduction to the mechanical properties of structural steel at elevated temperatures. *Fire Safety Journal*, 13(1):45–54. doi:10.1016/0379-7112(88)90032-X.
- Dieter, G.E. (1976). *Mechanical Steellurgy*, 2nd ed., McGraw-Hill, New York.

- ECCS (1983). European recommendations for the fire safety of steel structures: Calculation of the fire resistance of load bearing elements and structural assemblies exposed to the standard fire. Technical report, European Convention for Constructional Steelwork, Brussels, Belgium. Technical Committee 3–Fire Safety of Steel Structures. URL: <http://www.eccspublications.eu/index.php?section=library&content=&act=detail&id=95>.
- ECS (2005). Eurocode 3. Design of steel structures. General rules. Structural fire design. Standard EN 1993-1-2, European Committee for Standardization. URL: <http://eurocodes.jrc.ec.europa.eu/showpage.php?id=133>.
- Ellingwood, B., Galambos, T. V., MacGregor, J. G., and Cornell, C. A. (1980). Development of a probability-based load criterion for American National Standard A58 building code requirements for minimum design loads in buildings and other structures. *Special Publication 577*, National Bureau of Standards.
- European Committee for Standardization. (2001). “Eurocode 3: Design of steel structures. Part 1.2: General rules structural fire design.” *ENV 1993-1-2:2001*, Brussels, Belgium.
- European Committee for Standardization (CEN). (2004). Eurocode 2: Design of concrete structures - Part 1.2: General rules – Structural fire design (EN 1992-1-2). Brussels.
- Fan, L.; Bao, Y.; Meng, W.; Chen, G. (2019). "In-situ monitoring of corrosion-induced expansion and mass loss of steel bar in steel fiber reinforced concrete using a distributed fiber optic sensor", *Composites Part B: Engineering*.
- Fan, L., Bao, Y., Chen, G. (2018). “Feasibility of distributed fiber optic sensor for corrosion monitoring of steel bars embedded in concrete”, *Sensors*, 18(11), 3722.
- Fike, R. (2010). Strategies for enhancing the fire resistance of steel framed structures through composite construction. Ph.D. thesis, Michigan State Univ., East Lansing, MI.
- Flint, G., Lamont, S., Lane, B., Sarrazin, H., Lim, L., Rini, D., Roben, C. (2013). Recent Lessons Learned in Structural Fire Engineering for Composite Steel Structures. *Fire Technol* (2013) 49: 767. <https://doi.org/10.1007/s10694-012-0291-8>
- Froggatt, M. and Moore, J. (1998). “High-spatial-resolution distributed strain measurement in optical fiber with Rayleigh scatter.” *App. Opt.*, 37(10), pp. 1735-1740, 10.1364/AO.37.001735.
- Garlock, M.E. and Selamet. S. (2010). “Modeling and behavior of steel plate connections subject to various fire scenarios.” *Journal of Structural Engineering*, 136 (2010), pp. 897–906.
- Gustafsson, S. E. (1991). “Transient plane source techniques for thermal conductivity and thermal diffusivity measurements of solid materials.” *Review of Scientific Instruments*, 62(3), 797–804.
- Hoehler M., S., Andres, B., Bundy, M., F. (2019). “Influence of Fire on the Lateral Resistance of Cold-Formed Steel Shear Walls – Phase 2-Oriented Strand Board, Strap Braced, and Gypsum-Sheet Steel Composite.”, NIST Technical Note TN-2038, DOI: <https://doi.org/10.6028/NIST.TN.2038>
- Hamins, A.P., Maranghides, A., McGrattan, K.B., Ohlemiller, T.J., and Anleitner, R., Experiments and Modeling of Multiple Workstations Burning in a Compartment. Federal Building and



Fire Safety Investigation of the World Trade Center Disaster (NIST NCSTAR 1-5E), National Institute of Standards and Technology, 2008.

International Code Council. International Building code IBC (2018).

ISO (1999) ISO 834-1:1999: Fire Resistance Tests – Elements of Building Construction – Part 1: General Requirements. International Organization for Standardization, Geneva

ISO 834-11:2014, Fire resistance tests -- Elements of building construction -- Part 11: Specific requirements for the assessment of fire protection to structural steel elements, International Organization for Standardization.

International Organization for Standardization. Steellic materials – tensile testing – part 1: Method of test at room temperature. Standard 6892-1:2009, International Organization for Standardization, 2009. URL: [http://www.iso.org/iso/iso\\_catalogue/catalogue\\_ics/catalogue\\_detail\\_ics.htm?ics1=77&ics2=040&ics3=10&csnumber=51081](http://www.iso.org/iso/iso_catalogue/catalogue_ics/catalogue_detail_ics.htm?ics1=77&ics2=040&ics3=10&csnumber=51081).

Kawagoe, K., “Fire Behaviour in Rooms, Report No. 27, Building Research Institute, Tokyo, 1958.

Kishida, K., Yamauchi, Y. and Guzik, A. (2014). “Study of optical fibers strain-temperature sensitivities using hybrid Brillouin-Rayleigh system.” *Photonic Sen.*, 4(1), pp. 1-11, 10.1007/s13320-013-0136-1.

Kreger, S. T., Soller, B. J. Gifford, D. K., Duncan, R. G., Wolfe, M. S. and Froggatt, M. E. (2007). “Optical backscatter reflectometry as a measurement tool for fiber-optics in avionics and aerospace applications.” Technical Report No. 2007-01-3863. Soc. of Auto. Eng. International, Warrendale, PA, 10.4271/2007-01-3863.

Keltner, N.R., Beck, J.V., Nakos, J.T. (2008). “Using Directional Flame Thermometers for Measuring Thermal Exposure”. ASTM E5- Advances in the State of the Art of Fire Testing, Miami, FL.

Kordosky A (2017). Experimental and Computational Investigation of Composite Beam Response to Fire. M.S. Thesis, Lehigh University, Bethlehem, PA, USA

Kodur, V.K.R., and Shakya, A.M., “Effect of Temperature on Thermal Properties of Spray Applied Fire Resistive Materials,” *Fire Safety Journal* 61 (2013) 314-323.

Log, T., and Gustafsson, S. E. (1995). “Transient plane source (TPS) technique for measuring thermal transport properties of building materials.” *Fire and Materials*, 19(1), 43–49.

Macgregor, J. E., Wight, J. K., (2005). Reinforced Concrete: Mechanics and Design. 4th Edition, Pearson Prentice Hall, Upper Saddle River, NJ.

McGrattan, K., S. Hostikka, R. McDermott, J. Floyd, C. Weinschenk, and K. Overholt. Fire Dynamics Simulator, Technical Reference Guide, National Institute of Standards and Technology, Gaithersburg, Maryland, USA, and VTT Technical Research Centre of Finland, Espoo, Finland, sixth edition, September 2013.

McCaffrey, B.J. and Heskestad, G. (1976). Robust Bidirectional Low-Velocity Probe for Flame and Fire Applications, *Combustion and Flame* 1125-127.

- Pour-Ghaz, M., Castro, J., Kladvik, E. J., and Weiss, J. (2012). "Characterizing Lightweight Aggregate Desorption at High Relative Humidities Using a Pressure Plate Apparatus." *Journal of Materials in Civil Engineering*, 24(8), 961–969.
- R Core Team. R: A Language and Environment for Statistical Computing. R Foundation for Statistical Computing, Vienna, Austria, 2014. URL: <http://www.R-project.org/>.
- Ruddy, J.L., Marlo, J.P., Ioannides, S. A., Alfawakhiri, F. (2003). Design Guide 19: Fire Resistance of Structural Steel Framing. Results and observations from a full-scale fire test at BRE Cardington, 16 Jan 2003, Client Report 215-741, 2004.
- SCI (Steel Construction Institute). (2008). Best practice in steel construction, commercial buildings, guidance for architects, designers, and constructors, Ascot, U.K
- Seif, M.S., Main, J.A., McAllister, T.P. (2013) "Performance of Steel Shear Tab Connections at Elevated Temperatures." *Proceedings of the Annual Stability Conference, Structural Stability Research Council*, St. Louis, Missouri, April 16-20, 2013.
- Selden, K., Fischer, E., Varma, A. (2016). Experimental Investigation of Composite Beams with Shear Connections Subjected to Fire Loading. *Journal of Structural Engineering*, 142(2):04015118.
- Shyam-Sunder, S. et al. (2008). Final Report on the Collapse of World Trade Center Building 7, Federal Building and Fire Safety Investigation of the World Trade Center Disaster. National Construction Safety Team Act Reports (NIST NCSTAR).
- Soller, B. J., Wolfe, M. and Froggatt, M. E. (2005). "Polarization resolved measurement of Rayleigh backscatter in fiber-optic components." *Nat. Fiber Opt. Eng. Conf.*, Anaheim, CA, 1-55752-784-9.
- Taylor, B. N., and Kuyatt, C. E. (1994). "Guidelines for Evaluating and Expressing the Uncertainty of NIST Measurement Results." NIST Technical Note TN-1297, Gaithersburg, MD.
- Tsavidaridis, Konstantinos. (2015). Seismic Resistant Design of Connections with the Use of Perforated Beams. The 428th OMICS International Conference, Proceedings of World Congress and Exhibition of Construction and Steel Structure, Volume: 5
- UL (2011). Fire Resistance Ratings – ANSI/UL 263. Design NO. N791.
- Wellman, E., Varma, A. H., Kodur, V., and Fike, R. (2011). Experimental evaluation of thin composite floor assemblies under fire loading. *J. Struct. Eng.*, 10.1061/(ASCE)ST.1943-541X.0000451, 1002–1016.
- Yang J. C., Bundy M. F., Gross J. L., Hamins A. P., Sadek F., Raghunathan A. (2015). International R&D Roadmap for Fire Resistance of Structures Summary of NIST/CIB Workshop. Special Publication (NIST SP) – 1188.
- Zhao, B., and Kruppa, J. (1997). Fire resistance of composite slabs with profiled steel sheet and of composite steel concrete beams. Part 2: Composite beams. Final Rep., CTICM, Luxembourg, France.

# APPENDIX A

## DRAWINGS FOR TEST SETUP

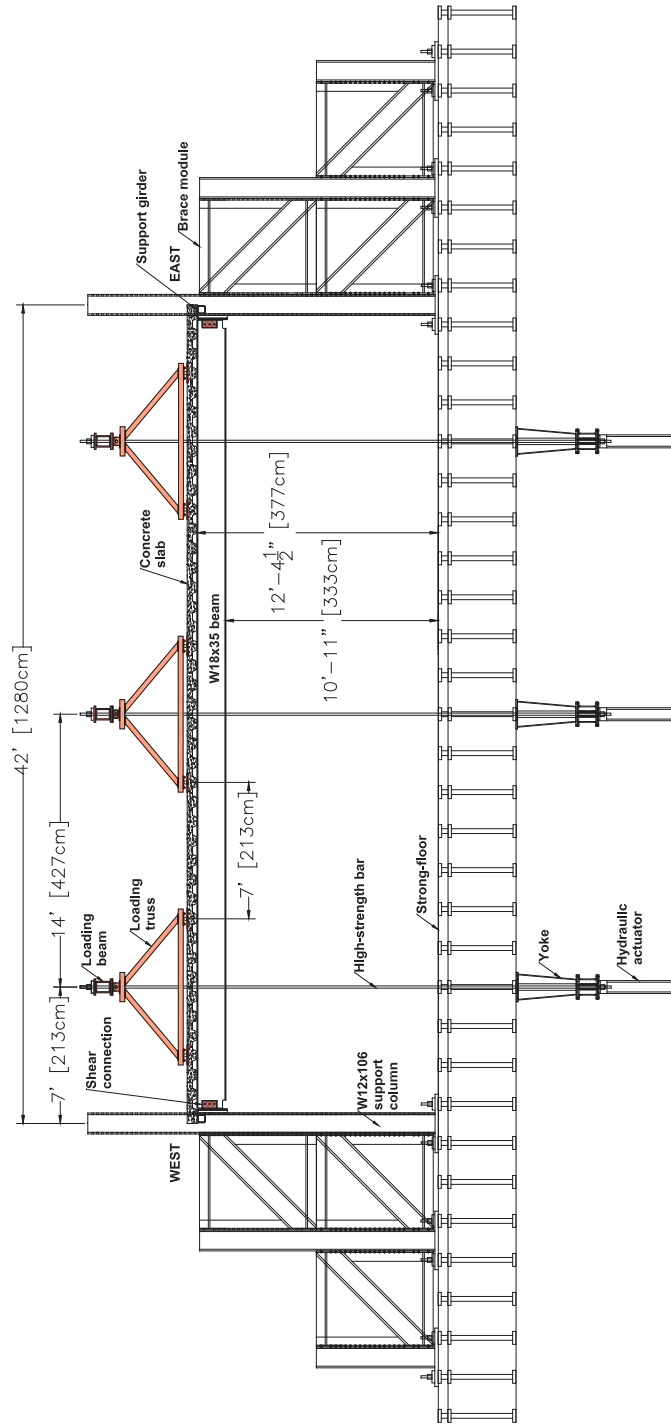


**Figure A- 1 Test setup – front view.**

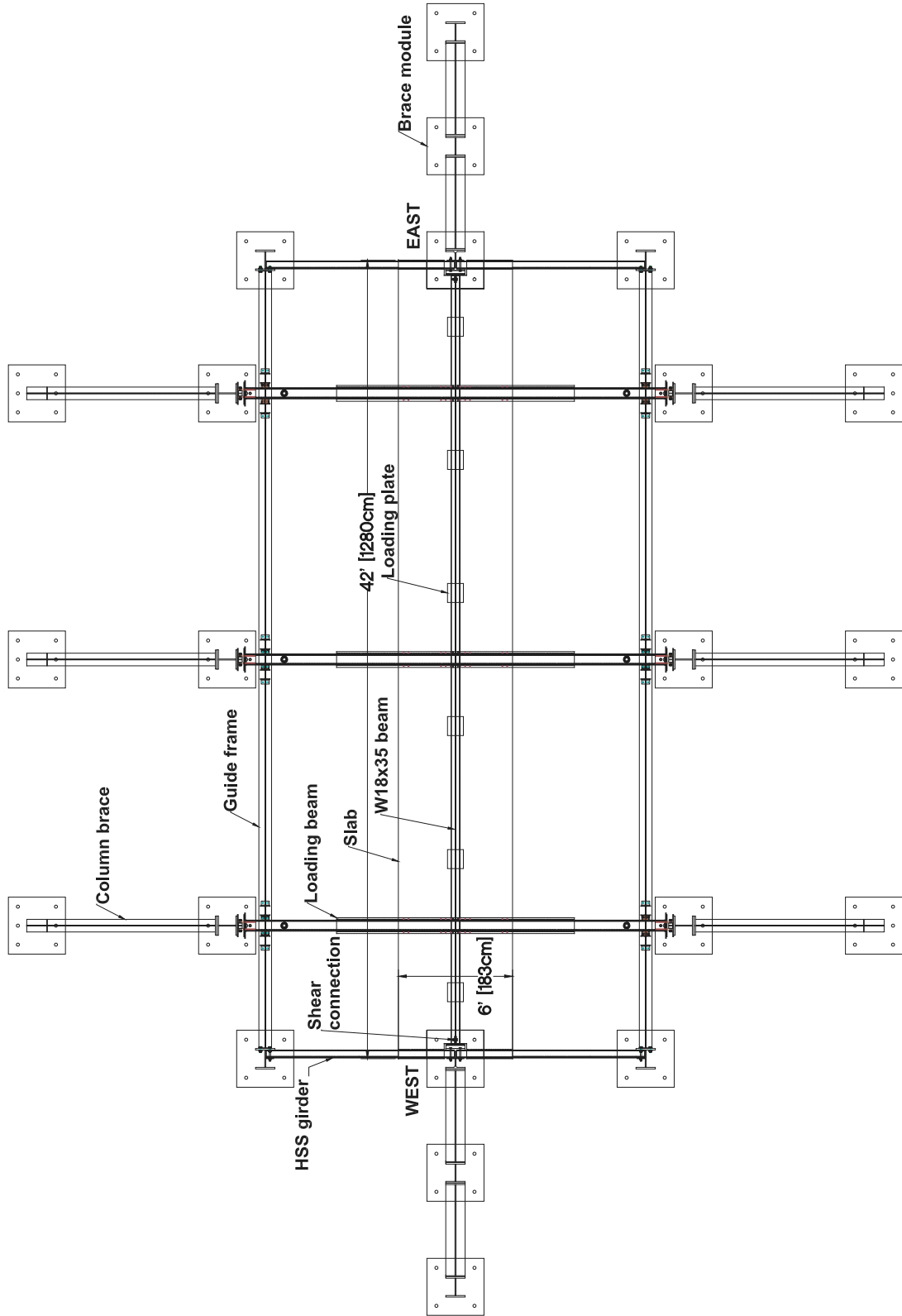


Figure A- 2 Test setup – plan view.

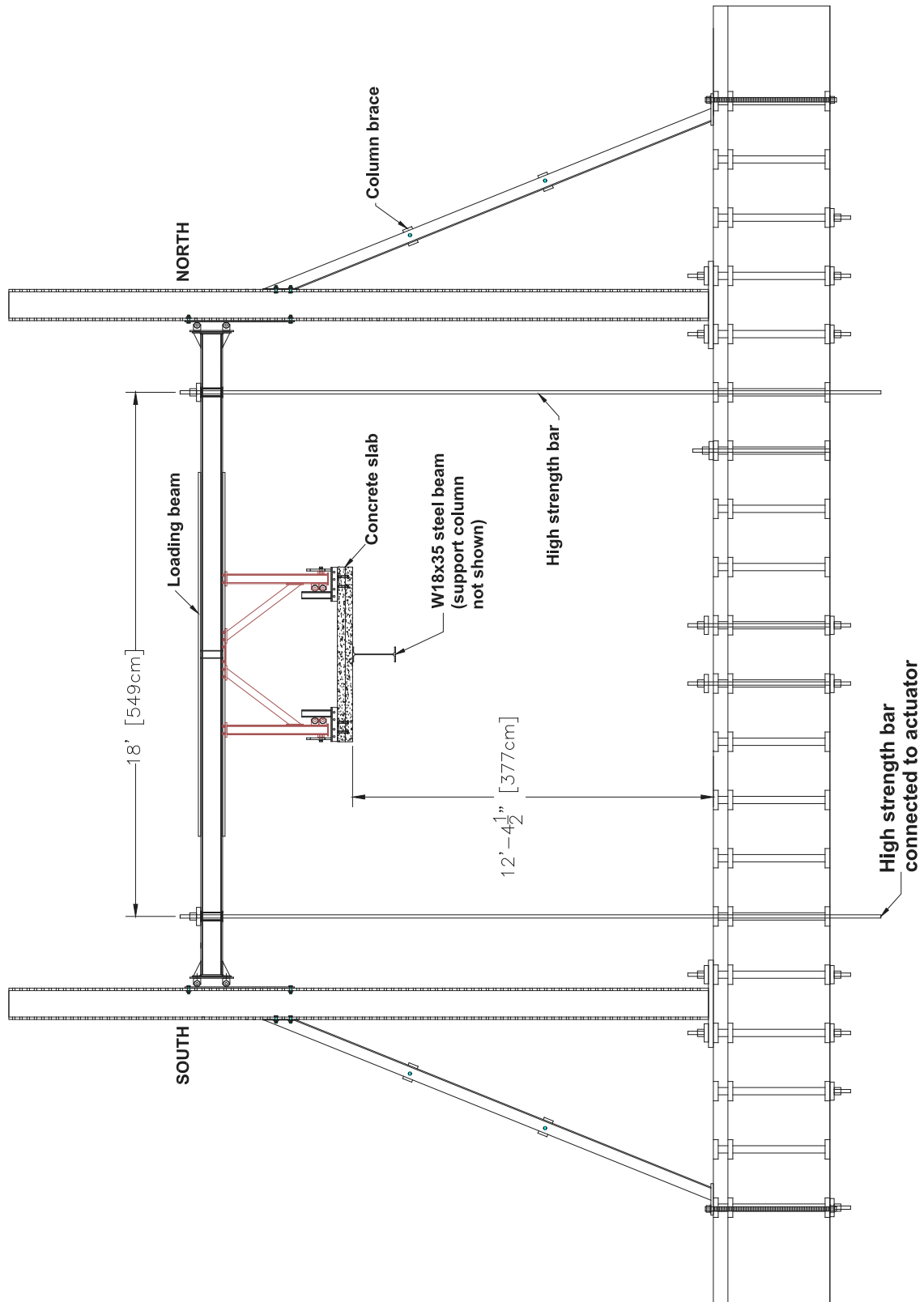


Figure A- 3 Test setup – side view.

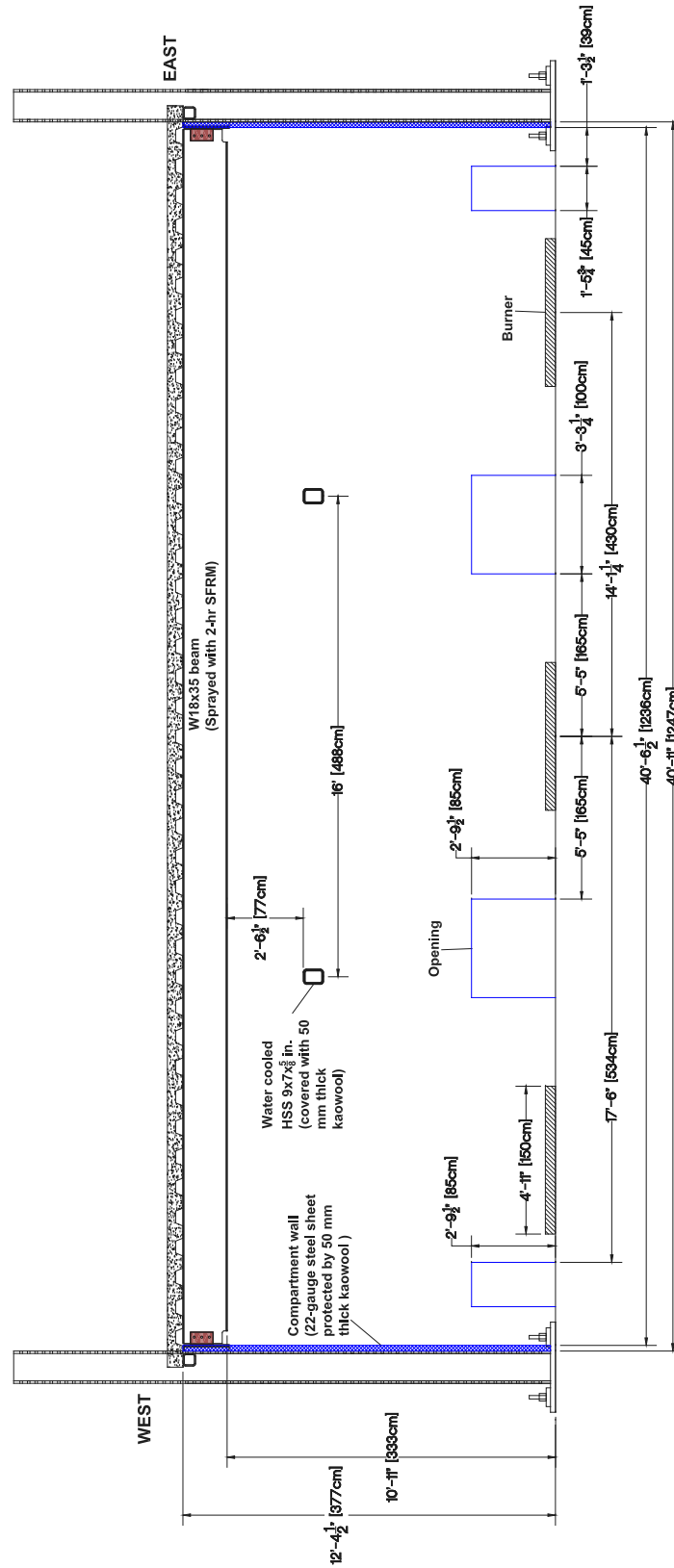
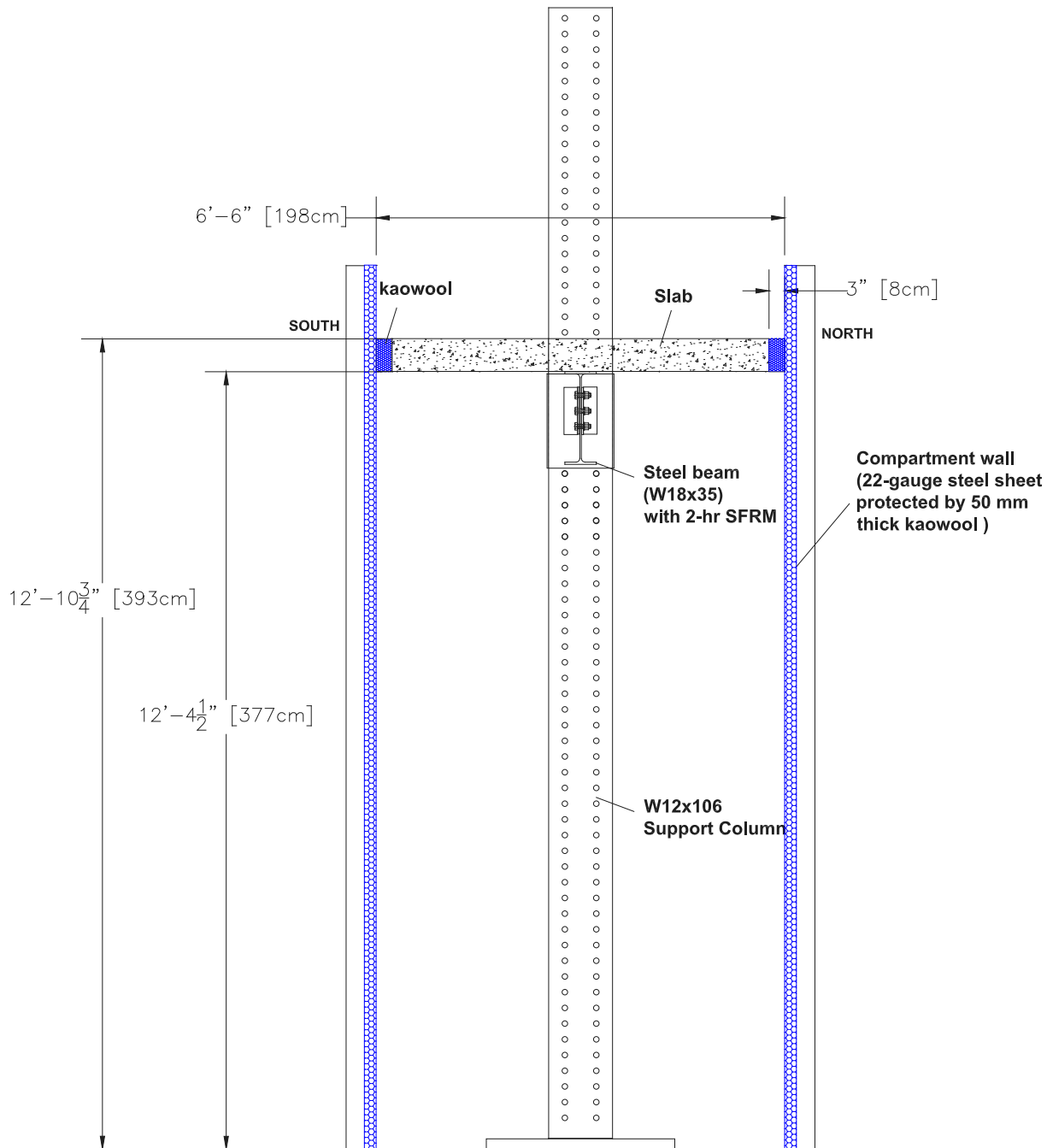


Figure A- 4 Compartment wall layout – front view.





**Figure A- 6 Compartment wall layout – side view.**



# APPENDIX B

## SURVEY RESULTS FOR DESIGN PARAMETERS AND SPECIMEN DESIGN CALCULATIONS

Survey results of parameters used for design of composite floor systems

Design Parameter	Firm 1	Firm 2	Firm 3		Firm 4	Firm 5	Firm 6			NFRL Composite Beam Specimen
							Response 1	Response 2	Response 3	
Percent composite action	45-50%	50%	one stud per foot		25% to 50%	min. 25%	100%	min. 25%	min. 25%	One stud per foot (82%)
Beam Spacing	10 ft	10 ft	10 ft		10-12 ft	10 ft	8-10 ft	8-12 ft	8-11 ft	10 ft
Construction live load	25 psf	20 psf	25 psf		20psf	20 psf (15 psf to 50 psf)	40 psf	20 psf	20 psf	20 psf
Live load (LL)	65 psf (including 15 psf for partition)	65 psf (including 15 psf for partition)	50 psf		80 to 100 psf	70 psf (including 20 psf for partition)	50 psf	(40 psf for residential or 100 to 125 psf for office) + 20 to 30 psf for partitions	(40 psf for residential or 50 psf for office) + 20 to 30 psf for partitions	70 psf (including 20 psf for partition)
Concrete strength	3000 psi	4000 psi	5000 psi		4000 psi	3,000 psi for LW and 3,500 psi for NW	4000 psi	3,000 to 5,000 psi (4000 psi is the most typical)	4000 psi	4000 psi
Light weight/Normal weight concrete	Light weight	Light weight	Light weight	Normal weight	Light weight	Light weight for short, 30-ft spans; Normal weight for longer, 40-ft or 45-ft span	Light weight		Light weight	Light weight
Metal deck gauge	20 ga	20 ga	20 ga	20 ga	20 ga	20 ga	16 ga	18-20 ga	20 ga min.; often 18 ga	20 ga
Metal deck dimension	3 in.	2 in (3 in. is most common)	3 in.	3 in.	3 in.	3 in.	3 in.	2 in. or 3 in.	Typically 3 in. though sometimes 2 in.	3 in.
Slab thickness	3.5 in.	3.25 in.	3.25 in.	2.5 in.	3.25 in.	3.25 in. for LW or 4.5 in. for NW		5.25 in. or 6.25 in. (Total thickness)	3.25 in. for LW or 4.5 in. for NW	3.25 in.
WWF or Rebar	6X6 W1.4XW1.4	6x6 - W2.1xW2.1	6x6 - W1.4xW1.4	6x6 - W1.4xW1.4	no. 4 rebars @12 in. spacing	6x6-W2.0XW2.0 (6x6-W1.4 XW1.4 for 3.25 in. slab thickness)	no. 4 or no. 5 bars	Advice against using WWF	no. 3 rebars @15 in. spacing	6X6 W1.4XW1.4
Negative reinforcement over girders	5-ft long no. 4 rebars @ 24 in. spacing (crack control reinforcement)	3-ft long no. 4 rebars @ 12 in. spacing (crack control reinforcement)	Just the mesh	Just the mesh	no. 4 rebars @ 12 in. spacing	5-ft long no. 4 rebars @ 18 in. spacing	no. 5 rebars @ 12 in. spacing	Maybe with heavier loads	no. 3 rebars @ 12 in. spacing	5-ft long no. 4 rebars @ 18 in. spacing (crack control reinforcement)
Fire resistance rating (h)	2 hr	2 hr	2 hr	2 hr	2 hr	2 hr	2 hr	2 hr	2 hr	2 hr
Camber/shore	camber	No Shoring	No	1" on the beams	camber (never shored)	Camber – yes for beams, no for girders / no shoring.	Yes		Camber for beams if needed; no camber for girders if beams are cambered	Specimens cast on floor
Superimposed dead	10 psf (additional 5-10 psf for an office partition)	10 psf	30 psf							10 psf

This publication is available free of charge from: <https://doi.org/10.6028/NIST.TN.2054>

This calculation shows the design of a 42-ft long composite beam with a 2-hour fire resistance rating, spaced at 10 ft. For the design, ASCE 7 (2016) gravity load combination of (1.2 Dead Load +1.6 Live Load) with design loads of a construction live load of 20 psf, a superimposed dead load of 10 psf, and a live load of 70 psf was used. Design of bolted welded double-angle and single plate shear connections is also included.

### 1. Design parameters: Dimensions, Material properties, and Loads

Length of beam  $L := 42 \text{ ft}$

Beam spacing  $S_{beam} := 10 \text{ ft}$

Effective width of the concrete slab  
(AISC 360-10 Section I3.1a)  $b_E := \min\left(S_{beam}, \frac{L}{4}\right) = 10 \text{ ft}$

**Try W18X35 for the beam**

From ANSI/AISC 360-16 Manual Table 2-4, the material properties of ASTM A992 steel are as follows:

Specified minimum yield stress of the type of steel being used

$$F_y := 50 \cdot \text{ksi}$$

Specified minimum tensile strength of the type of steel being used

$$F_u := 65 \cdot \text{ksi}$$

Modulus of elasticity of steel

$$E_s := 29000 \cdot \text{ksi}$$

From ANSI/AISC 360-10 Manual Table 1-1, the geometric properties of W18X35 are as follows:

Flange width:  $b_f := 6.00 \cdot \text{in}$       Flange Thickness:  $t_f := 0.425 \cdot \text{in}$

Web thickness  $t_w := 0.300 \cdot \text{in}$       Section depth:  $d := 17.7 \cdot \text{in}$

Cross sectional area of beam  $A_s := 10.3 \cdot \text{in}^2$

Moment of inertia about the strong axis  $I_x := 510 \cdot \text{in}^4$

Plastic section modulus taken about the strong axis  $Z_x := 66.5 \cdot \text{in}^3$

Clear distance between flanges less the corner radius  $h := 53.5 \cdot t_w = 16.05 \text{ in}$

Nominal weight of the beam  $w_{beam} := 0.035 \frac{\text{kip}}{\text{ft}}$

Select Vulcraft 3VLI20 deck with 3 1/4 in. thick slab for concrete floor for a beam spacing of 10 ft, light weight concrete, and two hour fire rating from the manufacturer catalog

Concrete material properties are as follows:

Nominal compressive strength of concrete  $f'_c := 4 \cdot ksi$   $3 ksi \leq f'_c \leq 6 ksi$  AISC 360-16 Section I1.3)

Unit weight of light weight concrete  $w_c := 110 pcf$

Elastic modulus of concrete (AISC 360-16 Section I8-2a)  $E_c := \left(\frac{w_c}{pcf}\right)^{1.5} \cdot \sqrt{\frac{f'_c}{ksi}} \cdot ksi = (2.307 \cdot 10^3) ksi$

From steel deck manufacturer catalog (Vulcraft 3VLI20, Light Weight Concrete)

Slab thickness above rib  $t_s := 3.25 in$  (Selected for a 2 hour fire rating)

Nominal rib height  $h_r := 3 in$   $h_r \leq 3 in$  OK! Per AISC 360-16 Section I3.2c

Average rib width  $w_r := 6 in$   $w_r \geq 2 in$

Nominal weight of the slab (From Vulcraft catalog)  $w_{slab} := 46 psf$

Try Nelson S3L 3/4 X 5 3/16 MS for shear studs

Shear connector dimensions and material properties

Nelson S3L 3/4 X 5 3/16 MS

Burnout length = 3/16 in.

Type B shear stud connectors made from ASTM A108

Diameter of shear stud  $d_{sa} := \frac{3}{4} \cdot in$   $2.5 \cdot t_f = 1.063 in$

$d_{sa} < 2.5 \cdot t_f$  OK! Per AISC 360-16 Section I8.1

Cross-sectional area of shear stud  $A_{sa} := \frac{\pi}{4} \cdot (d_{sa})^2 = 0.442 in^2$

Minimum tensile strength of shear stud material  $F_{u.sa} := 65 ksi$

Length of 3/4" headed shear studs (after installment)  $h_{sa} := 5.0 \cdot in$   $h_{sa} \geq 4 \cdot d_{sa} = 3 in$  Ok! Per AISC 360-16 Section I8.2

AISC 360-16 Section I3.2c  $t_s + h_r - h_{sa} = 1.25 in$   $t_s + h_r - h_{sa} \geq 0.5 in$  Ok!

$h_{sa} - h_r = 2 in$   $h_{sa} - h_r \geq 1.5 in$  Ok!

$t_s = 3.25 in$   $t_s \geq 2 in$  Ok!

## Loads

Self weight  $w_{D,SW} := \left( w_{slab} + \frac{w_{beam}}{b_E} \right) = 49.5 \text{ psf}$

Construction live load  $w_{L,CL} := 20 \text{ psf}$

Superimposed dead load  $w_{D,SL} := 10 \text{ psf}$

Service dead load  $w_D := w_{D,SW} + w_{D,SL} = 59.5 \text{ psf}$

Service live load  $w_{L,1} := 70 \text{ psf}$

Service live load (after reduction)  
(From AISC 7-16, Section 4.7.2,  
KLL=2 for interior beams in Table  
4-2)

$$w_L := w_{L,1} \cdot \left( 0.25 + \frac{15}{\sqrt{2 \cdot \left( \frac{L}{ft} \cdot \frac{S_{beam}}{ft} \right)}} \right)$$

$$w_L = 53.728 \text{ psf}$$

Factored construction load  $w_{u,c} := 1.2 \cdot w_{D,SW} + 1.6 \cdot w_{L,CL} = 91.4 \text{ psf}$

Factored service load  $w_u := 1.2 \cdot w_D + 1.6 \cdot w_L = 157.366 \text{ psf}$

## 2. Flexural Strength and Deflection During Construction (Pre-Composite):

Maximum moment due to factored  
load during construction:

$$M_{u,c} := \frac{w_{u,c} \cdot S_{beam} \cdot L^2}{8} = 201.537 \text{ kip} \cdot \text{ft}$$

Maximum shear due to factored  
load during construction:

$$V_{u,c} := \frac{w_{u,c} \cdot S_{beam} \cdot L}{2} = 19.194 \text{ kip}$$

Check compactness per AISC 360-16 Section F2

$$\frac{h}{t_w} = 53.5 \quad 3.76 \cdot \sqrt{\frac{E_s}{F_y}} = 90.553 \quad \frac{b_f}{2 \cdot t_f} = 7.059 \quad 0.38 \cdot \sqrt{\frac{E_s}{F_y}} = 9.152$$

$$\frac{h}{t_w} < 3.76 \cdot \sqrt{\frac{E_s}{F_y}} \quad \text{OK !} \quad \frac{b_f}{2 \cdot t_f} < 0.38 \cdot \sqrt{\frac{E_s}{F_y}} \quad \text{OK !}$$

Assume that adequate bracing is provided by the deck attached (perpendicular) to the beam

Flexural capacity of beam during  
construction:

$$\phi_b M_p := 0.9 \cdot F_y \cdot Z_x = 249.375 \text{ kip} \cdot \text{ft}$$

$$M_{u,c} = 201.537 \text{ kip} \cdot \text{ft} \quad \phi_b M_p > M_{u,c} \quad \text{OK !}$$

Maximum deflection during construction  $\Delta_c := \frac{5 \cdot w_{D,SW} \cdot S_{beam} \cdot L^4}{384 \cdot E_s \cdot I_x} = 2.343 \text{ in}$

Limiting dead load deflection according to AISC Design Guide 3 (2nd Edition)  $\min\left(\frac{L}{360}, 1 \text{ in}\right) = 1 \text{ in}$

$\Delta_{DL} > \min\left(\frac{L}{360}, 1 \text{ in}\right)$  No Good !

Select a camber of about 80% of the the deflection ( $\Delta_c$ ) according to AISC Design Guide 3 (2nd Edition)

Camber  $\Delta_{camber} := 1.75 \text{ in}$

$\Delta_c - \Delta_{camber} = 0.593 \text{ in}$   $\Delta_c - \Delta_{camber} < \min\left(\frac{L}{360}, 1 \text{ in}\right)$  OK !

### 3. Strength and Deflection due to Service Load (Composite):

Maximum moment due to factored service load:  $M_u := \frac{w_u \cdot b_E \cdot L^2}{8} = 346.991 \text{ kip} \cdot \text{ft}$

Maximum shear at support due to factored service load:  $V_u := \frac{w_u \cdot b_E \cdot L}{2} = 33.047 \text{ kip}$

#### Shear strength of Shear Studs

Shear stud diameter  $d_{sa} = 0.75 \text{ in}$

Cross-sectional area of shear stud  $A_{sa} = 0.442 \text{ in}^2$

Minimum tensile strength of shear stud material  $F_{u,sa} = 65 \text{ ksi}$

Nominal compressive strength of concrete  $f'_c = 4 \text{ ksi}$

Elastic modulus of concrete  $E_c = (2.307 \cdot 10^3) \text{ ksi}$

Per AISC 360-16 Section I8.2a

For Steel deck oriented perpendicular to the beam with 1 stud per decking rib, emid-ht > 2 in.

$R_g := 1.0$   $R_p := 0.75$

Nominal shear strength of one stud (for one stud per deck rib)  $Q_n := \min\left(0.5 \cdot A_{sa} \cdot \sqrt{f'_c \cdot E_c}, R_g \cdot R_p \cdot A_{sa} \cdot F_{u,sa}\right)$

$Q_n = 21.221 \text{ kip}$

$$0.5 \cdot A_{sa} \cdot \sqrt{f'_c \cdot E_c} = 21.221 \text{ kip}$$

$$R_g \cdot R_p \cdot A_{sa} \cdot F_{u.sa} = 21.537 \text{ kip}$$

Spacing Limits (AISC 360-16 Section I8.2d)

$$S_{max} := \min(8 \cdot (t_s + h_r), 36 \text{ in}) = 36 \text{ in}$$

$$S_{min} := 6 \cdot d_{sa} = 4.5 \text{ in}$$

Try

$$S_{studs} := 12 \text{ in}$$

Maximum of 18 in. to satisfy AISC 360-16 Section I3.2c, otherwise need to use puddle welds to anchor the deck to the beam

$$S_{min} < S_{studs} < S_{max} \quad \text{OK !}$$

Place the first shear stud at or beyond 12 in. from the column center line in order to allocate the connection at the end. Furthermore, AISC 360-16 Section I8.2d requires a minimum distance of 10 in. from the center of the stud to a free edge in the direction of shear for lightweight concrete.

Number of shear studs between maximum moment and zero moment (between the center and the support)

$$n_{studs.1} := \left( \frac{\frac{L}{2} - 12 \text{ in}}{S_{studs}} \right) = 20$$

Choose the number of shear studs

$$n_{studs} := 20 \quad (\text{place the first stud at 18 in. from the column centerline and the 21st stud at 6 in. from the center of the beam})$$

$$\Sigma Q_n := Q_n \cdot n_{studs} = 424.426 \text{ kip}$$

Nominal strength for tensile yielding of steel section

$$A_s \cdot F_y = 515 \text{ kip}$$

Nominal strength for Concrete crushing

$$0.85 \cdot f'_c \cdot b_E \cdot t_s = (1.326 \cdot 10^3) \text{ kip}$$

Commentary I3.2 of AISC 360-16 recommends (but does not require) at least 50% of composite action or one 3/4" dia. stud per foot to have enough ductility after reaching the nominal strength.

$$\text{Percentage of composite action} = \frac{\Sigma Q_n}{\min(A_s \cdot F_y, 0.85 \cdot f'_c \cdot b_E \cdot t_s)} \cdot 100 = 82.413 > 50 \% \quad \text{Ok !}$$

## Flexural strength of composite beam

Check the compactness per AISC 360-16 Section I3.2 and Table B4.1b

$$\frac{h}{t_w} = 53.5 \quad 3.76 \cdot \sqrt{\frac{E_s}{F_y}} = 90.553$$

$$\frac{h}{t_w} < 3.76 \cdot \sqrt{\frac{E_s}{F_y}} \quad \text{Ok !} \quad \text{Per AISC 360-16 Section I3.2}$$

$$\Sigma Q_n < A_s \cdot F_y \quad \text{Hence, plastic neutral axis is below the slab}$$

Assume that the depth of stress block = a  $a := \frac{\Sigma Q_n}{0.85 \cdot f'_c \cdot b_E} = 1.04 \text{ in}$

Assume that the plastic neutral axis is in the flange and distance "x" below the top of the flange

For equilibrium  $\Sigma Q_n + x_1 \cdot b_f \cdot F_y = (A_s - x_1 \cdot b_f) \cdot F_y$

$$x_1 := \frac{A_s \cdot F_y - \Sigma Q_n}{2 \cdot b_f \cdot F_y} = 0.151 \text{ in}$$

while,  $t_f = 0.425 \text{ in}$

$x_1 < t_f$  Hence the assumption that the plastic neutral axis is in the beam flange is correct

Nominal moment capacity (moment about PNA) using Equation C-I3-10 of AISC 360-16

Distance from the centroid of the compression force in the concrete to the top of the steel section  $d_1 := h_r + t_s - \frac{a}{2} = 5.73 \text{ in}$

Distance from the centroid of the compression force in the steel section to the top of the steel section  $d_2 := \frac{x_1}{2} = 0.075 \text{ in}$

Distance from the centroid of the steel section to the top of the steel section  $d_3 := \frac{d}{2} = 8.85 \text{ in}$

$$M_n := \Sigma Q_n \cdot (d_1 + d_2) + A_s \cdot F_y \cdot (d_3 - d_2) = 581.902 \text{ kip} \cdot \text{ft}$$

$$\phi_b M_n := (0.90) \cdot M_n = 523.711 \text{ kip} \cdot \text{ft}$$

$$M_u = 346.991 \text{ kip} \cdot \text{ft} \quad \phi_b M_n > M_u \quad \text{Ok !}$$

### Shear strength of steel beam

For the steel: AISC 360-16 Section I4.1 and Section G2

$$\frac{h}{t_w} = 53.5 < 2.24 \cdot \sqrt{\frac{E_s}{F_y}} = 53.946$$

$$C_v := 1 \quad \phi_v := 1$$

The nominal shear strength is:

$$V_n := 0.6 \cdot F_y \cdot (d \cdot t_w) \cdot C_v = 159.3 \text{ kip}$$

$$\phi_v \cdot V_n = 159.3 \text{ kip} \quad V_u = 33.047 \text{ kip}$$

$$\phi_v \cdot V_n > V_u \quad \text{Ok!}$$

### Check for deflection and vibration

Calculate the second moment of area of the transformed section

$$\text{Transform concrete to steel} \quad n := \frac{E_s}{E_c} = 12.568$$

$$\text{Transformed width of slab} \quad b_{tr} := \frac{b_E}{n} = 9.548 \text{ in}$$

$$\text{Neutral axis depth (from top of slab)} \quad y_{NA} := \frac{(b_{tr} \cdot t_s) \cdot \frac{t_s}{2} + (A_s) \cdot \left(t_s + h_r + \frac{d}{2}\right)}{(b_{tr} \cdot t_s) + (A_s)} = 4.983 \text{ in}$$

$$I_{tr} := \left( \frac{1}{12} b_{tr} \cdot t_s^3 + b_{tr} \cdot t_s \cdot \left(y_{NA} - \frac{t_s}{2}\right)^2 \right) + \left( I_x + A_s \cdot \left(t_s + h_r + \frac{d}{2} - y_{NA}\right)^2 \right) = (1.941 \cdot 10^3) \text{ in}^4$$

$$I_{equiv} := I_x + \sqrt{\frac{\Sigma Q_n}{A_s \cdot F_y}} \cdot (I_{tr} - I_x) = (1.809 \cdot 10^3) \text{ in}^4 \quad \text{Eq C-I3-3 from AISC 360-10}$$

$$I_{eff} := I_{equiv} \quad \text{From AISC 360-16}$$

Effective second moment of area of the composite section

$$I_{eff} = (1.809 \cdot 10^3) \text{ in}^4$$



Dead load deflection:

Maximum deflection for superimposed dead load  $\Delta_{SDL} := \frac{5 \cdot w_{D,SL} \cdot b_E \cdot L^4}{384 \cdot E_s \cdot I_{eff}} = 0.133 \text{ in}$

Maximum deflection during construction  $\Delta_c = 2.343 \text{ in}$  (from page 4)

Camber  $\Delta_{camber} = 1.75 \text{ in}$

Maximum deflection for total dead load  $\Delta_{DL} := \Delta_{SDL} + (\Delta_c - \Delta_{camber})$

$\Delta_{DL} = 0.727 \text{ in}$

Limiting dead load deflection according to AISC Design Guide 3 (2nd Edition)  $\min\left(\frac{L}{360}, 1 \text{ in}\right) = 1 \text{ in}$

$\Delta_{DL} < \min\left(\frac{L}{360}, 1 \text{ in}\right)$  OK!

Live load deflection:

Maximum deflection for live load  $\Delta_{LL} := \frac{5 \cdot w_L \cdot b_E \cdot L^4}{384 \cdot E_s \cdot I_{eff}}$

$\Delta_{LL} = 0.717 \text{ in}$

Limiting live load deflection according to IBC 2018  $\frac{L}{360} = 1.4 \text{ in}$   $\Delta_{LL} < \frac{L}{360}$  OK!

Deflection at mid point for 50% Live Load  $\Delta_{0.5LL} := \frac{1}{2} \cdot \Delta_{LL} = 0.358 \text{ in}$

Limiting deflection for half of live load according to AISC Design Guide 3 (2nd Edition) = 1 in.

$\Delta_{0.5LL} < 1 \text{ in}$  OK!

Total deflection:

Total Deflection (D+L)

$\Delta_{T1} := \Delta_{DL} + \Delta_{LL} = 1.444 \text{ in}$

For the load combination (1.0 DL + 1.0 LL) in Equation CC-1a, in Commentary Appendix C of AISC/SEI 7-16

Limiting total deflection according to IBC 2018  $\frac{L}{240} = 2.1 \text{ in}$   $\Delta_{T1} < \frac{L}{240}$  Good!

Check for Vibration:

AISC Design Guide 11-2015, Refer to the design guide for the notations

For Beam: Transform area:

Effective width  $b_{E.vib} := \min(S_{beam}, 0.4 \cdot L) = 10 \text{ ft}$

Transform concrete to steel  $n_{vib} := \frac{E_s}{1.35 \cdot E_c} = 9.31$

Transformed width of slab  $b_{tr.vib.beam} := \frac{b_{E.vib}}{n_{vib}} = 12.889 \text{ in}$

Neutral axis depth (from top of slab)  $y_{NA.vib.beam} := \frac{(b_{tr.vib.beam} \cdot t_s) \cdot \frac{t_s}{2} + (A_s) \cdot \left(t_s + h_r + \frac{d}{2}\right)}{(b_{tr.vib.beam} \cdot t_s) + (A_s)} = 4.284 \text{ in}$

$$I_j := \left( \frac{1}{12} b_{tr.vib.beam} \cdot t_s^3 + b_{tr.vib.beam} \cdot t_s \cdot \left( y_{NA.vib.beam} - \frac{t_s}{2} \right)^2 \right) + I_x + A_s \cdot \left( t_s + h_r + \frac{d}{2} - y_{NA.vib.beam} \right)^2$$

$$I_j = (2.048 \cdot 10^3) \text{ in}^4$$

Uniform distributed loading

$$w_j := S_{beam} \cdot (w_D + 11 \text{ psf})$$

$$\Delta_j := \frac{5 \cdot w_j \cdot L^4}{384 \cdot E_s \cdot I_j} = 0.831 \text{ in}$$

$$g := 386 \frac{\text{in}}{\text{s}^2}$$

$$f_j := 0.18 \cdot \sqrt{\frac{g}{\Delta_j}} = 3.879 \frac{1}{\text{s}} \quad \text{Eq. 3.3 (Design Guide 11)}$$

$$D_s := \frac{\left( t_s + \frac{h_r}{2} \right)^3}{12 \cdot n_{vib}} = 11.512 \frac{\text{in}^4}{\text{ft}}$$

$$D_j := \frac{I_j}{S_{beam}} = 204.801 \frac{\text{in}^4}{\text{ft}}$$

$C_j := 2$  Beam Length  $L_j := L = 42 \text{ ft}$  Girder Length  $L_g := 30 \text{ ft}$

$$B_j := \min \left( C_j \cdot \left( \frac{D_s}{D_j} \right)^{0.25} \cdot L_j, \frac{2}{3} \cdot 3 \cdot L_g \right) = 40.901 \text{ ft} \quad \text{Eq. 4.3a (Design Guide 11)}$$

$$W_j := 1.5 \cdot \left( \frac{w_j}{S_{beam}} \right) \cdot B_j \cdot L_j = 181.66 \text{ kip} \quad \text{Eq. 4.2 (Design Guide 11)}$$

For Girder:

Assume W24x62 Girder with 44ft x 30 ft bay

$$L_g := 30 \text{ ft} \quad I_{x2} := 1550 \cdot \text{in}^4 \quad w_{girder} := 0.062 \frac{\text{kip}}{\text{ft}}$$

$$A_{g2} := 18.2 \cdot \text{in}^2 \quad d_2 := 23.0 \text{ in}$$

Transform area:

$$\text{Effective width} \quad b_{E.vib.girder} := 0.4 \cdot L_g = 12 \text{ ft}$$

$$\text{Transform concrete to steel} \quad n_{vib} := \frac{E_s}{1.35 \cdot E_c} = 9.31$$

$$\text{Transformed width of slab} \quad b_{tr.vib.girder} := \frac{b_{E.vib.girder}}{n_{vib}} = 15.467 \text{ in}$$

$$\text{Neutral axis depth (from top of slab)} \quad y_{NA.vib.girder} := \frac{(b_{tr.vib.girder} \cdot t_s) \cdot \frac{t_s}{2} + (A_{g2}) \cdot \left( t_s + h_r + \frac{d_2}{2} \right)}{(b_{tr.vib.girder} \cdot t_s) + (A_{g2})} = 5.911 \text{ in}$$

$$I_g := \left( \frac{1}{12} b_{tr.vib.girder} \cdot t_s^3 + b_{tr.vib.girder} \cdot t_s \cdot \left( y_{NA.vib.girder} - \frac{t_s}{2} \right)^2 \right) + I_{x2} + A_{g2} \cdot \left( t_s + h_r + \frac{d_2}{2} - y_{NA.vib.girder} \right)^2$$

$$I_g = (5.069 \cdot 10^3) \text{ in}^4$$

Uniform distributed loading

$$w_g := L_j \cdot \left( \frac{w_j}{S_{beam}} \right) + w_{girder}$$

$$\Delta_g := \frac{5 \cdot w_g \cdot (L_g)^4}{384 \cdot E_s \cdot I_g} = 0.375 \text{ in}$$

$$g := 386 \frac{\text{in}}{\text{s}^2}$$

$$f_g := 0.18 \cdot \sqrt{\frac{g}{\Delta g}} = 5.776 \frac{1}{s} \quad \text{Eq. 3.3 (Design Guide 11)}$$

$$D_g := \frac{I_g}{L_j} = 10.057 \text{ in}^3$$

$$C_g := 1.8$$

$$B_g := \min \left( C_g \cdot \left( \frac{D_j}{D_g} \right)^{0.25} \cdot L_g, \frac{2}{3} \cdot 3 \cdot L_j \right) = 61.633 \text{ ft} \quad \text{Eq. 4.3b (Design Guide 11)}$$

$$W_g := \left( \frac{w_g}{L_j} \right) \cdot B_g \cdot L_g = 133.084 \text{ kip} \quad \text{Eq. 4.2 (Design Guide 11)}$$

$$L_g = 30 \text{ ft} \quad B_j = 40.901 \text{ ft} \quad L_g < B_j$$

$$\Delta g_{new} := \frac{L_g}{B_j} \cdot \Delta g = 0.275 \text{ in} \quad \text{Eq. 4.5 (Design Guide 11)}$$

$$f_{floor} := 0.18 \cdot \sqrt{\frac{g}{\Delta j + \Delta g_{new}}} = 3.363 \frac{1}{s} \quad \text{Eq. 3.4 (Design Guide 11)}$$

$$W := \frac{\Delta j}{\Delta j + \Delta g} \cdot W_j + \frac{\Delta g}{\Delta j + \Delta g} \cdot W_g = 166.562 \text{ kip} \quad \text{Eq. 4.4 (Design Guide 11)}$$

From AISC Steel Design Guide 11, Table 4.1

$$P_0 := 65 \text{ lbf}$$

$$\beta := 0.04 \quad (\text{selected for offices})$$

$$a_p := \frac{P_0 \cdot \exp(-0.35 \cdot f_{floor} \cdot s) \cdot g}{\beta \cdot W} = 0.097 \frac{\text{ft}}{\text{s}^2} \quad \text{Eq. 4.1 (Design Guide 11)}$$

$$\frac{a_p}{g} = 0.003$$

$$a_0 := 0.005 \cdot g$$

$$\frac{a_0}{g} = 0.005 \quad \frac{a_p}{g} \leq \frac{a_0}{g} \quad \text{Good}$$

#### 4. Welded Wire Reinforcement

Use welded wire fabric for minimum reinforcement (WWR)

From Vulcraft Product catalog for 3VLI20, 6.25 in. total slab depth, use 6x6- W1.4xW1.4 welded wire fabric

From SDI C-2017 Standard for Composite Steel Floor Deck - Slabs for crack control

$$A_{crack.control.min} := 0.00075 \cdot (t_s \cdot 1 \text{ ft}) = 0.029 \text{ in}^2$$

$$\text{Area of WWR per foot} \quad A_{Fabric} := \frac{1 \text{ ft}}{6 \text{ in}} \cdot \left( \frac{1.4}{100} \cdot \text{in}^2 \right) = 0.028 \text{ in}^2$$

$$A_{Fabric} = A_{crack.control.min} \quad \text{Ok !}$$

#### 5. Connection between the beam specimen and columns: Bolted Welded Double Angles

$$\text{Reaction at support at service load} \quad V_u := V_u = 33.047 \text{ kip}$$

$$\text{Shear strength of steel beam} \quad \phi_v \cdot V_n = 159.3 \text{ kip}$$

Try 5x5x3/8 angle

From Table 10-1 of AISC 360-16 for W18 shapes, try 3/4 in. bolts (A325) at 3 rows

$$\text{Thickness of angle} \quad t_{angle} := 0.375 \text{ in}$$

$$\text{Number of bolt rows} \quad n_{rows} := 3$$

$$\text{Vertical spacing of bolts} \quad s_{bolts} := 3 \text{ in}$$

$$\text{Vertical length of angle} \quad l_{angle} := n_{rows} \cdot s_{bolts} = 9 \text{ in}$$

$$d_b := 0.75 \text{ in} \quad A_b := \frac{\pi}{4} \cdot (d_b)^2 = 0.442 \text{ in}^2 \quad d_h := \frac{13}{16} \cdot \text{in}$$

From Table J3.2 of AISC 360-16,  $F_{nv} := 68 \text{ ksi}$  Threads are excluded from the shear plane

$$\phi R_{n.shear.bolt.1} := 0.75 \cdot (F_{nv}) \cdot (A_b) = 22.531 \text{ kip}$$

Considering shear strength of bolt, shear yielding, shear rupture, bolt bearing, and block shear rupture of angles, from Table 10-1,

$$\phi R_{n.shear.1} := 115 \text{ kip}$$

Considering bolt bearing and block shear rupture of beam web, from Table 10-1, (for  $L_{ev} = 3$  in. (min) and  $L_{eh} = 1.75$  in., for uncoped beam)

$$L_{ev} := 3 \text{ in} \quad L_{eh} := 1.75 \text{ in} \quad \phi R_{n, shear.2} := 263 \frac{\text{kip}}{\text{in}} \cdot t_w = 78.9 \text{ kip}$$

From Table 10-2 of AISC 360-10 for bolts at 3 rows, and weld B of 5/16 in.

$$\phi R_{n, shear.3} := 60.2 \text{ kip}$$

Shear yielding along beam web (per Section J4)

$$\phi R_{n, shear.4} := (1.0) \cdot (0.6 \cdot F_y) \cdot (t_w \cdot (d - t_f)) = 155.475 \text{ kip}$$

Shear rupture along beam web (per Section J4)

$$\phi R_{n, shear.5} := (0.75) \cdot (0.6 \cdot F_u) \cdot \left( t_w \cdot \left( d - t_f - n_{rows} \cdot \left( d_h + \frac{1}{16} \cdot \text{in} \right) \right) \right) = 128.554 \text{ kip}$$

$$\phi R_{n, shear} := \min(\phi R_{n, shear.1}, \phi R_{n, shear.2}, \phi R_{n, shear.3}, \phi R_{n, shear.4}, \phi R_{n, shear.5}) = 60.2 \text{ kip}$$

$$\phi R_{n, shear} > V_u$$

$$\frac{\phi R_{n, shear}}{V_u} = 1.822$$

## 6. Connection between the beam specimen and columns: Single Plate Shear Connection

Reaction at support at service load  $V_u := V_u = 33.047 \text{ kip}$

Shear strength of steel beam  $\phi_v \cdot V_n = 159.3 \text{ kip}$

Try 7/16 in. thick plate

From Table 10-1 of AISC 360-16 for W18 shapes, try 3/4 in. bolts (A325) at 3 rows

Thickness of Plate  $t_p := \frac{7}{16} \text{ in}$

Number of bolt rows  $n_{rows} := 3$

Vertical spacing of bolts  $s_{bolts} := 3 \text{ in}$

Vertical length of plate  $l_p := n_{rouss} \cdot s_{bolts} = 9 \text{ in}$

$$d_b := 0.75 \text{ in} \quad A_b := \frac{\pi}{4} \cdot (d_b)^2 = 0.442 \text{ in}^2 \quad d_h := \frac{13}{16} \cdot \text{in}$$

From Table J3.2 of AISC 360-16,  $F_{nv} := 68 \text{ ksi}$  Threads are excluded from the shear plane

$$\phi R_{n, shear, bolt.1} := 0.75 \cdot (F_{nv}) \cdot (A_b) = 22.531 \text{ kip}$$

Considering shear strength of bolt, shear yielding, shear rupture, bolt bearing, and block shear rupture of the plate and the shear strength of weld, from Table 10-10a,

$$\phi R_{n, shear.1} := 55.6 \text{ kip} \quad \text{Weld size} \quad a_{weld} := \frac{5}{8} \cdot t_p = 0.273 \text{ in}$$

Considering bolt bearing and block shear rupture of beam web, from Table 10-1, (for  $L_{ev} = 3 \text{ in. (min)}$  and  $L_{eh} = 1.75 \text{ in.}$ , for coped at top flange only)

$$L_{ev} := 3 \text{ in} \quad L_{eh} := 1.75 \text{ in} \quad \phi R_{n, shear.2} := 251 \frac{\text{kip}}{\text{in}} \cdot t_w = 75.3 \text{ kip}$$

Shear yielding along beam web (per Section J4)

$$\phi R_{n, shear.3} := (1.0) \cdot (0.6 \cdot F_y) \cdot (t_w \cdot (d - t_f)) = 155.475 \text{ kip}$$

Shear rupture along beam web (per Section J4)

$$\phi R_{n, shear.4} := (0.75) \cdot (0.6 \cdot F_u) \cdot \left( t_w \cdot \left( d - t_f - n_{rouss} \cdot \left( d_h + \frac{1}{16} \cdot \text{in} \right) \right) \right) = 128.554 \text{ kip}$$

$$\phi R_{n, shear} := \min(\phi R_{n, shear.1}, \phi R_{n, shear.2}, \phi R_{n, shear.3}, \phi R_{n, shear.4}) = 55.6 \text{ kip}$$

$$\phi R_{n, shear} > V_u$$

$$\frac{\phi R_{n, shear}}{V_u} = 1.682$$

## APPENDIX C

### FIRE DYNAMICS SIMULATOR INPUT FILES

---

This Appendix presents the FDS input file for Case 5Be as an example for the input files used for the analysis of this study.

```
&HEAD CHID='isolated_beam_case_B5e', TITLE='Proposed NFRL structure fire' /
&MESH IJK=46,32,80, XB=-0.5,1.8,-0.6,1.0,0.0,4.0, MULT_ID='mesh' /
&MULT ID='mesh', DX=2.3, DY=1.6, I_UPPER=5, J_UPPER=1 /
&TIME T_END=14400.0, TIME_SHRINK_FACTOR=10. /
&REAC FUEL='METHANE', SOOT_YIELD=0.001 /
&SURF ID='BURNER1', COLOR='BROWN',
      HRRPUA=888.9, RAMP_Q='fire' /
&RAMP ID='fire', T= 0., F=0. /
&RAMP ID='fire', T= 600., F=1. /
&RAMP ID='fire', T=10800., F=1. /
&RAMP ID='fire', T=12610., F=0. /
&MATL ID='CONCRETE'
  DENSITY = 2000.
  CONDUCTIVITY = 0.8
  EMISSIVITY = 0.63
  SPECIFIC_HEAT = 0.85 /
&MATL ID='CERAMIC BLANKET'
  EMISSIVITY = 0.7
  DENSITY = 96.
  SPECIFIC_HEAT = 1.13
  CONDUCTIVITY_RAMP = 'k-ramp' /
&RAMP ID='k-ramp', T= 25., F=0.04 /
&RAMP ID='k-ramp', T=400., F=0.12 /
&RAMP ID='k-ramp', T=800., F=0.30 /
&MATL ID='STEEL'
  SPECIFIC_HEAT = 0.45
  EMISSIVITY = 0.7
```



DENSITY = 7800.  
 CONDUCTIVITY = 45. /  
 &MATL ID= 'INSULATION' FYI = 'Carboline MK5'  
 EMISSIVITY = 0.7  
 DENSITY = 350.  
 CONDUCTIVITY\_RAMP = 'k\_insulation'  
 SPECIFIC\_HEAT\_RAMP = 'c\_insulation' /  
 &RAMP ID='c\_insulation', T= 25., F=2.00 /  
 &RAMP ID='c\_insulation', T=200., F=3.50 /  
 &RAMP ID='c\_insulation', T=400., F=2.00 /  
 &RAMP ID='c\_insulation', T=700., F=5.00 /  
 &RAMP ID='k\_insulation', T= 25., F=0.10 /  
 &RAMP ID='k\_insulation', T=250., F=0.05 /  
 &RAMP ID='k\_insulation', T=700., F=0.08 /  
 &SURF ID='BEAM FLANGE' COLOR = 'GRAY 60'  
 MATL\_ID = 'INSULATION','STEEL','INSULATION' THICKNESS = 0.016,0.011,0.016 /  
 &SURF ID='BEAM WEB' COLOR = 'GRAY 60'  
 MATL\_ID = 'INSULATION','STEEL','INSULATION' THICKNESS = 0.016,0.011,0.016 /  
 &SURF ID='COLUMN' COLOR = 'BLACK'  
 MATL\_ID = 'STEEL' THICKNESS = 0.011 /  
 &SURF ID='WALL FRONT FACE' DEFAULT = .TRUE. RGB = 200,200,200  
 MATL\_ID = 'CERAMIC BLANKET','CONCRETE' THICKNESS = 0.025,0.0125 /  
 &SURF ID='WALL COLUMN FRONT FACE' RGB = 200,200,200  
 MATL\_ID = 'CERAMIC BLANKET','CONCRETE','STEEL' THICKNESS = 0.025,0.0125,0.011 /  
 &SURF ID='WALL BACK FACE' RGB = 100,100,100  
 MATL\_ID = 'CONCRETE','CERAMIC BLANKET' THICKNESS = 0.0125,0.025 /  
 &SURF ID='WALL COLUMN BACK FACE' COLOR = 'BLACK'  
 MATL\_ID = 'STEEL', 'CONCRETE', 'CERAMIC BLANKET' THICKNESS = 0.011,0.0125,0.025 /  
 &SURF ID='FLOOR' RGB = 100,100,100  
 MATL\_ID = 'CONCRETE' THICKNESS = 1.0 /  
 &SURF ID='CEILING BOTTOM' COLOR = 'SILVER'  
 MATL\_ID = 'STEEL','CONCRETE' THICKNESS = 0.003,0.1 /  
 &SURF ID='CEILING TOP' COLOR = 'GRAY 50'  
 MATL\_ID = 'CONCRETE','STEEL' THICKNESS = 0.1,0.003 /

&OBST XB= 0.30, 0.35, 0.0, 0.9, 0.0, 3.7, SURF\_ID6='WALL BACK FACE','WALL FRONT FACE',  
'WALL BACK FACE','WALL BACK FACE','WALL BACK FACE','WALL BACK FACE'/west  
wall

&OBST XB= 0.30, 0.35, 0.9, 1.1, 0.0, 3.7, SURF\_ID6='WALL COLUMN BACK FACE', 'WALL  
COLUMN FRONT  
FACE', 'WALL BACK FACE','WALL BACK FACE','WALL BACK FACE','WALL BACK  
FACE'/west wall

&OBST XB= 0.30, 0.35, 1.1, 2.0, 0.0, 3.7, SURF\_ID6='WALL BACK FACE','WALL FRONT FACE',  
'WALL BACK FACE','WALL BACK FACE','WALL BACK FACE','WALL BACK  
FACE'/west wall

&OBST XB=12.45,12.50, 0.0, 0.9, 0.0, 3.7, SURF\_ID6='WALL FRONT FACE','WALL BACK FACE',  
'WALL BACK FACE','WALL BACK FACE','WALL BACK FACE','WALL BACK FACE'/east  
wall

&OBST XB=12.45,12.50, 0.9, 1.1, 0.0, 3.7, SURF\_ID6='WALL COLUMN FRONT FACE','WALL  
COLUMN

BACK FACE','WALL BACK FACE','WALL BACK FACE','WALL BACK FACE','WALL BACK  
FACE'/e. wall

&OBST XB=12.45,12.50, 1.1, 2.0, 0.0, 3.7, SURF\_ID6='WALL FRONT FACE','WALL BACK FACE',  
'WALL BACK FACE','WALL BACK FACE','WALL BACK FACE','WALL BACK FACE'/east  
wall

&OBST XB= 0.3,12.5, 0.0, 2.0, 3.7, 3.75, SURF\_ID6='CEILING BOTTOM','CEILING BOTTOM',  
'CEILING BOTTOM','CEILING BOTTOM','CEILING BOTTOM','CEILING TOP'/concrete slab

&OBST XB= 0.3,12.5,-0.05, 0.0, 0.0, 3.7, SURF\_ID6='WALL BACK FACE','WALL BACK FACE',  
'WALL BACK FACE','WALL FRONT FACE','WALL BACK FACE','WALL BACK  
FACE'/front wall

&OBST XB= 0.3,12.5, 2.0, 2.05, 0.0, 3.7, SURF\_ID6='WALL BACK FACE','WALL BACK FACE',  
'WALL FRONT FACE','WALL BACK FACE','WALL BACK FACE','WALL BACK  
FACE'/back wall

&HOLE XB= 0.75, 1.20,-0.2, 0.1, 0.0, 0.85 / Ventilation opening

&HOLE XB= 3.75, 4.75,-0.2, 0.1, 0.0, 0.85 / Ventilation opening

&HOLE XB= 8.05, 9.05,-0.2, 0.1, 0.0, 0.85 / Ventilation opening

&HOLE XB=11.60,12.05,-0.2, 0.1, 0.0, 0.85 / Ventilation opening

&HOLE XB= 0.75, 1.20, 1.9, 2.2, 0.0, 0.85 / Ventilation opening

&HOLE XB= 3.75, 4.75, 1.9, 2.2, 0.0, 0.85 / Ventilation opening

&HOLE XB= 8.05, 9.05, 1.9, 2.2, 0.0, 0.85 / Ventilation opening

&HOLE XB=11.60,12.05, 1.9, 2.2, 0.0, 0.85 / Ventilation opening

&OBST XB= 1.35, 2.85, 0.5, 1.5, 0.0, 0.1, SURF\_IDS='BURNER1','COLUMN','COLUMN' / west  
burner

&OBST XB= 5.65, 7.15, 0.5, 1.5, 0.0, 0.1, SURF\_IDS='BURNER1','COLUMN','COLUMN' / center burner

&OBST XB= 9.95,11.45, 0.5, 1.5, 0.0, 0.1, SURF\_IDS='BURNER1','COLUMN','COLUMN' / east burner

&OBST XB= 0.35,12.45, 0.9, 1.1, 3.69, 3.70, SURF\_ID='BEAM FLANGE' / beam, upper flange

&OBST XB= 0.35,12.45, 1.0, 1.0, 3.30, 3.70, SURF\_ID='BEAM WEB' / beam, web

&OBST XB= 0.35,12.45, 0.9, 1.1, 3.30, 3.30, SURF\_ID='BEAM FLANGE' / beam, lower flange

&OBST XB= 0.00, 0.00, 0.9, 1.1, 0.00, 3.70, SURF\_ID='COLUMN' /west column, flange away from wall

&OBST XB= 0.00, 0.30, 1.0, 1.0, 0.00, 3.70, SURF\_ID='COLUMN' /west column web

OBST XB= 0.29, 0.30, 0.9, 1.1, 0.00, 3.70, SURF\_ID='WALL COLUMN BACK FACE' /west column, flange abutting wall (this BC is applied to wall section)

OBST XB=12.50,12.51, 0.9, 1.1, 0.00, 3.70, SURF\_ID='WALL COLUMN BACK FACE' /east column, flange abutting wall (this BC is applied to wall section)

&OBST XB=12.50,12.80, 1.0, 1.0, 0.00, 3.70, SURF\_ID='COLUMN' /east column, web

&OBST XB=12.80,12.80, 0.9, 1.1, 0.00, 3.70, SURF\_ID='COLUMN' /east column, flange away from wall

&VENT MB='XMIN', SURF\_ID='OPEN' /

&VENT MB='XMAX', SURF\_ID='OPEN' /

&VENT MB='YMIN', SURF\_ID='OPEN' /

&VENT MB='YMAX', SURF\_ID='OPEN' /

&VENT MB='ZMIN', SURF\_ID='FLOOR' /

&VENT MB='ZMAX', SURF\_ID='OPEN' /

&DUMP NFRAMES=3600, DT\_DEVC=60., DT\_HRR=60., SIG\_FIGS=4, SIG\_FIGS\_EXP=2 /

&DEVC ID='T\_HGL-1', QUANTITY='UPPER TEMPERATURE', XB=4.8,4.8,0.8,0.8,0.0,3.7 /

&DEVC ID='T\_HGL-2', QUANTITY='UPPER TEMPERATURE', XB=9.6,9.6,0.8,0.8,0.0,3.7 /

&DEVC ID='T\_Beam-01', QUANTITY='INSIDE WALL TEMPERATURE', DEPTH=0.016,

XYZ= 1.1,1.01,3.3, IOR=-3 /

&DEVC ID='T\_Beam-02', QUANTITY='INSIDE WALL TEMPERATURE', DEPTH=0.016,

XYZ= 2.0,1.01,3.3, IOR=-3 /

&DEVC ID='T\_Beam-03', QUANTITY='INSIDE WALL TEMPERATURE', DEPTH=0.016,

XYZ= 3.1,1.01,3.3, IOR=-3 /

&DEVC ID='T\_Beam-04', QUANTITY='INSIDE WALL TEMPERATURE', DEPTH=0.016,

XYZ= 4.0,1.01,3.3, IOR=-3 /

&DEVC ID='T\_Beam-05', QUANTITY='INSIDE WALL TEMPERATURE', DEPTH=0.016,

XYZ= 5.0,1.01,3.3, IOR=-3 /

```
&DEVC ID='T_Beam-06', QUANTITY='INSIDE WALL TEMPERATURE', DEPTH=0.016,  
    XYZ= 6.1,1.01,3.3, IOR=-3 /  
&DEVC ID='T_Beam-07', QUANTITY='INSIDE WALL TEMPERATURE', DEPTH=0.016,  
    XYZ= 7.0,1.01,3.3, IOR=-3 /  
&DEVC ID='T_Beam-08', QUANTITY='INSIDE WALL TEMPERATURE', DEPTH=0.016,  
    XYZ= 8.0,1.01,3.3, IOR=-3 /  
&DEVC ID='T_Beam-09', QUANTITY='INSIDE WALL TEMPERATURE', DEPTH=0.016,  
    XYZ= 9.1,1.01,3.3, IOR=-3 /  
&DEVC ID='T_Beam-10', QUANTITY='INSIDE WALL TEMPERATURE', DEPTH=0.016,  
    XYZ=10.0,1.01,3.3, IOR=-3 /  
&DEVC ID='T_Beam-11', QUANTITY='INSIDE WALL TEMPERATURE', DEPTH=0.016,  
    XYZ=11.0,1.01,3.3, IOR=-3 /  
&DEVC ID='T_Beam-12', QUANTITY='INSIDE WALL TEMPERATURE', DEPTH=0.016,  
    XYZ=11.9,1.01,3.3, IOR=-3 /  
&DEVC ID='T_Column-1', QUANTITY='INSIDE WALL TEMPERATURE', DEPTH=0.0375,  
    XYZ= 0.35,1.01,3.2, IOR=1 /  
&DEVC ID='T_Column-2', QUANTITY='INSIDE WALL TEMPERATURE', DEPTH=0.0375,  
    XYZ=12.45,1.01,3.2, IOR=-1 /  
&BNDF QUANTITY='GAUGE HEAT FLUX', CELL_CENTERED=.TRUE. /  
&BNDF QUANTITY='WALL TEMPERATURE', CELL_CENTERED=.TRUE. /  
&BNDF QUANTITY='ADIABATIC SURFACE TEMPERATURE', CELL_CENTERED=.TRUE. /  
&SLCF PBY=0.80, QUANTITY='TEMPERATURE', VECTOR=.TRUE. /  
&TAIL /
```

# APPENDIX D STEEL MILL CERTIFICATES

**Steel Dynamics, Inc.**  
Long Products Group  
Structural and Flat Division

(260) 625-8100 (260) 625-8950 FAX  
Quality Steel 100% EAF Melted  
and Manufactured in the USA  
Recycled content: PC = 77.0%, PI = 19.4%  
ISO 9001:2008 and ABS Certified

**Ship to:**  
Alro Steel Corporation  
1035 Freeman S.W.  
P.O. Box 1846  
Clinton Rapids MI, 49503 US  
Attn: Receiving

**Customer #** 000088

**Printed:** 07 / 11 / 2016  
**Produced:** 06 / 26 / 2016

**Bill to:**  
ALRO STEEL CORPORATION  
3100 East High Street  
Jackson MI, 49204 US  
Attn: Steve Beckelman

**CERTIFIED MILL TEST REPORT**

**SHIPMENT DETAILS**  
BOL # 0000418659 - 4725.00 lbs  
Bundle / ASN # Length pcs Cust PO | Recv PO | Job  
060653125 45' 0" 3 GR1216069

---

**GENERAL INFORMATION**

Product Wide Flange Beam  
Size W18X35  
Heat Number A124019  
Condition(s) As-Rolled  
Fine Grained  
Fully Killed  
No Weld Repair

**SPECIFICATIONS**

Standards  
ASTM A588M - 16  
» ASTM A992/A992M - 11  
ASTM A709/A709M - 16a  
ASTM A572/A572M - 15  
AASHTO M270/M270 - 12  
CSA G40.21-13  
ASTM A36/A36M - 14

Grades  
A992 / A992M  
A709 gr50/gr345  
A572 gr50/gr345  
M270 gr345/gr50  
50W/350W  
A36 / A36M

**CHEMICAL ANALYSIS** (weight percent)

C	Mn	P	S	Si	Cu	Ni	Cr	Mo	Sn	V	Nb/Cb	Al	N	B	*C1	*C2	*C3	*PC	*I	Analysis Type
.06	1.23	.012	.029	.22	.23	.07	.10	.022	.008	.034	.001	.001	.0125	.0003	.32	.35	.30	.15	4.99	Heat

---

**MECHANICAL TESTING**

Test	Yield (fy)		Tensile Strength	Elong. ratio	% Elong. (8" gage)
	ksi / MPa	ksi / MPa			
1	56 / 386	75 / 518	74 / 511	.74	23
2	59 / 408	74 / 511		.80	23
3					
4					

Temp F / C

Test 1 2 3 4 5 6 7

**CHARPY IMPACT TESTS** (available only when specified at time of order)

Temp	Absorbed Energy ft.-lb. / J	Specimen 1	Specimen 2	Specimen 3	Average	Minimum

ALRO STEEL/METAL  
RT08053162

JUL 11 2016  
*[Signature]*

---

**NOTES:** \*Calculates Charpy Values, Carbon Equivalents (C1, C2, C3, PC), Conversion Factor (F), ASTM G1012-26 (1)(C)(1)-(3.88)(M)+1 20(C)(1), 48(S)(1)+7.26(P), 28(C)(U)(1)+9 10(N)(P) 33.38(C)(P)  
CEI (1)(W)-C-1001-C-2-M02-U/S-04-C015 CEZ (A)(S)(C)-M-1015-(C)(M)-U/S-04-C015 CEZ (C)(E) 7-C-1001-C-2-M02-U/S-04-C015 CEZ (C)(E) 7-C-1001-C-2-M02-U/S-04-C015  
I hereby certify that the material described herein has been made to the applicable specification by the electric arc remelted continuous cast process and tested in accordance with the requirements of American Bureau of Shipping Rules with satisfactory results.

**ABS CERTIFICATION**

Signed: \_\_\_\_\_  
Notary Public

State of Indiana, County of Whitley Sworn to and subscribed before me  
this \_\_\_\_\_ day of \_\_\_\_\_  
My commission expires: \_\_\_\_\_

---

Signed: **Jeremy Cronkhite**  
Quality Manager

ASTM A6 - 14.6

I hereby certify that the content of this report are accurate and correct. All tests and operations performed by this material manufacturer are in compliance with the requirements of the material specifications and applicable purchaser designated requirements.

Notwithstanding the absence of a signature, the organization submitting the report is responsible for the content of the report.

Figure D-1 W18x35 Steel Beam Mill Certificate.

**Customer Name** National Institute of Standards and Tech      **Customer PO#** DORIS      **Invoice No** 882126      **Shipper No** 858182      **Heat Number** 60114888

Page 1/1

**CERTIFIED MATERIAL TEST REPORT**

<p><b>CUSTOMER SHIP TO</b> INFRA METALS CO 4501 CURTIS AVE BALTIMORE, MD 21226-1355 USA</p> <p><b>SALES ORDER</b> 3194885/000040</p>	<p><b>CUSTOMER BILL TO</b> INFRA METALS CO 580 MIDDLETOWN BLVD LANGHORNE, PA 19047-1877 USA</p> <p><b>BILL OF LADING</b> 1330-0000063902</p> <p><b>DATE</b> 01/19/2016</p>	<p><b>GRADE</b> A992/A372-50</p> <p><b>LENGTH</b> 45'00"</p> <p><b>SPECIFICATION / DATE OF REVISION</b> ASTM A6-14 ASTM A709-13A ASTM A992-11, A572-15 CSA G40.21-13 345WM</p>	<p><b>SHAPE / SIZE</b> Wide Flange Beam / 18 X 35# / 460 X 52</p> <p><b>WEIGHT</b> 20,475 LB</p> <p><b>HEAT / BATCH</b> 60114888/02</p>
--	--	--	---

<p><b>CUSTOMER PURCHASE ORDER NUMBER</b> MA-502789</p>	<p><b>CUSTOMER MATERIAL N°</b></p>
--	------------------------------------

<p><b>CHEMICAL COMPOSITION</b> CE9/A6 0.32</p>	<p><b>CHEMICAL COMPOSITION</b></p>	<p><b>CHEMICAL COMPOSITION</b></p>	<p><b>CHEMICAL COMPOSITION</b></p>
<p>C 0.09</p> <p>Mn 0.97</p> <p>P 0.019</p> <p>S 0.023</p> <p>Si 0.21</p> <p>Cr 0.13</p> <p>Cu 0.35</p> <p>Ni 0.12</p> <p>Mo 0.027</p> <p>Al 0.002</p>	<p>C 0.09</p> <p>Mn 0.97</p> <p>P 0.019</p> <p>S 0.023</p> <p>Si 0.21</p> <p>Cr 0.13</p> <p>Cu 0.35</p> <p>Ni 0.12</p> <p>Mo 0.027</p> <p>Al 0.002</p>	<p>C 0.09</p> <p>Mn 0.97</p> <p>P 0.019</p> <p>S 0.023</p> <p>Si 0.21</p> <p>Cr 0.13</p> <p>Cu 0.35</p> <p>Ni 0.12</p> <p>Mo 0.027</p> <p>Al 0.002</p>	<p>C 0.09</p> <p>Mn 0.97</p> <p>P 0.019</p> <p>S 0.023</p> <p>Si 0.21</p> <p>Cr 0.13</p> <p>Cu 0.35</p> <p>Ni 0.12</p> <p>Mo 0.027</p> <p>Al 0.002</p>

<p><b>MECHANICAL PROPERTIES</b></p> <p>YS<sub>0.2</sub> % 54700</p> <p>YS<sub>0.01</sub> % 55400</p> <p>UTS 68200</p> <p>UTS 69300</p> <p>Elong 200.0</p> <p>GI 200.0</p> <p>GI 200.0</p>	<p><b>MECHANICAL PROPERTIES</b></p> <p>UTS 68200</p> <p>UTS 69300</p> <p>Elong 200.0</p> <p>GI 200.0</p> <p>GI 200.0</p>	<p><b>MECHANICAL PROPERTIES</b></p> <p>UTS 68200</p> <p>UTS 69300</p> <p>Elong 200.0</p> <p>GI 200.0</p> <p>GI 200.0</p>	<p><b>MECHANICAL PROPERTIES</b></p> <p>UTS 68200</p> <p>UTS 69300</p> <p>Elong 200.0</p> <p>GI 200.0</p> <p>GI 200.0</p>
---	--	--	--


  

<p><b>MECHANICAL PROPERTIES</b></p> <p>UTS 470</p> <p>UTS 478</p> <p>Y/T<sub>0.01</sub> rati 0.802</p> <p>Y/T<sub>0.01</sub> rati 0.799</p> <p>GI 8.000</p> <p>GI 8.000</p>	<p><b>MECHANICAL PROPERTIES</b></p> <p>UTS 470</p> <p>UTS 478</p> <p>Y/T<sub>0.01</sub> rati 0.802</p> <p>Y/T<sub>0.01</sub> rati 0.799</p> <p>GI 8.000</p> <p>GI 8.000</p>	<p><b>MECHANICAL PROPERTIES</b></p> <p>UTS 470</p> <p>UTS 478</p> <p>Y/T<sub>0.01</sub> rati 0.802</p> <p>Y/T<sub>0.01</sub> rati 0.799</p> <p>GI 8.000</p> <p>GI 8.000</p>	<p><b>MECHANICAL PROPERTIES</b></p> <p>UTS 470</p> <p>UTS 478</p> <p>Y/T<sub>0.01</sub> rati 0.802</p> <p>Y/T<sub>0.01</sub> rati 0.799</p> <p>GI 8.000</p> <p>GI 8.000</p>
---	---	---	---

**COMMENTS / NOTES**

The above figures are certified chemical and physical test records as contained in the permanent records of company. We certify that these data are correct and in compliance with specified requirements. This material, including the billets, was melted and manufactured in the USA. CMTR complies with EN 10204 3.1.


  
 BHASKAR YALAMANCHILI  
 QUALITY DIRECTOR

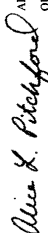

  
 ALICE K. PITCHFORD  
 QUALITY ASSURANCE MGR.

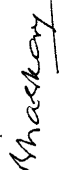
Figure D-2 W18x35 Steel Beam Mill Certificate.

**Customer Name** National Institute of Standards and Tech      **Customer PO#** DORIS      **Invoice No** 882126      **Shipper No** 858182      **Heat Number** 60114887

Page 1/1

CERTIFIED MATERIAL TEST REPORT																																	
<b>CUSTOMER SHIP TO</b> INFRA METALS CO 4501 CURTIS AVE BALTIMORE, MD 21226-1355 USA	<b>CUSTOMER BILL TO</b> INFRA METALS CO 580 MIDDLETOWN BLVD LANGHORNE, PA 19047-1877 USA	<b>GRADE</b> A992/A572-50	<b>SHAPE / SIZE</b> Wide Flange Beam / 18 X 35# / 460 X 52																														
<b>US-ML-PETERSBURG</b> 25801 HOFHEIMER WAY PETERSBURG, VA 23803-8905 USA	<b>SALES ORDER</b> 3194885/000040	<b>LENGTH</b> 45'00"	<b>WEIGHT</b> 7,875 LB																														
<b>CUSTOMER PURCHASE ORDER NUMBER</b> MA-502789		<b>SPECIFICATION / DATE of REVISION</b> ASTM A6-14 ASTM A709-13A ASTM A992-11, A572-15 CSA G40.21-13 345WM																															
<b>BILL OF LADING</b> 1330-0000063902		<b>HEAT / BATCH</b> 60114887/02																															
<b>CUSTOMER MATERIAL N°</b> 01/19/2016																																	
<table style="width: 100%; border-collapse: collapse;"> <tr> <td style="width: 10%;"><b>C</b></td> <td style="width: 10%;">0.10</td> <td style="width: 10%;"><b>S</b></td> <td style="width: 10%;">0.026</td> <td style="width: 10%;"><b>P</b></td> <td style="width: 10%;">0.029</td> <td style="width: 10%;"><b>Mn</b></td> <td style="width: 10%;">0.93</td> <td style="width: 10%;"><b>Si</b></td> <td style="width: 10%;">0.21</td> <td style="width: 10%;"><b>Co</b></td> <td style="width: 10%;">0.37</td> <td style="width: 10%;"><b>Ni</b></td> <td style="width: 10%;">0.13</td> <td style="width: 10%;"><b>Cr</b></td> <td style="width: 10%;">0.22</td> <td style="width: 10%;"><b>Mo</b></td> <td style="width: 10%;">0.030</td> <td style="width: 10%;"><b>S<sub>p</sub></b></td> <td style="width: 10%;">0.015</td> <td style="width: 10%;"><b>V</b></td> <td style="width: 10%;">0.003</td> <td style="width: 10%;"><b>Nb</b></td> <td style="width: 10%;">0.018</td> <td style="width: 10%;"><b>Al</b></td> <td style="width: 10%;">0.002</td> </tr> </table>				<b>C</b>	0.10	<b>S</b>	0.026	<b>P</b>	0.029	<b>Mn</b>	0.93	<b>Si</b>	0.21	<b>Co</b>	0.37	<b>Ni</b>	0.13	<b>Cr</b>	0.22	<b>Mo</b>	0.030	<b>S<sub>p</sub></b>	0.015	<b>V</b>	0.003	<b>Nb</b>	0.018	<b>Al</b>	0.002				
<b>C</b>	0.10	<b>S</b>	0.026	<b>P</b>	0.029	<b>Mn</b>	0.93	<b>Si</b>	0.21	<b>Co</b>	0.37	<b>Ni</b>	0.13	<b>Cr</b>	0.22	<b>Mo</b>	0.030	<b>S<sub>p</sub></b>	0.015	<b>V</b>	0.003	<b>Nb</b>	0.018	<b>Al</b>	0.002								
<b>CHEMICAL COMPOSITION</b> CE9yA6 0.34																																	
<b>MECHANICAL PROPERTIES</b> <table style="width: 100%; border-collapse: collapse;"> <tr> <td style="width: 30%;">YS, 0.2%</td> <td style="width: 10%;">71100</td> <td style="width: 10%;">YS</td> <td style="width: 10%;">390</td> <td style="width: 10%;">YS</td> <td style="width: 10%;">490</td> <td style="width: 10%;">Y/T<sub>rati</sub></td> <td style="width: 10%;">0.796</td> <td style="width: 10%;">G/L</td> <td style="width: 10%;">8.000</td> </tr> <tr> <td>PSI</td> <td>68900</td> <td>MPa</td> <td>379</td> <td>MPa</td> <td>475</td> <td></td> <td>0.797</td> <td>Inch</td> <td>8.000</td> </tr> <tr> <td></td> <td></td> <td></td> <td></td> <td></td> <td></td> <td></td> <td></td> <td></td> <td></td> </tr> </table>				YS, 0.2%	71100	YS	390	YS	490	Y/T <sub>rati</sub>	0.796	G/L	8.000	PSI	68900	MPa	379	MPa	475		0.797	Inch	8.000										
YS, 0.2%	71100	YS	390	YS	490	Y/T <sub>rati</sub>	0.796	G/L	8.000																								
PSI	68900	MPa	379	MPa	475		0.797	Inch	8.000																								
<b>MECHANICAL PROPERTIES</b> <table style="width: 100%; border-collapse: collapse;"> <tr> <td style="width: 30%;">Elong.</td> <td style="width: 10%;">21.90</td> <td style="width: 10%;">Elong.</td> <td style="width: 10%;">24.10</td> </tr> <tr> <td>G/L</td> <td>200.0</td> <td>G/L</td> <td>200.0</td> </tr> <tr> <td>mm</td> <td></td> <td>mm</td> <td></td> </tr> </table>				Elong.	21.90	Elong.	24.10	G/L	200.0	G/L	200.0	mm		mm																			
Elong.	21.90	Elong.	24.10																														
G/L	200.0	G/L	200.0																														
mm		mm																															
<b>COMMENTS / NOTES</b>																																	

The above figures are certified chemical and physical test records as contained in the permanent records of company. We certify that these data are correct and in compliance with specified requirements. This material, including the billets, was melted and manufactured in the USA. CMTR complies with EN 10204 3.1.

  
**BHASKAR YALAMANCHILI**  
 QUALITY DIRECTOR

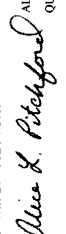

  
**Alice K. Pitchford**  
 ALICE PITCHFORD  
 QUALITY ASSURANCE MGR

Figure D-3 W18x35 Steel Beam Mill Certificate.

# APPENDIX E CONCRETE BATCH TICKETS

This publication is available free of charge from: <https://doi.org/10.6028/NIST.TN.2054>



a US CONCRETE company

DISPATCH	TICKET NUMBER
<b>DC DISPATCH</b> (301) 516-7900  <b>DULLES DISPATCH</b> (703) 471-6969	1601 S. Capitol Street, SW Washington, DC 20003 (301) 577-8800 (301) 577-5840 Fax

**WARNING: IRRITATION TO THE SKIN AND EYES:** Contains Portland Cement. Wear rubber boots and gloves. **PROLONGED CONTACT MAY CAUSE BURNS.** Avoid contact with eyes and prolonged contact with skin. In case of contact with skin or eyes, flush thoroughly with water. If irritation persists, get medical attention. **KEEP CHILDREN AWAY.**

CONCRETE IS A PERISHABLE COMMODITY AND BECOMES THE PROPERTY OF THE PURCHASER UPON LEAVING THE PLANT. ANY CHANGES OR CANCELLATION OF ORIGINAL INSTRUCTIONS MUST BE TELEPHONED TO THE OFFICE BEFORE LOADING STARTS.

WE DO NOT GUARANTEE FINISHED RESULTS OBTAINED FROM THIS LOAD OF CONCRETE AS MANY IMPORTANT FACTORS AFFECTING THE ULTIMATE QUALITY OF THE COMPLETED JOB ARE OUT OF OUR CONTROL. We do not warrant that the concrete can be used in any particular environment or soil conditions or that the concrete is fit for any particular use. Selection of the mix design and/or specification of the mix design parameters are solely the responsibility of the Customer, and we assume no liability therefor.

PLEASE NOTE: THIS LOAD OF CONCRETE IS PRODUCED IN ACCORDANCE WITH STANDARD SPECIFICATIONS FOR READY MIX CONCRETE ASTM. ANY DEFICING MATERIALS, IMPROPER FINISHING AND LACK OF CURING WILL CAUSE DAMAGE OR A DECREASE IN STRENGTH.

NOTICE: MY SIGNATURE BELOW INDICATES THAT I HAVE READ THE HEALTH WARNING NOTICE AND SUPPLIER WILL NOT BE RESPONSIBLE FOR ANY DAMAGE CAUSED WHEN DELIVERING INSIDE CURB LINE AND AGREE TO THE TERMS AND CONDITIONS ON REVERSE SIDE. TIME IN EXCESS OF FREE TIME WILL BE CHARGED AT CURRENT DELAY RATE. ALL C.O.D. DELIVERIES MUST BE PAID IN ADVANCE AND LOAD ACCEPTED BY SIGNING THIS DELIVERY TICKET BEFORE POURING.

LOAD RECEIVED BY:  
[Signature]

**PROPERTY DAMAGE RELEASE**  
(TO BE SIGNED IF DELIVERY TO BE MADE INSIDE CURB LINE)

Dear Customer - The size and weight of this truck could cause damage to the premises and/or adjacent property if this load is placed where you desire. It is our wish to help you in every way that we can, but in order to do this we are requesting that you sign this RELEASE relieving this supplier and its affiliates from any responsibility from damage that may occur to the premises and/or adjacent property, buildings, sidewalks, drive-ways, curbs, etc., due to the delivery of this material, and that you also agree to help the driver remove mud from the wheels of his vehicle so that it will not litter the public street. Further, as additional consideration, the undersigned agrees to indemnify and hold harmless the driver of this truck and this supplier and its affiliates for any and all damage to the premises and/or adjacent property which may be claimed by anyone to have arisen out of delivery of this order.

SIGNED: **X**

**WEIGHMASTER CERTIFICATE**

THIS IS TO CERTIFY that the following described commodity was weighed, measured or counted by a weighmaster whose signature is on this certificate, who is a recognized authority of accuracy, as prescribed by Chapter 7 (commencing with Section 12700) of Division 5 of the California Business and Professions Code, administered by the Division of Measurement Standards of the California Department of Food and Agriculture.

**WATER ADDED AT CUSTOMER REQUEST**  
EXCESSIVE WATER IS DETRIMENTAL TO CONCRETE PERFORMANCE.

X \_\_\_\_\_  
REQUESTOR'S NAME

SA \_\_\_\_\_

FULL LOAD	1/4 LOAD	1/2 LOAD	3/4 LOAD
(GALLONS)	(GALLONS)	(GALLONS)	(GALLONS)

**TEST RESULTS**

SLUMP	CONC. TEMP.	AIR%


CYLINDERS TAKEN:  YES  NO

NAME OF TESTING LAB: \_\_\_\_\_

CUSTOMER DOD N I S T TESTIN	CUSTOMER CODE 1600001	DELIVERY ADDRESS 100 Bureau Dr. Gaithersburg
PROJECT NAME DOD - MD	PROJECT CODE 1500018	
CUSTOMER P.O. # 0004045655 Dry	SPECIAL INSTRUCTIONS Bld#205	
CUSTOMER JOB ID #		

LOAD QUANTITY	ORDERED QTY	CUMULATIVE QTY	PRODUCT ID	DESCRIPTION	UNIT PRICE	EXTENDED PRICE
10.0 yd	20.0 yd	10.0 yd	L40FE6P3	4K-PSI, LTWT with High Fiber1C	158.00	1,580.00
10.0 ea	0.0 ea	0.0 ea	EENV1	ENVIRONMENTAL IMPACT CHARGE	2.00	20.00
10.0 ea	0.0 ea	0.0 ea	EFUEL1	FUEL SURCHARGE	2.00	20.00
<b>COLD WEATHER CONCRETE</b>						35.00

BATCH TIME 3:44	LEAVE PLANT 4:30	ARRIVE JOB 5:20	BEGIN POUR 5:40	FINISH POUR 7:00	LEAVE JOB	ARRIVE AT PLANT	USAGE CODE	SUB TOTAL 1,655.00
TOTAL WAIT TIME	PREVIOUS TRUCK	LOAD #	SLUMP	MAP PAGE	TIME DUE ON JOB	TAX RATE	TAX	95.16
DATE 12/06/16	ORDER # 7017	PLANT 101	TRUCK # 5248	DELIVERY PROFESSIONAL WHITEHEAD, MARVI	ORDER GRAND TOTAL 1,750.16	TOTAL 1,750.16		

TRUCK REV - AT PLANT	TRUCK REV - START	TRUCK REV - FINISH	DEPUTY WEIGHMASTER	CONTROL # 
----------------------	-------------------	--------------------	--------------------	--

Truck	Driver	User	Disp Ticket Num	Ticket ID	Time Date	
5248	1852	user	20220470	19178	3:44 12/6/16	
Load Size	Mix Code	Returned	Qty	Mix Age	Seq Load ID	
10.00 CYDS	L40FE6P3				W3 19972 <i>M4</i>	
Material	Design Qty	Required	Batched	% Moisture	Actual Wat	Trim
CUCEM12	520 lb	5200 lb	5200 lb			
CLFRASH	130 lb	1300 lb	1295 lb			
AUCSDA	1370 lb	14856 lb	14880 lb	8.44% A	139 g/l	
AULMGA	890 lb	9034 lb	9000 lb	1.50% M	16 g/l	
WATER	36.0 gl	159.5 gl	159.0 gl		159.0 g/l	
XUM31	27 oz	270 oz	272 oz			
XUM61	26 oz	260 oz	258 oz			
XUZ11	20 oz	195 oz	192 oz			
Actual	Num Batches: 1	Manual	3:44:32			
Load Total: 31745 lb	Design 0.461 Water/Cement	0.403 A	Design 360.0 g/l	Actual 314.0 g/l	To Add: 46.3 g/l	
Slump: 7.00 in	Water in Truck: 0.0 gl	Adjust Water: 0.0 gl	/ Load	Trim Water: -4.0 gl/ CYD		

H2O added @ plant = 30 gals  
 (25 gals @ plant + 5 gals @ N)  
 H2O added 65 oz  
 = 1.0 oz/100 total 500/100

Figure E-1 Concrete batch ticket for main pour Truck 1.





DISPATCH	
DC DISPATCH (301) 516-7900	1601 S. Capitol Street, SW Washington, DC 20003 (301) 577-8800
DULLES DISPATCH (703) 471-6969	(301) 577-5840 Fax

TICKET NUMBER
 20220471

**WARNING: IRRITATION TO THE SKIN AND EYES:** Contains Portland Cement. Wear rubber boots and gloves. **PROLONGED CONTACT MAY CAUSE BURNS.** Avoid contact with eyes and prolonged contact with skin. In case of contact with skin or eyes, flush thoroughly with water. If irritation persists, get medical attention. **KEEP CHILDREN AWAY.**

CONCRETE IS A PERISHABLE COMMODITY AND BECOMES THE PROPERTY OF THE PURCHASER UPON LEAVING THE PLANT. ANY CHANGES OR CANCELLATION OF ORIGINAL INSTRUCTIONS MUST BE TELEPHONED TO THE OFFICE BEFORE LOADING STARTS.

WE DO NOT GUARANTEE FINISHED RESULTS OBTAINED FROM THIS LOAD OF CONCRETE AS MANY IMPORTANT FACTORS AFFECTING THE ULTIMATE QUALITY OF THE COMPLETED JOB ARE OUT OF OUR CONTROL. We do not warrant that the concrete can be used in any particular environment or soil conditions or that the concrete is fit for any particular use. Selection of the mix design and/or specification of the mix design parameters are solely the responsibility of the Customer, and we assume no liability therefor.

PLEASE NOTE THIS LOAD OF CONCRETE IS PRODUCED IN ACCORDANCE WITH STANDARD SPECIFICATIONS FOR READY MIX CONCRETE ASTM ANY DEFICIENCIES, IMPROPER FINISHING AND LACK OF CURING WILL CAUSE DAMAGE OR A DECREASE IN STRENGTH.

NOTICE: MY SIGNATURE BELOW INDICATES THAT I HAVE READ THE HEALTH WARNING NOTICE AND SUPPLIER WILL NOT BE RESPONSIBLE FOR ANY DAMAGE CAUSED WHEN DELIVERING INSIDE CURB LINE AND AGREE TO THE TERMS AND CONDITIONS ON REVERSE SIDE. TIME IN EXCESS OF FREE TIME WILL BE CHARGED AT CURRENT DELAY RATE. ALL C.O.D. DELIVERIES MUST BE PAID IN ADVANCE AND LOAD ACCEPTED BY SIGNING THIS DELIVERY TICKET BEFORE POURING.

LOAD RECEIVED BY: X *[Signature]*

**PROPERTY DAMAGE RELEASE**  
(TO BE SIGNED IF DELIVERY TO BE MADE INSIDE CURB LINE)

Dear Customer - The size and weight of this truck could cause damage to the premises and/or adjacent property if this load is placed where you desire. It is our wish to help you in every way that we can, but in order to do this we are requesting that you sign this RELEASE relieving this supplier and its affiliates from any responsibility from damage that may occur to the premises and/or adjacent property, buildings, sidewalks, drive-ways, curbs, etc. due to the delivery of this material, and that you also agree to help the driver remove mud from the wheels of his vehicle so that it will not litter the public street. Further, as additional consideration, the undersigned agrees to indemnify and hold harmless the driver of this truck and this supplier and its affiliates for any and all damage to the premises and/or adjacent property which may be claimed by anyone to have arisen out of delivery of this order.

SIGNED: X *[Signature]*

**WEIGHMASTER CERTIFICATE**

THIS IS TO CERTIFY THAT THE FOLLOWING DESCRIBED COMMODITY WAS WEIGHED, MEASURED OR COUNTED BY A WEIGHMASTER WHOSE SIGNATURE IS ON THIS CERTIFICATE, WHO IS A RECOGNIZED AUTHORITY OF ACCURACY, AS PRESCRIBED BY CHAPTER 7 (COMMENCING WITH SECTION 12700) OF DIVISION 5 OF THE CALIFORNIA BUSINESS AND PROFESSIONS CODE, ADMINISTERED BY THE DIVISION OF MEASUREMENT STANDARDS OF THE CALIFORNIA DEPARTMENT OF FOOD AND AGRICULTURE.

**WATER ADDED AT CUSTOMER REQUEST**  
EXCESSIVE WATER IS DETRIMENTAL TO CONCRETE PERFORMANCE.

X \_\_\_\_\_  
REQUESTOR'S NAME

SA \_\_\_\_\_  
FULL LOAD (GALLONS)    1/4 LOAD (GALLONS)    1/2 LOAD (GALLONS)    3/4 LOAD (GALLONS)

TEST RESULTS  
SLUMP: 8    CONC. TEMP:    AIR%:   

CYLINDERS TAKEN:  YES     NO  
NAME OF TESTING LAB: \_\_\_\_\_

CUSTOMER: N I S T TESTIN    CUSTOMER CODE: 1000001    DELIVERY ADDRESS: 100 Bureau Dr. Gaithersburg

PROJECT NAME: COD - MD    PROJECT CODE: 1500018

CUSTOMER P.O. #: 202-494-5655 Bvy    SPECIAL INSTRUCTIONS: Bld#205

CUSTOMER JOB ID #: \_\_\_\_\_

LOAD QUANTITY	ORDERED QTY	CUMULATIVE QTY	PRODUCT ID	DESCRIPTION	UNIT PRICE	EXTENDED PRICE
10.0 yd	20.0	20.0	L40FE6P3	4K-PSI, LTWT with High Fiber	150.00	3,000.00
10.0 ea	0.0	0.0	EENV1	ENVIRONMENTAL IMPACT CHARGE	2.00	20.00
10.0 ea	0.0	0.0	EFUEL1	FUEL BURCHARGE	2.00	20.00
<b>COLD WEATHER CONCRETE</b>						35.00
BATCH TIME: <u>4:30</u> LEAVE PLANT: <u>4:45</u> ARRIVE JOB: <u>6:00</u> BEGIN POUR: <u>6:15</u> FINISH POUR: <u>8:50</u>						SUB TOTAL
TOTAL WAIT TIME: _____    PREVIOUS TRUCK: <u>5248</u> LOAD #: <u>2</u> SLUMP: _____    MAP PAGE: _____    TIME DUE ON JOB: <u>5:43</u> TAX RATE: _____						TAX
DATE: <u>12/06/16</u> ORDER #: <u>7017</u> PLANT: <u>101</u> TRUCK #: <u>5249</u> DELIVERY PROFESSIONAL: <u>HALE, MORRIS</u>						ORDER GRAND TOTAL
DRUM REV - AT PLANT: _____    DRUM REV - START: _____    DRUM REV - FINISH: _____    DEPUTY WEIGHMASTER: _____						TOTAL
						CONTROL #

Truck	Driver	User	Disp Ticket Num	Ticket ID	Time	Date
5249	3896	user	20220471	19179	4:30	12/6/16
Load Size	Mix Code	Returned	Qty	Mix Age	Seq	Load ID
10.00 CYDS	L40FE6P3				W3	19973
Material	Design Qty	Required	Batched	% Moisture	Actual Wat	Tris
CUM12	520 lb	520 lb	5175 lb			
CLFASH	130 lb	130 lb	1298 lb			
AUCSDR	1370 lb	14930 lb	14968 lb	9.04% A	149 g	
AULH6A	890 lb	9834 lb	8968 lb	1.58% M	16 g	
WATER	36.0 gl	149.1 gl	149.0 gl		149.0 gl	
XUN31	27 oz	270 oz	260 oz			
XUN61	33 oz	330 oz	330 oz			
XUZ11	20 oz	195 oz	196 oz			
Actual	Num Batches: 1					
Load Total:	31676 lb	Design 0.461	Water/Cement: 0.461		Design 360.0 gl	Actual 313.8 gl
Slump:	7.00 in	Water in Truck: 0.0 gl	Adjust Water: 0.0 gl		/ Load	Tris Water: -4.0 gl / CYD

*Handwritten notes:*  
 H2O = 25 added @ plant  
 + 5 @ job site  
 - 4.0 gl  
 30 gals  
 Manual = 97.0 added  
 Manual = 6.5 @ 100%  
 Manual 4:30:35  
 To Add: 46.5 gl  
 Note: Manual feed ok  
 MX Another 19.02 added on last 3 yds

Figure E-2 Concrete batch ticket for main pour Truck 2.

This publication is available free of charge from: <https://doi.org/10.6028/NIST.TN.2054>

# SUPERIOR

## CONCRETE MATERIALS, INC.

a US CONCRETE company

**DISPATCH**  
**DC DISPATCH**  
**(301) 516-7900**  
**DULLES DISPATCH**  
**(703) 471-6969**

1601 S. Capitol Street, SW  
 Washington, DC 20003  
**(301) 577-8800**  
**(301) 577-5840 Fax**

**TICKET NUMBER**

20263908

**WARNING: IRRITATION TO THE SKIN AND EYES:** Contains Portland Cement. Wear rubber boots and gloves. PROLONGED CONTACT MAY CAUSE BURNS. Avoid contact with eyes and prolonged contact with skin. In case of contact with skin or eyes, flush thoroughly with water. If irritation persists, get medical attention. KEEP CHILDREN AWAY.

CONCRETE IS A PERISHABLE COMMODITY AND BECOMES THE PROPERTY OF THE PURCHASER UPON LEAVING THE PLANT. ANY CHANGES OR CANCELLATION OF ORIGINAL INSTRUCTIONS MUST BE TELEPHONED TO THE OFFICE BEFORE LOADING STARTS.

WE DO NOT GUARANTEE FINISHED RESULTS OBTAINED FROM THIS LOAD OF CONCRETE AS MANY IMPORTANT FACTORS AFFECTING THE ULTIMATE QUALITY OF THE COMPLETED JOB ARE OUT OF OUR CONTROL. We do not warrant that the concrete can be used in any particular environment or soil conditions or that the concrete is fit for any particular use. Selection of the mix design and/or specification of the mix design parameters are solely the responsibility of the Customer, and we assume no liability therefore.

PLEASE NOTE: THIS LOAD OF CONCRETE IS PRODUCED IN ACCORDANCE WITH STANDARD SPECIFICATIONS FOR READY MIX CONCRETE ASTM. ANY DEFICING MATERIALS, IMPROPER FINISHING AND LACK OF CURING WILL CAUSE DAMAGE OR A DECREASE IN STRENGTH.

NOTICE: MY SIGNATURE BELOW INDICATES THAT I HAVE READ THE HEALTH WARNING NOTICE AND SUPPLIER WILL NOT BE RESPONSIBLE FOR ANY DAMAGE CAUSED WHEN DELIVERING INSIDE CURB LINE AND AGREE TO THE TERMS AND CONDITIONS ON REVERSE SIDE. TIME IN EXCESS OF FREE TIME WILL BE CHARGED AT CURRENT DELAY RATE. ALL C.O.D. DELIVERIES MUST BE PAID IN ADVANCE AND LOAD ACCEPTED BY SIGNING THIS DELIVERY TICKET BEFORE POURING.

LOAD RECEIVED BY: \_\_\_\_\_

**PROPERTY DAMAGE RELEASE**  
 (TO BE SIGNED IF DELIVERY TO BE MADE INSIDE CURB LINE)

Dear Customer - The size and weight of this truck could cause damage to the premises and/or adjacent property if this load is placed where you desire. It is our wish to help you in every way that we can, but in order to do this we are requesting that you sign this RELEASE relieving this supplier and its affiliates from any responsibility from damage that may occur to the premises and/or adjacent property, buildings, sidewalks, drive-ways, curbs, etc. due to the delivery of this material, and that you also agree to help the driver remove mud from the wheels of his vehicle so that it will not litter the public street. Further, as additional consideration, the undersigned agrees to indemnify and hold harmless the driver of this truck and this supplier and its affiliates for any and all damage to the premises and/or adjacent property which may be claimed by anyone to have arisen out of delivery of this order.

SIGNED: **X** \_\_\_\_\_

**WEIGHMASTER CERTIFICATE**

THIS IS TO CERTIFY that the following described commodity was weighed, measured or counted by a weighmaster whose signature is on this certificate, who is a recognized authority of accuracy, as prescribed by Chapter 7 (commencing with Section 12700) of Division 5 of the California Business and Professions Code, administered by the Division of Measurement Standards of the California Department of Food and Agriculture.

**WATER ADDED AT CUSTOMER REQUEST**  
 EXCESSIVE WATER IS DETRIMENTAL TO CONCRETE PERFORMANCE.

**TEST RESULTS**

SA \_\_\_\_\_  
 REQUERSTOR'S NAME \_\_\_\_\_

SA \_\_\_\_\_  
 FULL LOAD \_\_\_\_\_ % LOAD \_\_\_\_\_ % LOAD \_\_\_\_\_ % LOAD \_\_\_\_\_  
 (GALLONS) (GALLONS) (GALLONS) (GALLONS)

TEST RESULTS  
 SLUMP \_\_\_\_\_ CONC. TEMP. \_\_\_\_\_ AIR% \_\_\_\_\_  
 CYLINDERS TAKEN:  YES  NO

NAME OF TESTING LAB: \_\_\_\_\_

**CUSTOMER** COD MATT HOECHLER **CUSTOMER CODE** 1600001 **DELIVERY ADDRESS** GAITHERSBURG MD- 100 BUREAU DR- BLDG 205

**PROJECT NAME** NIST GAITHERSBURG MD - COD SH **PROJECT CODE** 1546696

**CUSTOMER P.O. #** \_\_\_\_\_ **SPECIAL INSTRUCTIONS** ENTER OFF QUINCE ORCHARD RD TO GATE C

**CUSTOMER JOB ID** MATT 301.975.8517

LOAD QUANTITY	ORDERED QTY	CUMULATIVE QTY	PRODUCT ID	DESCRIPTION	UNIT PRICE	EXTENDED PRICE
3.0 yd	3.0	3.0	L40FE6P3	4K-PSI, LTWT with High Fiber	215.00	636.00
3.0 ea	0.0	ea	ENV1	ENVIRONMENTAL IMPACT CHARGE	2.00	6.00
3.0 ea	0.0	ea	EFUEL1	FUEL SURCHARGE	1.00	3.00
MINIMUM LOAD CHARGE						150.00

BATCH TIME	LEAVE PLANT	ARRIVE JOB	BEGIN POUR	FINISH POUR	LEAVE JOB	ARRIVE AT PLANT	USAGE CODE	SUB TOTAL
5:20	5:45	6:05						795.00
TOTAL WAIT TIME	PREVIOUS TRUCK	LOAD #	SLUMP	MAP PAGE	TIME DUE ON JOB	TAX RATE	TAX	
		1	7		6:22		44.01	
DATE	ORDER #	PLANT	TRUCK #	DELIVERY PROFESSIONAL	ORDER GRAND TOTAL	TOTAL		
10/26/17	7050	101	5249	HALE, MORRIS	839.01	839.01		

**DRUM REV - AT PLANT** \_\_\_\_\_ **DRUM REV - START** \_\_\_\_\_ **DRUM REV - FINISH** \_\_\_\_\_ **DEPUTY WEIGHMASTER** \_\_\_\_\_ **CONTROL #** \_\_\_\_\_


Truck	Driver	User	Disp Ticket Num	Ticket ID	Time	
5249	3896	user	20263908	42290	5:20 10/26/17	
Load Size	Mix Code	Returned	Qty	Mix Age	Seq	Load ID
3.00	CYDS L40FE6P3				W3	43844
Material	Design Qty	Required	Batched	% Moisture	Actual Wat	Tri
CUCM12	560 lb	1680 lb	1705 lb			
CUFASH	140 lb	420 lb	420 lb			
AUCSDA	1370 lb	4314 lb	4280 lb	4.97% A	24 gl	
AULM5A	890 lb	2697 lb	2680 lb	1.00% M	3 gl	
WATER	34.1 gl	68.3 gl	61.0 gl		61.0 gl	-4.0 gl
XUN31	35 oz	105 oz	106 oz			
XUN21	35 oz	105 oz	108 oz			
XUZ11	28 oz	84 oz	82 oz			
Actual	Num Batches: 1					
Load Total:	9607 lb	Design 0.405	Water/Cement 0.347 A	Manual 5:20:15	Design 102.3 gl	Actual 88.5 gl To Add: 13.8 gl
Slump: 7.00 in		Water in Truck: 0.0 gl	Adjust Water: 0.0 gl	/ Load	Tri Water: -4.0 gl/ CYD	

Figure E-3 Concrete batch ticket for repair concrete.

This publication is available free of charge from: https://doi.org/10.6028/NIST.TN.2054

# APPENDIX F CONCRETE RESULTS

CONCRETE INSPECTION



Page 1 of 1

---

**Project Name:** NIST Facility

**Client's Name:** National Institute of Standards and Technology

**General Contractor:** \_\_\_\_\_

**Project Location:** 100 Bureau Drive, Gaithersburg, MD 20899

**Project No.:** 5-526 **Permit No.:** \_\_\_\_\_

**Concrete Supplier:** Superior

---

**Design Strength (PSI @ 28 Days)**

2500  3000  4000  5000  Other (Specify): \_\_\_\_\_

**Mix Type**

Normal Weight Concrete  Lightweight Concrete  Other (Specify): \_\_\_\_\_

Air Entrained  Non Air Entrained  Mix Design (Specify): L40FE6P3

**Method of Placement:**  Pump  Bucket  Buggy  Chute  Other (Specify): \_\_\_\_\_

**Method of Consolidation:**  Mechanical Vibrators  Other (Specify): \_\_\_\_\_

**Cylinder Storage Location:**  Curing Box  Other (Specify): \_\_\_\_\_

---

Load #	Truck #	Ticket #	Time Batched	Mix Durati on (min)	Conc. Temp (F)	Slump (in)	Air-%	Plastic Unit Weight (pcf)	Water Added on Site (gal)	Placement Location	Specimen			
											Exact Grid Coordinates & Level or Elevation	Test Time	Cum. Conc. Placed	Set
1	5248		03:44 AM	195	56	8.5	2.5	120.9	5	Sod	05:40 AM	10		
2	5249		04:30 AM	200	56	8.25	2.5	122	5	Sod	07:10 AM	20		

---

**Non Compliances:** \_\_\_\_\_ **Who Advised:** \_\_\_\_\_ **How Corrected:** \_\_\_\_\_

**Technician:** Will **Weather:** Clouds **Air Temp:** 55 **Date:** 12/06/2016 **Field Copy Given to Client:**  Yes  No

FR009.CV-201605

**Figure F- 1 Fresh concrete measurements for main pour.**